Multi-scale Modeling and Optimization of Energy Absorption and Anisotropy in Aluminum Alloys

by

Christopher Peter Kohar

A thesis

presented to the University of Waterloo

in fulfillment of the

thesis requirement for the degree of

Doctor of Philosophy

in

Mechanical and Mechatronics Engineering

Waterloo, Ontario, Canada, 2017

EXAMINING COMMITTEE MEMBERSHIP

The following served on the Examining Committee for this thesis. The decision of the Examining Committee is by majority vote.

Supervisor(s)	Kaan Inal, PhD NSERC/General Motors Industrial Research Chair in "Integrated Computational Mechanics for Mass Efficient Automotive Structures"; Associate Professor, University of Waterloo
External Examiner	Stelios Kyriakides, PhD Professor, The University of Texas at Austin
Internal Examiner	Michael J. Worswick, PhD, PEng Tier 1 Canada Research Chair in Light Weight Materials under Extreme Deformation: Fabrication and Performance; Professor, University of Waterloo
Internal Examiner	William Melek, PhD, PEng Director of Mechatronics Engineering; Professor, University of Waterloo
Internal-External Examiner	Susan L. Tighe, PhD, PEng Norman W. McLeod Chair, Director of the Centre for Pavement & Transportation Technology; Professor, University of Waterloo

AUTHOR'S DECLARATION

This thesis consists of material of which I authored or co-authored: see Statement of Contributions included in this thesis. This is a true copy of the thesis, including any required final revisions, as accepted by my examiners.

I understand that my thesis may be made electronically available to the public.

STATEMENT OF CONTRIBUTIONS

The follow co-authors have contributed to the current work:

Professor Kaan Inal supervised this PhD thesis.

Dr. Raja K. Mishra provided EBSD measurements of the microstructure studied, provided various experimental data, such as coupon level experiments for calibrating and validation numerical frameworks.

Professor Michael Worswick, Mr. Amir Zhumagulov, Dr. Jose Imbert, and Mr. Jeff Wemp performed crash sled testing experiments and provided moderate-strain rate characterization.

Dr. Jidong Kang and Mr. Waqas Muhammad performed uniaxial tensile tests for material characterization of AA6063-T6.

Dr. Abhijit Brahme converted EBSD measurements to the synthetic microstructure for simulations; Furthermore, he assisted the authors in editing parts of the work.

Professor Mohsen Mohammadi helped in developing various post-processing subroutines; Furthermore, he assisted the authors in editing parts of the work.

Professor John Bassani provided valuable discussions and contributions to the development of theory for the phenomenological-based texture evolution model.

The balance of this work is my own.

ABSTRACT

This thesis outlines a study on the multi-scale modeling and optimization of lightweight aluminum front rails for automotive crashworthiness applications. This research is aimed to enhance the crashworthiness characteristics of aluminum front crush rail for mass-production mid-size vehicles. Understanding the performance of these components during a collision is critical to the successful implementation of aluminum into crashworthiness applications. Accurate simulation of energy absorption structures during crush is a challenging task due to large and various strain paths that the structure undergoes during collapse. Material anisotropy that is introduced from manufacturing presents an additional complexity that affects the deformation development. Furthermore, current methods that predict a material's initial microstructure and the evolution are not feasible in a component-scale simulation due to current computational limitations. Thus, new knowledge in optimization with advanced constitutive modeling for crashworthiness is required.

In this thesis, optimization techniques, using artificial intelligence techniques (neural networks, genetic algorithms, and adaptive simulated annealing) are used to study and identify elastic-plastic characteristics that are best suited for energy absorption in axial crush. New definitions and analytical equations for crush efficiency and energy absorption are developed and calibrated with the axial crush simulations to develop a framework for optimal material selection for axial crush. This work shows that the yield stress increases the energy absorption, peak crush force and steady state crush force, while tending to decrease the crush efficiency. Lightweight alloys with a low yield stress that have significant work hardening capabilities outperform materials with a high yield stress and low work hardening in terms of energy absorption when a constraint is imposed on the peak crushing force.

The effects of anisotropy on the axial crush response are studied using advanced phenomenological constitutive models. Dynamic crush simulations of tubes are performed using different yield surface shapes calibrated to the same experimental anisotropy. Simulations of axial crush show that the yield surface shape affects the collapse mode and predicted energy absorption characteristics of the crush tube. The analysis indicates that the deformation is predominately controlled by balanced biaxial deformation. However, characterization of both the

plane strain and pure shear points on the yield surface for energy absorption are also important. The shape and the area of the yield function governs the loading condition, which dictates the deformation and energy absorption.

A novel framework for structural optimization is developed to design an optimized front rail that maximizes crash energy absorption characteristics. The new design is coupled with material and process development to provide a component with superior energy absorption and strength characteristics that are commercially sustainable. Simulations are compared to the dynamic crush results for this new design. The size of the structure is optimized using the response surface methodology to enhance the specific energy absorption (SEA) of the structure. An analytical relationship that relates the SEA function to the crush efficiency is derived to show that a single optimization function parameter may be sufficient for mass minimization. The new optimization framework can increase the mean crush force and energy absorption by 21.9% and 26.7% more energy absorption than baseline geometries. Coupling the optimization framework with advanced constitutive models to can further enhance the energy absorption characteristics energy absorption and mean crush force of +4.2% and +2.5% respectively. Relaxing mass constraints, combined with anisotropic yield functions, can enhance SEA by +10%.

Finally, a framework for multi-scale modeling that bridges crystal plasticity to phenomenological plasticity is developed to study the significance of microstructural evolution on the enhancement of aluminum structures. Crystal plasticity is used to calibrate yield functions and microstructural evolution through the phenomenological-based texture evolution (PBTE) model. Simulations show that microstructural evolution can impact localization behaviour and ultimately, the energy absorption behaviour of the structure. The results of this thesis highlight the importance of coupling mechanical properties, such as initial anisotropy, microstructure evolution and flow stress behaviour with optimization of axial crush rails.

ACKNOWLEDGEMENTS

First, I would like to thank my supervisor, Professor Kaan Inal, for providing me with the opportunity to work on a project of my dreams in the automotive industry at the University of Waterloo Computational Mechanics Research Group. I am truly grateful for all of his leadership and support throughout all of my endeavours during my five-years. I would like to thank the members of my committee: Professor Michael Worswick (U. Waterloo), Professor William Melek (U. Waterloo), Professor Susan Tighe (U. Waterloo) and Professor Stelios Kyriakides (U. Texas at Austin) for all of their contributions to ensure the thesis is of top caliber.

There are many people I would to thank for helping me throughout my journey: Dr. Raja K. Mishra of General Motors Research & Development Center in Warren, Michigan for his mentorship in bridging the needs of the automotive industry to the scientific community; Dr. Justin Gammage (currently at the University of Ontario Institutive of Technology) for all his support during his tenure at General Motors Canadian Regional Engineering Center in Oshawa, Ontario; Professor Sanjeev Bedi at the University of Waterloo for all of his words of encouragement; Professor Mohsen Mohammadi (currently at the University of New Brunswick) for his early guidance at the beginning of my doctorate during his tenure at Waterloo as a post-doctorate fellow; Dr. Abhijit Brahme at the University of Waterloo for all of his assistance in textural and microstructural analysis.

I would like to acknowledge all of those who provided me assistance throughout this work: the high performance computing center at the University of Sherbrooke, and Dr. HuiZhong Lu at the Reseau Quebecois de Calcul de Haute Performance (RQCHP) for his technical support; Professor Michael Worswick, Dr. Jose Imbert-Boyd, Jeff Wemp and Amir Zhumagulov for their technical expertise and support in the crashworthiness experiments; Dr. Jidong Kang at CanmetMATERIALS and Waqas Muhammad at the University of Waterloo for performing tensile tests for material characterization.

Financial support for this work was provided by: Natural Sciences and Engineering Research Council of Canada – Automotive Partnership of Canada (NSERC-APC) under Grant number APCJ 441668-12, General Motors of Canada, Ontario Graduate Scholarship (OGS), Toyota Canada Automotive Safety Graduate Scholarship, President's Graduate Scholarship of

Waterloo, the Robbert Hartog Graduate Scholarship of Waterloo, Queen Elizabeth II Graduate Scholarship in Science and Technology (QEII-GSST) and the Doctoral Thesis Completion Award of Waterloo.

I would like to thank all of those who were part of the Computational Mechanics Research Group during my tenure. I would like to thank all the undergraduate, graduate students, and post-doctorate fellows who kept me company throughout the late nights of work, conferences and extra-curricular activities. Special acknowledgements go to: Kaab Omer who has been a fantastic office-mate who often offers his "unique" form of entertainment; Luke ten Kortenaar who spent many nights organizing the grilling, smoking, and BBQ adventures; Pingcheng Zhang for all the late-night discussions, road trips, and friendship; Joanna Majarreis for putting up with the all the "banana" moments throughout the completion of this thesis.

Last, and certainly not least, I would like to thank my family. To my brother, Richard, who helped me with my understanding of machine learning and their applications. To my father, Rick, who introduced me to the world of engineering and finite element analysis by letting me decorate my bedroom floor with his simulation and analysis contour plots. To my mother, Anneliese, who urged me to do as much schooling as possible and supported my "garage education" of late night dissection and rebuilding of cars for racing.

TABLE OF CONTENTS

LIST OF FIGURES

LIST OF TABLES

1 INTRODUCTION

Government regulations that reduce the carbon footprint of a vehicle, along with better fuel economy requirements, are driving vehicle mass reduction strategies. Manufacturers must balance cost, mass, and performance with innovative technologies in design, engineering and manufacturing to accomplish this goal [1]. In particular, the use of lightweight alloys, such as aluminum, has been studied for their implementation into these structural components for their distinctive weight saving and manufacturing advantages. Lightweight alloys offer a distinctive mass advantage that can translate to performance gains over automotive structural steels while the latter offers design, engineering and manufacturing flexibilities. Use of new design and engineering approaches can enable lightweight alloys to successfully compete for applications in vehicle structural components, such as front rails, bumpers, and B-pillars. These structural components are excellent candidates for vehicle weight reduction because they contribute substantially to the overall vehicle weight without direct interaction with the passenger. Moreover, these structures serve a critical function of dissipating the vehicle's kinetic energy through systematic crushing mechanisms during the event of a collision. These energy-absorbing components are always at the forefront of vehicle design [2]. As a result, government standards, such as the National Highway Traffic Safety Administration (NHTSA) in North America and the European New Car Assessment Program (Euro NCAP), have emerged to set more progressive standards in crashworthiness for various load cases [3]. Such a standard is the frontal barrier crashworthiness test, which evaluates a vehicles performance in an impacting scenario. Thus, understanding the performance of these components during axial crush must be considered alongside weight reduction.

These axial crush components are often simulated using finite element methods and verified through experimental testing. In recent years, the use of optimization software that utilize artificial intelligence and machine learning algorithms have been coupled with finite element simulations to enhance crashworthiness performance; see e.g. [4, 5, 6, 7, 8, 9, 10, 11]. A mathematical model is developed to predict the crash response of finite element simulations as a function of input parameters. Once this model was obtained, machine learning and optimization techniques were applied to the mathematical model to determine parameters that optimized the

shape for crash performance. This is known as structural optimization through the surface response methodology [12]. However, axial crushing is a complicated problem to simulate accurately due to the large and complex strain paths that the structure undergoes during collapse. Material anisotropy that is introduced from manufacturing presents an additional complexity that affects the deformation development. Modeling these complex strain paths and material behaviours accurately is critical to the successful implementation of numerical simulations as a product development tool. Two major classes of modeling anisotropy have been developed to incorporate anisotropy into numerical simulation tools: phenomenological (macro-scale) and polycrystalline (micro-scale) plasticity modeling [13].

Phenomenological-based plasticity models are derived from fitting a mathematical function, called a yield function, to the macroscopic anisotropy that is observed experimentally. Several works have emerged where anisotropy is incorporated into finite element simulations to better predict the axial crush response of aluminum structures [14, 15, 16]. Although phenomenological plasticity models may be appropriate for crashworthiness and metal forming applications, these models do not capture the microstructural evolution that develops during large plastic strain [17, 18, 13]. It is well known that the evolution of the microstructure greatly affects the anisotropy; this in turn, affects the localization for fracture due to plastic flow [19, 20, 21].

The polycrystalline plasticity model, also known as crystal plasticity, is a physics-based model that computes the crystallographic slip that results from dislocation glide. Taylor [22] explained that a dislocation is the shearing of atoms along a row of slip planes in a localized region along crystal lattice planes with the highest atomic density. In a material such as aluminum, dislocation glide is the main deformation mechanism at room temperature. Throughout the material, different grains have different orientations that compose the material texture. This gives rise to localized stress incompatibilities where certain grains have favourable orientations for dislocation glide to occur when a deformation field is applied. This orientation of favourable grain orientations, or the lack there of, causes plastic anisotropy. In the presence of dislocation glide, the crystal lattice continues to shear and change orientation, which evolves the microstructure and anisotropy. The average over the domain of these local incompatibilities produces the macroscopic stress-strain response. Several attempts have been made to implement

the crystal plasticity formulation in finite element framework to predict the final texture of aluminum during deformation [18, 23, 24, 25]. However, due to the limitations of computational resources, performing complete microstructural simulations of large-scale components, such as axial crush of aluminum structures, is still a distant future. Recently, an effort has been made to develop a microstructural evolution model of polycrystalline materials in a more computationally efficient manner [26]. Yet, this framework is still in the early stages of development and is a subject of this thesis.

The objective of this present work is to investigate and enhance the crashworthiness characteristics of aluminum front crush rails for mass-production mid-size vehicles through coupling optimization frameworks with advanced constitutive modeling techniques. A new framework for determining optimal mechanical and geometrical properties, through the use of nonlinear finite element analysis and optimization techniques, is presented. The influence of the initial material anisotropy is incorporated through advanced phenomenological models and systematically studied throughout this work. A new framework is developed to bridge the initial anisotropy and microstructural evolution from crystal plasticity to these advanced phenomenological models and study the performance gains in energy absorption capabilities for aluminum structures.

In Chapter 2, the current state of the art in constitutive modeling, crashworthiness, and optimization techniques is presented. A literature review on crystal plasticity, phenomenological plasticity, and phenomenological-based texture evolution and their corresponding model formulations are presented. A review of the analytical and finite element methods for predicting energy absorption is presented and detailed. The response surface methodology for performing structural optimization is detailed. The methods for the mathematical modeling technique, known as metamodeling, and optimization strategies are derived and detailed. Chapter 3 presents the research strategy that is employed throughout this work. Chapter 4 - Chapter 8 presents the research results of this thesis. Each of these chapters are from either a published, submitted, or in-progress peer-reviewed manuscript. Each of these chapters will introduce the problem, method of solution, finite element simulation results, discussion, and conclusions. Chapter 9 presents a summary of the key contributions and conclusions. Future work to improve on these phenomenological and optimization frameworks is presented.

2 LITERATURE REVIEW

2.1 Constitutive Modeling

In this thesis, three constitutive formulations are utilized to simulate the behaviour of aluminum: Crystal plasticity, phenomenological, and phenomenological-based texture evolution constitutive models. The framework that was proposed by Asaro and Needleman [19] and used by Inal *et al.* [18] with power law [27] and Chang-Asaro [28] hardening is used as the basis of the crystal plasticity constitutive model. In the phenomenological plasticity constitutive model, the following yield functions are presented: i) the von Mises [29], ii) Hill 1948 [30], iii) Hosford 1972 [31], iv) Hill 1979 [32], v) Barlat et al. 1989 [33] vi) Yld2000 [34], vii) Yld2004-18p [35] and viii) CPB06 [36]. The constitutive model, proposed by Bassani and Pan [26], for phenomenological-based texture evolution (PBTE) is also presented. Finally, these phenomenological plasticity models are implemented using the incremental plasticity procedure that was proposed by Yoon *et al*. [37]. Although some aluminum alloys exhibit advanced deformation phenomenon, such as minor tension-compression asymmetry [36, 38, 39] and kinematic hardening behaviours [40, 41, 42, 14], these influences are assumed to be negligible for this thesis.

2.1.1 Crystal Plasticity Constitutive Models

Typical metals are composed of polycrystals that consist of a spatial arrangement of atoms forming lattice cells. These lattice cells represent the microstructure of the material and describe how the geometric structuring of atoms occurs throughout the material. Common microstructures are: Body-Centered Cubic (BCC), Face-Centered Cubic (FCC) and Hexagonal Closed Packed (HCP). Figure 2.1 shows models of these common microstructures. The focus of this work is on the FCC microstructure. Some materials that have an FCC microstructure are aluminum, silver and gold. Taylor [22] explained that a dislocation is the shearing of atoms along a row of slip planes in a localized region. Figure 2.2 presents a schematic of dislocation slip.

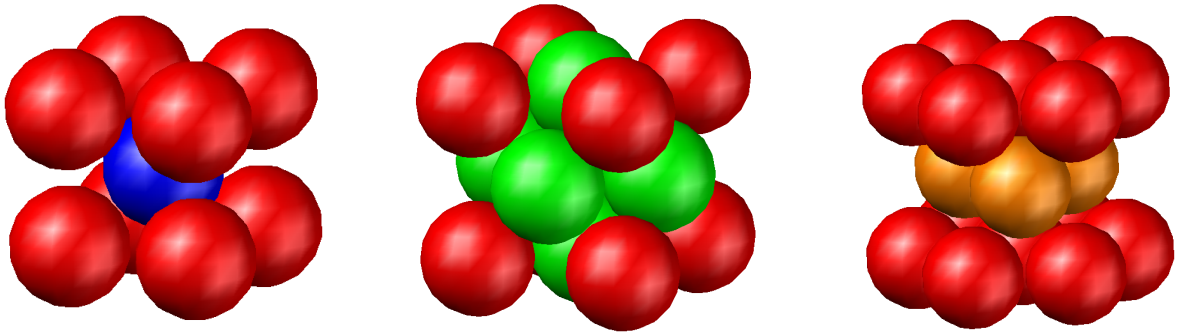

a) Body-Centered Cubic **b) Face-Centered Cubic** **c) Hexgonal Close-Packed**

Figure 2.1 – a) BCC, b) FCC, and c) HCP Crystal Structures

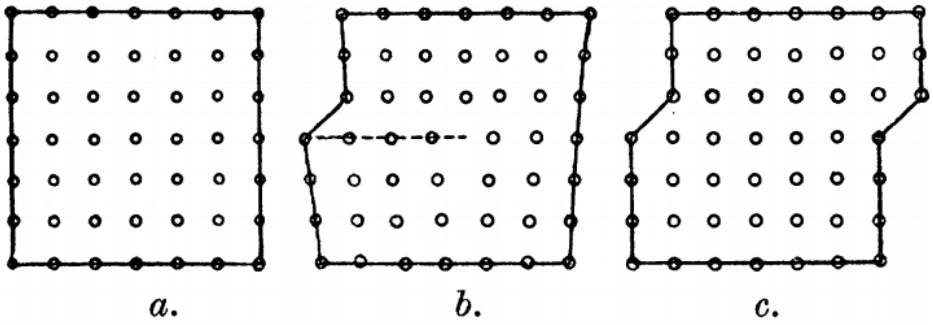

Figure 2.2 – Dislocation Slip Along a Row of Atoms [22]

Crystallographic slip is an anisotropic deformation where a large dislocation occurs on a slip plane. Dislocation occurs in the planes and directions of the lattice cell with the maximum atomic density. In FCC microstructure, the symmetric structuring of the microstructure results in 12 unique slip systems {111} with Burger's Vectors <110> which represent the slip directions. The slip systems and directions for an FCC microstructure can be seen below in Figure 2.3.

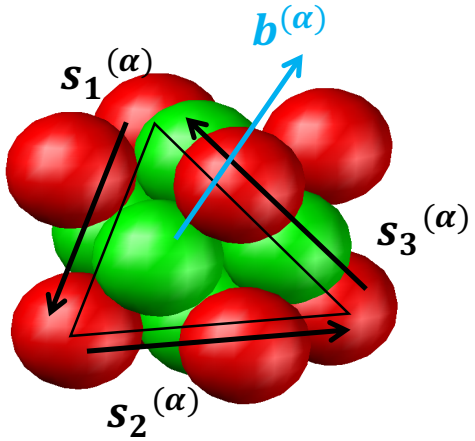

Figure 2.3 – The plane {111} and three <110> Slip Directions Within the Plane

Dislocation slip occurs when the shear stress along a slip plane reaches a critical stress. This is known as Schmid's Law. Schmid's Law acts as a yield criterion along the slip direction of a crystal where

$$\boldsymbol{\tau}^{(\alpha)} = s_i{}^{(\alpha)} b_j{}^{(\alpha)} \sigma_{ij} = \boldsymbol{\tau_y}{}^{(\alpha)} \qquad (2.1)$$

where α is the slip system, $\boldsymbol{\tau_y}{}^{(\alpha)}$ is the current yield stress for the current slip system, σ_{ij} is the state of stress acting on the crystal, $s_i{}^{(\alpha)}$ are the components of the slip vector and $b_j{}^{(\alpha)}$ are the components of the slip plane normal. As planes of atoms are dislocated, there is an increase in the required yield stress along the slip system for shearing to occur; this phenomenon is known as strain hardening. The resulting plastic deformation is visualized as a result of the total simple shear applied along the various slip systems that leaves the lattice and slip system vectors undistorted. Thus, the material and lattice are considered to deform elastically and rotate rigidly from the plastically deformed state of the current configuration.

The implementation of this constitutive model, known as the crystal plasticity, follows the framework proposed by Wu *et al.* [23] and Inal *et al.* [18]. The deformation gradient, $\boldsymbol{F}$, is then defined as

$$F_{ij} = \frac{dx_i}{dX_j} \qquad (2.2)$$

where x_i is a particle's current material point location in space and X_j is a particle's initial material point location. The deformation gradient can be decomposed into a component that contains crystallographic slip, $\boldsymbol{F^P}$ and a component that contains rigid body rotations and elastic deformation, $\boldsymbol{F^*}$, so that it is written as

$$\boldsymbol{F = F^* F^P} \qquad (2.3)$$

Figure 2.4 presents a schematic of the elastic and plastic deformation gradient decomposition. The velocity gradient, $\boldsymbol{L}$, can also be decomposed into components that contain crystallographic slip, $\boldsymbol{L^P}$ and a component that contains rigid body rotations and elastic deformation, $\boldsymbol{L^*}$

$$\boldsymbol{L = \dot{F} F^{-1} = L^* + L^P} \qquad (2.4)$$

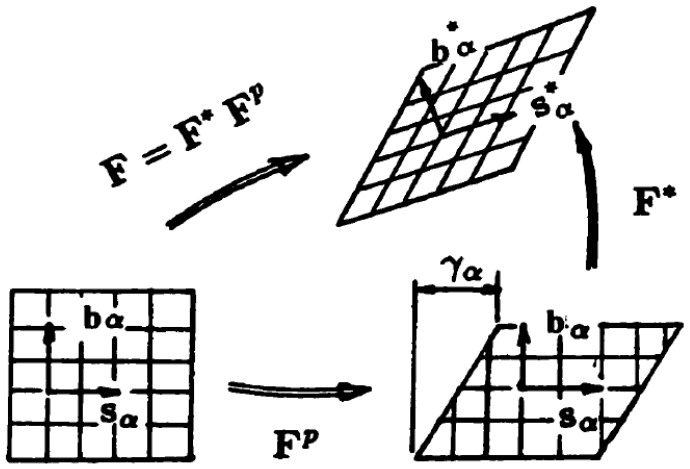

Figure 2.4 – Decomposition of the Deformation Gradient [13]

Each velocity gradient component can be defined as

$$\textbf{(a)} \quad \boldsymbol{L^* = \dot{F}^* F^{*-1}} \qquad \textbf{(b)} \quad \boldsymbol{L^P = F^* \left(\dot{F}^P F^{P^{-1}}\right) F^{*-1}} \qquad (2.5)$$

The slip plane, $s^{(\alpha)}$, and slip normal vectors, $b^{(\alpha)}$ stretch and rotate

$$\textbf{(a)} \quad \boldsymbol{s^{*(\alpha)} = F^* s^{(\alpha)}} \qquad \textbf{(b)} \quad \boldsymbol{b^{*(\alpha)} = b^{(\alpha)} F^{*-1}} \qquad (2.6)$$

From definition, the symmetric strain rates, $\boldsymbol{D}$, and skew symmetric spin tensors, $\mathbf{W}$, can be decomposed from the velocity gradient

$$\boldsymbol{L = D + W} \qquad (2.7)$$

where

$$\textbf{(a)} \quad \boldsymbol{D = \frac{1}{2}(L + L^T)} \qquad \textbf{(b)} \quad \mathbf{W = \frac{1}{2}(L - L^T)} \qquad (2.8)$$

Accordingly, elastic and plastic components can be decomposed as follows

$$\textbf{(a)} \quad \boldsymbol{D = D^* + D^P} \qquad \textbf{(b)} \quad \mathbf{W = W^* + W^P} \qquad (2.9)$$

The plastic strain rate, $\boldsymbol{D^P}$, and plastic spin, $\mathbf{W^P}$, for a crystal can be stated as

$$\textbf{(a)} \quad D^P = \frac{1}{2}\sum_{\alpha} \boldsymbol{P^{(\alpha)} \dot{\gamma}^{(\alpha)}} \qquad \textbf{(b)} \quad \mathbf{W^P} = \frac{1}{2}\sum_{\alpha} \boldsymbol{W^{(\alpha)} \dot{\gamma}^{(\alpha)}} \qquad (2.10)$$

where $\dot{\gamma}^{(\alpha)}$ is the shear strain rate along a slip vector, $P^{(\alpha)}$ and $W^{(\alpha)}$ are written as

(a) $P^{(\alpha)} = \frac{1}{2}\left[s^{*(\alpha)} \otimes b^{*(\alpha)} + b^{*(\alpha)} \otimes s^{*(\alpha)}\right]$ **(b)** $W^{(\alpha)} = \frac{1}{2}\left[s^{*(\alpha)} \otimes b^{*(\alpha)} - b^{*(\alpha)} \otimes s^{*(\alpha)}\right]$ **(2.11)**

The rate dependent elastic constitutive model for a single crystal is as follows

$$\check{\boldsymbol{\tau}}^{*} = \dot{\boldsymbol{\tau}}^{*} - \mathbf{W}^{*}\boldsymbol{\tau} - \boldsymbol{\tau}\mathbf{W}^{*} = \boldsymbol{C}\boldsymbol{D}^{*} \qquad \textbf{(2.12)}$$

where $\check{\boldsymbol{\tau}}^{*}$ is the Jaumann rate of Kirchoff Stress, $\boldsymbol{\tau}$ is Kirchoff Stress and $\boldsymbol{C}$ the elastic moduli tensor. In commercial finite element software, Jaumann rate of Cauchy stress, $\boldsymbol{\sigma}$, is used, which is written as

$$\boldsymbol{\sigma} = J^{-1}\boldsymbol{\tau} \qquad \textbf{(2.13)}$$

where $J = \det \boldsymbol{F}$ is the Jacobian. The constitutive model can be rewritten into the form of the Jaumann stress, $\check{\sigma}$

$$\check{\boldsymbol{\sigma}} = \boldsymbol{C}\boldsymbol{D} - \dot{\boldsymbol{\sigma}}^{\mathbf{0}} - \boldsymbol{\sigma}\, tr\boldsymbol{D} \qquad \textbf{(2.14)}$$

where $\dot{\boldsymbol{\sigma}}^{\mathbf{0}}$ is the visco-plastic stress rate. The visco-plastic stress rate is expressed as the summation of the crystallographic slip and rotation of each slip system as follows

$$\dot{\boldsymbol{\sigma}}^{\mathbf{0}} = \sum_{\boldsymbol{\alpha}} \left(\boldsymbol{C}\boldsymbol{P}^{(\boldsymbol{\alpha})} + \boldsymbol{W}^{(\boldsymbol{\alpha})}\boldsymbol{\sigma} - \boldsymbol{\sigma}\boldsymbol{W}^{(\boldsymbol{\alpha})}\right) \dot{\boldsymbol{\gamma}}^{(\boldsymbol{\alpha})} \qquad \textbf{(2.15)}$$

The slip vector shear strain rate, $\dot{\gamma}^{(\alpha)}$, is governed by a power law expression

$$\dot{\gamma}^{(\alpha)} = \dot{\gamma}_{(0)}\mathbf{sgn}\tau^{(\alpha)} \left|\frac{\tau^{(\alpha)}}{g^{(\alpha)}}\right|^{1/m} \qquad \textbf{(2.16)}$$

where $\gamma_{(0)}$ is the assumed shear rate for all slip systems, $\tau^{(\alpha)}$ is the resolved shear stress onto the slip system, $g^{(\alpha)}$ is the current hardness of the material and m is the strain rate sensitivity exponent. The hardness of a crystal evolves according to

$$\dot{g}^{(\alpha)} = \sum_{\beta} h_{(\alpha\beta)}\left|\dot{\gamma}^{(\beta)}\right| \qquad \textbf{(2.17)}$$

where $h_{(\alpha\beta)}$ is the hardening modulus. The hardening modulus described by Asaro and Needleman [19] takes the form

$$h_{(\alpha\beta)} = q_{(\alpha\beta)}h_{(\beta)} \ \ (\text{no sum on } \beta) \qquad \textbf{(2.18)}$$

with $q_{(\alpha\beta)}$ is the latent hardening behaviour of polycrystalline and $h_{(\beta)}$ is a single slip hardening rate.

Many models exist in literature that describe the hardening rate of single crystals, such as the models proposed by Pierce-Asaro-Needleman [27], Anand *et al*. [45, 46], Chang-Asaro [28] and the Bassani and Wu [47] model. In this work, the power law hardening model was used to simulate single crystal models and the Chang-Asaro hardening model was used for polycrystalline simulations where saturation occurs. The crystal power law hardening model is

$$h_{(\beta)} = h_0 \left(\frac{h_0 \gamma_a}{\tau_0 n_{xp}} + 1 \right)^{n_{xp}-1} \qquad (2.19)$$

where h_0 is the initial hardening rate of the system, τ_0 is the initial critically resolved shear stress, n_{xp} is the crystal hardening exponent and γ is the resolved shear strain. The Chang-Asaro hardening model is

$$h_{(\beta)} = h_s + (h_0 - h_s)\,\mathrm{sech}^2 \left\{ \left(\frac{h_0 - h_s}{\tau_s - \tau_0} \right) \gamma_a \right\} \qquad (2.20)$$

where h_0 is the initial hardening rate of the system, h_s is the asymptotic hardening rate, τ_0 is the initial critically resolved shear stress and τ_s is the saturation shear stress.

2.1.2 Phenomenological Plasticity

Phenomenological-based flow rules relate the flow stress, $\bar{\sigma}$, to a yield criterion, $\mathrm{f}(\sigma_{ij})$, that characterizes the material anisotropy during plastic flow, such that

$$\mathrm{f}(\sigma_{ij}) = \bar{\sigma} \qquad (2.21)$$

Various yield functions and flow stress models exist that are calibrated to the material anisotropy and flow stress behaviour. These various flow stress models and yield functions are discussed in detail. The experimental measurements used to calibrate the material anisotropy is also presented.

2.1.2.1 Calibration of Phenomenological Yield Functions

The parameters of the presented yield functions are determined by fitting selected material anisotropy measurements for various strain paths. These include but not limited to the

normal and shear yield stress variation with respect to loading direction, Lankford coefficient with respect to loading direction, balanced biaxial yield stress, yield surface curvature, the balanced biaxial Lankford coefficient.

The Lankford coefficients are strain ratios that are satisfied through Equation 2.22 [48]

$$R_\theta = \frac{d\varepsilon_{22}(\theta)}{d\varepsilon_{33}(\theta)} = -\frac{\sin^2\theta\,\dot{\varepsilon}_{11}^P - \sin(2\theta)\dot{\varepsilon}_{12}^P + \cos^2\theta\,\dot{\varepsilon}_{22}^P}{\frac{\partial f(\theta)}{\partial \sigma_{11}} + \frac{\partial f(\theta)}{\partial \sigma_{22}}} \quad (2.22)$$

where $\dot{\varepsilon}_{ij}^P$ are the plastic strain rate components that can be related through an associative flow rule [49, 50]

$$\dot{\boldsymbol{\varepsilon}}^{\boldsymbol{P}} = (\dot{\bar{\varepsilon}}^P)\frac{\partial \Phi}{\partial \boldsymbol{\sigma}} \quad (2.23)$$

where $\dot{\bar{\varepsilon}}^P$ is an effective plastic strain rate and $\frac{\partial \Phi}{\partial \boldsymbol{\sigma}}$ are the yield function normal. This leads to

$$R_\theta = \frac{d\varepsilon_{22}(\theta)}{d\varepsilon_{33}(\theta)} = -\frac{\sin^2\theta\frac{\partial f(\theta)}{\partial \sigma_{11}} - \sin(2\theta)\frac{\partial f(\theta)}{\partial \sigma_{12}} + \cos^2\theta\frac{\partial f(\theta)}{\partial \sigma_{22}}}{\frac{\partial f(\theta)}{\partial \sigma_{11}} + \frac{\partial f(\theta)}{\partial \sigma_{22}}} \quad (2.24)$$

where $\sigma_{11} = \sigma_\theta \cos^2\theta$, $\sigma_{12} = \sigma_\theta \sin\theta\cos\theta$, $\sigma_{22} = \sigma_\theta \sin^2\theta$, θ is the orientation and σ_θ is the corresponding yield stress with respect to the extrusion/sheet direction. The uniaxial tension yield stress variation, σ_θ, the balanced biaxial yield stress, σ_b, and the shear yield stress, τ_s, are satisfied through the corresponding yield function. The yield stress variation is determined by satisfying the yield function for σ_θ. Furthermore, the shear yield stress variation, τ_θ, is satisfied through the corresponding yield function where $\sigma_{11} = 2\tau_\theta \sin\theta\cos\theta$, $\sigma_{22} = -2\tau_\theta \sin\theta\cos\theta$, $\sigma_{12} = \tau_\theta(\cos^2\theta - \sin^2\theta)$. The balanced biaxial Lankford coefficient is satisfied through

$$R_b = \frac{d\varepsilon_{22}}{d\varepsilon_{11}} = \left.\frac{\frac{\partial \Phi}{\partial \sigma_{22}}}{\frac{\partial \Phi}{\partial \sigma_{11}}}\right|_{\sigma_{11}=\sigma_{22}=\sigma_b} \quad (2.25)$$

The coefficients for each yield function are obtained by selecting the desired anisotropy

parameters and minimizing an error function between the predicted and measured response. This minimization is achieved by using the genetic algorithm scheme in Section 0 and then refined using the gradient descent method presented in Section 2.3.1.2. The minimization error function (MEF) is defined as

$$MEF = W_1 \sum_{i=1}^{P_1} \left(\frac{R_{\theta_i} - \hat{R}_{\theta_i}}{R_{\theta_i}} \right)^2 + W_2 \sum_{i=1}^{P_2} \left(\frac{\sigma_{\theta_i} - \hat{\sigma}_{\theta_i}}{\sigma_{\theta_i}} \right)^2 + W_3 \sum_{i=1}^{P_3} \left(\frac{\tau_{\theta_i} - \hat{\tau}_{\theta_i}}{\tau_{\theta_i}} \right)^2 + W_4 \left(\frac{\sigma_b - \hat{\sigma}_b}{\sigma_b} \right)^2 + W_5 \left(\frac{R_b - \hat{R}_b}{R_b} \right)^2 \quad (2.26)$$

where P_i is the number of points for each anisotropy measurement, W_i are applied weights for each component to be fit, R_{θ_i}, σ_{θ_i}, τ_{θ_i}, σ_b, R_b are the actual measured values, and $\hat{R}_{\theta_i}$, $\hat{\sigma}_{\theta_i}$, $\hat{\tau}_{\theta_i}$, $\hat{\sigma}_b$, $\hat{R}_b$ are the fitted values.

2.1.2.2 Flow Stress Hardening Models

Two flow stress hardening are used throughout this work: Power Law Hardening [49] and Voce [51] hardening law. The power law model has the advantage of a continuous hardening behaviour, while the Voce hardening law saturates. The power law hardening relation relates the quasi-static effective stress, $\bar{\sigma}_{0,p}$, to the total plastic strain, $\bar{\varepsilon_p}$, and it is written as

$$\bar{\sigma}_{0,p} = K\left(\varepsilon_0 + \bar{\varepsilon}_p\right)^n \quad (2.27)$$

where K is the strength coefficient, ε_0 is the total elastic strain, $\bar{\varepsilon}_p$ is the total plastic strain, n is the work hardening exponent. The Voce [51] hardening law relation relates the quasi-static effective stress, $\bar{\sigma}_{0,V}$ to the total plastic strain through

$$\bar{\sigma}_{0,V} = \sigma_{UTS} - (\sigma_{UTS} - \sigma_0) \exp\left(-D\bar{\varepsilon}_p\right) \quad (2.28)$$

where σ_0 is the quasi-static yield strength, σ_{UTS} is the ultimate tensile strength, D is the Voce hardening saturation coefficient.

In order to take into account the effects of strain rate sensitivity, two strain-rate sensitivity models are also used throughout this work: the Johnson-Cook strain rate sensitivity [52] and the Cowper-Symonds [53] strain rate sensitivity models. These strain rate sensitivity

models scale the the quasi-static effective stress, $\bar{\sigma}_0$. The Johnson-Cook strain rate sensitivity model is defined as

$$\bar{\sigma} = \bar{\sigma}_0 \left(1 + \mathrm{C} \ln\left(\frac{\dot{\varepsilon}}{\dot{\varepsilon}_\mathrm{o}}\right)\right) \quad (2.29)$$

where C is the strain rate sensitivity parameter, $\dot{\varepsilon}$ is the strain rate and $\dot{\varepsilon}_\mathrm{o}$ is a reference strain rate. In this work, the strain-rate is defined as the effective von Mises strain rate, such that

$$\dot{\varepsilon} = \sqrt{\frac{2}{3} D'_{ij} D'_{ij}} \quad (2.30)$$

where $D'_{ij} = D_{ij} - \frac{1}{3} D_{kk} \delta_{ij}$. The Cowper-Symonds strain rate sensitivity [53]

$$\bar{\sigma} = \bar{\sigma}_0 \left(1 + \left(\frac{\dot{\varepsilon}}{M}\right)^{\frac{1}{P}} \right) \quad (2.31)$$

where M is the reference material strain-rate sensitivity coefficient and P is the strain-rate sensitivity exponent. Similar to calibration for anisotropy variation, the flow stress hardening models are calibrated to uniaxial tensile experiments by minimizing a global error function, such that

$$MEF = \sum_{j=1}^{m} \sum_{i=1}^{n} \left(\frac{\bar{\sigma}\left(\varepsilon_i, \dot{\varepsilon}_j\right) - \hat{\bar{\sigma}}\left(\varepsilon_i, \dot{\varepsilon}_j\right)}{\bar{\sigma}\left(\varepsilon_i, \dot{\varepsilon}_j\right)} \right)^2 \quad (2.32)$$

where $\bar{\sigma}\left(\varepsilon_i, \dot{\varepsilon}_j\right)$ is the measured flow stress at a given strain level, ε_i, for a given strain rate, $\dot{\varepsilon}_j$, n is the number of experimental measurements and m is the number of different strain rates experiments.

2.1.2.3 Phenomenological Yield Functions

2.1.2.3.1 von Mises (1913) Isotropic Yield Function

The classical 3-dimensional isotropic von Mises [29] yield function is defined as

$$\Phi_{vm} = 3J_2 - \bar{\sigma}^2 = 0 \qquad (2.33)$$

where J_2 is the sum of the tensor product of the deviatoric stress of the Cauchy stress tensor, **s**

$$J_2 = \frac{1}{2} s_{ij} s_{ij} \quad (i = 1 \ldots 3,\ j = 1 \ldots 3) \qquad (2.34)$$

such that

$$\mathbf{s} = \boldsymbol{\sigma} - \frac{1}{3} tr\boldsymbol{\sigma} \qquad (2.35)$$

The von Mises yield function can be expressed in principal stress form

$$\Phi_{vm} = (\sigma_1 - \sigma_2)^2 + (\sigma_2 - \sigma_3)^2 + (\sigma_3 - \sigma_1)^2 - 2\bar{\sigma}^2 = 0 \qquad (2.36)$$

where σ_i are the principal stresses of the Cauchy stress tensor. In plane stress form, the von Mises yield function simplifies to

$$\Phi_{vm} = {\sigma_{11}}^2 - \sigma_{11}\sigma_{22} + {\sigma_{22}}^2 + 3{\sigma_{12}}^2 - \bar{\sigma}^2 = 0 \qquad (2.37)$$

This yield function has no yield stress or Lankford coefficient variation.

2.1.2.3.2 Hill's (1948) Anisotropic Yield Function

Hill [30] proposed an extension to the isotropic yield function to be able to capture material anisotropy by introducing calibration coefficients to the formulation. The 3-dimensional Hill-48 yield function is defined as

$$\Phi_{H48} = c_1(\sigma_{33} - \sigma_{11})^2 + c_2(\sigma_{22} - \sigma_{33})^2 + c_3(\sigma_{11} - \sigma_{22})^2 + c_4{\sigma_{12}}^2 + c_5{\sigma_{23}}^2 + c_6{\sigma_{13}}^2 - 2\bar{\sigma}^2 = 0 \qquad (2.38)$$

where the parameters, c_i, are calibrated to the material anisotropy. When $c_1 = c_2 = c_3 = 1$ and $c_4 = c_5 = c_6 = 6$, the Hill-48 yield function decomposes into the von Mises yield function. In a plane stress formulation, Hill's yield function reduces to

$$\Phi_{H48} = c_1{\sigma_{11}}^2 + c_2{\sigma_{22}}^2 + c_3(\sigma_{11} - \sigma_{22})^2 + 6c_6{\sigma_{12}}^2 - 2\bar{\sigma}^2 = 0 \qquad (2.39)$$

2.1.2.3.3 Hosford (1972) Generalized Isotropic Yield Function

The Hosford [31] yield function is a simplified form of the generalized isotropic yield criteria, such that

$$\Phi_{Hosford} = |\sigma_1 - \sigma_2|^a + |\sigma_2 - \sigma_3|^a + |\sigma_3 - \sigma_1|^a - 2\bar{\sigma}^a = 0 \quad (2.40)$$

where σ_i are the principal stresses of the stress tensor. The coefficient a is an exponential hardening coefficient that is a function of the crystal structure that controls the yield function curvature. For face centered cubic material, such as aluminum, the coefficient is $a = 8$ [54]. When $a = 2$, the Hosford yield criteria reverts to the von Mises yield criteria.

2.1.2.3.4 Hill (1979) Generalized Anisotropic Yield Function

The plane stress generalized Hill [32] anisotropic yield criteria is used as a simplified model to capture anisotropic behaviour of polycrystalline behaviour. The yield function is defined as

$$\Phi_{H79} = c_1|\sigma_2 - \sigma_3|^a + c_2|\sigma_3 - \sigma_1|^a + c_3|\sigma_1 - \sigma_2|^a + c_4|2\sigma_1 - \sigma_2 - \sigma_3|^a + c_5|2\sigma_2 - \sigma_1 - \sigma_3|^a + c_6|2\sigma_3 - \sigma_1 - \sigma_2|^a - \bar{\sigma}^a = 0 \quad (2.41)$$

where σ_i are the principal stresses, c_i, are calibrated to the material anisotropy, and a is an exponential hardening coefficient that controls the curvature. The coefficients are calibrated to the material anisotropy and yield surface curvature. When $a = 2$, the generalized anisotropic yield criterion reverts to the quadratic Hill-1948 yield criterion. For a plane stress formulation ($\Sigma_3 = 0$), the yield function simplifies to

$$\Phi_{H79} = c_1|\sigma_2|^a + c_2|\sigma_1|^a + c_3|\sigma_1 - \sigma_2|^a + c_4|2\sigma_1 - \sigma_2|^a + c_5|2\sigma_2 - \sigma_1|^a + c_6|\sigma_1 + \sigma_2|^a - \bar{\sigma}^a = 0 \quad (2.42)$$

and the principal intermediate stresses are calculated as

$$\sigma_{1,2} = \frac{1}{2}\left(\sigma_{11} + \sigma_{22} \pm \sqrt{(\sigma_{11} - \sigma_{22})^2 + 4{\sigma_{12}}^2}\right) \quad (2.43)$$

2.1.2.3.5 Barlat et al. (1989) Yield Function

Barlat and Richmond (1987) [55] introduced the plane stress yield function in the form of

$$\Phi_{B87} = |K_1 - K_2|^a + |K_1 + K_2|^a + |2K_2|^a - 2\bar{\sigma}^a = 0 \qquad (2.44)$$

where K_1 and K_2 are stress tensor invariants defined as

$$K_1 = \frac{\sigma_{11} + \sigma_{22}}{2} \qquad K_2 = \sqrt{\left(\frac{\sigma_{11} - \sigma_{22}}{2}\right)^2 + {\sigma_{12}}^2} \qquad (2.45)$$

and the coefficient a is an exponential hardening coefficient. This representation is an alternative representation to the generalized isotropic Hosford [31] and the isotropic form of Hill (1979) [32] yield function. Since K_1 and K_2 are invariants, adding constants in front of these terms would lead to a planar isotropic yield function [55]. However, in the work of Barlat and Lian (1989) [33], it was shown that simply adding coefficients to the stress invariants that were stress independent, as presented in the Hill (1979) [32] yield function, would lead to a planar isotropic formulation (no Lankford variation) and would require the enforcement of orthotropic/anisotropic axes. Furthermore, Barlat and Lian commented that allowing the coefficients to be stress dependent would result in the loss of convexity, which is an assumption of incremental plasticity with associative flow rules [56]. Thus, Barlat and Lian (1989) [33] introduced the coefficients into the stress invariants to transform them. This lead to the plane stress yield function as [33]

$$\Phi_{B89} = c_1|K_1 + K_2|^a + c_1|K_1 - K_2|^a + c_2|2K_2|^a - 2\bar{\sigma}^a = 0 \qquad (2.46)$$

Where the modified K_1 and K_2 are stress tensor invariants defined as

$$K_1 = \frac{\sigma_{11} + c_3\sigma_{22}}{2} \qquad K_2 = \sqrt{\left(\frac{\sigma_{11} - c_3\sigma_{22}}{2}\right)^2 + {c_3}^2{\sigma_{12}}^2} \qquad (2.47)$$

The anisotropic material constants c_i are obtained by satisfying Equation 2.46 and for three Lankford coefficients: $R_{00}, R_{45}, \text{and } R_{90}$. Extension from plane stress to 3D formulation is obtained by solving the Cayley-Hamilton eigenvalue problem for 3D stress tensors, transforming the planar stress components and adding additional parameters to the out of planar shear components [57].

2.1.2.3.6 Barlat et al. (2003) Yld2000 Yield Function

The plane stress yield function proposed by Barlat *et al.* [34], known as the Yld2000 yield function, is defined in Equation 2.48 as [34]

$$\Phi_{Yld2000} = \phi' + \phi'' - 2\sigma_Y^a = 0 \qquad (2.48)$$

where σ_Y is the yield stress and ϕ' and ϕ'' are anisotropic functions that are linearly transformed, such that

$$\textbf{(a)} \quad \phi' = |{X_1}' - {X_2}'|^a \qquad \textbf{(b)} \quad \phi'' = |{X_1}'' + 2{X_2}''|^a + |2{X_1}'' + {X_2}''|^a \qquad (2.49)$$

where ${X_i}'$and ${X_i}''$ are the principal stresses of the linearly transformed Cauchy stress tensor, $\boldsymbol{\sigma}$. The transformed stress state is defined as

$$\textbf{(a)} \quad \boldsymbol{X}' = \boldsymbol{L}' \cdot \boldsymbol{\sigma} \qquad \textbf{(b)} \quad \boldsymbol{X}'' = \boldsymbol{L}'' \cdot \boldsymbol{\sigma} \qquad (2.50)$$

where the $\boldsymbol{L}'$ and $\boldsymbol{L}''$ are linear stress transformation tensors defined as

$$\textbf{(a)} \quad \boldsymbol{L}' = \begin{bmatrix} {L_{11}}' & {L_{12}}' & 0 \\ {L_{21}}' & {L_{22}}' & 0 \\ 0 & 0 & {L_{66}}' \end{bmatrix} \qquad \textbf{(b)} \quad \boldsymbol{L}'' = \begin{bmatrix} {L_{11}}'' & {L_{12}}'' & 0 \\ {L_{21}}'' & {L_{22}}'' & 0 \\ 0 & 0 & {L_{66}}'' \end{bmatrix} \qquad (2.51)$$

such that

$$\textbf{(a)} \quad \begin{bmatrix} {L_{11}}' \\ {L_{12}}' \\ {L_{21}}' \\ {L_{22}}' \\ {L_{66}}' \end{bmatrix} = \begin{bmatrix} 2/3 & 0 & 0 \\ -1/3 & 0 & 0 \\ 0 & -1/3 & 0 \\ 0 & 2/3 & 0 \\ 0 & 0 & 1 \end{bmatrix} \begin{bmatrix} \alpha_1 \\ \alpha_2 \\ \alpha_7 \end{bmatrix} \qquad \textbf{(b)} \quad \begin{bmatrix} {L_{11}}'' \\ {L_{12}}'' \\ {L_{21}}'' \\ {L_{22}}'' \\ {L_{66}}'' \end{bmatrix} = \frac{1}{9} \begin{bmatrix} -2 & 2 & 8 & -2 & 0 \\ 1 & -4 & -4 & 4 & 0 \\ 4 & -4 & -4 & 1 & 0 \\ -2 & 8 & 2 & -2 & 0 \\ 0 & 0 & 0 & 0 & 9 \end{bmatrix} \begin{bmatrix} \alpha_3 \\ \alpha_4 \\ \alpha_5 \\ \alpha_6 \\ \alpha_8 \end{bmatrix} \qquad (2.52)$$

The principal transformation stress for the first transformed plane stress state, ${X_{1,2}}'$, is determined as

$${X_{1,2}}' = \frac{1}{2}\left({X_{xx}}' + {X_{yy}}' \pm \sqrt{({X_{xx}}' - {X_{yy}}')^2 + 4({X_{xy}}')^2} \right) \qquad (2.53)$$

A similar formulation is defined for the second transformed stress state, ${X_{1,2}}''$. The coefficient a is an exponential hardening coefficient that is a function of the crystal structure. The parameters

α_i are determined by fitting the material anisotropy. Through incorporating more coefficients, additional control of anisotropic variation can be achieved.

2.1.2.3.7 Barlat et al. (2005) Yld2004-18p Yield Function

The Barlat et al. [35] yield function, known as the Yld2004-18p, is a 3-dimensional flow rule that utilizes two transformations of the deviatoric Cauchy stress tensor. The first and second transformed deviatoric stress tensor is defined as

$$\tilde{\boldsymbol{S}}' = \boldsymbol{c}' \cdot \mathbf{s} \qquad\qquad \boldsymbol{S}'' = \boldsymbol{c}'' \cdot \mathbf{s} \qquad (2.54)$$

where the $\boldsymbol{c}'$ and $\boldsymbol{c}''$ are linear stress transformation tensors defined as

$$\boldsymbol{c}' = \begin{bmatrix} 0 & -c_{12}' & -c_{13}' & 0 & 0 & 0 \\ -c_{21}' & 0 & -c_{23}' & 0 & 0 & 0 \\ -c_{31}' & -c_{32}' & 0 & 0 & 0 & 0 \\ 0 & 0 & 0 & c_{44}' & 0 & 0 \\ 0 & 0 & 0 & 0 & c_{55}' & 0 \\ 0 & 0 & 0 & 0 & 0 & c_{66}' \end{bmatrix} \quad \boldsymbol{c}'' = \begin{bmatrix} 0 & -c_{12}'' & -c_{13}'' & 0 & 0 & 0 \\ -c_{21}'' & 0 & -c_{23}'' & 0 & 0 & 0 \\ -c_{31}'' & -c_{32}'' & 0 & 0 & 0 & 0 \\ 0 & 0 & 0 & c_{44}'' & 0 & 0 \\ 0 & 0 & 0 & 0 & c_{55}'' & 0 \\ 0 & 0 & 0 & 0 & 0 & c_{66}'' \end{bmatrix} \qquad (2.55)$$

This introduces 18 parameters that are calibrated to the material anisotropy. The Yld2004-18p yield function is defined as

$$\begin{aligned} \Phi_{YLD2004-18p} = {} & \left|\tilde{S}'_1 - \tilde{S}''_1\right|^a + \left|\tilde{S}'_1 - \tilde{S}''_2\right|^a + \left|\tilde{S}'_1 - \tilde{S}''_3\right|^a + \left|\tilde{S}'_2 - \tilde{S}''_1\right|^a + \left|\tilde{S}'_2 - \tilde{S}''_2\right|^a \\ & + \left|\tilde{S}'_2 - \tilde{S}''_3\right|^a + \left|\tilde{S}'_3 - \tilde{S}''_1\right|^a + \left|\tilde{S}'_3 - \tilde{S}''_2\right|^a + \left|\tilde{S}'_3 - \tilde{S}''_3\right|^a = 4\bar{\sigma}^a \end{aligned} \qquad (2.56)$$

where $\tilde{S}'_i$ and $\tilde{S}''_i$ are the principal transformed stresses of the first and second transformed deviatoric Cauchy stresses, which are determined from eigenvalue solutions to the Cayley-Hamilton theorem of a tensor.

2.1.2.3.8 Cazacu, Plunkett and Barlat (2006) Anisotropic Yield Function

The Cazacu, Plunkett and Barlat [36, 39] yield function is an extension to the Yld2000 and Yld2004-18p yield function, that utilizes multiple linear transformations of the deviatoric Cauchy stress tensor. The first and second transformed deviatoric stress tensors are defined as

$$\tilde{\boldsymbol{s}}' = \boldsymbol{C}' \cdot \mathbf{s} \qquad\qquad \boldsymbol{s}'' = \boldsymbol{C}'' \cdot \mathbf{s} \qquad (2.57)$$

where the $\boldsymbol{C}'$ and $\boldsymbol{C}''$ are linear stress transformation tensors defined as

$$\boldsymbol{C}' = \begin{bmatrix} C_{11}' & C_{12}' & C_{13}' & 0 & 0 & 0 \\ C_{12}' & C_{22}' & C_{23}' & 0 & 0 & 0 \\ C_{13}' & C_{23}' & C_{33}' & 0 & 0 & 0 \\ 0 & 0 & 0 & C_{44}' & 0 & 0 \\ 0 & 0 & 0 & 0 & C_{55}' & 0 \\ 0 & 0 & 0 & 0 & 0 & C_{66}' \end{bmatrix} \quad \boldsymbol{C}'' = \begin{bmatrix} C_{11}'' & C_{12}'' & C_{13}'' & 0 & 0 & 0 \\ C_{12}'' & C_{22}'' & C_{23}'' & 0 & 0 & 0 \\ C_{13}'' & C_{23}'' & C_{33}'' & 0 & 0 & 0 \\ 0 & 0 & 0 & C_{44}'' & 0 & 0 \\ 0 & 0 & 0 & 0 & C_{55}'' & 0 \\ 0 & 0 & 0 & 0 & 0 & C_{66}'' \end{bmatrix} \quad (2.58)$$

These coefficients are calibrated to the material anisotropy and yield surface curvature. In a plane stress formulation, the first transformed principal stresses are

$$\tilde{s}'_{1,2} = \frac{1}{2}\left(\tilde{s}'_{11} + \tilde{s}'_{22} \pm \sqrt{(\tilde{s}'_{11} - \tilde{s}'_{22})^2 + 4\tilde{s}'^2_{12}}\right), \quad \tilde{s}'_3 = \tilde{s}'_{33} \qquad (2.59)$$

Further transformations are defined in a similar manner. Using one linear transformation, the yield function, here known as CPB06ex1, is defined as

$$\Phi_{CPB06ex1} = (|\tilde{s}'_1| - k\tilde{s}'_1)^a + (|\tilde{s}'_2| - k\tilde{s}'_2)^a + (|\tilde{s}'_3| - k\tilde{s}'_3)^a - \bar{\sigma}^a = 0 \qquad (2.60)$$

where k is a parameter that can be used to capture tension-compression asymmetry. However, the tension-compression asymmetry is assumed to be negligible ($k = 0$) for FCC single and polycrystalline materials. This reduces the yield function to summation of raised transformed principal stresses

$$\Phi_{CPB06ex1} = |\tilde{s}'_1|^a + |\tilde{s}'_2|^a + |\tilde{s}'_3|^a - \bar{\sigma}^a = 0 \qquad (2.61)$$

Using two transformations, the yield function, here known as CPB06ex2, is defined as an additional summation of the raised transformed principal stresses, such that

$$\Phi_{CPB06ex2} = |\tilde{s}'_1|^a + |\tilde{s}'_2|^a + |\tilde{s}'_3|^a + |\tilde{s}''_1|^a + |\tilde{s}''_2|^a + |\tilde{s}''_3|^a - \bar{\sigma}^a = 0 \qquad (2.62)$$

Using three transformations, the yield function, here known as CPB06ex3, is defined as

$$\Phi_{CPB06ex3} = \sum_{j=1}^{3}\sum_{i=1}^{3}\left|\tilde{s}_i^{(j)}\right|^a - \bar{\sigma}^a = 0 \qquad (2.63)$$

Additional linear transformations are defined in a similar manner.

2.1.2.4 Implementation into an Incremental Finite Element Formulations

These phenomenological constitutive models can be implemented into a user-defined material subroutine (UMAT) in commercial finite element software, such as LS-DYNA. LS-DYNA is a non-linear explicit dynamic formulation for stress analysis that utilizes an updated-Lagrangian formulation [58] where the configuration of the system is updated at the end of each time step. For simulations that utilize the plane stress assumption, the LS-DYNA code performs a transformation from the global system of coordinates to a local elemental system of coordinates prior to entering the UMAT subroutine. This allows for the local elemental coordinate system to rotate with the material to account for large rotations [58], such that the Cauchy stress rate is equivalent to the Jaumann stress rate. Thus, the Cauchy stress tensor can be used with a small-strain formulation with minimal error (assuming that the increment in strain is small in the given time step). The stress integration scheme follows the cutting plane algorithm that was formulated by Chung and Richmond [59] and Yoon et al. [37] and used by Abedrabbo et al. [60].

The stress integration scheme follows an incremental form of rate-independent plasticity using an associative flow rule. The elasto-plastic constitutive equations are

$$\boldsymbol{\Delta D} = \boldsymbol{\Delta D}^{*} + \boldsymbol{\Delta D}^{\boldsymbol{P}} \qquad (2.64)$$

$$\boldsymbol{\Delta \sigma} = \boldsymbol{L}^{el} : \boldsymbol{\Delta D}^{*} \qquad (2.65)$$

$$\text{Associative flow rule:} \quad \boldsymbol{\Delta D}^{\boldsymbol{P}} = (\Delta \bar{\varepsilon}^{P}) \frac{\partial \Phi}{\partial \boldsymbol{\sigma}} \qquad (2.66)$$

$$\text{Yield Function:} \quad \Phi \leq 0 \qquad (2.67)$$

$$\text{Normality Rule:} \quad \Delta \bar{\varepsilon}^{P} \geq 0 \qquad (2.68)$$

where the partial $\frac{\partial \Phi}{\partial \boldsymbol{\sigma}}$ are yield function dependent.

In the UMAT implementation, for a given iteration in time, $\boldsymbol{t}$, the next increment in stretch, $\boldsymbol{\Delta D_{t+1}}$, is an input into the subroutine, the current stress state, $\boldsymbol{\sigma_t}$, and material history is also known, and the subroutine requires the stress state, $\boldsymbol{\sigma_{t+1}}$, at the next increment in time. Following the cutting plane algorithm, a trial stress is calculated for the next iteration of stress, $\boldsymbol{\sigma}_{\boldsymbol{t+1}}^{(\boldsymbol{i})}$, where i is the current iteration of the trial stress, assuming that the increment in stretch is elastic, such that

$$\Delta \boldsymbol{D}_{t+1}^{*\,(i)} = \Delta \boldsymbol{D}_{t+1} \qquad (2.69)$$

$$\Delta \boldsymbol{D}_{t+1}^{\boldsymbol{p}\,(i)} = \boldsymbol{0} \qquad (2.70)$$

$$\bar{\varepsilon}_{t+1}^{\boldsymbol{p}\,(i)} = \bar{\varepsilon}_{t}^{\boldsymbol{p}} \qquad (2.71)$$

$$\Delta \bar{\varepsilon}^{p\,(i)} = 0 \qquad (2.72)$$

and that the trial stress is

$$\boldsymbol{\sigma}_{t+1}^{(i)} = \boldsymbol{\sigma}_{t} + \boldsymbol{L}^{el} : \Delta \boldsymbol{D}_{t+1}^{*\,(i)} = \boldsymbol{\sigma}_{t} + \boldsymbol{L}^{el} : \Delta \boldsymbol{D}_{t+1} \qquad (2.73)$$

For a plane stress formulation, the through thickness strain increment is assumed

$$\Delta D_{33,\ t+1} = \frac{\nu(\Delta D_{22,\ t+1} + \Delta D_{11,\ t+1})}{\nu - 1} \qquad (2.74)$$

where ν is the isotropic Poisson ratio. The trial stress is used to determine if the material yields, through the calculation of the yield function

$$\Phi^{(i)}\left(\boldsymbol{\sigma}_{t+1}^{(i)}, \bar{\varepsilon}_{t+1}^{\boldsymbol{p}\,(i)}, \Delta \boldsymbol{D}_{t+1}\right) = \sigma_{eq}{}^{(i)}\left(\boldsymbol{\sigma}_{t+1}^{(i)}, \bar{\varepsilon}_{t+1}^{\boldsymbol{p}\,(i)}\right) - \bar{\sigma}\left(\bar{\varepsilon}_{t+1}^{\boldsymbol{p}\,(i)}, \Delta \boldsymbol{D}_{t+1}\right) \leq 0 \qquad (2.75)$$

If the condition in Equation 2.75 is satisfied, then the initial assumption of an elastic trial stress is correct and the stress state and material history is returned

$$\boldsymbol{\sigma}_{t+1} = \boldsymbol{\sigma}_{t+1}^{(i)}, \qquad \bar{\varepsilon}_{t+1}^{\boldsymbol{p}} = \bar{\varepsilon}_{t+1}^{\boldsymbol{p}\,(i)} \qquad (2.76)$$

For plane stress formulations

$$\Delta D_{33,t+1} = \Delta D_{33,t+1}^{(0)} \qquad (2.77)$$

If the condition is not satisfied, then the trial stress is iterated on the plastic multiplier using an iterative scheme

Trial Stress Update:

$$\begin{aligned} \boldsymbol{\sigma}_{t+1}^{(i+1)} &= \boldsymbol{\sigma}_{t+1}^{(i)} - \boldsymbol{L}^{el} : \Delta \boldsymbol{D}_{t+1}^{\boldsymbol{P}\,(i+1)} \\ &= \boldsymbol{\sigma}_{t+1}^{(i)} - \boldsymbol{L}^{el} : \left(\Delta \bar{\varepsilon}^{p\,(i)}\right) \frac{\partial \Phi\left(\boldsymbol{\sigma}_{t+1}^{(i)}\right)}{\partial \boldsymbol{\sigma}} \end{aligned} \qquad (2.78)$$

with

Effective Plastic Strain Update:

$$\bar{\varepsilon}_{t+1}^{p\,(i+1)} = \bar{\varepsilon}_{t+1}^{p\,(i)} + \Delta \bar{\varepsilon}^{p\,(i)} \qquad (2.79)$$

The increment in effective plastic strain, $\Delta\bar{\varepsilon}_{t+1}^{p\ (i+1)}$, is determined through a first order Taylor series expansion of $\Phi\left(\boldsymbol{\sigma}_{t+1}^{(i)}, \bar{\varepsilon}_{t+1}^{\boldsymbol{p}\ (i)}, \boldsymbol{\Delta D}_{t+1}\right)$ such that

$$\Phi^{(i+1)}\left(\boldsymbol{\sigma}_{t+1}^{(i+1)}, \bar{\varepsilon}_{t+1}^{p\ (i+1)}, \boldsymbol{\Delta D}_{t+1}\right) = \Phi^{(i)}\left(\boldsymbol{\sigma}_{t+1}^{(i)}, \bar{\varepsilon}_{t+1}^{\boldsymbol{p}\ (i)}, \boldsymbol{\Delta D}_{t+1}\right) + \frac{d\Phi^{(i)}\left(\boldsymbol{\sigma}_{t+1}^{(i)}\right)}{d\boldsymbol{\sigma}} : \left(\boldsymbol{\sigma}_{t+1}^{(i+1)} - \boldsymbol{\sigma}_{t+1}^{(i)}\right) + \left(\frac{d\Phi^{(i)}\left(\bar{\varepsilon}_{t+1}^{p\ (i)}, \boldsymbol{\Delta D}_{t+1}\right)}{d(\Delta\bar{\varepsilon}^{p})}\right)\left(\bar{\varepsilon}_{t+1}^{p\ (i+1)} - \bar{\varepsilon}_{t+1}^{p\ (i)}\right) \quad (2.80)$$

where the scheme converges when the yield function criteria satisfies a prescribed tolerance

$$\Phi^{(i+1)}\left(\boldsymbol{\sigma}_{t+1}^{(i+1)}, \bar{\varepsilon}_{t+1}^{p\ (i+1)}, \boldsymbol{\Delta D}_{t+1}\right) \leq \varepsilon_{tol} \approx \mathbf{0} \quad (2.81)$$

where ε_{tol} is selected to be a small number (10^{-6}). Evaluating $\frac{d\Phi^{(i)}\left(\bar{\varepsilon}_{t+1}^{p\ (i)}, \boldsymbol{\Delta D}_{t+1}\right)}{d(\Delta\bar{\varepsilon}^{p})} = -\frac{d\bar{\sigma}^{(i)}\left(\bar{\varepsilon}_{t+1}^{p\ (i)}, \boldsymbol{\Delta D}_{t+1}\right)}{d(\Delta\bar{\varepsilon}^{p})}$ from the flow stress model, substituting the rearrangement of Equation 2.78 for $\left(\boldsymbol{\sigma}_{t+1}^{(i+1)} - \boldsymbol{\sigma}_{t+1}^{(i)}\right)$ and substituting the rearrangement of Equation 2.90

$$0 = \Phi^{(i)}\left(\boldsymbol{\sigma}_{t+1}^{(i)}, \bar{\varepsilon}_{t+1}^{\boldsymbol{p}\ (i)}, \boldsymbol{\Delta D}_{t+1}\right) + \frac{d\Phi^{(i)}\left(\boldsymbol{\sigma}_{t+1}^{(i)}\right)}{d\boldsymbol{\sigma}} : \left(-\boldsymbol{L}^{el} : \left(\Delta\bar{\boldsymbol{\varepsilon}}^{\boldsymbol{p}\ (i)}\right)\frac{\partial\Phi\left(\boldsymbol{\sigma}_{t+1}^{(i)}\right)}{\partial\boldsymbol{\sigma}}\right) - \left(\frac{d\bar{\boldsymbol{\sigma}}^{(i)}\left(\bar{\varepsilon}_{t+1}^{p\ (i)}, \boldsymbol{\Delta D}_{t+1}\right)}{d(\Delta\bar{\varepsilon}^{p})}\right)\left(\Delta\bar{\boldsymbol{\varepsilon}}^{\boldsymbol{p}\ (i)}\right) \quad (2.82)$$

Since the time step is internally controlled within LS-DYNA by the, the time step size is sufficiently small $(\Delta t \approx 10^{-8}s)$ that the higher order terms of the Taylor series expansion can be neglected. This linearizes the formulation such that the increment can be solved using the Newton-Raphson method

$$\Delta\bar{\varepsilon}^{p\ (i)} = \frac{\Phi^{(i)}\left(\boldsymbol{\sigma}_{t+1}^{(i)}, \bar{\varepsilon}_{t+1}^{\boldsymbol{p}\ (i)}, \boldsymbol{\Delta D}_{t+1}\right)}{\frac{\partial\Phi^{(i)}\left(\boldsymbol{\sigma}_{t+1}^{(i)}\right)}{\partial\boldsymbol{\sigma}} : \boldsymbol{L}^{el} : \frac{\partial\Phi^{(i)}\left(\boldsymbol{\sigma}_{t+1}^{(i)}\right)}{\partial\boldsymbol{\sigma}} + \frac{\partial\bar{\sigma}^{(i)}\left(\bar{\varepsilon}_{t+1}^{p\ (i)}, \boldsymbol{\Delta D}_{t+1}\right)}{\partial(\Delta\bar{\varepsilon}^{p})}} \quad (2.83)$$

where the plastic strain increments are

$$\boldsymbol{D}_{t+1}^{\boldsymbol{p}\ (i+1)} = \boldsymbol{\Delta D}_{t+1}^{\boldsymbol{p}\ (i)} + \left(\Delta\bar{\varepsilon}^{p\ (i)}\right)\frac{\partial\Phi^{(i)}\left(\boldsymbol{\sigma}_{t+1}^{(i)}\right)}{\partial\boldsymbol{\sigma}} \quad (2.84)$$

At the end of the iteration scheme

$$\boldsymbol{\sigma}_{t+1} = \boldsymbol{\sigma}_{t+1}^{(i+1)}, \qquad \bar{\varepsilon}_{t+1}^{\boldsymbol{p}} = \bar{\varepsilon}_{t+1}^{\boldsymbol{p}\ (i+1)}, \qquad \Delta \boldsymbol{D}_{t+1}^{\boldsymbol{P}} = \Delta \boldsymbol{D}_{t+1}^{\boldsymbol{p}\ (i+1)} \tag{2.85}$$

For plane stress formulations, the through thickness strain increment is updated as

$$\Delta D_{33,t+1} = \frac{v\left(\Delta D_{22,t+1} + \Delta D_{11,t+1}\right) + (2v-1)\left(\Delta D_{33,t+1}^{P}\right)}{v-1} \tag{2.86}$$

2.1.2.4.1 Stress Integration Algorithm

This section details the stress integration scheme used in the finite element simulations. For models without the plane stress assumption, the through thickness strain calculations are neglected. The steps in the stress integration scheme are as follows

(1) Subroutine entry with known values of $\boldsymbol{\sigma}_t, \Delta \boldsymbol{D}_{t+1}, \bar{\varepsilon}_t^{\boldsymbol{p}}, \Delta t_{t+1}$

(2) Perform an elastic predictor

$\Delta D_{33,t+1}^{(0)} = \frac{v(\Delta D_{22,t+1} + \Delta D_{11,t+1})}{v-1}$	Calculate an initial through thickness strain
$\boldsymbol{\sigma}_{t+1}^{(0)} = \boldsymbol{\sigma}_t + L^{el} : \Delta \boldsymbol{D}_{t+1}$	Assume an initial elastic increment
$\bar{\varepsilon}_{t+1}^{\boldsymbol{p}\ (0)} = \bar{\varepsilon}_t^{\boldsymbol{p}}$	Assume that plastic slip has not changed
$\bar{\sigma}^{(0)} = \bar{\sigma}\left(\bar{\varepsilon}_{t+1}^{\boldsymbol{p}\ (0)}, \Delta \boldsymbol{D}_{t+1}\right)$	Calculate a new flow stress
$\sigma_{eq}{}^{(\mathbf{0})} = \Phi(\sigma^{(0)})$	Calculate the equivalent stress of the yield function

(3) Check yielding

$$\Phi^{(\mathbf{0})} = \sigma_{eq}{}^{(\mathbf{0})} - \bar{\sigma}^{(0)} \leq 0$$

i. IF TRUE: then the material is elastic

$$\bar{\varepsilon}_{t+1}^{\boldsymbol{p}} = \bar{\varepsilon}_{t+1}^{\boldsymbol{p}\ (0)}$$
$$\boldsymbol{\sigma}_{t+1} = \boldsymbol{\sigma}_{t+1}^{(0)}$$
$$\Delta D_{33,t+1} = \Delta D_{33,t+1}^{(0)}$$

GO TO Step (6)

ii. ELSE: CONTINUE — The material is plastic

(4) Perform Incremental Plasticity

i. Set an incremental counter $i = 0$ and total plastic strain increment $\Delta \bar{\varepsilon}^{p\ (0)} = 0$

ii. Calculate the plastic corrector

$$\Delta\bar{\varepsilon}^{p\,(i)} = \frac{\Phi^{(i)}\left(\boldsymbol{\sigma}_{t+1}^{(i)}, \bar{\varepsilon}_t^{\boldsymbol{p}}, \Delta\boldsymbol{D}_{t+1}\right)}{\frac{\partial\Phi^{(i)}\left(\boldsymbol{\sigma}_{t+1}^{(i)}\right)}{\partial\boldsymbol{\sigma}} : \boldsymbol{L}^{el} : \frac{\partial\Phi^{(i)}\left(\boldsymbol{\sigma}_{t+1}^{(i)}\right)}{\partial\boldsymbol{\sigma}} + \frac{\partial\bar{\sigma}^{(i)}\left(\bar{\varepsilon}_{t+1}^{p\,(i)}, \boldsymbol{\Delta D}_{t+1}\right)}{\partial(\Delta\bar{\varepsilon}^{p})}}$$

$$\bar{\varepsilon}_{t+1}^{p\ (i+1)} = \bar{\varepsilon}_{t+1}^{p\ (i)} + \Delta\bar{\varepsilon}^{p\,(i)}$$

$$\boldsymbol{\Delta D}_{t+1}^{\boldsymbol{p}\ (i+1)} = \boldsymbol{\Delta D}_{t+1}^{\boldsymbol{p}\ (i)} + \left(\Delta\bar{\varepsilon}^{p\,(i)}\right)\frac{\partial\Phi^{(i)}\left(\boldsymbol{\sigma}_{t+1}^{(i)}\right)}{\partial\boldsymbol{\sigma}}$$

iii. Update the stress, yield function, and flow stress

$$\boldsymbol{\sigma}_{t+1}^{(i+1)} = \boldsymbol{\sigma}_{t+1}^{(i)} - \boldsymbol{L}^{el} : \left(\Delta\bar{\varepsilon}^{p\,(i)}\right)\frac{\partial\Phi\left(\boldsymbol{\sigma}_{t+1}^{(i)}\right)}{\partial\boldsymbol{\sigma}}$$

$$\bar{\sigma}^{(i+1)} = \bar{\sigma}\left(\bar{\varepsilon}_{t+1}^{\boldsymbol{p}\ (i+1)}, \boldsymbol{\Delta D}_{t+1}\right)$$

$$\sigma_{eq}{}^{(i+1)} = \Phi(\sigma^{(i+1)})$$

iv. Convergence Check

$$\Phi^{(i+1)} = \sigma_{eq}{}^{(i+1)} - \bar{\sigma}^{(i+1)} \leq \varepsilon_{tol}$$

where ε_{tol} is an error tolerance that is set to 10^{-6}.

IF FALSE: $i = i + 1$ and GO TO (ii)

ELSE: CONTINUE

(5) Update states to converged values

$$\bar{\varepsilon}_{t+1}^{\boldsymbol{p}} = \bar{\varepsilon}_{t+1}^{\boldsymbol{p}\ (i)}$$

$$\boldsymbol{\sigma}_{t+1} = \boldsymbol{\sigma}_{t+1}^{(i)}$$

$$\Delta D_{33,t+1} = \Delta D_{33,t+1}^{(0)} + \frac{(2v-1)\left(\Delta D_{33,t+1}^{P\,(i)}\right)}{v-1}$$

(6) Exit Stress Integration Subroutine

2.1.3 Phenomenological-based Texture Evolution Model

During large deformation, microstructure changes can influence the localization and straining behaviour of polycrystalline materials. In phenomenological plasticity, anisotropy is represented on three mutually orthogonal symmetry planes. However, these orthogonal planes evolve with non-linear deformation and strain path changes and thus, the anisotropy evolves with

deformation. The framework for the phenomenological-based texture evolution (PBTE) model proposed by Bassani and Pan [26] is a model that can capture this evolution. This framework assumes that anisotropy occurs on an orthonormal axes, $\hat{e}_1 - \hat{e}_2$, from the sample frame $e_1 - e_2$. Figure 2.5 presents a planar representation of these orthonormal axes.

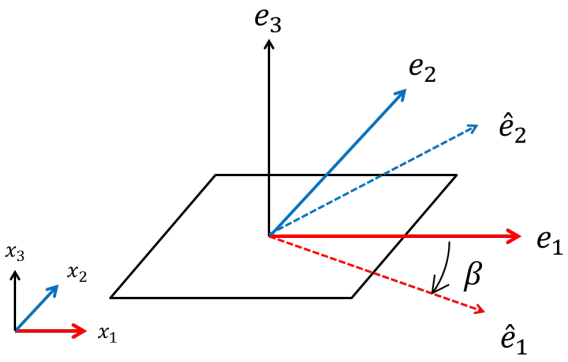

Figure 2.5 – Angle β between loading axes ($e_1 - e_2$) and principle axes ($\hat{e}_1 - \hat{e}_2$) [26]

In planar loading, the orthotropic axes are related to each other, through a single orientation angle, β, which evolves with texture through large plastic straining. In three dimensional loading, the rotation of the orthotropic axes, β, can be presented by three Euler angles. The microstructural vectors are assumed to remain orthogonal at every stage of deformation, and that the spin of the microstructure is governed by

$$\dot{\hat{\boldsymbol{e}}}_i = \omega \hat{\boldsymbol{e}}_i = (\mathbf{W} - \mathbf{W}^{\boldsymbol{P}})\boldsymbol{e}_i \qquad (2.87)$$

where $\mathbf{W}$ and $\mathbf{W}^{\boldsymbol{P}}$ are the skew symmetric total and plastic spin tensor respectively.

Using the concept of work conjugacy, the intermediate configuration from the rate of stress work, $\dot{\Psi}$, in the intermediate configuration is written as

$$\dot{\Psi} = \boldsymbol{\tau}\colon \boldsymbol{D} = \boldsymbol{S}^*\colon \dot{\boldsymbol{E}}^* + \boldsymbol{\Sigma}\colon \boldsymbol{D}^{\boldsymbol{P}} = \dot{\Psi}^* + \dot{\Psi}^P \qquad (2.88)$$

where

$$\boldsymbol{S}^* = \boldsymbol{F}^{*-1}\boldsymbol{\tau}\boldsymbol{F}^{*-T} \qquad \dot{\boldsymbol{E}}^* = \frac{1}{2}(\boldsymbol{F}^{*T}\boldsymbol{F}^* - \boldsymbol{I}) \qquad (2.89)$$

and the intermediate stress state is as follows

$$\boldsymbol{\Sigma} = \boldsymbol{F}^{*T}\boldsymbol{\tau}\boldsymbol{F}^{*-T} = (\boldsymbol{\Sigma})_{\boldsymbol{s}} + (\boldsymbol{\Sigma})_{\boldsymbol{a}} \qquad (2.90)$$

The rate of energy dissipation is then written as

$$\dot{\boldsymbol{\Psi}}^{P} = (\boldsymbol{\Sigma})_{\boldsymbol{s}} : \boldsymbol{D}^{\boldsymbol{P}} + (\boldsymbol{\Sigma})_{\boldsymbol{a}} : \mathbf{W}^{\boldsymbol{P}} \qquad (\ 2.91\ )$$

such that $(\boldsymbol{\Sigma})_{\boldsymbol{s}}$ and $(\boldsymbol{\Sigma})_{\boldsymbol{a}}$, which are the symmetric and anti-symmetric intermediate stress states, are conjugates to the $\boldsymbol{D}^{\boldsymbol{P}}$ and $\mathbf{W}^{\boldsymbol{P}}$ respectively. If the material exhibits isotropic elasticity, then $(\boldsymbol{\Sigma})_{\boldsymbol{a}} = \mathbf{0}$ [61].

In this constitutive formulation, the plastic rate of stretching is assumed to follow a normality flow rule on the intermediate frame, such that

$$\widehat{\boldsymbol{D}}^{P} = \dot{\bar{\varepsilon}}^{P} \frac{\partial \Phi}{\partial \boldsymbol{\Sigma}} \qquad (\ 2.92\ )$$

where $\dot{\varepsilon}^{P}$ is the plastic strain rate and $\frac{\boldsymbol{\partial F}}{\boldsymbol{\partial (\Sigma)_s}}$ is the normality of the yield surface. This framework is yield function independent, such that any yield function may be used. In the work proposed by Bassani and Pan [26], the shear components of the plastic stretch rate tensor on the intermediate reference frame, $\widehat{\boldsymbol{D}}^{\boldsymbol{P}}$, can be shown to be related to the intermediate plastic spin terms $\widehat{\boldsymbol{W}}^{\boldsymbol{P}}$

$$\textbf{(a)}\quad \widehat{W}^{P}{}_{12} = \eta_3 \widehat{D}^{P}{}_{12} \qquad \textbf{(b)}\quad \widehat{W}^{P}{}_{13} = \eta_2 \widehat{D}^{P}{}_{13} \qquad \textbf{(c)}\quad \widehat{W}^{P}{}_{23} = \eta_1 \widehat{D}^{P}{}_{23} \qquad (\ 2.93\ )$$

where η_i are parameters that are a function of the invariants of stress. Nesterova *et al.* [60] observed that the orthotropic axes of microstructure tend to rotate towards the pulling direction during off axis loading. Furthermore, they reported that microstructural evolution returns to a stable orientation, which leads to an even function formulation of η_i

$$\begin{aligned}
&\textbf{(a)} \qquad \eta_1 = \eta_{o1} + \frac{\xi_1}{(\dot{\bar{\varepsilon}}^{P})^2} \widehat{D}^{P}{}_{11} (\widehat{D}^{P}{}_{33} - \widehat{D}^{P}{}_{22}) \\
&\textbf{(b)} \qquad \eta_2 = \eta_{o2} + \frac{\xi_2}{(\dot{\bar{\varepsilon}}^{P})^2} \widehat{D}^{P}{}_{22} \left(\widehat{D}^{P}{}_{11} - \widehat{D}^{P}{}_{33}\right) \\
&\textbf{(c)} \qquad \eta_3 = \eta_{o3} + \frac{\xi_3}{(\dot{\bar{\varepsilon}}^{P})^2} \widehat{D}^{P}{}_{33} (\widehat{D}^{P}{}_{22} - \widehat{D}^{P}{}_{11})
\end{aligned} \qquad (\ 2.94\ )$$

where η_{oi} and ξ_i are phenomenological constants that describe the microstructural orthotropic evolution. The Cauchy stress tensor, $\boldsymbol{\sigma}$, on the reference configuration can be related to an intermediate stress tensor, $\boldsymbol{\Sigma}$, on the orthotropic axes through the evolution of the orthotropic axes

$$\boldsymbol{\Sigma} = \boldsymbol{R}(\boldsymbol{\beta}) : \boldsymbol{\sigma} \qquad (2.95)$$

where the direction of the orthotropic axes, $\boldsymbol{\beta}$, evolve with ω and $\boldsymbol{R}(\boldsymbol{\beta})$ is the direction cosine tensor. Assuming planar loading within the 12-plane ($\Sigma_{33} = D^P{}_{13} = D^P{}_{23} = 0$), incompressible plastic deformation $\left(\frac{\partial \Phi}{\partial \Sigma_{kk}} = 0\right)$, orthotropic symmetry ($W^P{}_{13} = W^P{}_{23} = 0$), and assuming small elastic strains ($W^P{}_{12} \approx \widehat{W}^P{}_{12}$), the microstructure evolution within the 12-plane can be expressed as

$$\omega_{12} = -\dot{\beta} = W - \dot{\bar{\varepsilon}}^P \left(\eta_{o3} + \xi_3 \left(\left(\frac{\partial \Phi}{\partial \Sigma_{22}} \right)^2 - \left(\frac{\partial \Phi}{\partial \Sigma_{11}} \right)^2 \right) \right) \frac{\partial \Phi}{\partial \Sigma_{12}} \qquad (2.96)$$

and the normality rule follows

$$\boldsymbol{D^P} = \dot{\bar{\varepsilon}}^P \frac{\partial \Phi}{\partial \boldsymbol{\Sigma}} \frac{\partial \boldsymbol{\Sigma}}{\partial \boldsymbol{\sigma}} \qquad (2.97)$$

If there is no plastic deformation ($\dot{\bar{\varepsilon}}^P = 0$), the orthotropic axes rotate with the material.

2.1.4 Summary of Constitutive Models

Table 2.1 provides a summary of the constitutive models. The type of model (physics-based/phenomenological), if evolutionary behaviour is captured, the number of parameters, advantages and disadvantages of each model are presented. The yield function comparisons are presented for the plane stress formulation. The isotropic von Mises yield function is the simplest model to represent multi-dimensional plasticity. The isotropic Hosford yield function is an extension to the von Mises yield function where better yield surface curvature can be obtained for FCC materials. Both the von Mises and Hosford yield functions are computationally efficient models. However, these models cannot account for directional anisotropy. The Hill 1948 yield function is the simplest anisotropic yield function, but is limited to three experimental measurements of anisotropy. Depending on the level of complexity, the Barlat et al. yield functions can capture significant variations in anisotropy at the cost in calibration effort and computational efficiency.

Table 2.1 – Summary of Constitutive Models

* H.R.S.C. – Hardening and Rate Sensitivity Coefficients, Y.F.C. – Yield Function Coefficients, TFRM – Transformations

Model	# Parameters	Advantages	Disadvantages
Crystal Plasticity	• 6 - 7 H.R.S.C.	• Physics-based model • Utilizes microstructure information • Complete evolution through microstructure evolution and texture strengthening	• Most expensive computationally • No direct insight into hardening coefficient effect for uniaxial stress-strain response
von Mises	• 5 H.R.S.C. • 0 Y.F.C.	• Simplest model • Least expensive computationally	• Isotropic model • Quadratic functionality does not describe FCC
Hill 1948	• 5 H.R.S.C. • 4 Y.F.C	• One of the simplest anisotropic models (calibration/computation)	• Quadratic functionality does not describe FCC • Limited control of additional anisotropic measurements (i.e. balanced biaxial, shear) • Cannot simultaneously capture yield stress variation with Lankford variation
Hosford 1972	• 5 H.R.S.C. • 1 Y.F.C.	• Non-quadratic functionality that can describe FCC • Computationally efficient	• Isotropic model
Hill 1979	• 5 H.R.S.C. • 7 Y.F.C.	• Non-quadratic functionality that can describe FCC • Captures yield surface variation, shear, biaxial	• Planar isotropic (without imposing anisotropic axes)
Barlat et al. 1989	• 5 H.R.S.C. • 5 Y.F.C	• Non-quadratic functionality that can describe FCC that has good convergence rate • Captures planar anisotropy through Lankford Coefficients	• Limited control of additional anisotropic measurements (i.e. balanced biaxial, shear) • Cannot simultaneously capture yield stress variation with Lankford variation
Barlat et al. 2000: Yld2000	• 5 H.R.S.C. • 8 Y.F.C.	• Non-quadratic functionality that can describe FCC • Captures yield stress and Lankford variation, as well as two of the three: balanced biaxial yield, Lankford coefficient, yield stress	• Requires different experiments to generate different strain paths to calibrate model
Barlat et al. 2004: Yld2004-18p	• 5 H.R.S.C. • 15 Y.F.C.	• Non-quadratic functionality that can describe FCC • Captures same anisotropic variation as Yld2000 with better resolution	• Expensive phenomenological model • Requires at least 15 experimental measurements to calibrate yield function
Cazacu et al. 2006: CPB06	• 5 H.R.S.C. • 7 × # TFRM Y.F.C	• Non-quadratic functionality that can describe FCC • Easy control of accuracy through summation of transformations	• Very Expensive phenomenological model (for large number of transformations)
Bassani and Pan 2012: PBTE Model	• 5 H.R.S.C. • Depends on Yield Function • 2 Evolution	• Microstructure evolution with the efficiency of a phenomenological computation • Yield function independent • Strain path independent evolution framework	• Most expensive phenomenological model (requires convergence on orthotropic axis) • Requires either the crystal plasticity framework or extensive EBSD measurements to calibrate this model • No texture strengthening in evolution model

2.2 Modeling Energy Absorption in Axial Crush

In this section, the techniques used for modeling axial crush are presented. Extensive literature reviews have been performed by Alghamdi [63], Olabi *et al*. [64], and Yuen and Nurick [65] on the various applications of these structures. The fundamental mechanics of axial crush are presented with common definitions and terminology of energy absorption characteristics. A review of modeling axial crush through finite element methods is also presented.

2.2.1 Mechanics of Energy Absorption in Crush Tubes using Analytical Methods

Figure 2.6 shows a typical front rail crush tube force-displacement response during an axial crush. At a component level, the front rail crush tube experiences an initial peak crushing force, $F_{peak,1}$, due to elastic load applied on the structure. Once the crush tube yields due to compression, the structure enters an instability mode of deformation that leads to bending and creates a plastic hinge. This results in a drop in the crushing force that is now required for the bending mode of deformation. As the fold completes, the structure begins to stiffen and triggers subsequent folds. As folding progresses, the force-displacement response of the crush tube transitions into an oscillatory steady state behaviour of plastic hinging. The oscillation of the crushing force in the steady state region is typically bounded by the steady state crushing peak, $F_{peak,2}$.

In the work of Hanssen *et al*. [66] [67], the definitions of energy absorption characteristics and crush efficiency were introduced. In their work, they defined energy absorption, E_{abs}, as the total integral of the force-displacement curve, $F(x)$, with respect to displacement, which can be written as

$$E_{abs} = \int_0^d F(x)dx \qquad (2.98)$$

where d is the total displacement. Furthermore, they defined the mean crush force as the total energy absorbed divided by the total displacement, which is written as

$$F_{mean} = \frac{\int_0^d F(x)dx}{d} \qquad (2.99)$$

They also introduced the conventional concept of crush efficiency, η, which is the ratio of the average crush force, F_{mean}, to the initial peak crushing force, $F_{peak,1}$ as follows

$$\eta = \frac{F_{mean}}{F_{peak,1}} \qquad (2.100)$$

This definition of average crushing force and conventional crush efficiency is a very simple performance metric of determining the energy absorption characteristics. The specific energy absorption (SEA) is another common performance metric that is used for evaluating the performance of a crush structure [68]

$$SEA = \frac{E}{Mass} = \frac{F_{mean}d}{Mass} \qquad (2.101)$$

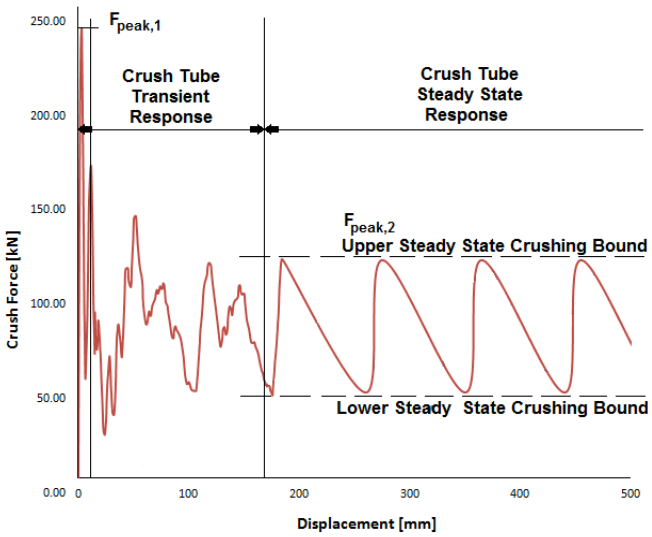

Figure 2.6 - Typical crush tube force-displacement and deceleration profile [69]

2.2.1.1 The Macro-Element Collapse Formulation

The total energy absorbed, E_{abs}, in a structure during progressive buckling can also be defined as

$$E_{abs} = \int_V \sigma_{ij}\, \varepsilon_{ij} dV \qquad (2.102)$$

where σ and ε are the stress and strain developed in the structure respectively and V is the entire volume of the structure. Many analytical models have been proposed to relate the kinematics of axial crush to material energy dissipation. Alexander [70] proposed an initial kinematic model to characterize the crushing of circular shells. Abramowicz and Wierzbicki [71, 72, 73] formulated a general kinematic model to characterize the crushing behaviour and energy absorption of both square and circular shells. They proposed that any crushing pattern in a structure could be decomposed into a series of plastic hinging collapse elements. Figure 2.6 shows two basic collapse element types. The average energy absorbed during the crushing of a Type I collapse element is given as [71, 72, 73]

$$E_1 = \frac{\sigma_0 h^2}{4}\left(16HI_1\frac{b}{h} + 2\pi C + 4I_3\frac{H^2}{b}\right) \qquad (2.103)$$

where $I_1 = 0.555$ and $I_3 = 1.148$ are constants, C is the macro element length, h is the material thickness and σ_0 is the material yield stress. H is defined as the plastic hinge length that describes the natural wavelength of the collapse element and b is the minor radius of a torodial surface representing the joint that the collapse element forms during the crushing at the hinge [74].

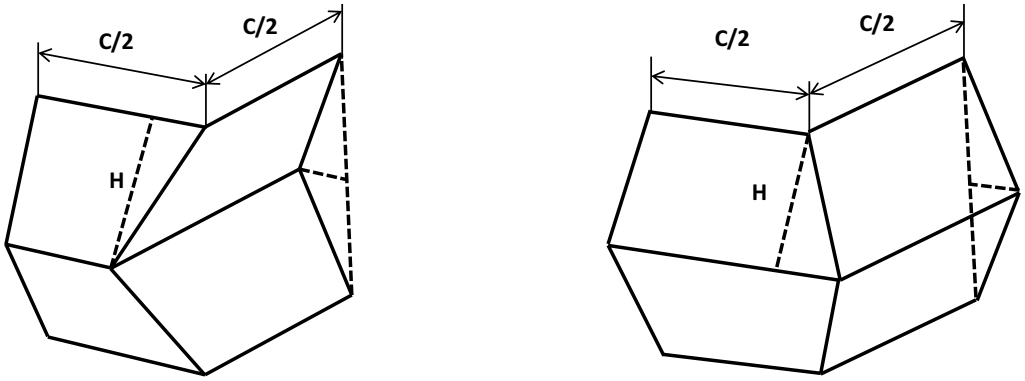

(a) Type I **(b) Type II**

Figure 2.7 - Basic collapse elements [74]

Wierzbicki and Abramowicz proposed that H and b are geometric energy absorption parameters that the system naturally minimizes

$$\frac{\partial E_1}{\partial H} = 0 \text{ and } \frac{\partial E_1}{\partial b} = 0 \qquad (2.104)$$

This assumption in the model presumes infinitesimal deformations and neglects reverse loading influences. More importantly, these models assume that the plastic hinge length, H, which describes the wavelength of the shell, remains constant throughout deformation. In other words, these models assume an infinite length shell in this model. Barbi et al. [75] showed that the plastic hinge length of these analytical models deviated from experiments and simulations. Nevertheless, this formulation still gives reasonable predictive capabilities for energy absorption characteristics.

Similarly, the energy absorption for a Type II collapse element can be written as [74]

$$E_2 = \frac{\sigma_0 h^2}{4}\left(16\frac{H^2}{h} + 2\pi C + 4H\right) \quad (2.105)$$

It should be noted that, in the above formulation, it is assumed that the material behaves as a rigid-perfectly plastic material and the material thickness does not change during deformation. The deformation mechanics of the bending and folding mechanics of the corner interfaces are also assumed to be negligible. Najafi *et al.* [76] later developed a formulation that incorporated these effects into a total energy dissipation formula.

2.2.1.2 Decoupling Geometry and Material Effects

The effects of geometry are decoupled from the material effects in terms of energy absorption so that

$$E = f(Geometry)f(Material) \quad (2.106)$$

where the geometry effects can be written as

$$f(Geometry) = f(H, C, h, b) \quad (2.107)$$

and the material effects are as follows

$$f(Material) = f\left(\sigma_0, U_0, \varepsilon_0, \varepsilon_f, \frac{d\sigma}{d\varepsilon}\right) \quad (2.108)$$

where σ_0 is the material quasi-static yield stress, U_0 is the ratio of the ultimate tensile strength to the quasi-static yield stress (σ_{UTS}/σ_0), ε_0 is the strain at the yield stress, ε_f is the associated

uniform elongation strain at the ultimate tensile strength, and $\frac{d\sigma}{d\varepsilon}$ is the hardening rate of material. The strain at yielding is determined from the ratio of the yield stress to the elastic modulus (σ_0/E) and the hardening rate is captured through the hardening law employed for the material. Upon analysis of the deformed structure, the deformation patterns through the cross section can be decomposed into four Type I collapse elements that absorb energy. By minimizing the energy function with respect to energy absorption, it can be written as

$$\frac{H}{h} = 0.99\left(\frac{C}{h}\right)^{2/3} \quad (2.109)$$

and

$$\frac{b}{h} = 0.72\left(\frac{C}{h}\right)^{1/3} \quad (2.110)$$

This leads to the geometric contribution of energy absorption, which is written as

$$f(H, C, h, b) = 4.73h^2C \quad (2.111)$$

For a square tube, the structure consists of four Type I collapse elements. Figure 2.8 presents an example of a hydroformed aluminum square tube with these Type I collapse elements. As such, the total geometric contribution for energy absorption can be calculated from

$$f(Geometry) = 18.86h^2C \quad (2.112)$$

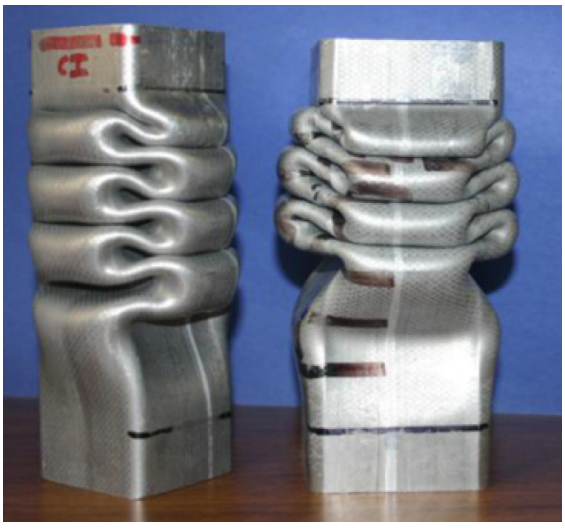

Figure 2.8 - Experimental symmetric folding behaviour of an aluminum square hydroformed tube [77]

2.2.2 Modeling Energy Absorption in Crush Tubes using Finite Element Methods

Although there is a wealth of literature dedicated to numerical modeling of crush, the following are a series of select publications that are significant to this work. With improvements in computational technology over time, commercial non-linear finite element packages, such as LS-DYNA, have been better utilized to predict the energy absorbing response of more complex structures. Numerical simulations of these lightweight alloys in axial crush have become an essential tool in product development by reducing the need for multiple experiments to validate the performance. Yet, simulation predictions of these lightweight alloys during axial crush is still a challenge because of large deformations and contact that the structure undergoes during collapse, and are often limited due to computational requirements. Simpler plane stress formulations are frequently used to simulate axial crush of thin-walled structures to reduce the computational cost compared to a 3-dimensional stress formulation.

Langseth et al. [78, 79] began to study the behaviour of aluminum and steel thin walled structures during axial crush using LS-DYNA, and validated their results with experiments. In their work, the conventional definitions of crush efficiency and energy absorption are introduced for crashworthiness analysis of axial crush tubes.

Abedrabbo et al. [80] performed finite element simulations of hydroformed square and circular advanced high strength steel (AHSS) tubes under axial crush. Williams et al. [14, 77] studied the influence of anisotropy and forming history on the axial crush response of hydroformed AA5754-O square tubes. Explicit dynamic finite element simulations of hydroformed square tubes were performed and showed good agreement with experiments. These works highlighted the importance of capturing advanced phenomenon such as anisotropy and kinematic hardening in aluminum crush.

However, a 3-dimensional stress formulation can capture the through-thickness energy absorption in simulations of axial crush that is neglected by a simpler plane-stress formulation; $\sigma_{33}\varepsilon_{33} = 0$. Giagmouris et al. [15] performed accurate experimental and numerical simulations in predicting the localization and failure in AA6061-T6 shells. Their work employed different yield functions to determine the influence on strain localization during crush induced bending and tension. Their study showed that the use of 3-dimensional formulations, coupled with non-

quadratic yield functions, can produce very accurate model predictions because they precisely capture the localization behaviour.

Several attempts have been made to implement the crystal plasticity formulation in finite element framework to predict the final texture of aluminum during deformation [18, 23]. Rossiter *et al.* [24] implemented a forward Euler time integration scheme for the crystal plasticity framework into the commercial finite element software, LS-DYNA, to study the effects of strain path, strain rate, and thermal softening of automotive-grade aluminum during shear. However, this implementation into finite element code to compute the dislocation slip requires a significant amount of computational processing power and memory resources. Najafi *et al.* [25] performed crystal plasticity simulations of the axial crush of polycrystalline square tubes. Figure 2.9 presents a summary of their analysis for Type I crush modes. In their work, four pre-strained microstructures were generated and their energy absorption response was simulated. A Taylor-type homogenization scheme of the crystal plasticity model with an explicit dynamic formulation of ABAQUS was utilized to study the effects of initial texture on the crush response.

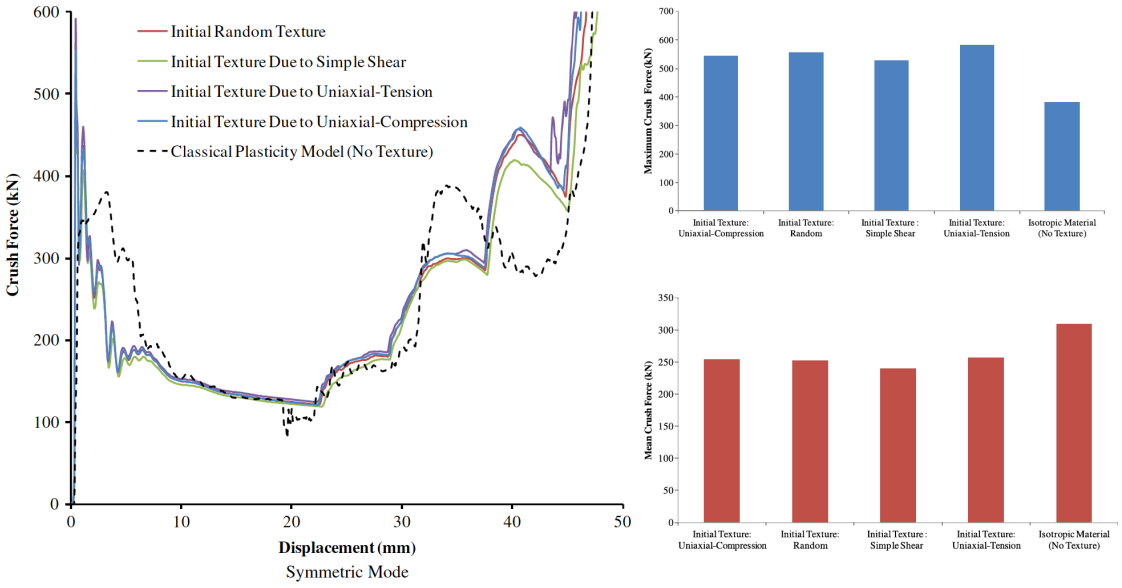

Figure 2.9 – Comparison of energy absorption in Type I deformation modes [25]

They observed that significant texture evolution can occur during axial crush and the initial microstructure had a significant influence on the resulting energy absorption response. However, due to the limitations of computational resources, i.e. memory and processing constraints, they

had to reduce the number of crystals from 500 to 40 per finite element, which causes a loss in textural information. Furthermore, a half symmetric model that was 40mm long and with one element in the wall thickness was used due to the limitations of computational speed. In automotive crashworthiness applications, the structure geometry can be very complex with crush lengths exceeding 200mm where the length can have an impact on the response [14]. Additionally, simulations with only one element in the wall thickness tend to under-predict the true crush force response [81]. However, using smaller elements in the wall thickness has the implication of reducing the time step for explicit dynamic solvers due to the Courant-Friedrichs-Lewy criterion [82], which further increases the computational requirements. Even at the current available computational resources, performing complete microstructural simulations of axial crush of aluminum structures is still a distant future.

2.3 Optimization using the Response Surface Methodology

The response surface methodology (RSM) is a framework that is used to construct a global approximation of a system's behaviour [12, 83]. The behaviour of a system is constructed as a mathematical model, known as a metamodel, that relates the input parameters and functions to an output function through minimization of statistical error. Once the system metamodel has been calibrated, an optimization scheme can be applied to the metamodel to determine the optimum input parameters that maximizes a desired objective function. In finite element based crashworthiness optimization, the calibration data is generated by simulating the energy absorption response within the design of experiments. In the work of Avalle *et al*. [84], a metamodel was developed to relate the geometric properties of a crush structure, such as the diameter of a tube and wall thickness, to the energy absorption of the structure during axial crush. Once the metamodel has been created and calibrated, it can be used to predict the output response of future simulations and utilized in optimization. In this work, the commercial optimization package, LS-OPT, is used to perform the metamodel and optimization process of the aluminum structure [85]. Additionally, in-house implementations using MATLAB [86] of these metamodels techniques and optimization are also used to perform parameter identification and optimization.

Figure 2.10 presents a flow chart of the RSM procedure. The RSM procedure for optimization is as follows:

1) **PROBLEM DEFINITION:** In this step, the optimization objective function (i.e. crush efficiency, energy absorption, specific energy absorption, etc.) is defined. The independent variables that the objective function is sensitive to (i.e. local material thickness, mechanical properties, etc.) are defined. The domain (upper and lower limits) of the independent variables are also defined. Furthermore, constraints on key performance metrics (i.e. minimum energy absorption, maximum allowable mass, etc.), metamodel accuracy, number of iterations, parameter discretization increments, and an initial guess for the optimum solution are also defined.
2) **DESIGN OF EXPERIMENTS (DoE):** Combinations of input parameters within the specified domain, known as the design of experiments [12], are generated. The number of sample points in the DoE is also specified.
3) **SIMULATE SAMPLE POINTS IN DoE:** Each sample point in the DoE is simulated using finite element analysis. The output response of each finite element simulation (i.e. mean crush force, energy absorption, mass, etc.) is measured and the corresponding objective function is calculated.
4) **CONSTRUCT METAMODEL:** A metamodel is selected and calibrated to the input-output response from the DoE. An appropriate selection of a metamodel that approximates the nonlinearity of the actual response of the output function is critical. Common metamodel techniques are: polynomial regression method [8], nonlinear regression [87], or neural networks [88]. These metamodeling techniques are discussed in detail in Section 2.3.1.
5) **CALCULATE METAMODEL ERROR:** In each of these metamodeling techniques, the input-output response is obtained through minimization of statistical error. The metamodel convergence error is calculated as the sum of relative residual errors

$$Err_{converge} = \frac{1}{m}\sum_{i=1}^{m}\left|r_i\left(\boldsymbol{x}^{(\alpha)}\right)\right| \times 100\% \qquad (2.113)$$

α is the current iteration of the optimization procedure, m is the number of total simulations at the given iteration, and a single residual error function, $r_j\left(x_i{}^{(\alpha)}\right)$, at a given design of experiment point is

$$r_i\left(\boldsymbol{x}^{(\alpha)}\right) = \frac{y_i\left(\boldsymbol{x}^{(\alpha)}\right) - g_i\left(\boldsymbol{x}^{(\alpha)}\right)}{y_i(\boldsymbol{x}^{(\alpha)})} \quad (2.114)$$

where i is a given point in the design of experiments, $g_i\left(\boldsymbol{x}^{(\alpha)}\right)$, is the corresponding metamodel response, and $y_i\left(\boldsymbol{x}^{(\alpha)}\right)$ is the actual measured value from the simulation.

6) **PERFORM OPTIMIZATION:** Once calibrated, the metamodel can be used to predict the output response of future simulations and thus, be utilized in an optimization scheme. Using an optimization algorithm, such as gradient descent (Newton's method), genetic algorithms [89], and adaptive simulated annealing [90], a new sample point of independent variables is generated within the DoE that optimizes the selected objective function. These metamodeling techniques are discussed in detail in Section 0.

7) **CONVERGENCE CHECK:** Two conditions are tested:

   A. *Does the calculated metamodel error satisfy the specified accuracy?*

   B. *Does the new optimum solution satisfy the constraints?*

   IF (A **AND** B) are FALSE: GO TO (2)

   This result indicates that more sample points are required to improve on the metamodel and/or optimization framework. Thus, more samples points need to be generated. Upon determining an initial optimal solution, a *new subspace* within the design could be generated within the previous design space using the sequential response surface method (SRSM). The new region is generated to encompass the current optimal solution through an adaptive contraction and panning window that are designed to alleviate oscillation and prevent premature convergence [91]. Further iterations and domain reductions can be performed until a local optimal solution is obtained for the given problem. This method assures that a local optimal solution is obtained. However, this solution is highly dependent on the accuracy of the metamodel, such that initial domain reductions may exclude a region where better performance could be obtained. Without domain reduction, a global optimization (within the specified domain) could be achieved, but may require more simulation sample points.

   ELSE: CONTINUE

8) **FINISH**

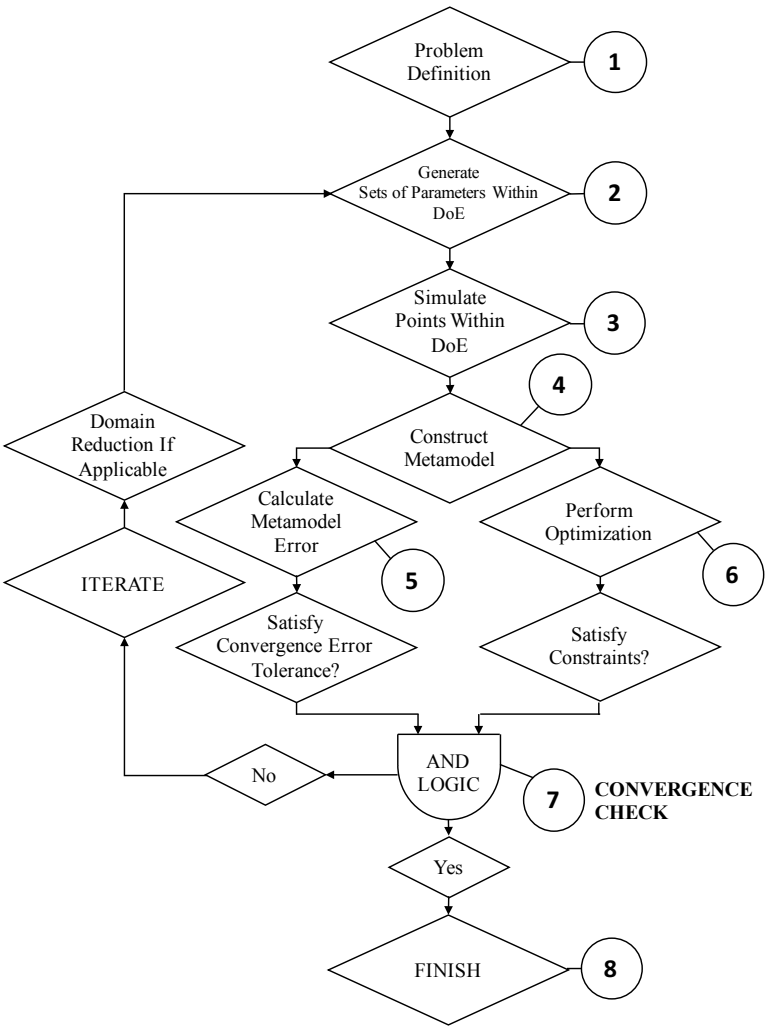

Figure 2.10 – Flow Chart of Optimization using the Response Surface Methodology

2.3.1 Metamodel Surface Response Methodologies

Three different metamodel techniques, including polynomial, nonlinear, and feed-forward neural network metamodeling, are to be utilized in this proposed work.

2.3.1.1 Polynomial Metamodel

Let the approximated output function, $\tilde{y}$, be defined as a function of j independent parameters, x_j, such that [87]

$$\tilde{y} = \tilde{y}(x_1, x_2, x_3, \dots x_j) \qquad (\ 2.115\ )$$

The approximated output function is expressed as a linear summation of the product of fitted $j+1$ coefficients, $\boldsymbol{\beta}$, with independent parameters, x_j, such that

$$\tilde{y} = \beta_0 + \beta_1 x_1 + \beta_2 x_2 + \cdots + \beta_j x_j = \beta_0 + \sum_{i=1}^{j} \beta_i x_i \qquad (\ 2.116\ )$$

To obtain higher order polynomial functions, a new independent parameter is defined as a function of previous parameters. Second order terms can be defined through linearization, (e.g. $x_{j+1} = {x_k}^2$) with a corresponding coefficient β_{j+1}. A similar approach can be applied for nonlinear functions. Given a set of p experimental data points, a matrix of input parameters, $\boldsymbol{X}$, and a vector of actual outputs, $\boldsymbol{y}$, is constructed such that

$$\boldsymbol{X} = x_{ij} \qquad \boldsymbol{y} = y_i \qquad i = 1..p \qquad (\ 2.117\ )$$

Thus, the solution to the fitted parameters is obtained by minimizing the sum of the square error function, $\boldsymbol{S}$

$$S = \sum_{i=1}^{n} (y_i - \tilde{y}_i)^2 = \sum_{i=1}^{n} (y_i - \beta_0 - \beta_1 x_{i1} - \beta_2 x_{i2} - \cdots - \beta_n x_{in})^2 \qquad (\ 2.118\ )$$

such that [85]

$$\boldsymbol{\beta} = (\boldsymbol{X^T X})^{-1} \boldsymbol{X^T y} \qquad (\ 2.119\ )$$

The polynomial metamodel technique is a simple method that is easy to compute. This technique can account for non-linearity; however, the number of terms becomes very large. Thus, it can be difficult to interpret the physical meaning of the coefficients and combination of parameters. Furthermore, the coefficients in the higher order terms become susceptible to statistical error.

2.3.1.2 Nonlinear Metamodel

Similar to the polynomial metamodel, let the approximated output function, $\tilde{y}$, be defined as a nonlinear function of j independent parameters, x_j, such that [87]

$$\tilde{y} = \tilde{y}(x_1, x_2, x_3, \ldots x_j) \qquad (\ 2.120\ )$$

where the output function is expressed as a nonlinear combination of k coefficients, $\boldsymbol{\beta}$, and independent parameters as follows

$$\tilde{y} = \tilde{y}\left([x_1, x_2, x_3, \dots x_j], [\beta_1, \beta_2, \beta_3, \dots \beta_k]\right) \quad (2.121)$$

A linear formulation of the Gauss-Newton method is used to determine the values of the coefficients. The Gauss-Newton method is an iterative solution that minimizes the error of the coefficients, using least squares method [92]. Given an experimental set of input parameters, $\boldsymbol{X}$, and a vector of actual outputs, $\boldsymbol{y}$, a residual error function, r, is defined as

$$\boldsymbol{r} = \boldsymbol{y} - \tilde{\boldsymbol{y}} \quad (2.122)$$

The values of coefficients are determined through iteration as follows

$$\boldsymbol{\beta}^{(\alpha+1)} = \boldsymbol{\beta}^{(\alpha)} - (\boldsymbol{J}^{\boldsymbol{T}}\boldsymbol{J})^{-1}\boldsymbol{J}^{T}\boldsymbol{r}^{(\boldsymbol{\alpha})}\boldsymbol{\beta}^{(\alpha)} \quad (2.123)$$

where α is the current iteration and J is the Jacobian of the residual vector that is evaluated at the current values of the coefficients such that

$$J = \frac{\partial r_i^{(\alpha)}}{\partial \beta_k} \quad (2.124)$$

An initial guess, $\boldsymbol{\beta}^{(0)}$, is required for the coefficients to start the procedure. A local minimum is established when the gradients of the residual error function at the current iteration of coefficients is zero. This convergence criterion is written as

$$J^T r^{(\alpha)} = 0 \quad (2.125)$$

Through analysis of the data, a metamodel can be formulated that captures the nonlinearity of the system. Thus, a formulation can be proposed that provides direct insight into the behaviour of system. However, this requires intimate knowledge of the expected behaviour of the system, which may not be known. The derivatives of the function must be continuous to be able to evaluate the Jacobian and the iterative procedure can become computationally expensive for more complex models.

2.3.1.3 Feed-forward Artificial Neural Network Metamodel

Artificial neural network (ANN) is a class of artificial intelligence that is commonly used for determining input-to-output relationships [93]. ANNs have become a common metamodel technique used to determine energy absorption functions for crashworthiness applications [7].

ANNs are structured to replicate the architecture of a human brain, where nodes are connected in a massively parallel network [94]. The value of each input parameter is passed into a node called a neuron. Figure 2.11 presents the schematic of a single-input-single output neuron.

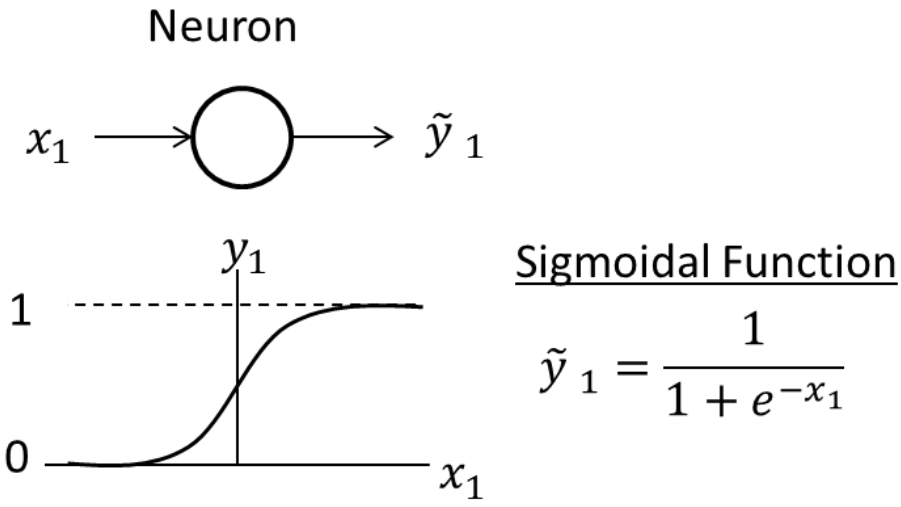

Figure 2.11 – Schematic of a single-input single output neuron

Each neuron is composed of a simple processing operation that has the natural property of storing information [95]. The value of the output of a neuron, $\tilde{y}$, follows the sigmoidal step function defined as follows

$$\tilde{y} = \frac{1}{1+e^{-x}} \qquad (2.126)$$

The step response of the sigmoidal function provides a continuous function that mimics the firing response of a neuron. This is typically known as the transfer function. A desirable feature of the sigmoidal transfer function is that the derivative of the transfer function is also continuous, such that

$$\frac{d\tilde{y}}{dx} = \frac{d}{dx}\left(\frac{1}{1+e^{-x}}\right) = \tilde{y}(1-\tilde{y}) \qquad (2.127)$$

With a neuron, the input, x, output, $\tilde{y}$, relationship is scaled by a coefficient, w. Figure 2.12 presents a schematic of a single-weighted-input single-output neuron.

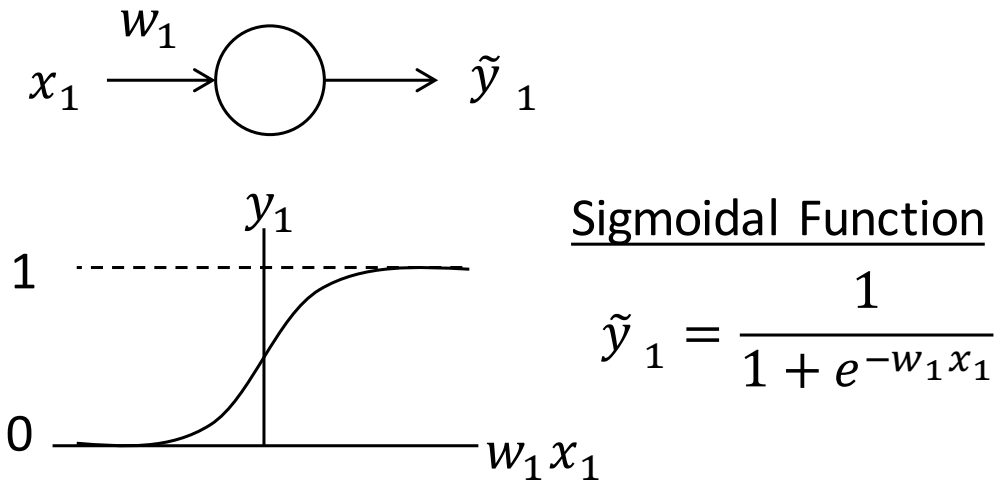

Figure 2.12 – Schematic of a single-weighted-input single-output neuron

Thus, the transfer function is

$$\tilde{y} = \tilde{y}(xw) = \frac{1}{1 + e^{-wx}} \qquad (\ 2.128\ )$$

Multiple inputs can be entering into a neuron. Figure 2.13 presents a schematic for a multi-weighted-input single output neuron. The values of inputs x_j into the neuron are scaled by weights, ${w_{jk}}^{(l)}$, and summed such that

$$v = \sum_j {w_{jk}}^{(l)} x_j \qquad \tilde{y}_l = \frac{1}{1 + e^{-v}} \qquad (\ 2.129\ )$$

where j is the index of the current input parameter, l is the current layer of the node, and k is the node in the layer. Figure 2.14 presents a schematic of a multilayer ANN, where multiple layers of neurons are connected. Since there are no feedback loops in this structure, this is known as a feed-forward artificial neural network. The input and output layer of an ANN corresponds to the input and output layer of the response.

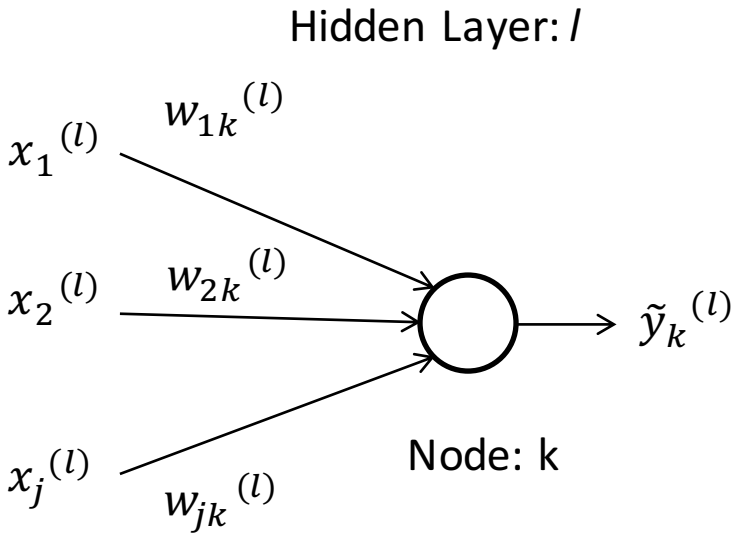

Figure 2.13 – Schematic of a multi-weighted-input single output neuron

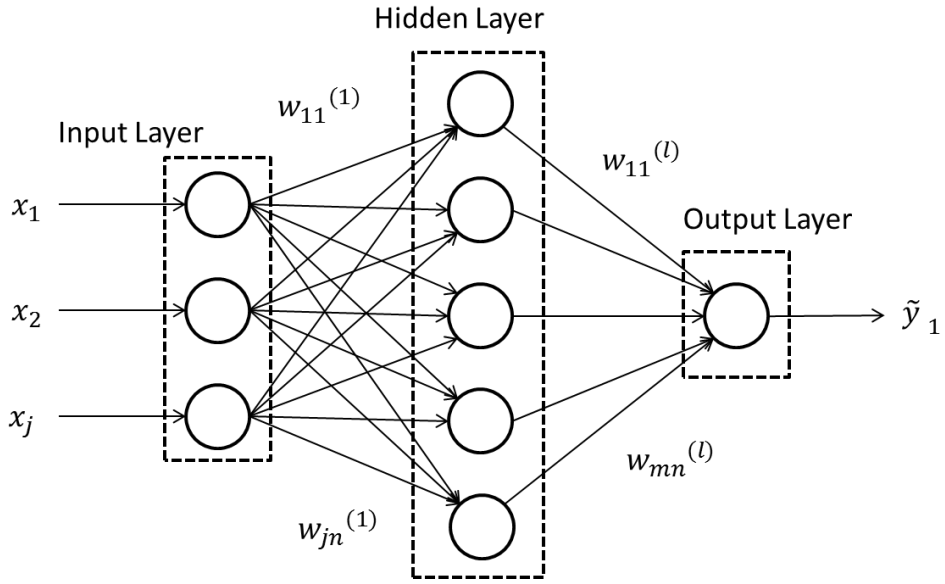

Figure 2.14 – Schematic of a multi-layer artificial neural network

Each input to a neuron has a unique weighting that is determined through a learning procedure called a learning algorithm. The back propagation algorithm proposed by Rumelhart *et al.* [96] is a popular learning algorithm for ANN. A set of training data, which is the matrix of input parameters, $\boldsymbol{X}$, and a vector of actual outputs, $\boldsymbol{y}$, is used in the learning process. The goal of the back propagation algorithm is to minimize the sum of the squared errors of the training data by updating the weights of each connection through an iterative process. The total error, E, is calculated as

$$E = \frac{1}{2}\sum_{m=1}^{n}\sum_{k=1}^{P}(\tilde{y}_{mk} - y_{mk})^2 \qquad (\ 2.130\ )$$

where n is the number of outputs in the layer and P is the total number of sample points. The error with respect to the output m

$$E = \frac{1}{2}\sum_{k=1}^{P}(\tilde{y}_{k} - y_{k})^2 \qquad (\ 2.131\ )$$

Similar to non-linear regression, the objective is to determine a set of coefficients, ${w_{jk}}^{(l)}$, that minimizes the error for a particular output case k. Initially, a guess is made for all the coefficients, ${w_{jk}^{(l)}}^{(\alpha)}$, where α represents the iteration of the coefficients. Thus, $\partial E/\partial w_{jk}^{(l)}$ represents the gradient of the error function with respect to the coefficients of the output layer. The new increment in coefficients, ${w_{jk}^{(l)}}^{(\alpha+1)}$ is

$${w_{jk}^{(l)}}^{(\alpha+1)} = {w_{jk}^{(l)}}^{(\alpha)} - \mathrm{N}\partial E/\partial w_{jk}^{(l)} \qquad (\ 2.132\ )$$

where α is the current iteration value of the weight layer and $\mathrm{N} < 2$ is the learning rate. This algorithm continues to propagate backwards until the first layer of weights is reached. The term, $\partial E/\partial w_{jk}$, is dependent on the values of x and $\tilde{y}$. Thus, chain rule is applied to determine $\partial E/\partial w_{jk}$

$$\frac{\partial E}{\partial w_{jk}^{(l)}} = (\tilde{y}_k - y_k)\frac{\partial}{\partial w_{jk}^{(l)}}\tilde{y}_k = (\tilde{y}_k - y_k)\frac{\partial \tilde{y}_k}{\partial x_k}\frac{\partial x_k}{\partial w_{jk}^{(l)}} \qquad (\ 2.133\ )$$

Substituting Equation 2.127

$$\frac{\partial E}{\partial w_{jk}^{(l)}} = (\tilde{y}_k - y_k)(\tilde{y}_k)(1 - \tilde{y}_k)\frac{\partial x_k}{\partial w_{jk}^{(l)}} \qquad (\ 2.134\ )$$

The total change of x_k for w_{jk} is the total output of the neuron from the previous layer ($x_k = w_{jk}^{(l)}\tilde{y}_j$)

$$\frac{\partial E}{\partial w_{jk}^{(l)}} = (\tilde{y}_k - y_k)(\tilde{y}_k)(1 - \tilde{y}_k)\tilde{y}_j \quad (2.135)$$

Simplifying the notation

$$\frac{\partial E}{\partial w_{jk}^{(l)}} = \tilde{y}_j \delta_k \quad (2.136)$$

where

$$\delta_k = (\tilde{y}_k - y_k)(\tilde{y}_k)(1 - \tilde{y}_k) \quad (2.137)$$

is the product of the current node output, $\tilde{y}_k$, and $\tilde{y}_j$ is the output of the previous layer node, j. In other words, δ_k represents the error for the given output from the previous layer. This yields the correction for the output layers.

Next, the error needs to propagate through the hidden layers to correct corresponding layers. The error in a hidden layer, l, is written as

$$\frac{\partial E}{\partial w_{ij}^{(l)}} = \frac{\partial}{\partial w_{ij}^{(l)}}\left(\frac{1}{2}\sum_{k=1}(\tilde{y}_k - y_k)^2\right) = \sum_k (\tilde{y}_k - y_k)\frac{\partial}{\partial w_{ij}^{(l)}}\tilde{y}_k \quad (2.138)$$

Applying chain rule and expanding $\frac{\partial x_k}{\partial w_{ij}^{(l)}}$

$$\frac{\partial E}{\partial w_{ij}^{(l)}} = \sum_{k=1}(\tilde{y}_k - y_k)\,(\tilde{y}_k)(1 - \tilde{y}_k)\frac{\partial x_k}{\partial \tilde{y}_j}\frac{\partial \tilde{y}_j}{\partial w_{ij}} \quad (2.139)$$

The input of x_k is related to the output $\tilde{y}_j$ through w_{jk}. The summation of the error is now independent of $\frac{\partial \tilde{y}_j}{\partial w_{ij}}$ and can be written as

$$\frac{\partial E}{\partial w_{ij}^{(l)}} = \frac{\partial \tilde{y}_j}{\partial w_{ij}^{(l)}}\sum_k (\tilde{y}_k - y_k)\,(\tilde{y}_k)(1 - \tilde{y}_k)w_{jk} \quad (2.140)$$

Equation 2.140 can be simplified into the form

$$\frac{\partial E}{\partial w_{ij}^{(l)}} = \frac{\partial \tilde{y}_j}{\partial w_{ij}^{(l)}} \sum_k \delta_k w_{jk} \qquad (2.141)$$

where δ_k is the error defined in Equation 2.137. Thus, this product represents the total error ahead of the current layer and the propagation influence onto the weights in the current layer. Applying chain rule on $\frac{\partial \tilde{y}_j}{\partial w_{ij}^{(l)}}$

$$\frac{\partial \tilde{y}_j}{\partial w_{ij}^{(l)}} = \frac{\partial \tilde{y}_j}{\partial x_j} \frac{\partial \tilde{y}_j}{\partial w_{ij}^{(l)}} = \tilde{y}_j\left(1 - \tilde{y}_j\right) \frac{\partial \tilde{x}_j}{\partial w_{ij}^{(l)}} = \tilde{y}_j\left(1 - \tilde{y}_j\right)\tilde{y}_i \qquad (2.142)$$

where $\tilde{y}_i$ is the output of the previous layer. Substituting Equation 2.142 into 2.141

$$\frac{\partial \tilde{y}_j}{\partial w_{ij}^{(l)}} = \tilde{y}_j\left(1 - \tilde{y}_j\right)\tilde{y}_i \sum_k \delta_k w_{jk} \qquad (2.143)$$

Finally, Equation 2.143 can be recast in the form

$$\frac{\partial \tilde{y}_j}{\partial w_{ij}^{(l)}} = \tilde{y}_i \delta_j \qquad (2.144)$$

where $\delta_j = \tilde{y}_j\left(1 - \tilde{y}_j\right) \sum_k \delta_k w_{jk}$.

The back propagation algorithm is as follows

1. Compute $\delta_k = (\tilde{y}_k - y_k)(\tilde{y}_k)(1 - \tilde{y}_k)$ for each output node.
2. Loop through all layers computing $\delta_j = \tilde{y}_j\left(1 - \tilde{y}_j\right) \sum_k \delta_k w_{jk}$
3. Calculate the correction to the weights in each layer: $\Delta w = -N\, \partial E / \partial w$ where
   $\frac{\partial E}{\partial w_{jk}} = \tilde{y}_j \delta_k$: **Output Node Layer**
   $\frac{\partial E}{\partial w_{ij}} = \tilde{y}_i \delta_j$: **Hidden Node Layer**
4. Update the weights in each layer: $w^{(\alpha+1)} = w^{(\alpha)} + \Delta w$

As a result of this architecture, a highly nonlinear and complex input-to-output relationship can be established. Since the ANN uses a parallel network of continuous functions, nonlinear and discontinuous functions can be approximated using an ANN. Utilizing multiple hidden layers can also establish multiple parameter interactions that are abstracted. As a result of this

design, the associated weights no longer have any physical meaning. Calculating the analytical derivatives of an ANN is quite difficult due to the interaction of all the nodes. Furthermore, ANNs require much more computational resources to train the network than the previous regression frameworks.

2.3.1.4 Summary of Metamodeling Techniques

Table 2.2 provides a summary of the metamodeling techniques. The advantages and disadvantages are also summarized.

Table 2.2 – Summary of Metamodeling Techniques

Technique	Advantages	Disadvantages
Polynomial Regression	• Simplest formulation • Trivial solution to determining coefficients (easiest method) • Continuous function ○ Derivatives are trivial to compute	• Little to no physical interpretation of coefficients • Higher order terms are susceptible to statistical error • Need to have an understanding of what level of functionality is required
Nonlinear Regression	• Tailored equations ○ Coefficients can give physical insight to the metamodel • Continuous function • Efficient iterative method for determining coefficients	• Determining formulation of equation is difficult and requires substantial insight • Derivatives can be complex to compute
Artificial Neural Network (ANN)	• Can capture discontinuous behaviours • Highly complex structure • System naturally identifies interaction between nodes and the level of complexity	• No physical interpretation of weights/coefficients in network ○ "Black-box" approach for mapping input-to-output relationship • Derivatives of ANN are too complex to compute • Requires significantly more computational resources to train the network

2.3.2 Optimization Algorithms

Once a metamodel has been calibrated, an optimal output response can be obtained by varying the input parameters to the metamodel.

2.3.2.1 Gradient Descent Methods

Gradient descent methods are the classical strategy for performing optimizations. Gradient descent uses a first and second order derivative approximation of the functions, such that [97]:

$$\frac{\partial \boldsymbol{y}}{\partial \boldsymbol{x}} \leq \varepsilon_{tol}; \quad \frac{\partial^2 \boldsymbol{y}}{\partial \boldsymbol{x^2}} \leq \varepsilon_{tol} \qquad (\ 2.145\ )$$

where $\boldsymbol{y}$ is the optimization objective function, $\boldsymbol{x}$ is an independent variable, and ε_{tol} is a convergence tolerance. The Gauss-Newton method presented in Section 2.3.1.2 is a form of gradient descent optimization that minimizes the error in the system. Rewriting the Gauss-Newton method using the notation in the optimization section, the independent variables

$$\boldsymbol{x}^{(i+1)} = \boldsymbol{x}^{(i)} - (\boldsymbol{J^T J})^{-1} \boldsymbol{J}^T \boldsymbol{y}^{(i)} \boldsymbol{x}^{(i)} \qquad (\ 2.146\ )$$

where i is the current iteration and J is the Jacobian of the optimization objective function that is evaluated at the current values of the independent variables, $\boldsymbol{x}$:

$$J = \frac{\partial \boldsymbol{y}}{\partial \boldsymbol{x}} \qquad (\ 2.147\ )$$

An initial guess, $\boldsymbol{x}^{(0)}$, is required for the coefficients to start the procedure and the partial derive of the optimization objective function with respect to each parameter is required at each iteration. These gradient descent methods are deterministic processes, such that the final converged solution will **always** be the same for the given initial guess. However, if a poor initial guess is made, the solution may diverge. Next, for a simple objective function model, such as a polynomial, the partial derivatives can be easily obtained. However, for an ANN model or some nonlinear analytical models, calculating the derivative analytically may be too difficult to obtain. A solution to this issue is to approximate the gradients using finite difference methods [87]. Furthermore, Newton's method may fail to converge if the objective function has any discontinuities.

Although these methods are deterministic, these gradient methods are susceptible to converging to local optimal solutions for objective functions that are complex in functionality and with a large number of independent variables. Thus, they require a significant amount of computational resources to evaluate the gradients through the domain for complex problems with multiple variables. Furthermore, calculating the analytical inverse of the Jacobian function can become computationally expensive for large sets of independent variables. This gives rise to stochastic machine learning procedures, such as genetic algorithms [89] and adaptive simulated annealing [90]. Although these stochastic methods can be more efficient in the optimization process, the final converged solution may not be the same for the given initial guess and thus, require convergence studies.

2.3.2.2 The Genetic Algorithm (GA)

The family of GAs is a probabilistic method that replicates the process of natural selection [98]. In other words, the optimization process is based on survival of the fittest through genetic evolution. In his pioneering work, Holland [98] structured GAs to follow the architecture of genetics in biology. Each input parameter, x_j, is called a *chromosome*. A set of chromosomes uniquely characterizes an *individual*, where a set of input parameters uniquely defines a point within the design of experiment. The group of *individuals* makes up a *population*; this makes up the entire design of experiments. The performance of the *individual* is defined as the measure of *fitness*; this relates to the output response, $\boldsymbol{y}$. Each chromosome is discretized into *genes,* where the value is called an *allele*, which is encoded to represent the value of the input parameter. Table 2.3 presents an example of encoding a *chromosome* into a set of *genes* and the corresponding *alleles*. The base 10 values of 6 (chromosome) is converted to a base 2 with 4 unique binary bits (*genes*).

Table 2.3 - Allele Encoding of a Chromosome

ID #:1	**Chromosome #1 Total Value: 6**			
Gene	2^3	2^2	2^1	2^0
Allele	0	1	1	0

The purpose of discretizing a *chromosome* into *genes* is to identify a set of genetics (value of input) that produce a strong level of *fitness* (optimal output).

The *evolution rule* is the framework for performing optimization to improve the genetics [99].

1) **POPULATION GENERATION:** The initial *population* is known as the *parent generation*. At this initial stage, the level of fitness is known for all *individuals*. The *population* consists of a total of *n* samples.

2) **REPRODUCTION:** In the *reproduction stage,* two *parent individuals* come together to mix *chromosomes* to generate a new set of *individuals* called the *child generation*. This follows the exchange of parental genetics during reproduction in biology. Figure 2.15 presents a schematic of the reproduction cycle. In the example, four *alleles* make up the encoding of the *chromosome.* The number of *alleles* that are carried over from one parent, which is known as the *cross-over point* is randomly selected. In this example, 2 *alleles* were selected from *Parent A* and the remainder come from *Parent B.* Furthermore, the indices for each *allele* can be randomly selected. These *alleles* are then carried over to the *parent chromosome* to be carried over to the *child*.

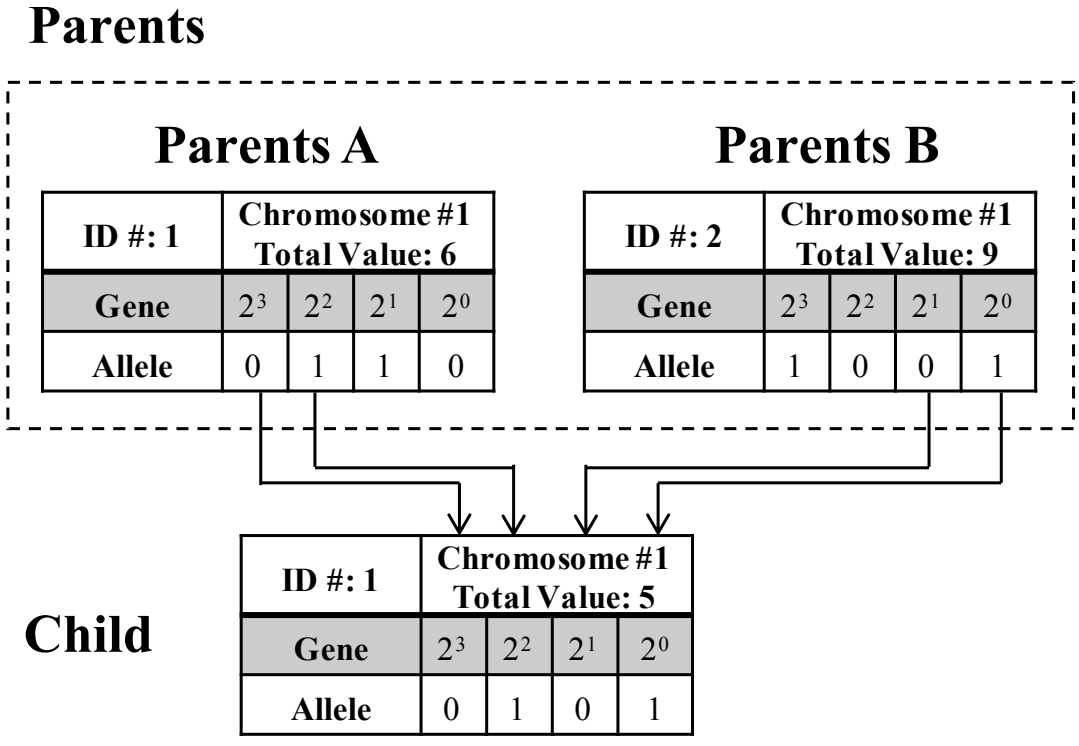

Figure 2.15 – Reproduction of Child from Parental Chromosomes

Select sets of *individuals* that are known to have stronger *fitness* are also carried over to the *child generation* to preserve the prevailing genetics. This is dependent on the *reproduction* criterion that governs the exchange of chromosomes. At the end, the total *population* remains constant from the *parent* to the *child* generation.

3) MUTATION: After the *population* is established, *alleles* within a set of *children* of moderate and weak *fitness* are randomly selected and changed to a random value. Figure 2.16 presents a schematic of a mutation of the alleles in a child. This is to simulate a genetic mutation that introduces diversity to the population. This diversity can introduce a new set of *genes* that generate a more dominant level of *fitness.*

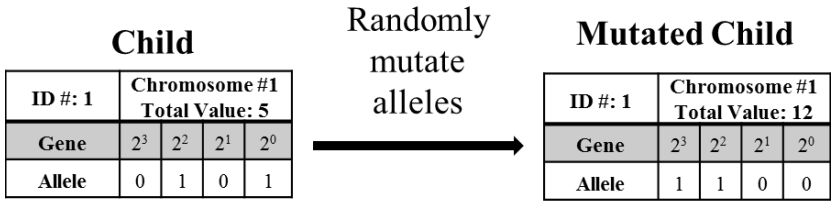

Figure 2.16 – Random mutation of alleles in a child

4) SELECTION: The level of *fitness* is evaluated for the newly generated *population.* A selection criterion is employed to determine which children will continue and which children will be terminated. A popular selection criterion is the roulette wheel selection criteria. In this selection criteria, the *total fitness, f,* for the *population* is computed as:

$$f = \sum_{j=1}^{n} y_j \qquad (\ 2.148\ )$$

The *selection fraction* of each individual is calculated as the ratio of the *fitness* to the *total fitness* and it is written as*:*

$$P_j = \frac{y_j}{f} \qquad (\ 2.149\ )$$

A percentage of total slots of a roulette wheel are allocated to an *individual* based on the *selection fraction*. Figure 2.17 shows an example of slot allocation for four *individuals*. A total of 16 slots are available for allocation.

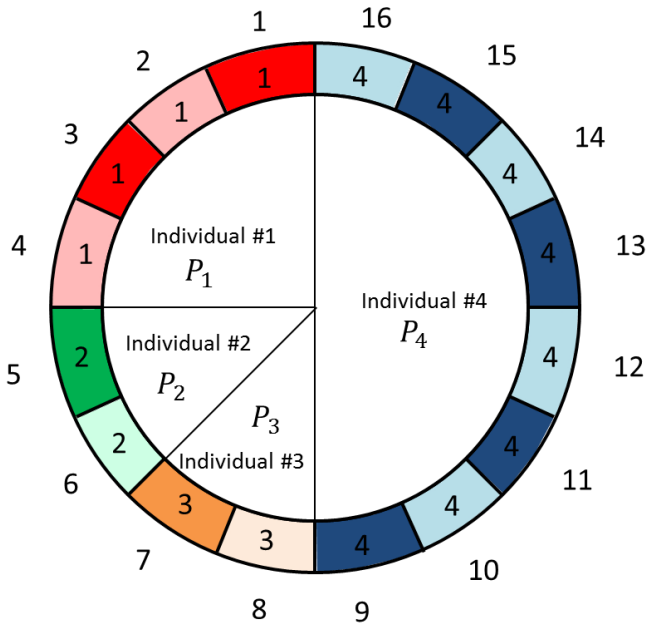

Figure 2.17 – Example of GA Roulette Wheel Allocation

The *selection fraction* represents the probability on the roulette wheel where *individuals* with higher *fitness* have higher probability of being selected for the next iteration of the *population.* The first 4 slots are allocated to *individual* #1, which indicates a 0.25 selection fraction. Slots 9 – 16 are allocated to *Individual #4*, which indicates a 0.50 selection fraction. To generate the next *population,* a random slot is selected on the roulette wheel and the *chromosomes* of the *individual* are carried to the next *population*. Once the population is generated, a reproduction stage is performed and the process repeats.

2.3.2.3 The Adaptive Simulated Annealing (ASA) Algorithm

The adaptive simulated annealing (ASA) algorithm is stochastic optimization procedure that mimics the annealing process in metallurgy [90]. In the metallurgical annealing process, an alloy is initially heated to a high temperature until the atoms in the alloy become free to move

throughout crystalline structures. In this work, the commercial optimization software, LS-OPT, was used to perform optimization using the ASA algorithm [85].

At this high temperature, the *total energy* and the level of entropy, which is a measurement of randomness, in the metal is high. This means that the atoms of the alloy are free to diffuse throughout the structure in an unstructured manner. This can result in the atoms taking on a structure that increases energy within the structure. During the annealing process, the temperature is lowered and the free atoms throughout the metal begins to solidify. With a decrease in temperature, the level of entropy begins to drop and the atoms start to form structured crystalline. During this crystallization, the atoms start to arrange themselves in specific atomic structures *that attempt to minimize the energy* state of the system. In the annealing process, desirable mechanical properties are obtained from having lower energy states during recrystallization. The annealing process is a dynamic process controlled by the *cooling schedule* or the rate of cooling. A fast *cooling schedule* can result in generating an alloy quickly, but result in lower energy states being missed that translate to poor mechanical properties. A slow *cooling schedule* can result in better alloys with lower energy states (that result in better mechanical properties), but require much more time and resources to achieve.

In the simulated annealing framework, the optimization objective function is the measurement of *energy* and the *candidate set* of atomic arrangements represents the values of the independent variables. At the initial high *temperature state*, the entropy in the system is high and the atoms are free to move around. In the optimization framework, there is no strict rule of always selecting one combinations of independent variables over another *candidate set* of atomic arrangements, regardless if one set has lower energy. However, as the *temperature* begins to decrease during the *cooling schedule*, the *candidate sets* of atoms begin to arrange them selves in a manner that minimizes energy. As such, there is a higher probability of a *set* of atoms with lower energy carrying forward throughout the process. This can be represented as a *probabilistic distribution function*, $P\left(\Delta \boldsymbol{E}^{(i)}, T^{(t)}\right)$, that is dependent on the difference in energy (optimization objective function) for two *candidate sets* of energy measurements, $\Delta \boldsymbol{E}^{(i)} = \boldsymbol{E}^{(trial)} - \boldsymbol{E}^{(i)}$, evaluated at the the *current candidate set*, $\boldsymbol{x}^{(i)}$, and a *trial candidate set*, $\boldsymbol{x}^{(trial)}$, for a specific temperature, $T^{(i)}$, at a given iteration, i, in the *cooling schedule.* In annealing, the distribution function used follows a Boltzmann's distribution, such that

$$P\left(\Delta \boldsymbol{E}^{(i)}, T^{(i)}\right) = \exp\left(-\frac{\Delta \boldsymbol{E}^{(i)}}{kT^{(t)}}\right) \quad (2.150)$$

where k is the Boltzmann constant equal to $1.38\times10^{-13}J/K$. A similar form of this distribution, known as the Metropolis criteria is used in this work. The Metropolis criteria for minimization is a widely used acceptance function [100], such that

$$P\left(\Delta \boldsymbol{E}^{(i)}, T^{(i)}\right) = \min\left\{1, exp\left(-\frac{\Delta \boldsymbol{E}^{(i)}}{T^{(i)}}\right)\right\} \quad (2.151)$$

This binds the distribution function $P\left(\Delta \boldsymbol{E}^{(i)}, T^{(i)}\right) = [0,1]$. For maximization of an objective function, the Metropolis criteria takes the form

$$P\left(\Delta \boldsymbol{E}^{(i)}, T^{(i)}\right) = \min\left\{1, exp\left(\frac{\Delta \boldsymbol{E}^{(i)}}{T^{(i)}}\right)\right\} \quad (2.152)$$

Figure 2.18 presents the Metropolis criteria sensitivity to the *temperature* and difference in *energy* for a minimization problem. When $\Delta \boldsymbol{E}^{(i)} < \mathbf{0}$, this implies that the trial *candidate set,* $\boldsymbol{x}^{(\boldsymbol{trial})}$, has lower energy and is automatically accepted for the next iteration. At higher *temperature*, the probability of accepting the trial *candidate set* , $\boldsymbol{x}^{(\boldsymbol{trial})}$, which has a higher energy state than the previous iteration is high. As mentioned earlier, this probabilistic function does not strictly reject a higher energy state, especially at higher *temperatures*. Figure 2.19 illustrates this example. Although the next iteration is in a higher energy state than the previous iteration, it may lead to a new energy state that is much lower than all previous energy states. In the optimization procedure, this would allow a solution *set* to be able to overcome convergence towards a local minimum. However, as the *temperature* cooling occurs, the probability of selecting a set of independent variables that has higher energy becomes stricter. At a very low *temperature*, the probability of selecting a set with higher energy $\boldsymbol{E}^{(\boldsymbol{trial})} > \boldsymbol{E}^{(\boldsymbol{i})}$ tends to approach $P = 0$. In other words, the only possibility of accepting the next *set* is if it has a lower energy state. This behaviour at *low temperatures* has a similar behaviour to the method of gradient descent, such that it will only carry forward the *trial candidate set* if it has lower *energy*. In essence, the solution *domain* reduces upon convergence for the *set* of independent variables. Therefore, the *cooling rate* and the selection algorithm for the *trial candidate set* iteration are

critical functions and often interrelated. In the traditional simulated annealing algorithm, the *cooling schedule* and *sampling* algorithm are independent, while the *adaptive simulated annealing* uses an independent cooling schedule that couples together with the sampling schedule [101].

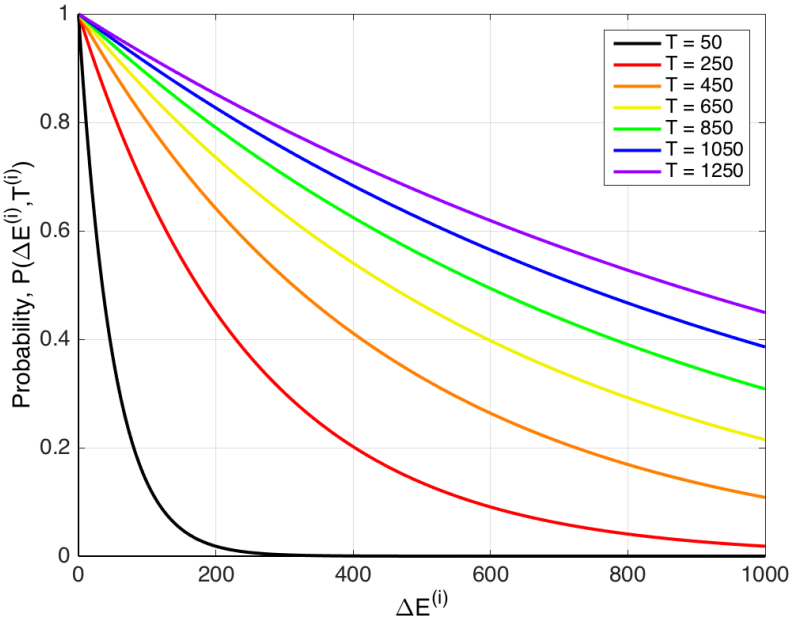

Figure 2.18 – Sensitivity of Metropolis Criteria to Temperature

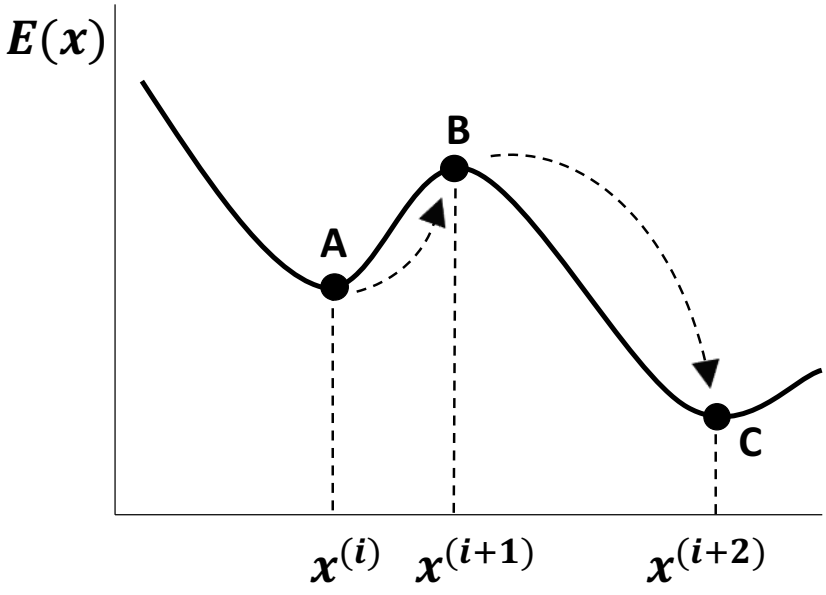

Figure 2.19 – Convergence of a solution from a local minimum to a new local minimum

The *adaptive simulated annealing rule* is the framework that follows:

1) **INITIALIZATION**: The search algorithm starts with an initial guess of the independent variables, $\boldsymbol{x^{(i)} = x^{(0)}}$, where $\boldsymbol{i}$ is the sample iteration, such that the initial guess lies within the bounds of the problem $\boldsymbol{x^{(0)} \in X}$. The energy in the system (optimization objective function) is calculated for the initial guess, such that $\boldsymbol{E^{(0)} = E\left(x^{(0)}\right)}$. Since this procedure is to replicate the annealing process, an initial temperature, $\boldsymbol{T^{(i)} = T^{(0)} = T_{max}}$, the final temperature, $\boldsymbol{T_{min}}$, the acceptance function, the *cooling schedule*, and maximum number of iterations, i^{max}, needs to be defined. A *cooling schedule* is defined for each independent variable.
2) **SAMPLING:** The *trial candidate set*, $\boldsymbol{x^{(trial)} \in X}$ is selected and the energy function for this set is calculated, $\boldsymbol{E^{(trial)} = E\left(x^{(trial)}\right).}$ Typically, the *trial candidate set* is selected as a random neighbour near to the current *candidate set,* $\boldsymbol{x^{(i)}}$. A typical sampling algorithm for the *next candidate* is

$$x_j{}^{(trial)} = x_j{}^{(i)} + v_j{}^{(i)}\left(B_j{}^{(i)} - A_j{}^{(i)}\right) \qquad (\ 2.153\ )$$

where $x_j{}^{(trial)} \in [A_j{}^{(i)}, B_j{}^{(i)}] \in X_j$, i is the iteration counter, j is the index of a parameter in the *candidate set*, and $v_j{}^{(i)}$ is a stochastic distribution function as proposed by Ingber [101]

$$v_j{}^{(i)} = \operatorname{sgn}\left(u^{(i)} - 0.5\right) T_{p,j}^{(i)} \left[\left(1 + \frac{1}{T_{p,j}^{(i)}}\right)^{\left|2u^{(i)}-1\right|} - 1\right] \qquad (\ 2.154\ )$$

where $u^{(i)}$ is a random number, such that $u^{(i)} \in [0,1]$ and $T_{p,j}^{(i)}$ is an independent temperature that cools during iterations of the *candidate set*. The independent temperature cooling schedule is

$$T_{p,j}^{(i)} = T_{p,j}^{(0)} \exp\left(-c_{p,j}\, k^{(i)\,1/N}\right) \qquad (\ 2.155\ )$$

where $T_{p,j}^{(0)}$ is the initial temperature of the independent *cooling schedule*, $k^{(i)}$ is the independent time for this independent cooling schedule, c_j is the time constant coefficient for the rate of independent cooling and N is the dimensional design vector. This time constant coefficient, $c_{p,j}$ is governed by

$$c_{p,j} = m_{p,j} \exp\left(-n_{p,j}/N\right) \quad (2.156)$$

and

$$m_{p,j} = \log\left(\frac{T_{p,j}^{(min)}}{T_{p,j}^{(0)}}\right) \text{ and } n_{p,j} = \log\left(N_{anneal}\right) \quad (2.157)$$

where $T_{p,j}^{(min)}$ is the final temperature of the independent cooling schedule and N_{anneal} is related to the time allowed at each state. These coefficients have to be carefully selected and studied [101].

3) **ACCEPTANCE FUNCTION:** After evaluating the energy of the *trial candidate set*, the difference in energy is calculated $\Delta \boldsymbol{E}^{(i)} = \boldsymbol{E}^{(trial)} - \boldsymbol{E}^{(i)}$, and the probability is calculated using the Metropolis criteria, $P\left(\Delta \boldsymbol{E}^{(i)}, T^{(i)}\right)$. A random number, $\zeta \in [0,1]$, is generated and compared to Metropolis criteria $P\left(\Delta \boldsymbol{E}^{(i)}, T^{(i)}\right)$. If $\zeta < P\left(\Delta \boldsymbol{E}^{(i)}, T^{(i)}\right)$ then the *trial candidate set* is carried forward. Else, the *current candidate set* is carried forward.

   IF $\zeta < P\left(\Delta \boldsymbol{E}^{(i)}, T^{(i)}\right)$ THEN $\boldsymbol{x}^{(i+1)} = \boldsymbol{x}^{(trial)}$

   ELSE $\boldsymbol{x}^{(i+1)} = \boldsymbol{x}^{(i)}$

   CONTINUE

4) **APPLY TEMPERATURE COOLING:** The purpose of the *cooling schedule* is to start at an elevated temperature and then continuously decrease it. There are several schedules:

   a. **Boltzmann Annealing** [102] **(modified by Laarhoven and Aarts** [103]**)**

$$\boldsymbol{T}^{(i+1)} = \boldsymbol{T}^{(0)}/i \quad (2.158)$$

b. Proportional Annealing

$$\boldsymbol{T}^{(i+1)} = \boldsymbol{T}^{(0)} / \mu_T \qquad (\ 2.159\ )$$

where $\boldsymbol{\mu_T}$ is a number slightly larger than 1.0, such that $\mu_T = 1.001$

c. Ingber Annealing [101]**:** following a similar form to the independent cooling schedule

$$T_j^{(i+1)} = T_j^{(0)} \exp\left(-c_j\, i^{1/N}\right) \qquad (\ 2.160\ )$$

This time constant coefficient, c_j is governed by

$$c_j = m_j \exp\left(-n_j\ /N\right), \qquad m_j = \log\left(\frac{T_j^{(min)}}{T_j^{(0)}}\right), \qquad n_j = \log\left(N_{anneal}\right) \qquad (\ 2.161\ )$$

5) REANNEALING: In multi-variable optimization problems, the objective function has different sensitivity rates to each independent parameter. In the annealing framework, the rate of energy decrease is dependent on the rate of specific atomic arrangements. Ingber [101] proposed that the independent cooling schedule follow an energy sensitivity function

$$s_j = \frac{\partial E}{\partial x_j} \qquad (\ 2.162\ )$$

and the independent temperatures updated as

$$T_{p,j}^{(i)} = T_{p,j}^{(i)} \left(\frac{\max(\boldsymbol{s})}{s_j}\right) \qquad (\ 2.163\ )$$

with the independent time $k^{(i)}$ updated as

$$k^{(i)} = \left(\log\left(\frac{T_{p,j}^{(0)}}{T_{p,j}^{(i)}}\right)\right)^N \qquad (\ 2.164\ )$$

This allows for the expansion of the parameter's domain when the parameter is exhibiting low sensitivity (small changes in energy) to large changes in the parameter.

6) **CONVERGENCE CHECK:** After updating the candidate set, the iteration counter, i, for the domain search is incremented and the algorithm goes back to STEP 2). This process continues until:

i) The change in energy $\Delta \boldsymbol{E}^{(i)}$ varies insignificantly during each iteration.

ii) the minimum temperature of the cooling schedule is reached.

iii) Iteration counter, i, reaches the maximum number of iterations, i^{max}.

2.3.2.4 Summary of Optimization Techniques

Table 2.4 provides a summary of the optimization techniques. The advantages and disadvantages are also summarized.

Table 2.4 – Summary of Optimization Techniques

Technique	Type	Advantages	Disadvantages
Gradient Ascent/ Descent	Deterministic	• Can converge very quickly to a solution • Assuming the same initial point, solution will **always** converge to the same solution	• Highly susceptible to converging to a poor local minimum for complex problems with large numbers of independent variables • Requires the calculation of a gradient of the optimization objective function • Poor initial guess may lead to divergence of solution • Discontinuities in the objective function may lead to divergence of solution
Genetic Algorithm	Stochastic	• Global optimization (for the specified domain) • Converged solution has excellent performance • Can leave a local minimum through the mutation steps	• Very Slow Convergence Rate o Need to generate a population size of $\boldsymbol{p}$ and create $\boldsymbol{g}$ generations o Number of Samples $(\# = p \times g)$ • Same initial point, solution may not converge to the same solution
Adaptive Simulated Annealing	Stochastic	• Good convergence rate to a solution • Can leave a local minimum through the stochastic step (in the sampling step)	• Local optimization o Iteration in the annealing process during *cooling schedule* can restrict global optimum • Same initial point, solution may not converge to the same solution

2.4 Current Deficiencies in Literature

While a significant amount of work has been performed to understand, predict and improve the behaviour of components during axial crush, there still is limited understanding of the influence of the mechanical properties of lightweight alloys on the axial crush response. In particular, very little understanding exists that provides direct insight into the effects of the elastic-plastic behaviour of the material on the energy absorption characteristics, such as crush efficiency, and mean, steady state and peak crush force.

Although there are abundant phenomenological constitutive models available that can capture initial anisotropy, they are often substituted for the classical von Mises yield function for simplicity and ease of performing axial crush finite element simulations. Thus, the initial anisotropy that is introduced into the material during manufacturing and the implication on the energy absorption characteristics is not understood and needs to be explored.

In addition, these phenomenological models currently cannot capture deformation-induced anisotropy as a result of microstructural development, such as crystallographic reorientation. The crystal plasticity framework is one of a few constitutive frameworks that can capture microstructural evolution in polycrystalline materials; however, the crystal plasticity framework currently cannot be used to simulate lab-scale components due to computational requirements. Thus, there is still a need to incorporate microstructural evolution into the large-scale simulations of large deformation applications, such as crashworthiness.

All of these individual deficiencies can be compounded upon each other when attempting to optimize the shape of a geometry for crashworthiness applications. Although there are some frameworks available for optimizing geometries, there is no framework for size optimization of front rail geometries. Furthermore, there is little understanding of the convergence behaviour of these optimization frameworks. Since the current frameworks employ simplified yield functions, there is no understanding of the influence of anisotropy on the optimization process, let alone the influence of microstructural evolution. All of these deficiencies can translate into the over-design of energy absorbing structures through the addition of unnecessary mass.

3 SCOPE AND RESEARCH OBJECTIVES

The scope of this research is to enhance the crashworthiness characteristics of aluminum front crush rail for mass-production mid-size vehicles through coupling optimization frameworks with advanced constitutive modeling techniques. As such, the research hypothesis is:

> "Coupling a constitutive model that captures initial anisotropy and evolving microstructural spin with an optimization framework will more accurately model and enhance energy absorption characteristics of aluminum structures during axial crush"

3.1 Objectives

The objectives of this research are to:

i) Develop a new framework for optimal material selection using an elastic-plastic model.
ii) Investigate the effects of yield surface curvature and anisotropy constants on axial crush response.
iii) Develop a new framework for the optimization of geometric cross section profiles for front rail applications
iv) Understand the effects of incorporating anisotropy into the optimization process of the front rail crush geometry.
v) Develop a multi-scale modeling framework that bridges crystal plasticity to phenomenological plasticity using the PBTE model proposed by Bassani and Pan [26].
vi) Employ the PBTE model to perform large-scale simulations of axial crush structures and study the influence of microstructural spin on energy absorption characteristics.

Figure 3.1 presents the research strategy that highlights the interaction between each task. As such, it is expected that the outcome of this research will expand the current knowledge base on three frontiers:

1) The influences of material properties and anisotropy on the axial crush response.
2) The use of nonlinear optimization techniques to improve energy absorption characteristics of aluminum structures in axial crush.
3) The use of multi-scale modeling for axial crushing of structures.

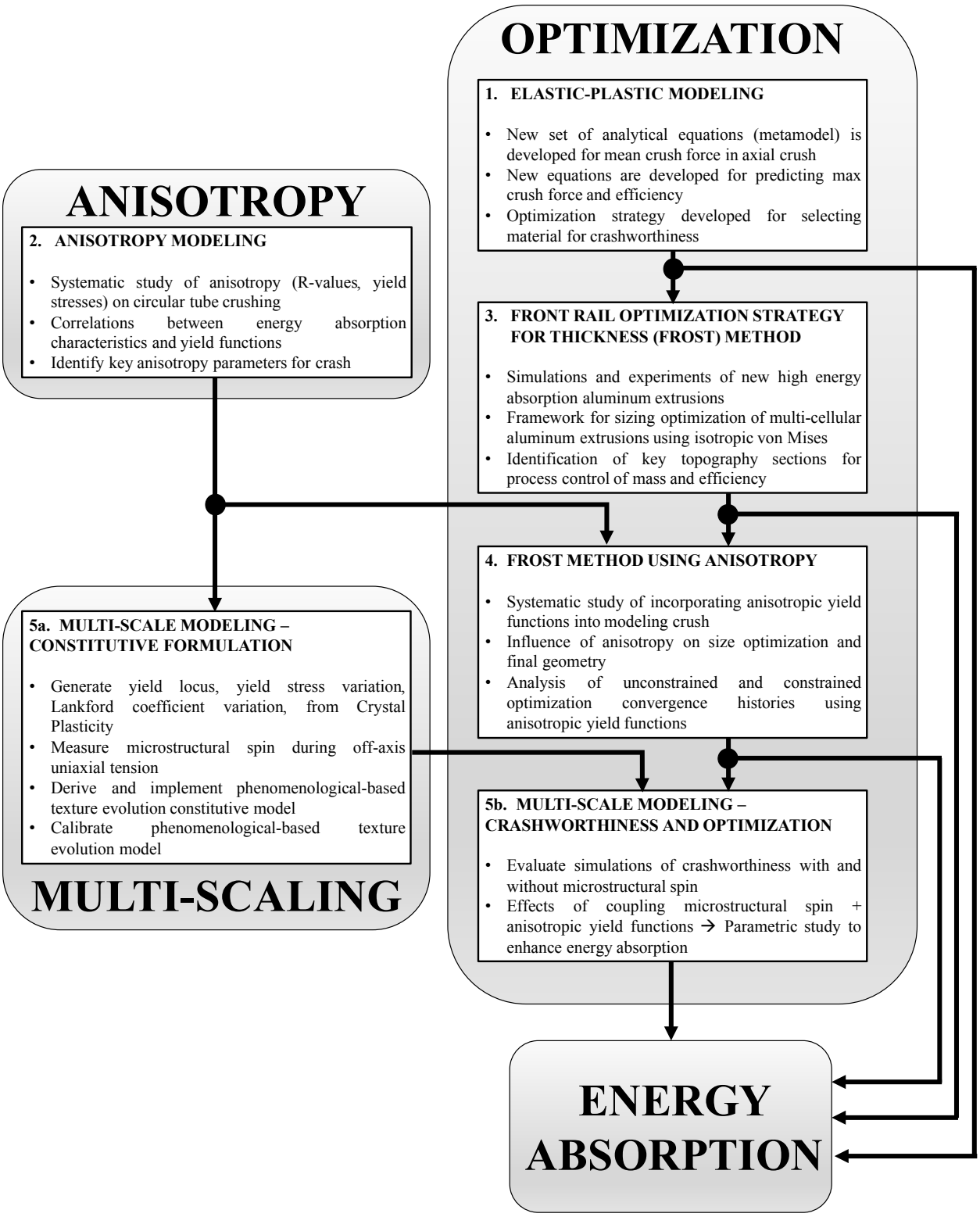

Figure 3.1 – Research Strategy

3.2 Summary of Contributions to Achieve Objectives

The work completed to achieve the research objectives are presented in next five chapters. Each chapter is based on the following published manuscripts:

Chapter 4 **Kohar, C.P.,** Mohammadi, M., Mishra, R.K., and Inal, K*. (2015). Effects of elastic-plastic behaviour on the axial crush response of square tubes. Thin-Walled Structures **90**, p. 64-87 [104].

Chapter 0 **Kohar, C.P.,** Mohammadi, M., Mishra, R.K., and Inal, K* (2016). The effects of the yield surface curvature and anisotropy constants on the axial crush response of circular tubes. Thin-Walled Structures, **106**, p. 28-50 [16].

Chapter 6 **Kohar, C.P.,** Zhumagulov, A., Brahme, A., Worswick, M.J., Mishra, R.K., Inal, K. (2016). Development of High Crush Efficient, Extrudable Aluminium Front Rails for Vehicle Lightweighting. International Journal of Impact Engineering, **95**, p. 17-34 [105].

Chapter 7 **Kohar, C.P.,** A., Brahme, A., Mishra, R.K., Inal, K. (2017). Effects of Coupling Anisotropic Yield Functions with the Optimization Process of Extruded Aluminum Front Rail Geometries in Crashworthiness. Under Revision at International Journal of Solids and Structures (IJSS-S-16-01573) on November 22, 2016 [106].

Chapter 8 **Kohar, C.P.,** Bassani, J.L., Brahme, A., Mishra, R.K., Inal, K. (2017). A New Multi-Scale Framework to Incorporate Microstructure Evolution into Phenomenological Plasticity: Part I – Model Formulation. In preparation for International Journal of Plasticity and Part II – Application to Crashworthiness and Optimization.

In addition to these publications, the following publications have been written as a result of this current research. However, these works do not have a direct impact on the overall research objectives of this thesis and are referenced only as supporting work:

- **Kohar, C.P.,** Cherkaoui, M., El Kadiri, H., Inal, K. (2016). Numerical Modeling of TRIP Steel in Axial Crashworthiness. International Journal of Plasticity, **84,** p. 224-254 [107].

- Zhumagulov, A., Imbert, J., **Kohar, C.P.,** Inal, K., Worswick, M., Mishra, R. (2016). Energy absorption characterization of multicellular AA6063-T6 extrusions. International Conference on Impact Loading of Structures and Materials (ICILSM 2016), Turin, Italy, May 22 – 26, 2016 [108].

3.3 Limitation of Modeling Approaches Used in Current Study

In each chapter of the results, finite element models were created to simulate the crushing response of automotive aluminum structures and compared to experimental measurements. The current study was limited to automotive aluminum sheet AA5754-O and extruded AA6063-T6. These aluminum alloys exhibit strong flow stress sensitivity at low and elevated temperatures [107, 108] and can change their mechanical properties, due to natural aging, over time. All simulations and experiments were performed using as produced material at room temperature under dynamic loading conditions. No scenarios of off-axis or oblique loading were considered. As the material deforms plastically during loading, a fraction of the plastic work ($W = \sigma_{ij} D_{ij}^{P}$) is converted into heat and dissipated to the surroundings. However, dynamic loading and crushing is a rapidly evolving process where there is insufficient time to allow for heat transfer. Furthermore, the thermal softening from plastic work was implicitly captured in the strain-rate sensitivity models. Thus, thermodynamic effects were not considered in the finite element models.

As mentioned earlier, advanced deformation phenomenon observed in aluminum such as minor tension-compression asymmetry [36, 38, 39] and kinematic hardening behaviours [40, 41, 42, 14] were not incorporated into this study. When coupling these finite element simulations with optimization strategies, the limit of the material can be reached and could result in fracture. Although models have been proposed to capture ductile failure and fracture in aluminum [109, 110, 111, 112], fracture modeling in aluminum was simplified to a single effective strain limit with element deletion [49]. In the optimization framework, the topology, topography, and length of geometries were fixed to satisfy an automotive packing envelope and reduce the number of free variables.

4 EFFECTS OF ELASTIC-PLASTIC BEHAVIOUR ON THE AXIAL CRUSH REPONSE OF SQUARE TUBES - C.P. Kohar, M. Mohammadi, R.K. Mishra, and K. Inal (2015). Thin-Walled Structures 90, p. 64-87

This chapter presents to the development of a new framework for optimal material selection using an isotropic elastic-plastic model. The effects of the elastic-plastic behaviour of lightweight alloys on the steady state crush force, peak crush force, energy absorption and crush efficiency response of the axial crushing of square tubes are studied. New definitions and analytical equations for crush efficiency and energy absorption are developed and calibrated with the axial crush simulations to develop a framework for optimal material selection for axial crush. This work shows that the yield stress increases the energy absorption, peak crush force and steady state crush force, while tending to decrease the crush efficiency. After sufficient increase in the hardening capabilities, positive gains are obtained in the crush efficiency when increasing the yield stress. The ultimate tensile strength, hardening rate and the yield stress of the material have a strong effect on improved energy absorption. Lightweight alloys with a low yield stress that have significant work hardening capabilities outperform materials with a high yield stress and very little work hardening in terms of energy absorption when a constraint is imposed on the peak crushing force. The results of this work have been published in Kohar et al. [104]. In an additional study by Kohar et al. [105], the material selection optimization framework was applied to determine optimal volume fraction compositions for transformation-induced plasticity (TRIP) steel in crashworthiness applications.

4.1 Introduction

In recent years, a renewed interest has arisen towards the investigation of crashworthy elements. In the work of Nagel and Thambiratnam [106, 107, 108] a systematic analysis was performed to calibrate an analytical equation to numerical results produced by finite element simulations of tapered rectangular tubes. Jones [36] performed a dimensionless analysis on the ratio of crush structure energy absorption to the total energy absorption during uniaxial tension to differentiate between materials for efficiency. It was found that an aluminum alloy was more efficient than conventional steels because the higher rupture strain of steel was classified as an inefficient use of material. While a significant amount of work has been performed to understand the behaviour of axial crush [109], very little research exists that provides direct

insight into the effects of the elastic-plastic behaviour of the material on the axial crush response for lightweight alloys. Additionally, the conventional definitions of crush efficiency and crushing force do not adequately capture the actual loading to a vehicle passenger during an impact. Currently, no work has been performed to relate the peak crush force to material properties. Thus, no analytical equation for crush efficiency has also been proposed in terms of material behaviour.

Furthermore, no work has focused on investigating the relationship between energy absorption characteristics and how they interact with each other through the material behaviour. For example, there is no study on the implications of peak crush force constraints on the steady state crushing force, energy absorption and crush efficiency of crush tubes when comparing different lightweight alloys. With a wide variety of available lightweight alloys with different large strain behaviour, automakers have been challenged to design and select materials that offer superior crashworthiness performance without additional cost or significant development time. Currently, automakers use commercial numerical simulation tools to accurately simulate and predict the effect of lightweight alloys for frontal crash scenarios, which requires a significant amount of time and resources. A structure for optimal material selection for axial crash and energy absorption to reduce front rail development time is required.

In this chapter, the effects of the elastic-plastic material behaviour on the energy absorption characteristics of axial crush are studied. In order to investigate the effects of the elastic-plastic material behaviour, axial crush finite element simulations are performed on a simple square front rail crush tube. The geometry of the crush tube remains constant for all simulations during the study. The yield stress and strain, ultimate tensile strength, hardening rate, and failure strain of the material are varied in each simulation. The objective of this study is to develop a new framework that can be used to select a set of material properties to achieve optimum energy absorption and crush efficiency. In this framework, new concepts are introduced for energy absorption and crush efficiency metrics. Furthermore, a new set of analytical equations, based on numerical simulations, are developed for the framework to predict the steady state crushing force, maximum crushing force, crush efficiency and energy absorption behaviour due to various elastic-plastic material responses. The analytical equations are derived from the macro-element formulation to separate geometric and material effects [71, 72, 73] and

calibrated from the results of numerical simulations. Constraints are imposed on the peak crushing force and energy absorption to develop the material selection framework. Validation simulations are performed to compare the set of analytical equations and the FE model to experimental work found in literature.

4.2 Problem Statement

Wierzbicki and Abramowicz assumed that the material contribution for energy absorption, $f(Material)$, is

$$f(Material) = \sigma_0 \quad (4.1)$$

for a rigid-perfectly plastic material [71, 72, 73]. Lightweight alloys typically work harden as they are deformed plastically. This means that the parameters associated with the work hardening of material during plastic deformation can have a significant impact on the energy absorption [110]. Abramowicz later used a power law model to extend his work to include plasticity effects by calculating the equivalent flow stress [110]

$$f(Material) = \sqrt{\frac{\sigma_0 \sigma_{UTS}}{n+1}} \quad (4.2)$$

where σ_{UTS} is the ultimate tensile strength and n is the power law hardening coefficient. However, the power law plasticity tends to over predict the stress response of lightweight alloys that have saturating flow stress behaviour. Additionally, this formulation does not take into account the initial elastic deformation and the effects of failure strain. Furthermore, the formulation assumes that the plastic hinging is developed along a single strain path where multi-directional strain paths, such as biaxial straining, are neglected. Thus, a new definition for the material contribution for energy absorption that incorporates these effects is required.

4.3 Method of Solution

In this chapter, it is considered that the energy absorption contribution from material effects is a function of the plastic deformation properties of the material so that

$$f(Material) = f\left(\sigma_0, U_0, \varepsilon_0, \varepsilon_f, \frac{d\sigma}{d\varepsilon}\right) \quad (4.3)$$

where σ_0 is the material quasi-static yield stress, U_0 is the ratio of the ultimate tensile strength to the quasi-static yield stress (σ_{UTS}/σ_0), ε_0 is the strain at the yield stress, ε_f is the associated uniform elongation strain at the ultimate tensile strength, and $\frac{d\sigma}{d\varepsilon}$ is the hardening rate of material. The strain at yielding is determined from the ratio of the yield stress to the elastic modulus (σ_0/E) and the hardening rate is captured through the hardening law employed for the material. In this chapter, a Voce-type plasticity law [51], as presented

$$\sigma_y = \sigma_0 + (\sigma_{UTS} - \sigma_0)(1 - \exp(-D\varepsilon^p)) \quad (4.4)$$

In Equation 4.4, D is the Voce hardening saturation coefficient and ε^p is the current plastic strain. The Voce plasticity law is used to capture the saturating behaviour of the flow stress observed in lightweight alloys. A Voce-type plasticity law also provides direct intuition into the effects of material parameters on the uniaxial tensile behaviour, which can be used for predicting the axial crush response.

As observed by Smerd *et al.* [111], automotive aluminum alloys generally have low strain rate sensitivity at room temperatures compared to conventional steels (see Ref [112]). However, at moderate strain-rates, aluminum alloys start to exhibit positive rate sensitivity. To account for dynamic loading effects, a material strain-rate sensitive model in employed that scales the quasi-static yield stress. In this study, the Cowper-Symonds rate-sensitivity formulation [53] is adopted

$$\frac{\sigma_d}{\sigma_0} = 1 + \left(\frac{\dot{\varepsilon}}{M}\right)^{\frac{1}{P}} \quad (4.5)$$

where σ_0 is the quasi-static yield stress, σ_d is the dynamic yield stress, $\dot{\varepsilon}$ is the strain-rate of the material in the fold, M is the reference material strain-rate sensitivity coefficient and P is the material strain-rate sensitivity exponent. The experimental values of $M = 9.39\times10^{10}s^{-1}$ and $P = 10.55$ are used for this study [113]. Abramowicz and Jones [114] demonstrated that the strain-rate in a Type I collapse element can be approximated by

$$\dot{\varepsilon} = \frac{V}{3C} \quad (4.6)$$

where V is the velocity of the impacting mass. Therefore, the dynamic yield stress formulation presented in Equation 4.5 is rearranged, so that

$$\frac{\sigma_d}{\sigma_0} = 1 + \left(\frac{V}{3CM}\right)^{\frac{1}{P}} \qquad (\ 4.7\ )$$

This term is significant because it accounts for the geometry and material interaction effects.

In this work, the following analytical equation is proposed to calculate the average energy absorption

$$E_{abs} = (18.86372h^2C)a_1\sigma_0\left(1 + \left(\frac{V}{3CM}\right)^{\frac{1}{P}}\right)\left(1 + (U_0 - 1)\left(a_2U_0\sqrt{D} + a_3\sqrt{D}\right)\right)\left(1 + a_4\frac{\sqrt{\varepsilon_f}}{\varepsilon_0} + a_5\sqrt{\varepsilon_f}\right)\ ,\ \varepsilon_0 \neq 0 \qquad (\ 4.8\ )$$

where a_i are constants to be determined. This formulation is selected to capture the additional influences of plasticity on the axial crush energy absorption response. It should be mentioned that when $U_0 = 1$, Equation 4.8 reduces to an elastic-perfectly plastic form that is similar to the work presented by Abramowicz and Wierzbicki [71, 72, 73] (with the additional contribution due to failure strain and elastic loading). It is important to note that $\varepsilon_0 \neq 0$ to keep Equation 4.8 as an elastic-plastic formulation. The constants, a_i, are obtained from performing numerical simulations of axial crushing of square crush tubes and performing a regression analysis on the energy absorption data.

Similarly, the following analytical equation for the steady state crushing force

$$F_{ss} = (18.86372h^2C)b_1\sigma_0\left(1 + \left(\frac{V}{3CM}\right)^{\frac{1}{P}}\right)\left(1 + (U_0 - 1)\left(b_2U_0\sqrt{D} + b_3\sqrt{D}\right)\right)\left(1 + b_4\frac{\sqrt{\varepsilon_f}}{\varepsilon_0} + b_5\sqrt{\varepsilon_f}\right)\ ,\ \varepsilon_0 \neq 0 \qquad (\ 4.9\ )$$

where b_i are constants to be determined.

The analytical equation for the maximum crushing force assumes that the failure strain has no effect on the response. Therefore, the proposed analytical equation for the maximum crushing force takes the form of

$$F_{max} = Ac_1\sigma_0\left(1+\left(\frac{V}{3CM}\right)^{\frac{1}{P}}\right)\left(1+c_2(U_0-1)(1+c_3\varepsilon_0+c_4U_0D)\right) \qquad (4.10)$$

where c_i are constants to be determined and A is the cross sectional area of the geometry. This formulation indicates that the peak crushing force is strongly dependent on the cross sectional area and not the shape of the cross section (i.e., parameters h^2C). Thus for materials that behave similar to elastic-perfectly plastic, $(U_0 = 1)$, the peak crushing force can be approximated by

$$F_{max} = Ac_1\sigma_0 \quad when \quad U_0 = 1 \qquad (4.11)$$

The crushing efficiency response is obtained by using the steady state crushing force and the maximum crush force response, so that

$$\eta_{ss} = \frac{F_{ss}}{F_{max}} = \frac{(18.86372h^2C)b_1\left(1+(U_0-1)\left(b_2U_0\sqrt{D}+b_3\sqrt{D}\right)\right)\left(1+b_4\frac{\sqrt{\varepsilon_f}}{\varepsilon_0}+b_5\sqrt{\varepsilon_f}\right)}{Ac_1\left(1+c_2(U_0-1)(1+c_3\varepsilon_0+c_4U_0D)\right)} \qquad (4.12)$$

This formulation takes into account the effects of both geometry and material properties in predicting the crush efficiency. Note that this formulation assumes that the crush efficiency is independent of the crushing velocity and the rate sensitivity. To reduce the computational work required, the lightweight alloy studied is limited to aluminum alloys that have low rate-sensitivity.

As mentioned earlier in Section 2.2.1.2 and stated in Equation 2.106, the effects of geometry and material on the energy absorption characteristics have been separated to isolate each contribution. It is noted that through the effects of strain rate sensitivity, the geometry and material interaction effects exist. The contribution from geometry in Equation 4.8 - 4.12 is presented via Equation 2.111 - 2.112, which is the geometry contribution for a Type I collapse element. This introduces the geometry cross section information into the energy absorption formulation in terms of the macro element length, *C,* and the material thickness, *h*.

4.4 Finite Element Modeling

In this study, a finite element (FE) model is created to simulate the axial crushing of a square crush tube at various velocities using the commercial FE software LS-DYNA. A non-linear explicit dynamic formulation is used throughout this study [58].

The FE model is shown in Figure 4.1. A 76.2mm [3.00"] × 76.2mm [3.00"] square crush tube with a 3.0mm wall thickness is placed between two rigid steel plates. The mean corner radius is 6.00mm and the initial length of the square crush tube is 400mm. The cross sectional area of the crush tube is 847.5 mm^2. The nodes in a 25mm long section of the top and bottom section of the crush tube, shown in yellow in Figure 4.1, are fixed in all motions except for the crushing direction. This simulates the crush tube in an boss fixture. A 5mm deep × 40mm wide crush initiator is placed 50mm from the bottom surface of the crush tube. The mass of the top loading plate is 560 kg and it is given an initial velocity of 15.50m/s (56km/h). The total simulation time is 15 milliseconds for this loading scenario. The force-displacement response of the mass is monitored to obtain the energy absorption characteristics. The Voce plasticity law is used to model the aluminum alloy behaviour and a rigid model with elastic properties of steel is used to model the plates. The Voce plasticity law is parameterized into an isotropic piece-wise plasticity model (*MAT_024) for the stress-plastic strain behaviour. The elastic material properties are listed in Table 4.1. In each simulation, the yield stress and strain, ultimate tensile strength, hardening rate, and failure strain is varied for the aluminum crush tube. The numerical testing matrix that details the simulation parameters and results are presented in APPENDIX A.1.

In the conventional method of modeling axial crush, shell element formulations are used for their computational efficiency and ease of utilizing large number of through thickness integration points (i.e., Ref [80, 115, 9, 79, 14, 77]). Although a large number of integration points can be implemented to capture the through thickness strain, the plane stress assumption of a shell element assumes that the through thickness stress is zero ($\sigma_{33} = 0$) [58]. Furthermore, large through thickness strains are developed through the bends. This means that the plane stress assumption will result in the through thickness energy dissipation contribution to be neglected; $\sigma_{33}\varepsilon_{33} = 0$. Thus, solid brick elements are used to capture this phenomenon. Eight-node fully integrated selective reduced (S/R) solid elements (ELFORM=2 for *ELEMENT_SOLID) are

used to capture the large strain and bending behaviour that develops in the crush folds. Element deletion is used to simulate failure within the material when the total plastic strain exceeds the uniform elongation strain, ε_f. In this work, this is known as the failure strain. Four mesh sizes are used to explore the mesh sensitivity for this analysis: 1.50mm × 1.50mm × 1.50mm, 1.00mm × 1.00mm × 1.00mm, 0.75mm × 0.75mm × 0.75mm, and 0.50mm × 0.50mm × 0.50mm. Each simulation is executed on a high performance computing cluster with 32 × 2.70GHz Intel Xeon E5-2680 processors allocated. Contact algorithms are placed between the crush tube and the rigid plates to capture the friction of the crush tube folds against the plate. The static and dynamic coefficients of friction are set to 0.45 and 0.40 respectively. Self-contact algorithms are also placed to capture the effects of the folds stacking onto each other. Accordingly, the static and dynamic coefficients of friction for this contact are set to 1.04 and 1.00 respectively.

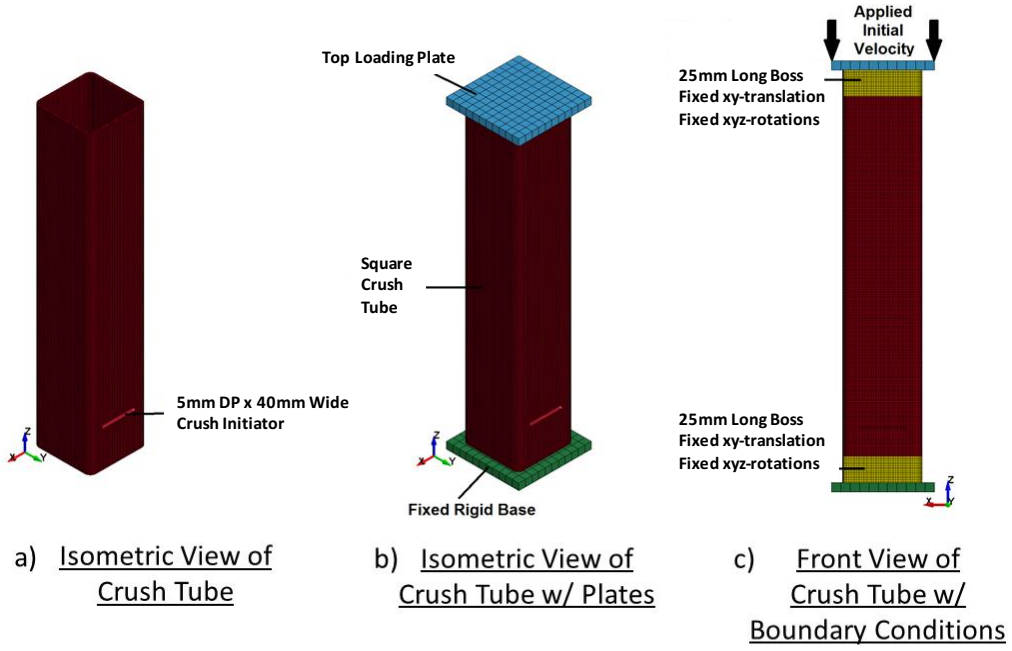

Figure 4.1 – a) Isometric View of FE Crush Tube, b) Isometric View of FE Crush Tube with Loading Plates and c) Front View of FE Model with Boundary Conditions for 1.50mm x 1.50mm x 1.50mm mesh

Table 4.1 – Elastic material properties of aluminum and steel

	Aluminum	Steel
Density [g/cm^2]	**2.7**	**7.8**
Elastic Modulus [MPa]	**67900**	**205000**
Poisson Ratio	**0.34**	**0.3**

4.5 Results

The constants employed in the equations for the steady state crushing force, maximum crushing force and energy absorption response are obtained by performing numerical simulations on the 1.50mm mesh. The validity of the numerical results obtained for the 1.50mm mesh simulation is discussed later in Section 4.5.5. The commercial optimization software LS-OPT is used to generate the sample space. A space-filling point selection scheme is used to determine the parameters for each simulation [49]. 23 simulations are required to obtain a sufficient data set for a minimum of a quadratic response for 4 parameters. The sample set is increased, such that 200 simulations are performed, to provide more data points for better predictive capability. This is further discussed in Section 4.5.1. A custom data processor script is written in the commercial software MATLAB to perform the regression analysis. In the simulations, the steady state regime begins after a crushing distance of 100mm. The upper and lower bounds of the test matrix (Appendix A.1) parameters are presented in Table 4.2. Figure 4.2 presents a graphical representation of the stress-strain responses that are studied. The lower (shown in blue) and upper limit (shown in red) stress-strain curves corresponds to $\sigma_0 = \{50, 300\}$MPa, $U_0 = \{1.001, 3.000\}$ and $D = \{5.00, 15.00\}$ respectively from Table 4.2. The associated strain at uniform elongation is $\varepsilon_f = 1.40$ for both limits. Extruded AA6063-T6/AA7003-T6 [116] and AA5754-O sheet are examples of automotive aluminum alloys that fall within the region of interest. Although the focus of this study is limited to aluminum alloys, these bounds are selected because it encompasses a wide variety of automotive alloys that are desirable in axial crashworthiness applications.

Table 4.2 – Upper and lower bounds on simulation parameters

	Lower Bound	Upper Bound
σ_0 [MPa]	50.00	300.00
U_0	1.001	3.000
D	5.000	15.00
ε_f	0.800	1.400

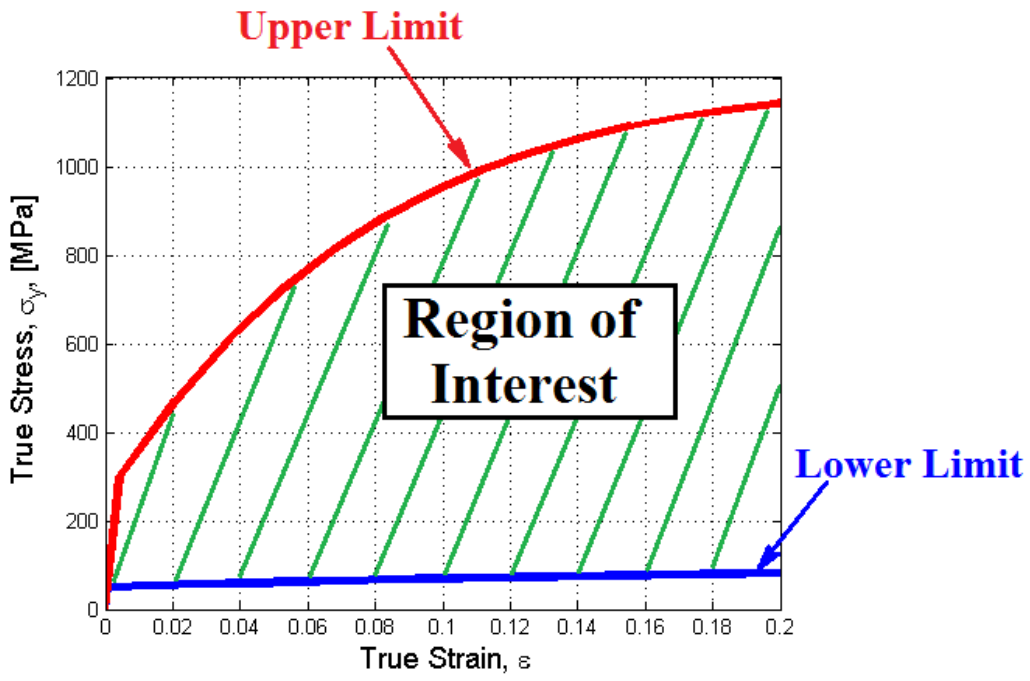

Figure 4.2 – Range of Stress-Strain Responses

4.5.1 Results of Regression Analysis, Error Statistics Between Simulation Results and Analytical Equations

A linear form of the Gauss-Newton method is used to determine the constants in Equation 4.8 - 4.12. The Gauss-Newton method is an iterative solution that minimizes the error of the coefficients as presented in Section 2.3.1.2. The obtained coefficients for each analytical equation from the Gauss-Newton method are presented in Table 4.3.

Table 4.3 – Fitted coefficients for energy absorption, steady state crushing force and peak crushing force response

i	Energy Absorption, E_{abs} Coefficients, a_i	Steady State Crushing Force, F_{ss}, Coefficients, b_i	Peak Crushing Force, F_{max}, Coefficients, c_i
1	**4.4930**	**0.0224**	**1.0715**
2	**0.0078**	**0.0263**	**0.1336**
3	**0.0867**	**0.0493**	**-300.7273**
4	**0.0003**	**0.0002**	**0.0187**
5	**-0.0994**	**-0.1176**	

The accuracy of the fitted constants is determined by calculating the average error and unbiased standard deviation for each simulation. The average error between the simulation results and the model formulations is defined as [85]

$$\bar{\epsilon} = \frac{1}{m}\sum_{i=1}^{m}\frac{|r_i|}{y_i}\times 100\% \qquad (4.13)$$

where m is the number of sample points. The unbiased standard deviation between the simulation results and the model formulations is defined as [85]

$$\hat{\sigma} = \sqrt{\frac{\sum_{i=1}^{m} {r_i}^2}{m-n}} \qquad (4.14)$$

where n is the number of free variables. The average error and unbiased standard deviation are calculated for each simulation and response and presented below in Table 4.4. The minimum and maximum obtained values for each response are also shown in Table 4.4. The average error for the data fit for the steady state crushing force, peak crushing force and energy absorption is 4.08%, 9.45%, and 3.10% respectively. The unbiased standard deviation for the data fit for the steady state crushing force, peak crushing force and energy absorption is 3.623kN, 12.251N and 0.424kJ respectively. These error analysis results show that the analytical equations have good predictive capabilities.

Table 4.4 – Minimum value, maximum value, average error, unbiased standard deviation and $R^2{}_{prediction}$ for steady state crush force, peak crush force and energy absorption responses

Response	Minimum Value	Maximum Value	Unbiased Standard Deviation, $\hat{\sigma}$	Average Error, $\bar{\epsilon}$ [%]	$R^2{}_{prediction}$
Steady State Crush Force, F_{ss} [kN]	16.71	155.04	3.623	4.08	0.9905
Peak Crush Force, F_{max} [kN]	70.70	319.00	12.251	9.45	0.9781
Energy Absorption, E_{abs} [kJ]	3.70	30.00	0.424	3.10	0.9966

The prediction sum of squares (PRESS) is a statistical measurement of the overall quality of the regression analysis. The PRESS is defined as [85]

$$PRESS = \sum_{i=1}^{m} \left(\frac{y_i - \hat{y}_i}{1 - h_{ii}} \right)^2 \quad (4.15)$$

where h_{ii} are the diagonal terms of

$$\boldsymbol{H} = \boldsymbol{X}(\boldsymbol{X}^{\boldsymbol{T}}\boldsymbol{X})^{-1}\boldsymbol{X}^{\boldsymbol{T}} \quad (4.16)$$

From the PRESS, the $R^2{}_{prediction}$ can be defined, which represents the ability of the model to determine the variability in predicting new responses [117]

$$R^2{}_{prediction} = 1 - \frac{PRESS}{S_{yy}} \quad (4.17)$$

where;

$$S_{yy} = \boldsymbol{y}^{\boldsymbol{T}}\boldsymbol{y} - \frac{1}{m}\left(\sum_{i=1}^{m} y_i \right)^2 \quad (4.18)$$

The $R^2{}_{prediction}$ for the steady state crush force, peak crush force, and energy absorption response is 0.9905, 0.9871, 0.9966 respectively and is also presented in Table 4.4. Having a $R^2{}_{prediction}$ value close to a value of 1 is an indication of low variability in the model predictive capability. Figure 4.3 presents the convergence plots for each response. The analysis shows that the $R^2{}_{prediction}$ converges at approximately 100 simulations and that small improvements in the predictive capability are realized up to 200 simulations. Thus, the selection of 200 simulations is an appropriate set for this analysis.

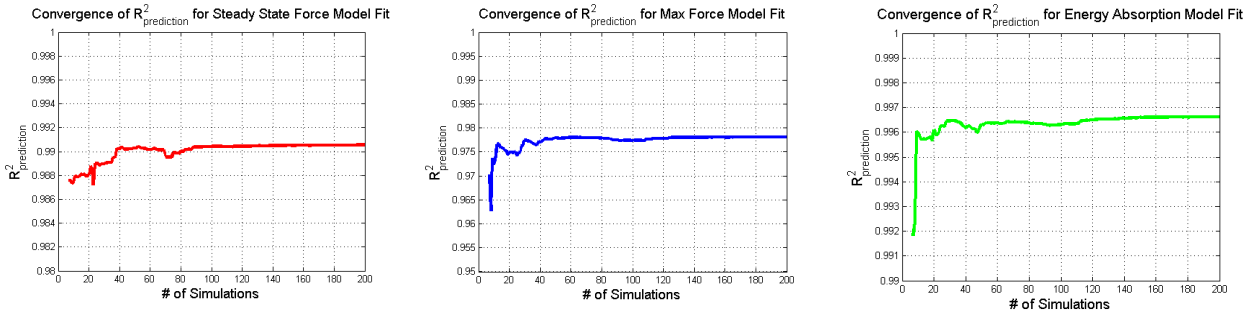

a) **b)** **c)**

Figure 4.3 - Convergence Plot of $R^2{}_{prediction}$ for Fitting a) Steady State Crush Force, b) Peak Crush Force, and c) Energy Absorption Response

4.5.2 ANOVA and Global Sensitivity Analysis

An analysis of the variance (ANOVA) is performed on the regression coefficients. The estimation of the square error, $\widehat{\boldsymbol{v}}(\widehat{\boldsymbol{\beta}})$, of the regression coefficients, $\widehat{\boldsymbol{\beta}}$, of the function, $\boldsymbol{f}$, is measured by [118, 119]

$$\widehat{\boldsymbol{v}}(\widehat{\boldsymbol{\beta}}) = s^2(\boldsymbol{F}'\boldsymbol{F})^{-1} \qquad (4.19)$$

where s^2 is the estimated error variance, and $\boldsymbol{F}'$ is a linearized formulation of the model;

$$F_{ij} = \frac{\partial f_i}{\partial \hat{\beta}_j}(\hat{\beta}, x) \qquad (4.20)$$

The p-value is computed to determine the statistical significance each parameter has on the response. The p-value is the probability that each regression coefficient has no statistical inference on the response, such that the true value of the regression coefficient $\beta_{actual,i}$=0. The p-value is computed via a t-score, $\boldsymbol{T}$, on a 90% confidence interval, $1-\alpha/2$, t-distribution, such that;

$$\boldsymbol{P}(\widehat{\boldsymbol{\beta}}) = 2\boldsymbol{t}_{\boldsymbol{T},\boldsymbol{m}-\boldsymbol{N}}, \quad T = \left| \frac{\widehat{\boldsymbol{\beta}}}{\sqrt{\widehat{\boldsymbol{v}}(\widehat{\boldsymbol{\beta}})}} \right| \qquad (4.21)$$

where N is the number of coefficients in the regression. Table 4.5 - Table 4.7 presents the estimation in the error of the coefficients in the regression analysis. All the P-values calculated have values that are less than 1×10^{-3} (0.1%), which means that each parameter is statistically relevant. The first term of each regression analysis that operates on the yield stress has the most significant influence, which is indicated by have the lowest P-value.

Table 4.5 – Estimated Error of Coefficients for Energy Absorption Response

i	E_{abs} Coefficients, a_i	$\hat{v}(\hat{\beta})_i$	$T(\hat{\beta})_i$	$P(\hat{\beta})_i$
1	4.4930	8.1278×10^{-2}	5.5279×10^{1}	4.2547×10^{-121}
2	0.0078	2.0083×10^{-3}	3.9000×10^{0}	1.3232×10^{-4}
3	0.0867	6.3372×10^{-3}	1.3682×10^{1}	2.5920×10^{-30}
4	0.0003	1.1629×10^{-5}	2.2410×10^{1}	7.5198×10^{-56}
5	-0.0994	1.5610×10^{-2}	6.3658×10^{0}	1.3597×10^{-9}

Table 4.6 - Estimated Error of Coefficients for Mean Crush Force Response

i	Steady State Crushing Force, F_{ss}, Coefficients, b_i	$\hat{v}(\hat{\beta})_i$	$T(\hat{\beta})_i$	$P(\hat{\beta})_i$
1	0.0224	6.7463×10^{-4}	3.3212×10^{1}	3.3489×10^{-82}
2	0.0263	3.5390×10^{-3}	7.4367×10^{0}	3.1950×10^{-12}
3	0.0493	1.1191×10^{-2}	4.4542×10^{0}	1.4167×10^{-5}
4	0.0002	1.8435×10^{-5}	9.4225×10^{1}	1.3067×10^{-17}
5	-0.1176	2.5339×10^{-2}	4.6404×10^{0}	6.3702×10^{-6}

Table 4.7 - Estimated Error of Coefficients for Peak Crush Force Response

i	Peak Crushing Force, F_{max}, Coefficients, c_i	$\hat{v}(\hat{\beta})_i$	$T(\hat{\beta})_i$	$P(\hat{\beta})_i$
1	1.0715	8.4622×10^{-3}	1.2731×10^{2}	2.1623×10^{-190}
2	0.1336	2.0946×10^{-2}	6.3768×10^{0}	1.2701×10^{-9}
3	-300.7273	2.7006×10^{1}	1.1136×10^{1}	1.2410×10^{-22}
4	0.0187	4.4019×10^{-3}	3.9776×10^{0}	9.7920×10^{-5}

The normalized global sensitivity is defined as the product of the derivative of the responses with respect to the material parameter and the range of the material parameter, such that [85]

$$\boldsymbol{S} = \frac{\boldsymbol{\partial f}}{\boldsymbol{\partial x}}[\max \boldsymbol{x} - \min x] \qquad (\ 4.22\ )$$

Figure 4.4 presents the global parameter sensitivity plot for the steady state crush force, peak crush force, and energy absorption. Equation 4.8 - 4.12. are expanded into polynomial form before calculating the derivate of the function. The crush efficiency cannot be decomposed into a polynomial because it is a ratio of two unique functions. The sensitivity analysis shows a strong dependence on the yield stress. Furthermore, a significant interaction effect is present between the yield stress, ultimate tensile strength ratio and Voce hardening saturation coefficient. The peak crush force exhibits a higher sensitivity to the yield stress than the steady state crush response. This means that increasing the yield stress may have a negative effect on the crush efficiency.

4.5.3 *Validation of Finite Element Model and Analytical Equations*

Two different simulations are performed to ensure that the numerical model is constructed properly and that the analytical model is predictive and robust. In the first simulation, the results from the FE model are compared to experimental data found in literature. The analytical equation is also used to predict the steady state crush force, peak crush force, energy absorption and crush efficiency. In the second simulation, the cross section geometry is varied and the predictions from this simulation are compared to the predictions from the analytical equation.

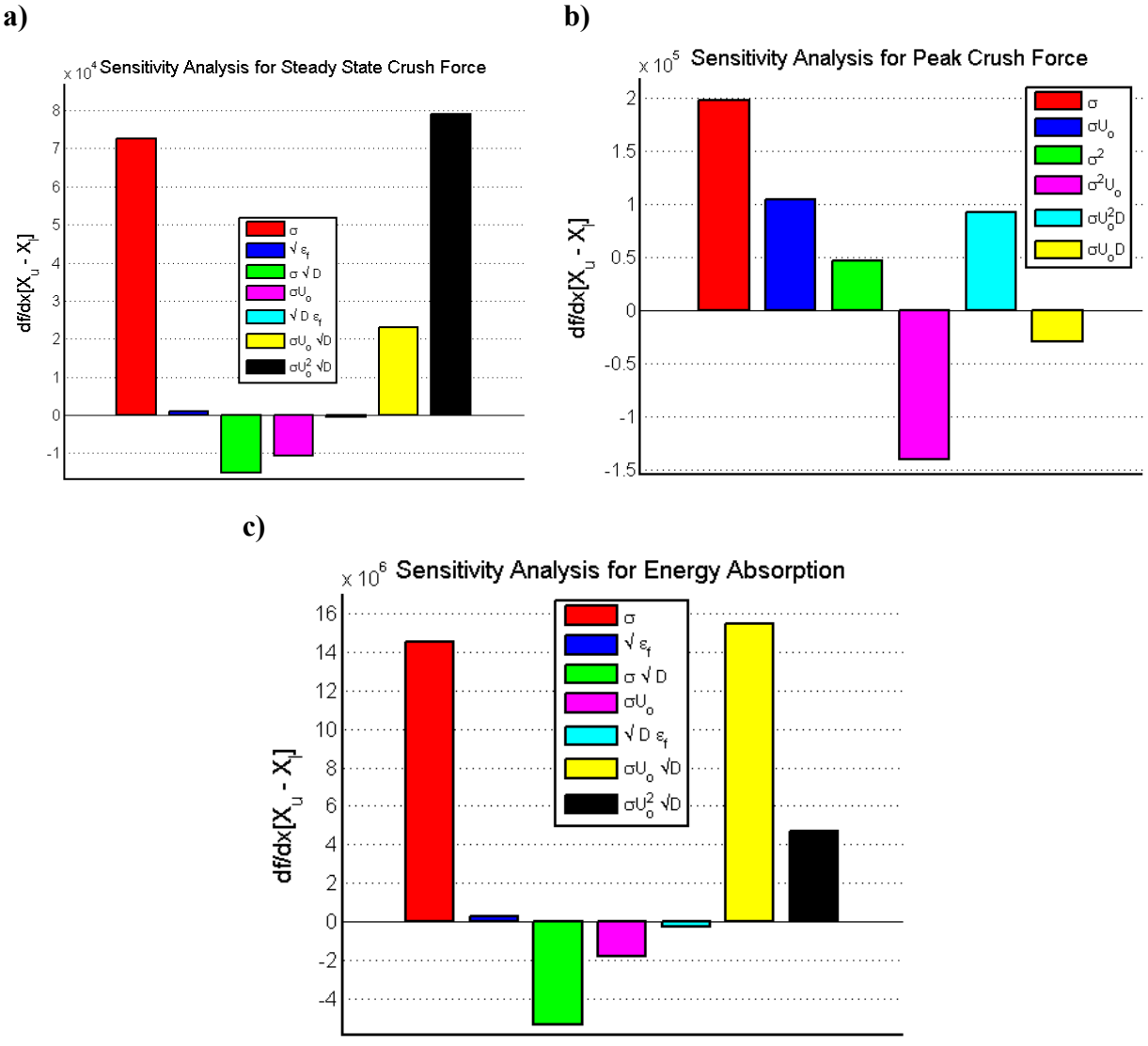

Figure 4.4 - Global Sensitivity Analysis for a) Steady State Crush Force, b) Peak Crush Force and c) Energy Absorption

4.5.4 Comparison of FE Model and Analytical Equation to Experimental Work

The experimental work presented by Williams *et al.* [14, 77] is employed in this research. In their work, dynamic axial crushing of hydroformed AA5754 aluminum tubes were performed where they used a 76.2mm [3.00"] × 76.2mm [3.00"] square crush tube with a 3.0mm wall thickness. The dynamic axial crushing was performed on a sled-track apparatus with two crush tubes per experiment. The mass and initial velocity of the sled was 1120kg and 7.0m/s respectively, while a mean corner radius of 6.00mm and the initial available crush length of 400mm were considered. A boss fixture was inserted 25mm deep on each end of the crush tube. The AA5754 aluminum alloy used in this study was characterized by performing uniaxial tensile testing on specimens that were cut out of hydroformed tubes [120]. Furthermore, the data was fit using a Voce plasticity law where

$$\sigma_y = 315 - 105\exp(-9.2\varepsilon^P) \qquad (4.23)$$

It should be mentioned that the pre-strain history (effects of the hydroforming) at 19% plastic strain are incorporated into the plasticity model. The stress-strain curve for AA5754 is presented in Figure 4.5. Results of the FE model (simulating the experimental setup shown in Williams *et al.* [14, 77]) are presented next.

In this model, a 1.50mm × 1.50mm × 1.50mm mesh is simulated and data is collected for a crush distance of 200mm. The experimental and simulated force-displacement and energy absorption responses are presented in Figure 4.6 and Figure 4.7. The raw simulation data is processed through a 1kHz SAE low pass filter to remove high frequency oscillations. The steady state crush force, peak crush force and energy absorption results from the numerical model and experiment, as well as the predictions with the analytical model, is presented in Table 4.8. The error, denoted as $\Delta\in$, between the simulation, analytical prediction and experiment is also presented in Table 4.8. The yield stress, ultimate tensile strength ratio, Voce hardening saturation coefficient and failure strain used in Equation 4.23 with the coefficients in Table 4.3 are 210MPa, 1.50, 9.20 and 1.21 respectively.

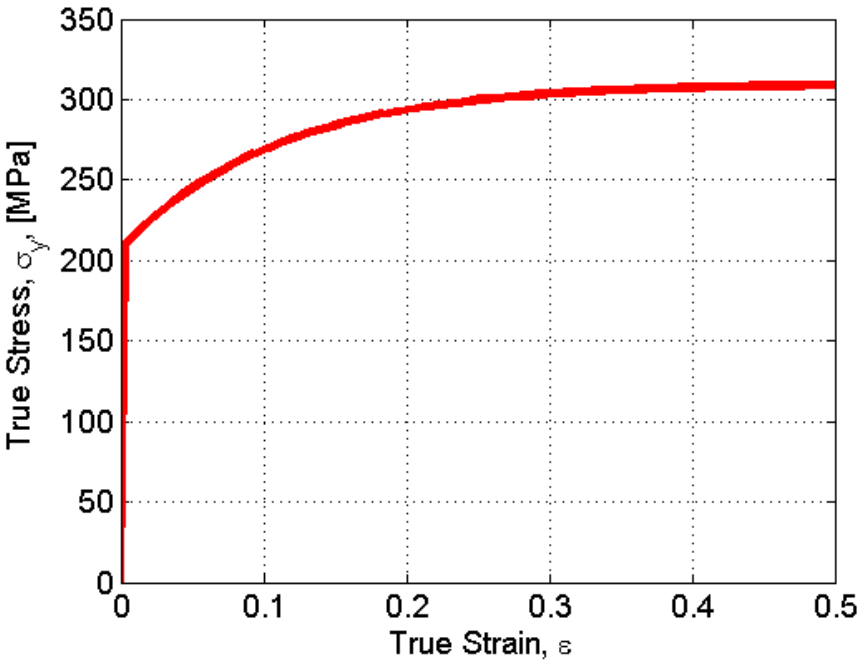

Figure 4.5 - True stress-true strain curve for AA5754 alloy [51, 14, 77]

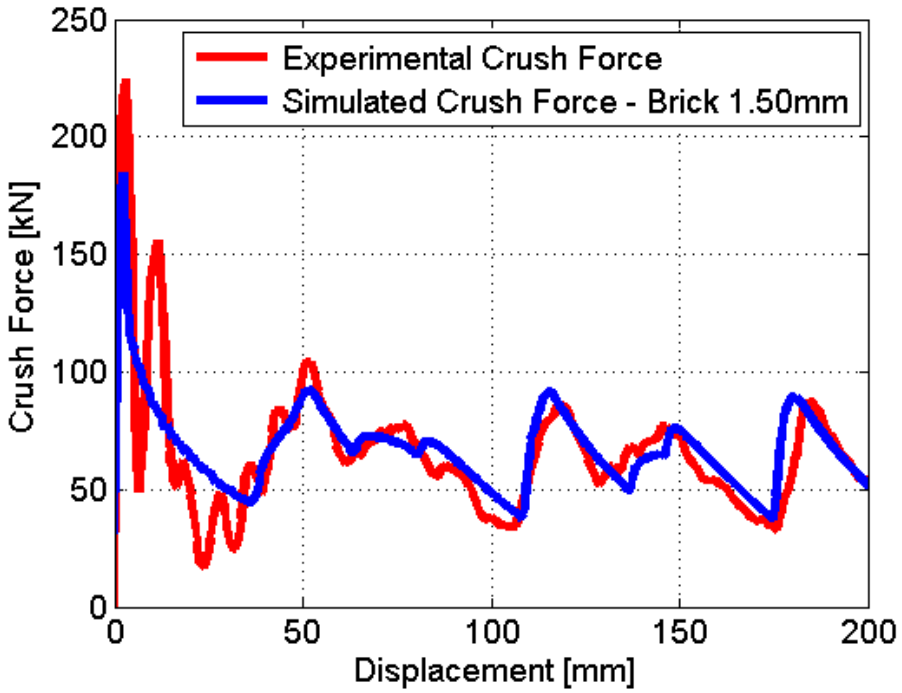

Figure 4.6 – Comparison of experimental [77] and simulated axial crush force-displacement response

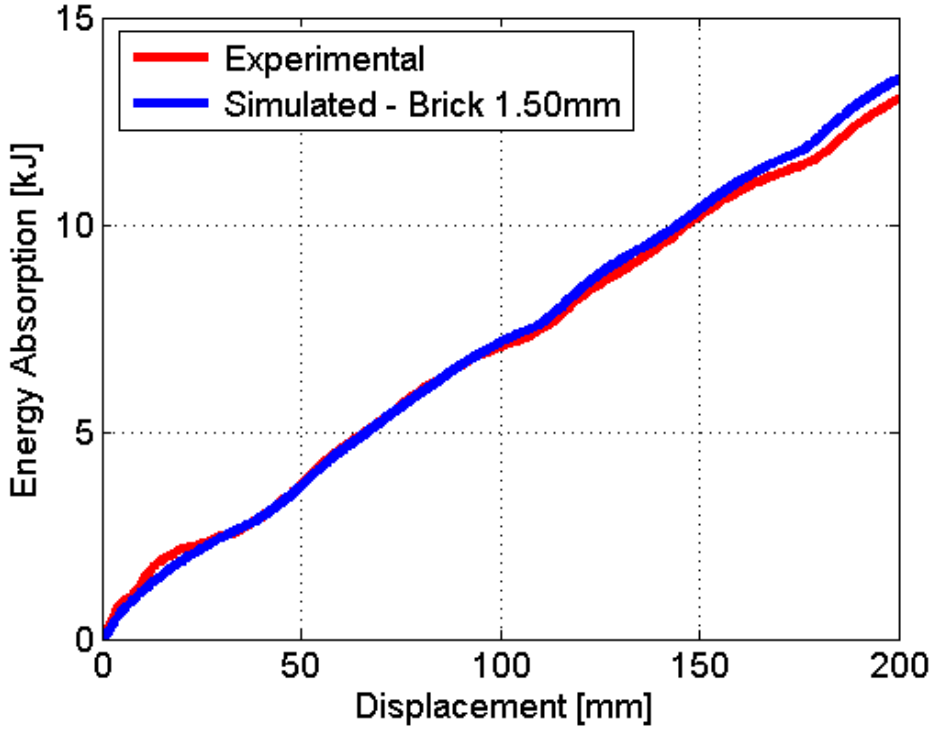

Figure 4.7 – Comparison of experimental [77] and simulated axial energy absorption response

Table 4.8 – Numerical and experimental results and error for steady state crush force, peak crush force, energy absorption and crush efficiency response

Response	Steady State Crush Force, F_{ss} [kN]	Peak Crush Force, F_{max} [kN]	Energy Absorption, E_{abs} [kJ]	Crush Efficiency
Exp.	65.13	224.30	13.026	0.290
Sim. Prediction	67.19	194.29	13.518	0.345
Analytical	64.22	197.74	13.821	0.325
$\Delta\in$ Exp. To Sim. (%)	3.16	13.38	3.78	5.50
$\Delta\in$ Exp. To Analytical (%)	1.40	11.84	6.10	3.50
$\Delta\in$ Sim. To Analytical (%)	4.42	1.78	2.24	2.00

The predictive error between the experimental and direct simulation steady state crushing force and energy absorption is 3.16% and 3.78% respectively. The oscillation of the experimental work can be attributed to mechanical ringing that is detected in the load cells from the testing apparatus. However, it is unlikely that this contributes significantly to the prediction error. The predictive error between the direct simulation and analytical steady crushing force and energy absorption is 4.42% and 1.78% respectively.

The predictive error between the experimental and direct simulation and analytical peak crushing force is 13.38 % and 11.84% respectively. The direct simulation and analytical equation under predicts the true experimental value, which contributes to the predictive error of the crush efficiency. This error can be caused by the pre-strain history of the experimental crush tube. It was shown in the work of Williams *et al.* [14, 77] that the forming history effects of the crush tube affected the energy absorption behaviour. Higher localized plastic strains of approximately 67% were observed in the corners of the crush tube compared to 19% in the main crush tube wall pre-crush and post hydroforming [14, 77]. A pre strain history of 67% plastic strain corresponds to a stress of 314.7MPa is required to cause yielding in the corners. This requires a larger peak crushing force to initiate folding of the corners during deformation. A pre strain of 19% plastic strain would require a stress of 210MPa to cause yielding. The FE Model assumes that the entire crush tube has the same pre-strain history of 19% plastic strain by using a yield stress of 210MPa. An initial reduction in the experimental force-displacement curve is observed at 25mm, which is more severe than the predicted force-displacement. This error can also be attributed to the pre-strain history of the experimental crush tube. During axial crush, the corners of the crush tube undergo the most plastic deformation. These higher initial pre-strains in the corners can lead to premature localized failure and a sudden reduction in the energy absorption rate, which is not captured in this FE model.

Even though there is minor deviation, the FE model predicts the period, valleys and peaks of the force-displacement curve with very good conformance to the experiment. The predicted and experimental crush patterns of the hydroformed square crush tube can be seen in Figure 4.8. This figure shows a symmetric deformation mode that was discussed previously and observed experimentally. The values obtained from direct simulation and the analytical equation show good agreement with the values calculated from experiment.

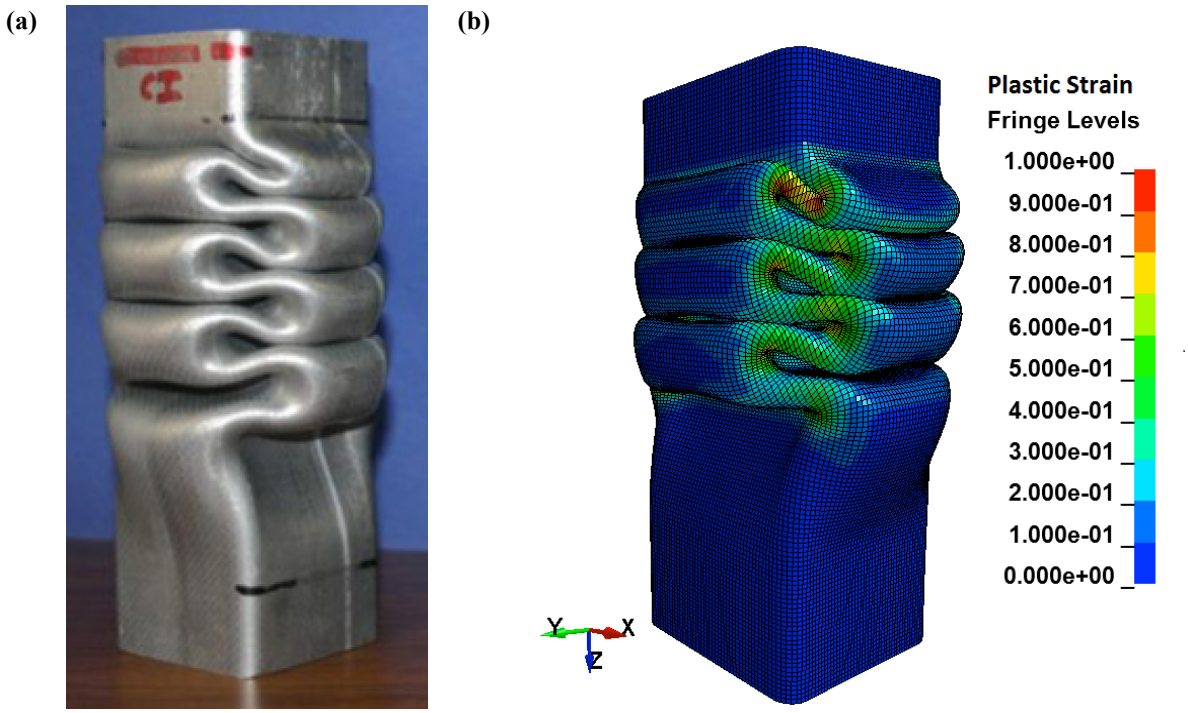

Figure 4.8 – (a) Experimental [77] and (b) predicted folding and plastic strain behavior of a hydroformed square crush tube

4.5.5 Comparison of Simulation Mesh Refinement to Experiment

Four meshes are presented to demonstrate the mesh convergence. The experimental and simulated force-displacement and energy absorption responses are presented in Figure 4.9 and Figure 4.10. The steady state crush force, peak crush force and energy absorption results from each numerical model and experiment is presented in Table 4.9. The simulation time and the number of elements are also presented in Table 4.9. Similar to the parameters presented above, the yield stress, ultimate tensile strength ratio, Voce hardening saturation coefficient and failure are 210MPa, 1.50, 9.20 and 1.21 respectively. The simulations all show good agreement with the experimental results. The difference in error between each simulation and the experiment is less than 2% for each level of mesh refinement. However, the computational requirements are significantly larger for the refined meshes for this difference. Thus, a mesh with 2 elements in the through thickness is sufficient for capturing the response of the crush tube for the level of accuracy achieved.

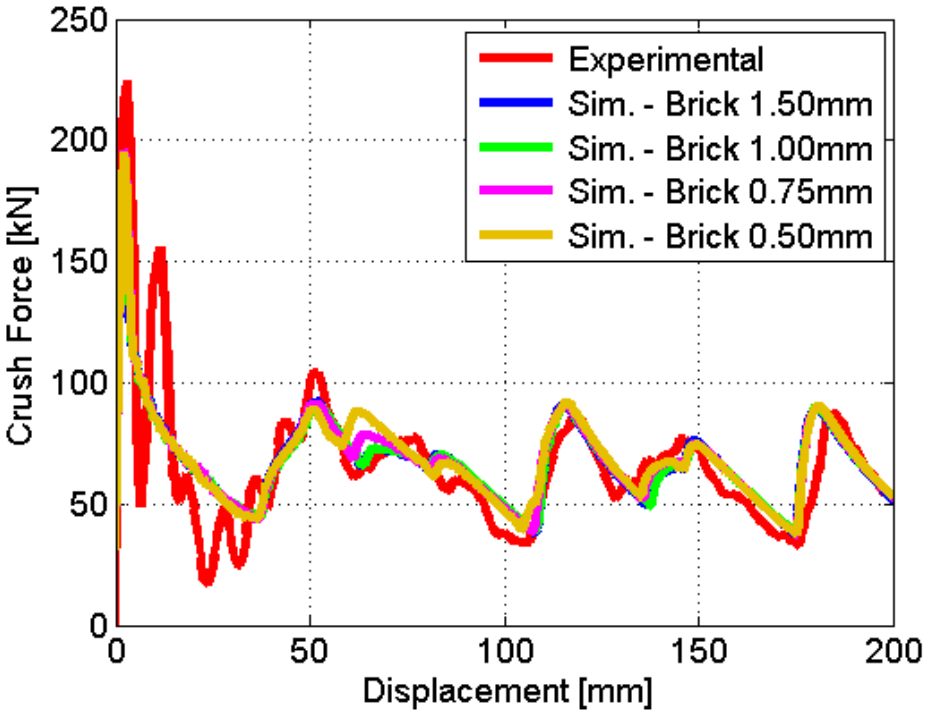

Figure 4.9 – Comparison of experimental [77] and simulated axial crush force-displacement response for different mesh refinements

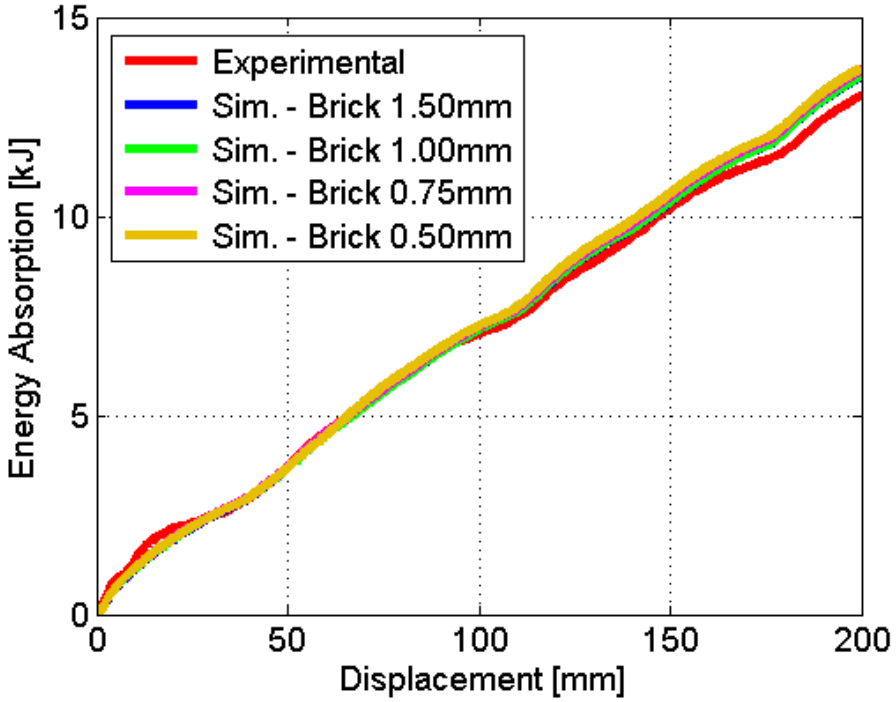

Figure 4.10 – Comparison of experimental [77] and simulated axial energy absorption response for different mesh refinements

Table 4.9 – Experimental and numerical results and error for steady state crush force, peak crush force, energy absorption and crush efficiency response for different mesh refinement

Response	Steady State Crush Force, F_{ss} [kN]	Peak Crush Force, F_{max} [kN]	Energy Absorption, E_{abs} [kJ]	Crush Efficiency	Simulation Time [hrs]	# of Elements
Exp.	65.13	224.30	13.026	0.290	- -	- -
1.50mm Sim.	67.19	194.29	13.518	0.345	2.133	102,528
1.00mm Sim.	67.40	195.44	13.547	0.348	10.85	336,000
0.75mm Sim.	68.26	195.53	13.675	0.349	32.30	801,630
0.50mm Sim.	68.68	194.37	13.728	0.353	194.25	2,668,000
$\Delta\in$ Exp. To 1.50mm Sim. (%)	3.16	13.38	3.78	5.50	- -	- -
$\Delta\in$ Exp. To 1.00mm Sim. (%)	3.47	12.86	3.78	5.53	- -	- -
$\Delta\in$ Exp. To 0.75mm Sim. (%)	4.84	12.82	4.98	5.54	- -	- -
$\Delta\in$ Exp. To 0.50mm Sim. (%)	5.44	13.34	5.39	5.58	- -	- -

4.5.6 Comparison of Brick/Shell Elements Simulations to Experiment

Two additional FE simulations with a 1.50mm × 1.50mm mesh using two common type of shell elements are presented: the Belytschko-Lin-Tsay (BLT) and the fully integrated (FI) scheme. The BLT elements and FI elements are implemented as ELFORM = 2 and ELFORM = 16 for *ELEMENT_SHELL in LS-DYNA. In each shell element formulation, seven integration points are used in the through thickness direction. Similar material parameters and experimental setup are used as discussed above. The experimental and simulated force-displacement and energy absorption responses are presented in Figure 4.11 and Figure 4.12. The steady state crush force, peak crush force and energy absorption predictions from the numerical models and experiment, are presented in Table 4.10. The simulation time and number of elements are also presented and compared in Table 4.10.

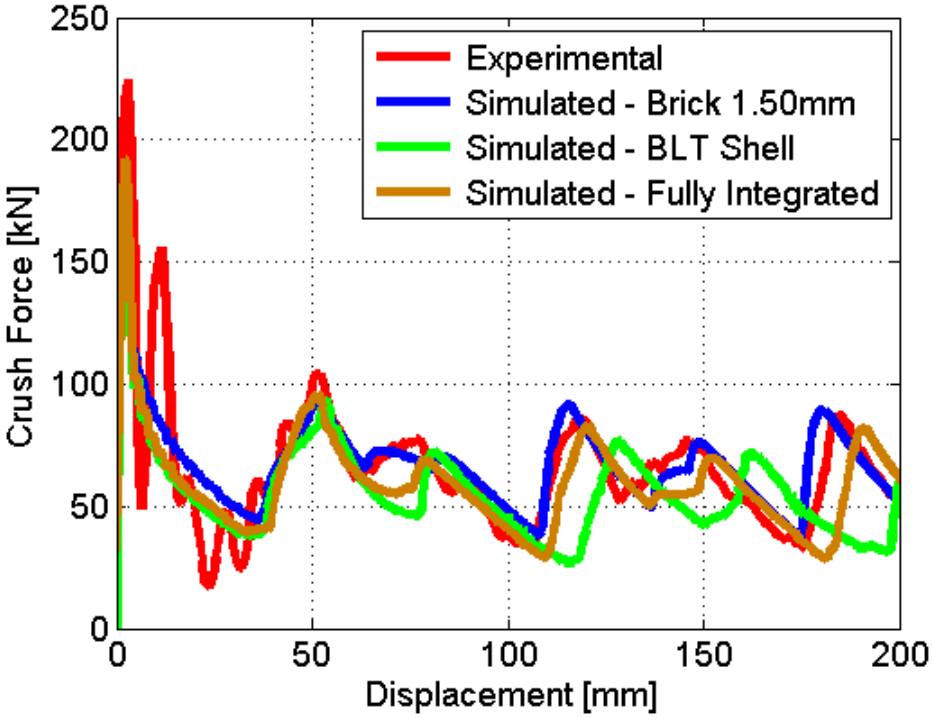

Figure 4.11 – Comparison of experimental [77] and simulated axial crush force-displacement response for different element formulations

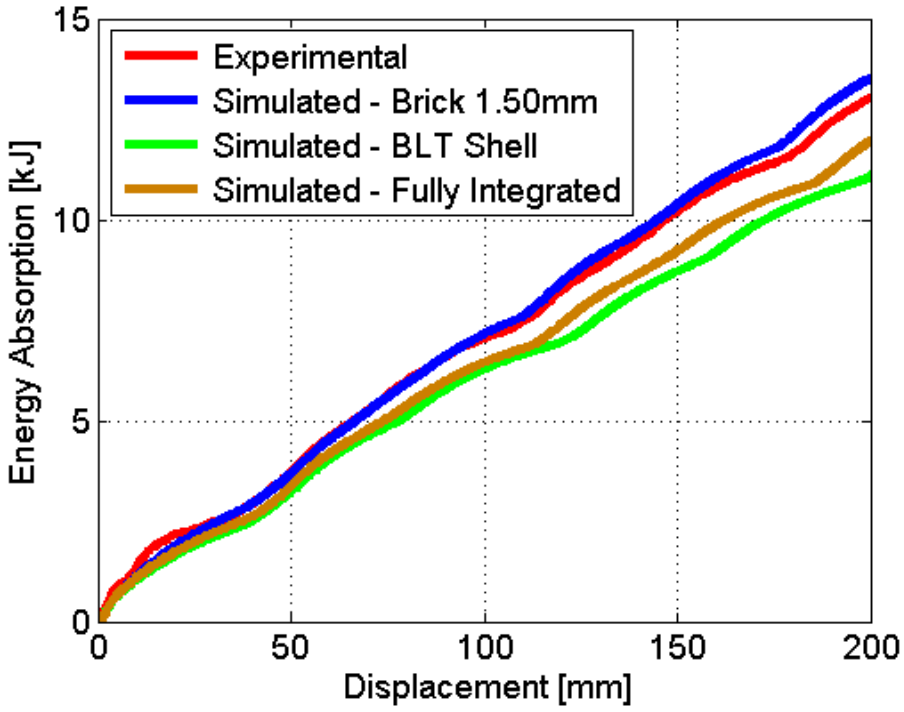

Figure 4.12 – Comparison of experimental [77] and simulated axial energy absorption response for different element formulations

Table 4.10 - Experimental and numerical results and error for steady state crush force, peak crush force, energy absorption, crush efficiency response and simulation time for different element formulations

Response	Steady State Crush Force, F_{ss} [kN]	Peak Crush Force, F_{max} [kN]	Energy Absorption, E_{abs} [kJ]	Crush Efficiency	Simulation Time [minutes]	# of Elements
Experimental Result	65.13	224.30	13.026	0.290	- -	- -
Brick 1.50mm	67.19	194.29	13.518	0.345	128	102,528
BLT Shell: 1.50mm	55.87	173.37	11.154	0.265	52	28,800
FI Shell: 1.50mm	59.72	191.77	12.006	0.283	56	28,800
$\Delta\in$ Exp. To 1.50mm Brick Sim. (%)	3.16	13.38	3.78	5.50	- -	- -
$\Delta\in$ Exp. To 1.50mm BLT Shell Sim. (%)	14.23	22.71	14.37	3.50	- -	- -
$\Delta\in$ Exp. To 1.50mm FI Shell Sim. (%)	8.30	14.50	7.83	0.70	- -	- -

Upon analysis of the force-displacement responses, the BLT simulation begins to deviate from the response at approximately 100mm. The fully-integrated solution maintains a better force-displacement response than the BLT response, but begins to deviate from the experimental response at approximately 175mm. Although the 1.50mm brick element simulation requires almost twice the amount of computational resources, the shell element responses all under predict the energy absorption response and mean crush force when compared to the brick element simulation. This is a result of neglecting the work dissipation that is developed in the through thickness direction. Therefore, using a 1.50mm x 1.50mm x 1.50mm mesh size is sufficient for the performed analysis.

4.6 Discussion

In this section, the proposed analytical expressions are employed to systematically evaluate the effects of the elastic-plastic behaviour of the material on the axial crush response of tubes. A framework for performing energy absorption optimization is also presented to determine the optimal set of material parameters.

4.6.1 Effects of Yield Stress and Ultimate Tensile Strength Ratio Interaction

The effect of yield stress and ultimate tensile strength ratio on the steady state crushing force, peak crushing force, energy absorption and crush efficiency responses are presented as a three-dimensional surface response in Figure 4.13. These figures are generated using Equation

4.8 - 4.12 with the coefficients in Table 4.3. The failure strain and the Voce hardening saturation coefficient are held constant at 1.400 and 14.00 respectively.

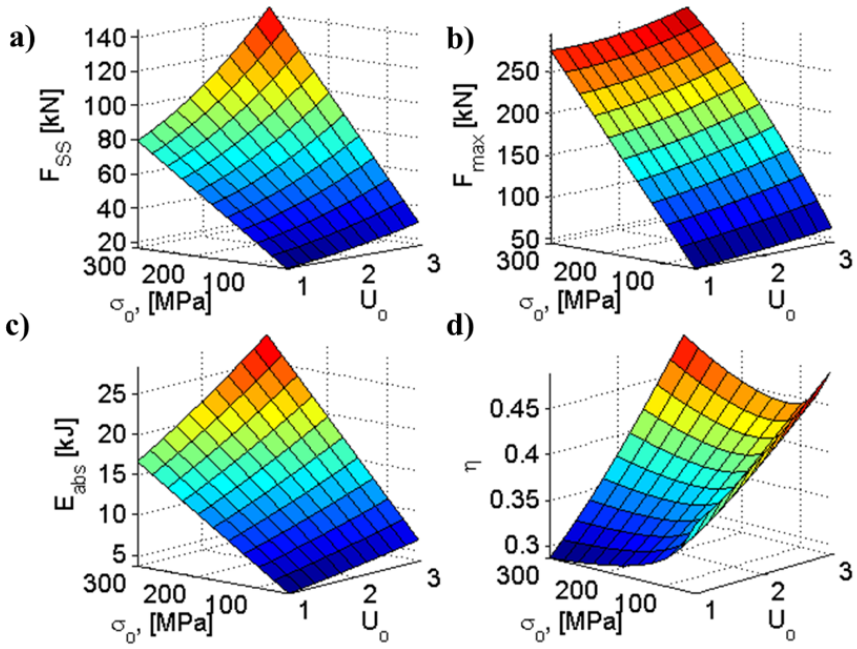

Figure 4.13 – Effects of σ_0 and U_0 on the (a) steady state crush force (b) peak crush force (c) energy absorption (d) crush efficiency response for ε_f = 1.400 and D = 14.0 using a 3-dimensional response plot

Two-dimensional plots are used to simplify the analysis and discussion. Figure 4.14 presents the two-dimensional plot of the effect of yield stress and ultimate tensile strength ratio on energy absorption characteristics. Large gains are obtained for the steady state crush force, peak crush force, and energy absorption by increasing the yield stress. When the structure yields due to compression, the structure enters the instability mode of deformation and transitions to bending and forms the plastic hinge. While the material is bending, the material begins to work harden towards the ultimate tensile strength to resist the collapse. The higher the ultimate tensile strength ratio, the more work hardening must be performed by the structure to complete the bend. This results in an increase in the ultimate tensile strength ratio that yields to a positive shift and scaling in the steady state crushing force and energy absorption. When both the yield stress and ultimate tensile strength ratio are increased, larger gains can be obtained by increasing only one parameter alone. However, the ultimate tensile strength ratio has a moderate interaction effect with the yield stress on the peak crushing force.

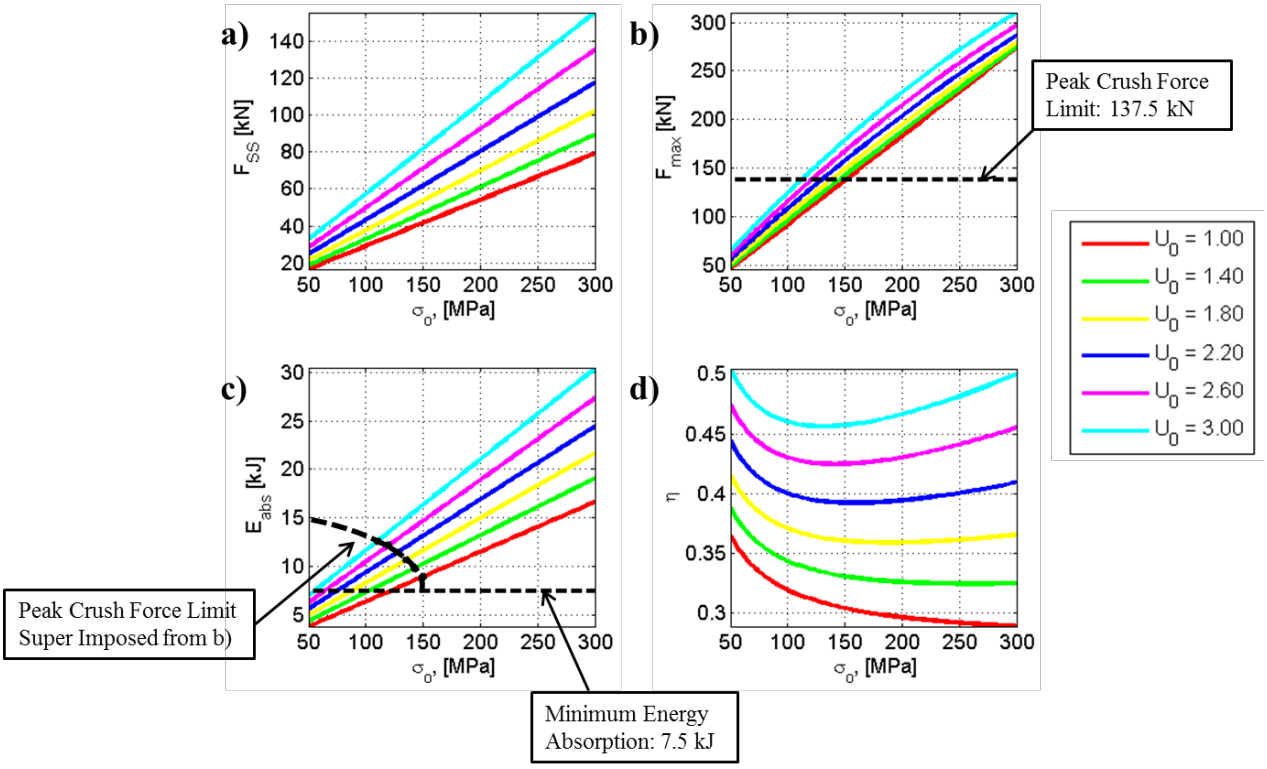

Figure 4.14 - Effects of σ_0 and U_0 on the (a) steady state crush force (b) peak crush force (c) energy absorption (d) crush efficiency response for $\varepsilon_f = 1.400$ and D = 14.0

The minimum energy absorption constraint of 7.50kJ is also plotted in Figure 4.14. This forms the lower threshold for the acceptable energy absorption for material selection. The minimum allowable yield stress is 105MPa for a material with an elastic-perfect plastic behaviour ($U_0 = 1$). This means that any material with yield stress higher than 105MPa satisfies this constraint, regardless of the hardening rate or ultimate tensile strength. In other words, a material has a very low yield stress and very little work hardening to the ultimate tensile strength, i.e., $\sigma_0 = 75$MPa and $U_0 = 1.0$, does not satisfy the energy absorption criteria. However, a material with a low yield stress and significant work hardening to the ultimate tensile strength, i.e., $\sigma_0 = 75$MPa and $U_0 = 2.5$, can satisfy this constraint.

The maximum allowable peak crush force of 137.3kN is also plotted in Figure 4.14. Points are indicated on the energy absorption curves showing the limit of energy absorption that can be satisfied the imposed constraint on the peak force. A line is drawn through the points to indicate the maximum energy absorption that satisfies the peak crushing force constraint. From this line, it is observed that the maximum energy absorption that can be absorbed while

satisfying the maximum crush force limitation drops rapidly as the yield stress is increased. The analyses show that increasing the ultimate tensile strength ratio and decreasing the yield stress will increase the energy absorption capability of the structure (satisfying the imposed constraint). It is important to note that this observation is independent of the peak crushing force constraint imposed. This means that when a constraint is imposed on the peak crushing force, materials with a low yield stress that have significant work hardening capabilities outperform materials with a high yield stress and very little work hardening. This trend leads to the positive shift observed in the crush efficiency when the ultimate tensile ratio is increased, while the yield stress is decreased.

An important observation is that an inflection point exists in the crush efficiency. When the yield stress is low, the crush response will generally have higher crush efficiency. As the yield stress increases from a lower value, the crush efficiency decreases. With a lower ultimate tensile strength ratio, increasing the yield stress of the material continues to reduce the crush efficiency. This means that there exists a trade-off between crush efficiency and energy absorption when the material exhibits low hardening capability. This trade-off exists due to the higher sensitivity of the yield stress in the peak crush force formulation compared to the steady state crush force formulation, which can be used to develop new alloys for axial crush. However, if the material exhibits large hardening capability, the crush efficiency of the structure improves. Transformation-induced plasticity (TRIP) and twinning-induced plasticity (TWIP) steels are examples of new lightweight alloys that are capable of such desired stress-strain behaviours [121, 122]. This means that a material with a low yield stress and higher hardening capability will have better crush efficiency. The lower yield stress results in a dampened response in the peak crush force, while the larger ultimate tensile strength results in higher crush force and energy absorption potential.

Figure 4.15 presents the effects of the ultimate tensile strength on the predicted final deformed crush tube and plastic strain distribution. Figure 4.15a-b present a crush tube where the ultimate tensile strength ratio is 1.00 and 3.00 respectively while the yield stress, failure strain and Voce hardening saturation coefficient are 300MPa, 1.400, and 14.00 respectively. When the ultimate tensile strength ratio is lower, larger plastic strains develop in the corners of the crush tube during deformation. This can lead to onset of failure earlier within the structure

during crushing. When the ultimate tensile strength ratio is lower, very little work hardening is present during deformation. Once the plastic hinge has completely folded and is self-contacting, the structure becomes stiff enough to initiate the next fold. This results in a more compact final folding pattern. When the ultimate tensile strength ratio is higher, as the material work hardens, the plastic hinge becomes stiffer, which initiates the next fold without fully completing the fold. Fewer folds also have to be developed because the additional work hardening dissipates more energy than plastic hinging alone.

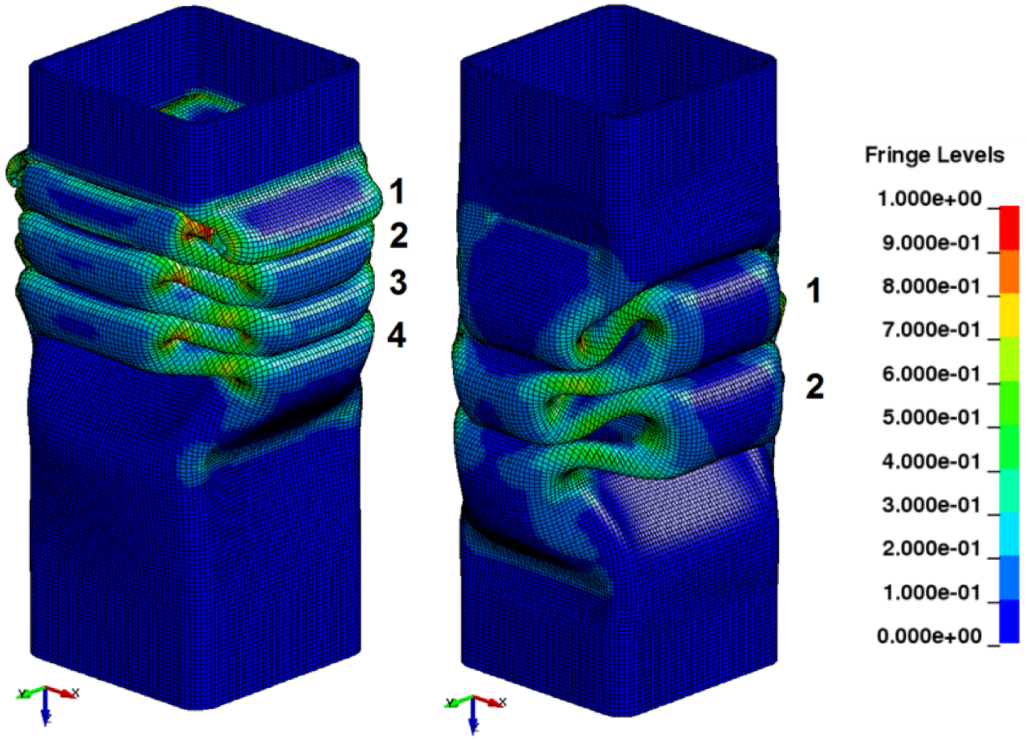

Figure 4.15 - Effects of ultimate tensile strength: Predicted folding and plastic strain behavior for (a) U_0= 1.00, (b) U_0= 3.00 with σ_0=300MPa, ε_f = 1.400 and D = 14.0

4.6.2 Effects of Voce Hardening Saturation Coefficient

The effect of the yield stress and the Voce hardening saturation coefficient on the steady state crushing force, peak crushing force, energy absorption and crush efficiency responses are presented in Figure 4.16. The failure strain and the ultimate tensile stress ratio are held constant at 1.40 and 2.00 respectively. The effect of ultimate tensile stress ratio and the Voce hardening saturation coefficient is also investigated Figure 4.17). The failure strain and the yield stress are held constant at 1.40 and 200MPa respectively. By analyzing the data presented in Figure 4.16 -

Figure 4.17, it is understood that the Voce hardening has a strong interaction with the ultimate tensile strength ratio and a moderate interaction with the yield stress. When the Voce hardening parameter is higher, the stress developed within the plastic hinge will approach the ultimate tensile strength faster, which results in more work hardening and better energy dissipation. The peak crush force shows a very low sensitivity to the Voce hardening parameter when varied alone. However, it shows a strong sensitivity when varied with the ultimate tensile strength ratio. When the Voce hardening parameter is higher, the material hardens quicker to the new yield stress, which approaches and saturates towards the ultimate tensile stress. This means the force needs to increase to compensate for the rapid work hardening to initiate the first fold. This results in a moderate positive shift outward in the crush efficiency that is similar to the shift due to the ultimate tensile strength ratio.

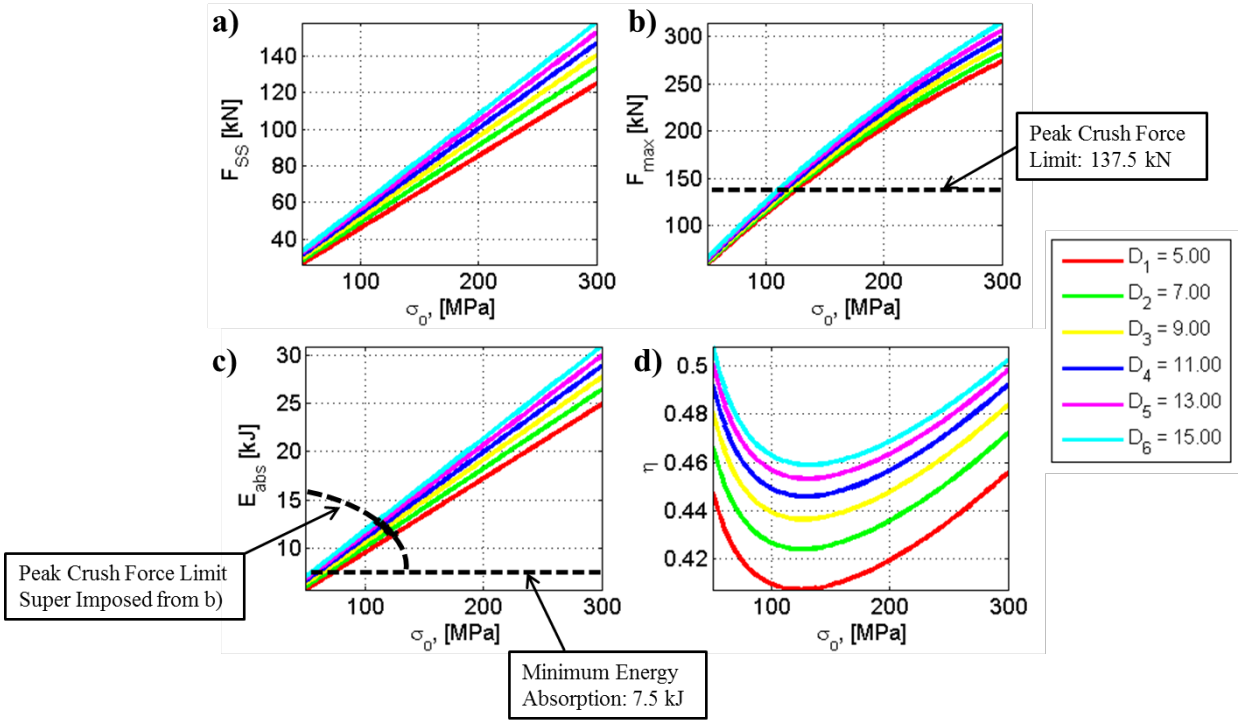

Figure 4.16 - Effects of σ_0 and D on the (a) steady State Crush Force (b) Peak Crush Force (c) Energy Absorption (d) Crush Efficiency Response for $\varepsilon_f = 1.400$ and $U_0 = 3.00$

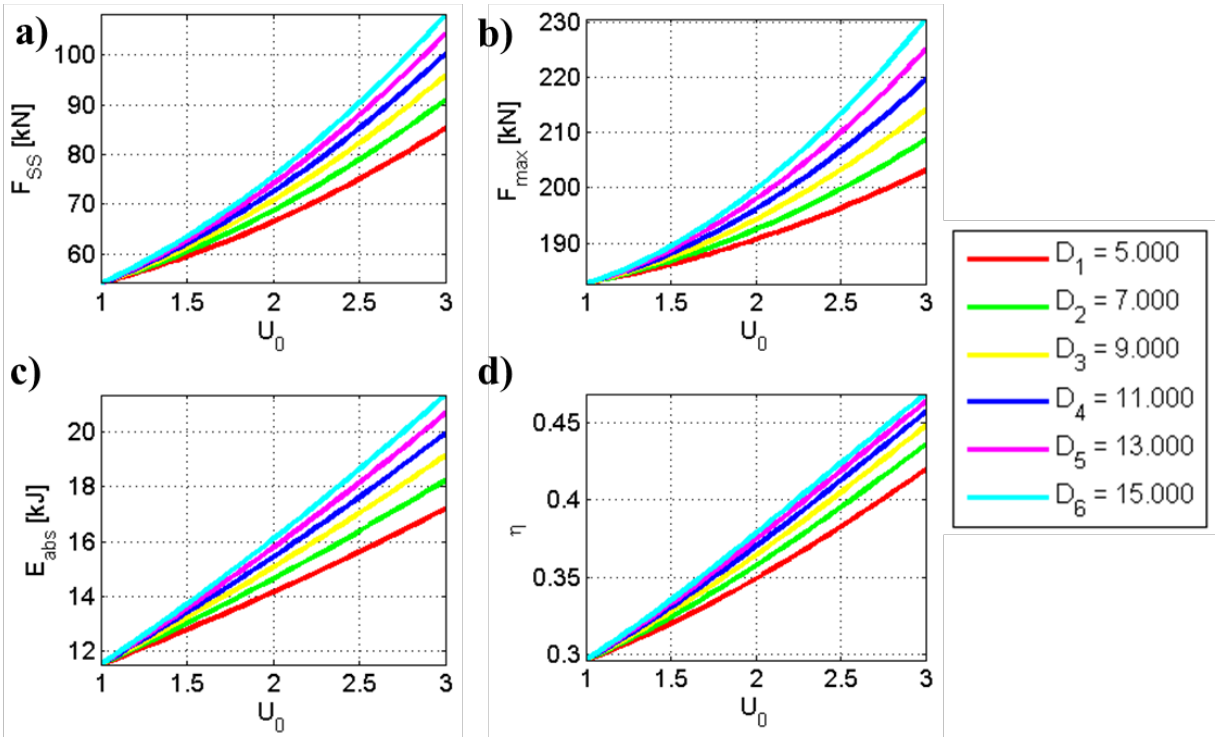

Figure 4.17 - Effects of U_0 and D on the (a) steady state crush force (b) peak crush force (c) energy absorption (d) crush efficiency response for $\varepsilon_f = 1.400$ and $\sigma_0 = 200$MPa

Figure 4.18a-b shows the effects of the Voce hardening saturation coefficient on the predicted final deformed crush tube and plastic strain where the Voce hardening saturation coefficient is 5.00 and 15.00 respectively. The yield stress, ultimate tensile stress ratio, and failure strain are 300MPa, 2.00, and 1.400 respectively. Similar folding patterns are observed during the deformation. In Figure 4.18a, the fourth fold that is further developed than the fourth fold in Figure 4.18b. This means that the crushing mass has collapsed the crush tube more when the Voce hardening saturation coefficient is lower. This is caused by lower work hardening that results in lower energy absorption.

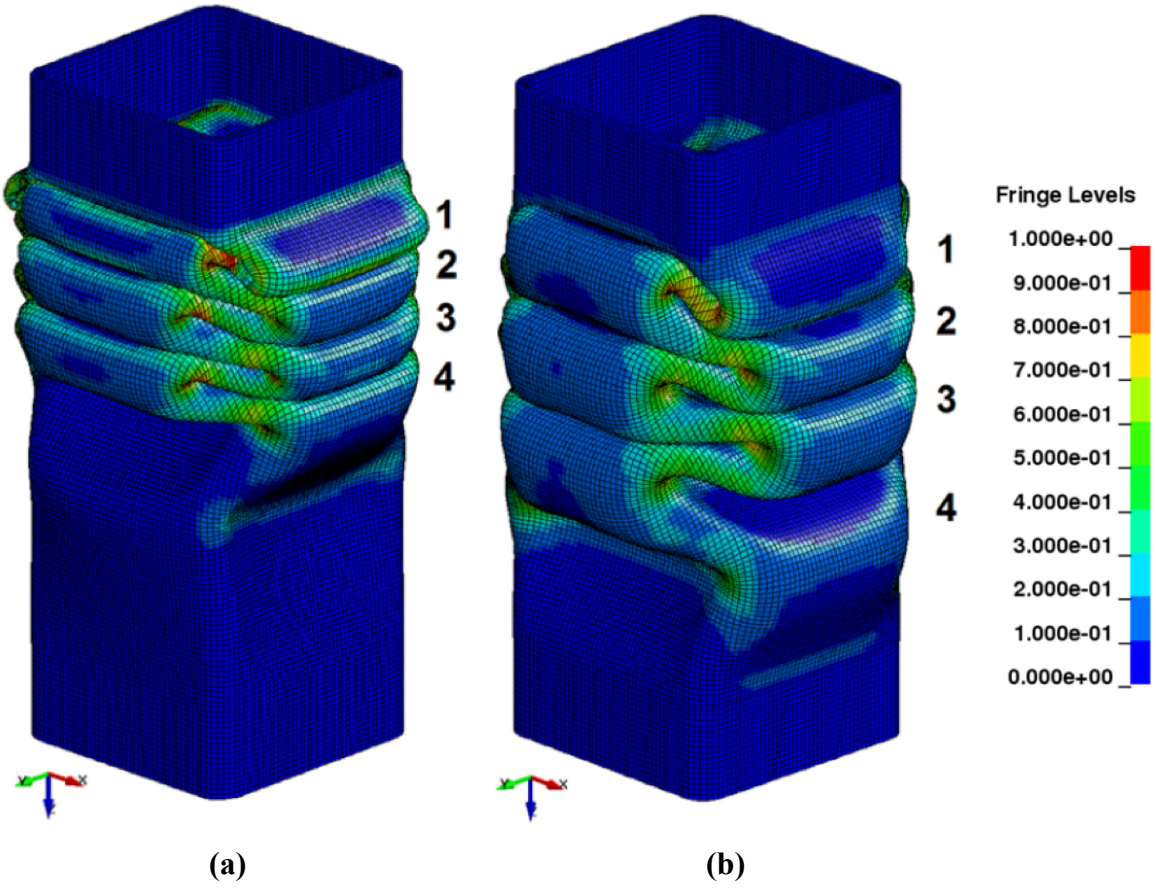

(a) **(b)**

Figure 4.18 - Effects of Voce hardening saturation parameter: Predicted folding and plastic strain behavior for (a) D= 5.00, (b) D= 15.00 with σ_0=50MPa, ε_f = 1.400 and U_0 = 3.0

4.6.3 Effects of Ultimate Tensile Stress Ratio and Failure Strain Interaction

Figure 4.19 presents the effect of ultimate tensile strength ratio and failure strain on the steady state and peak crushing force, energy absorption and crush efficiency. The yield stress and Voce hardening saturation coefficient are held constant at 50.00MPa and 15.00 respectively. The analysis shows that increasing the yield stress increases the steady state crush force, peak crush force, and energy absorption. When the failure strain is higher, the steady state crushing force and the average energy absorption increases. Increasing the failure strain allows local regions of large plasticity, such as the structure corners, to continue to absorb energy. It also allows the structure to remain stiff enough to trigger the next fold (Figure 4.20). The peak crush force shows no response to the failure strain. This means the positive increase in the energy absorption and steady state crushing force result in a positive increase in the crushing efficiency.

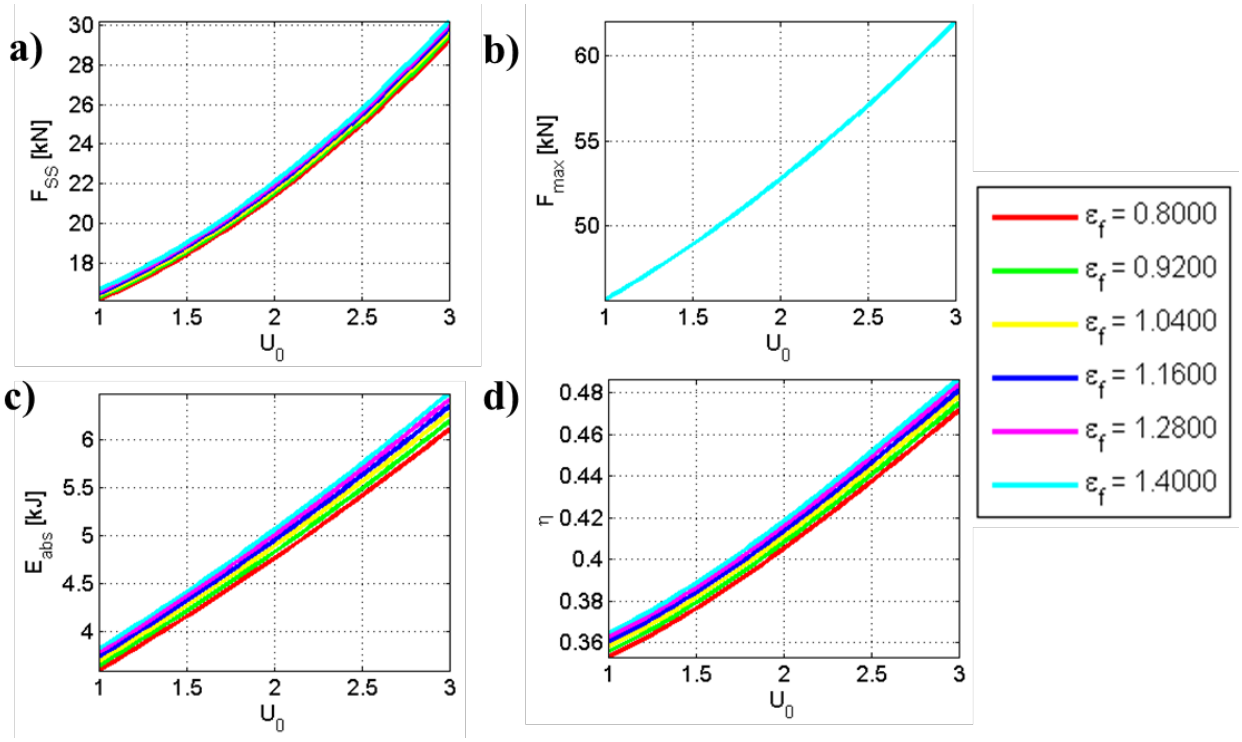

Figure 4.19 - Effects of U_0 and ε_f on the (a) steady state crush force (b) peak crush force (c) energy absorption (d) crush efficiency response for D = 10.00 and σ_0 = 50.00MPa

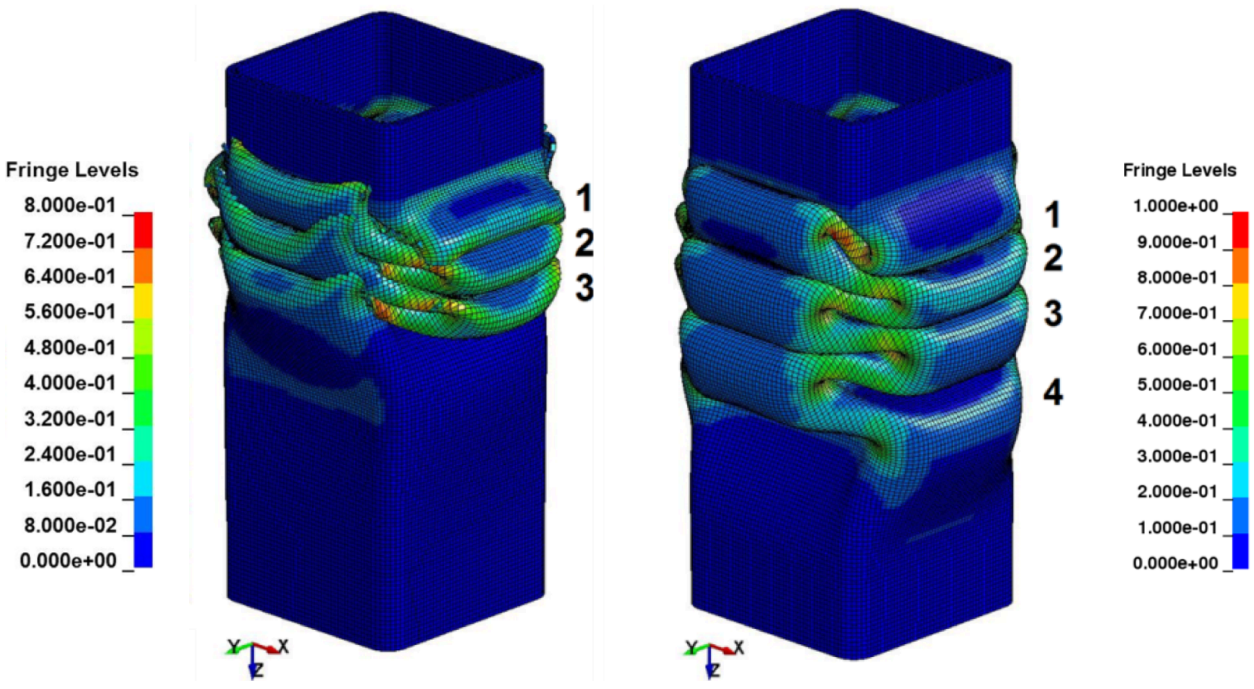

Figure 4.20 - Effects of failure strain: Predicted folding and plastic strain behavior for (a) ε_f= 0.860, (b) ε_f= 1.400 with *D*= 15.00 with σ_0=50MPa, *D*= 15.00 and U_0 = 2.20

4.6.4 Material Parameters for Optimal Crashworthiness Characteristics

Each surface response is evaluated within the domain to determine a set of parameters for optimal crashworthiness. Each material parameter is divided into 100 increments within the range and evaluated for the respective function. A gradient ascent/descent algorithm is employed to find the optimal set of parameters. Gradient descent uses a first and second order derivative approximation of the functions, such that [97]

$$\frac{\partial y_i}{\partial x_j} = 0; \quad \frac{\partial^2 y_i}{\partial x_j \partial x_k} = 0 \qquad (4.24)$$

These gradients are calculated using analytical or finite difference methods [87]. The Gauss-Newton method presented in Section 2.3.1.2. is a form of gradient descent optimization that minimizes the error in of a function. A similar formulation is employed for maximization of a function. The objective of the optimization is to minimize the peak crush force and maximize the steady state crush force, energy absorption and crush efficiency;

$$\max(\boldsymbol{F_{ss}});\ \min(\boldsymbol{F_{max}});\ \max(\boldsymbol{E_{abs}});\ \max(\boldsymbol{\eta_{ss}}) \qquad (4.25)$$

Table 4.11 presents the material parameters for unconstrained optimal crashworthiness characteristics. This means that no constraint is imposed on the allowable peak crush force and minimum energy absorption.

Table 4.11 - Material Parameters for Unconstrained Optimal Crashworthiness Characteristics

Optimization Objective	Optimal Steady State Crush Force, F_{ss}	Optimal Peak Crush Force, F_{max}	Optimal Energy Absorption, E_{abs}	Optimal Crush Efficiency, η
Steady State Crush Force, F_{ss} [kN]	**161.7**	**16.1**	**161.7**	**161.7**
Peak Crush Force, F_{max} [kN]	**314.4**	**45.7**	**314.4**	**314.4**
Energy Absorption, E_{abs} [kJ]	**31.2**	**3.60**	**31.2**	**31.2**
Crush Efficiency, η	**0.5145**	**0.3513**	**0.5145**	**0.5145**
σ_0 [MPa]	**300**	**50**	**300**	**300**
U_0	**3.000**	**1.001**	**3.000**	**3.000**
D	**15.000**	**5.00**	**15.000**	**15.000**
ε_f	**0.800**		**0.800**	**0.800**

No value is presented for the strain at uniform elongation for the peak crush force because the response is not dependent on the parameter. This optimization strategy leads to trivial results for the steady state crush force, energy absorption, and crush efficiency; the upper limit of the yield

stress, ultimate tensile strength to the quasi-static yield stress ratio, and hardening rate produces the highest energy absorbing characteristics. On the other hand, the lower limit of these parameters produces the lowest peak crush force.

Table 4.12 presents the material parameters for constrained optimal crashworthiness characteristics. Constraints are imposed on the allowable peak crush force and minimum energy absorption, such that;

$$\boldsymbol{F_{ss}} < 137.5kN\ ;\ \boldsymbol{E_{abs}} > 7.5kJ \qquad (\ 4.26\ )$$

The optimization produces two sets of material parameters for the four unique objectives. In each objective, the hardening rate and the ultimate tensile strength to the quasi-static yield stress ratio are the upper limits. The steady state crush force and energy absorption produce a similar set of material parameters because these responses have similar functionality. These two functions are limited by the peak allowable crush force. The peak crush force response and crush efficiency produce similar material properties. Even though the crush efficiency is a function of the steady state response, minimizing the peak crush force has a stronger influence. Furthermore, the optimal crush efficiency is the lower bound of the yield stress, which agrees with the findings of Jones [109].

Table 4.12 - Material Parameters for Constrained Optimal Crashworthiness Characteristics

Optimization Objective	Optimal Steady State Crush Force, F_{ss}	Optimal Peak Crush Force, F_{max}	Optimal Energy Absorption, E_{abs}	Optimal Crush Efficiency, η
Steady State Crush Force, F_{ss} [kN]	**63.3**	**35.4**	**63.2**	**35.4**
Peak Crush Force, F_{max} [kN]	**137.2**	**71.4**	**137.2**	**71.4**
Energy Absorption, E_{abs} [kJ]	**12.5**	**7.50**	**12.8**	**7.50**
Crush Efficiency, η	**0.461**	**0.496**	**0.460**	**0.496**
σ_0 [MPa]	**110**	**55**	**110**	**55**
U_0	**3.000**	**2.980**	**3.000**	**3.000**
D	**15.000**	**14.900**	**15.000**	**15.000**
ε_f	**0.800**		**1.4000**	**1.400**

4.7 Chapter Conclusions

In this chapter, the effects of elastic-plastic behaviour of lightweight alloys on the energy absorption characteristic of axial crush square tubes were analyzed. The steady state crushing

force of the crush tube was introduced to describe the constant crushing force profile observed after initial loading and to develop the component level crush efficiency. The yield strength, yield strain, ultimate tensile strength, hardening rate, and failure strain of a material were used to develop analytical equations for predicting the energy absorption, peak crush force, steady state crushing force and crush efficiency. The rate sensitivity parameters were fixed to study the response of aluminum-type alloys in axial crush. The analytical equations were calibrated to numerical simulations produced by axial simulations. Furthermore, a material selection framework was developed by using the analytical equations and imposing minimum energy absorption and maximum peak crushing force constraints. The analytical equation and numerical simulations developed showed good agreement with experimental data. A systematic study was carried on with the analytical equations and the predictions concluded that:

- The elastic-plastic material behaviour is critical to understanding the energy absorption characteristics of axial crush.
- Increasing the yield stress increases the energy absorption, peak crush force and steady state crush force.
- The ultimate tensile strength, hardening rate and the yield stress together have a strong positive effect on the energy absorption characteristics, while the failure strain has a weak contribution to the energy absorption characteristics of axial crush.
- Peak crushing force is more sensitive to the yield stress than the steady state crushing force.
- Increasing the yield stress results in a decrease in the crush efficiency when the hardening capabilities of the material are low; a trade-off exists between energy absorption and crush efficiency in terms of yield stress.
- Increasing the yield stress results in an increase in the crush efficiency when the hardening capabilities of the material is higher
- Imposing constraints on the peak crushing force results in lightweight alloys with a low yield stress that have significant work hardening capabilities outperform materials with a high yield stress and very little work hardening with respect to energy absorption.

5 THE EFFECTS OF THE YIELD SURFACE CURVATURE AND ANISOTROPY CONSTANTS ON THE AXIAL CRUSH RESPONSE OF CIRCULAR CRUSH TUBES – C.P. Kohar, M. Mohammadi, R.K. Mishra and K. Inal (2016). Thin-Walled Structures, 106, p 28-50.

This chapter presents an investigation on the effects of yield surface curvature and anisotropy constants on axial crush response. The yield function proposed by Plunkett, Cazacu, and Barlat. (2008) with two linear transformations, known as CPB06ex2, is employed in the commercial finite element software LS-DYNA to predict the crush response of the aluminum alloy AA5754-O circular tubes. This yield function represents anisotropy of aluminum alloys accurately by simultaneously capturing the variation of both the yield stress and the R-value with orientation. Dynamic crush simulations of tubes are performed using this yield function with four different yield surface shapes. The same sets of experimental uniaxial yield stresses and R-values along with various sample orientations are considered for determining the anisotropy coefficients of the yield function for each case (the coefficients are different even though the input experimental data is the same). Simulations of axial crush show that the yield surface shape affects the collapse mode and predicted energy absorption characteristics of the crush tube. The analysis shows that the deformation is predominately controlled by balanced biaxial deformation. However, characterization of both the plane strain and pure shear points on the yield surface for energy absorption are also important. The shape and the area of the yield function govern the loading condition, which dictates the deformation and energy absorption. The results demonstrate the importance of the shape of the yield surface in axial crush simulations of structural components using aluminum. The results of this work have been published in Kohar et al. [16].

5.1 Introduction

A significant amount of work has been presented in the literature for numerical modeling of axial crush with different yield surfaces and hardening rules (i.e., [80, 123, 124, 125, 104]. In particular, Williams *et al.* [14] investigated the effects of anisotropy on the response of hydroformed square aluminum tubes. They used the Yld2000 yield function and determined the material anisotropy parameters by experimental data and concluded that including the material anisotropy improved their predictions. However, there is no research in literature that

systematically investigates the influences of yield surface shape on the axial crush response. Multiple yield surfaces can be obtained that captures the anisotropy of the material obtained from experiment (as was shown for FLDs in Ref [126]). Furthermore, no work has been presented to understand the individual effects of the biaxial yield stress, yield stress and R-values on the crashworthiness response.

In this chapter, the effects of the yield surface shape (curvature) on the predicted crush response are investigated. The yield function proposed by Plunkett *et al*. [39] with two linear stress transformations is implemented into the commercial finite element software LS-DYNA to predict the crush response of AA5754-O aluminum alloy tubes. CPB06ex2 can provide an accurate representation of the anisotropy of aluminum alloys by simultaneously capturing the variation in both the yield stress and the R-value with orientation (w.r.t the length of the tube) and the balanced biaxial yield stress. Experimental balanced biaxial yield stress, R-values and yield stress as a function of sheet orientation are used to calibrate the coefficients of the yield function. Different sets of coefficients can generate different yield surface shapes, but still capture the same experimental anisotropy. Dynamic crush simulations of circular tubes are performed using CPB06ex2 with different yield surface shapes and coefficients. The crush force response and energy absorption characteristics are compared for each yield surface shape. The simulation results for the axial crush are compared with an experimental set of data found in literature. Finally, parametric studies are performed where specific combinations of the anisotropy parameters are employed.

5.2 Material characterization

The material selected for this analysis is the sheet aluminum alloy (AA) 5754-O. It should be mentioned that AA 5754-O has been employed in many previous studies (see [14, 127, 77]). In this research, the experimental data, in the form of stress-strain responses, R-values and yield stress variation as a function of sheet orientation, presented by Lee *et al.* [128] are used in the numerical analysis. The chemical composition of AA5754-O is presented in Table 2.3.

Table 5.1 - Chemical composition of aluminum alloy 5754-O (wt%) [128]

Al	Mg	Mn	Cr	Fe	Si	Cu	Ti	Zn
Bal	0.75	0.25	0.10	0.40	0.85	0.70	0.10	0.15

The experimental stress-strain curve that is employed in this work is presented in Figure 5.1. The strength coefficient, K, and work hardening exponent, n, for this set of experimental data is 457.22 MPa and 0.2862 respectively, while the value of normalized balanced biaxial yield stress, σ_b, is 0.996. The Johnson-Cook strain rate parameters used are $C = 0.0102$ and $\dot{\varepsilon}_o = 3.30 \times 10^{-3} s^{-1}$ [129]. The experimental R-values and yield stress for three directions [0° (rolling direction), 45°, and 90° (transverse direction)] presented by Lee *et al.* [128] are also employed in the numerical analyses.

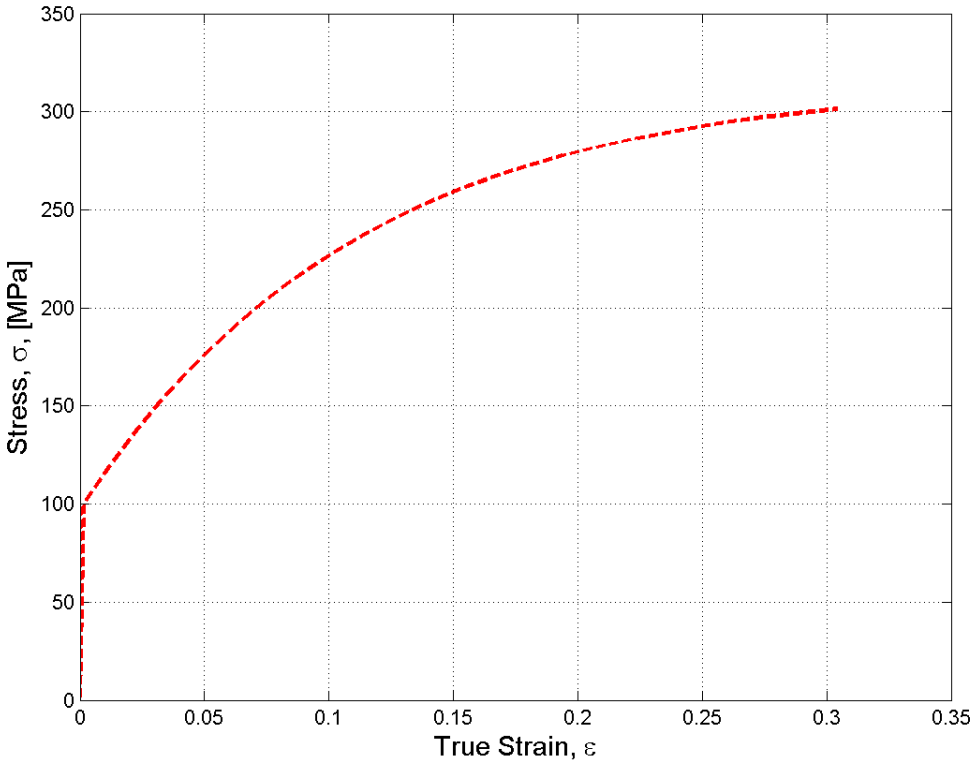

Figure 5.1 - Experimental stress-strain curve for AA5754-O [128]

The experimental points and their curve fit for the variation of R-values and yield stress as a function of sheet orientation is presented in Figure 5.2. Furthermore, since aluminium typically exhibits very little to no strength differential effects, the strength differential terms are taken as

$k = k' = 0.000$. The coefficients for CPB06ex2 were obtained for three values of $a = \{3, 8, 12\}$. It should be mentioned that, $a = \{3, 8, 12\}$ are used in the simulation since; $a = 3$ provides a yield surface shape similar to the shape produced by Hill [30] (i.e., Dasappa *et al.* [126]), $a = 8$ provides relatively accurate predictions for face centered cubic (FCC) materials [54], and $a = 12$ is a common value that produces accurate anisotropic fits for this particular yield function (Plunkett *et al.* [39]). The coefficients, C_{ij} and $C_{ij}{}'$, that are obtained for each value of a are presented in Table 5.2. The normalized yield stress and R-value as a function of sheet orientation are presented in Figure 5.3, while the normalized yield surfaces for each set of CPB06ex2 parameters are presented in Figure 5.4.

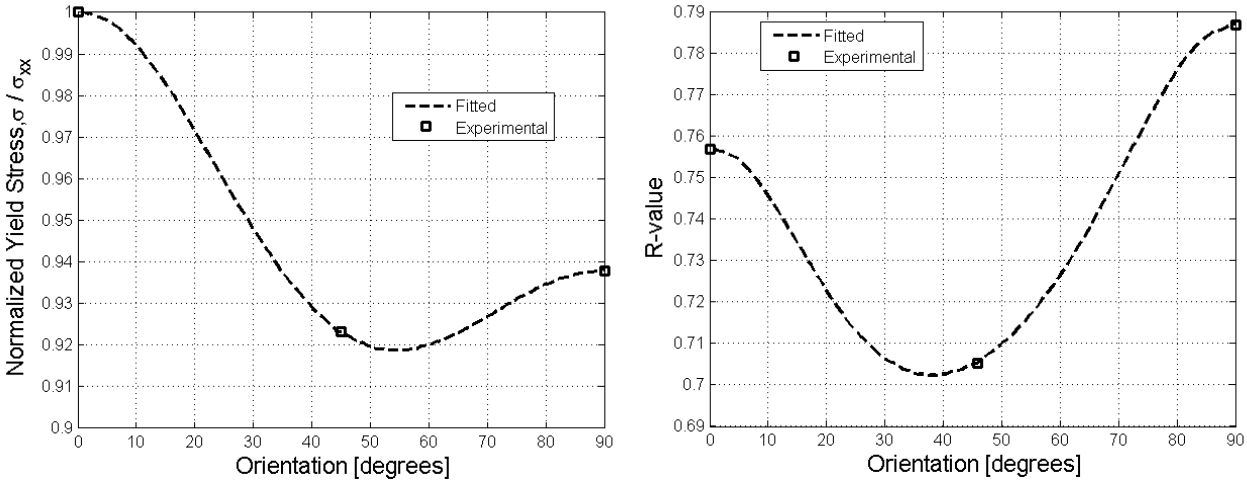

(a) **(b)**

Figure 5.2 - Experimental and fitted variations in (a) normalized yield stress and (b) Lankford coefficients as a function of orientation for AA5754-O [128]

Table 5.2 - Material parameters used in yield functions

a	C_{11}	C_{22}	C_{33}	C_{12}	C_{13}	C_{23}	C_{44}
3.00	-13.3867	-13.1294	-13.8268	-14.3002	-12.8721	-12.9936	1.2475
	$C_{11}{}'$	$C_{22}{}'$	$C_{33}{}'$	$C_{12}{}'$	$C_{13}{}'$	$C_{23}{}'$	$C_{44}{}'$
	-13.3867	-12.6138	-12.4926	-11.9990	-13.2326	-13.2500	-0.9998
a	C_{11}	C_{22}	C_{33}	C_{12}	C_{13}	C_{23}	C_{44}
8.00	-0.5969	0.3756922	0.8482	-1.2344	-0.7846	-0.4337	1.2281
	$C_{11}{}'$	$C_{22}{}'$	$C_{33}{}'$	$C_{12}{}'$	$C_{13}{}'$	$C_{23}{}'$	$C_{44}{}'$
	-0.5969	-0.464962	-0.9691	-1.9075	-2.2045	-2.1731	1.5149
a	C_{11}	C_{22}	C_{33}	C_{12}	C_{13}	C_{23}	C_{44}
12.00	4.0850	3.6354	4.3201	2.2818	3.5011	3.8487	1.6331
	$C_{11}{}'$	$C_{22}{}'$	$C_{33}{}'$	$C_{12}{}'$	$C_{13}{}'$	$C_{23}{}'$	$C_{44}{}'$
	4.0850	4.1831	6.1634	3.0073	4.9341	4.4892	1.2735

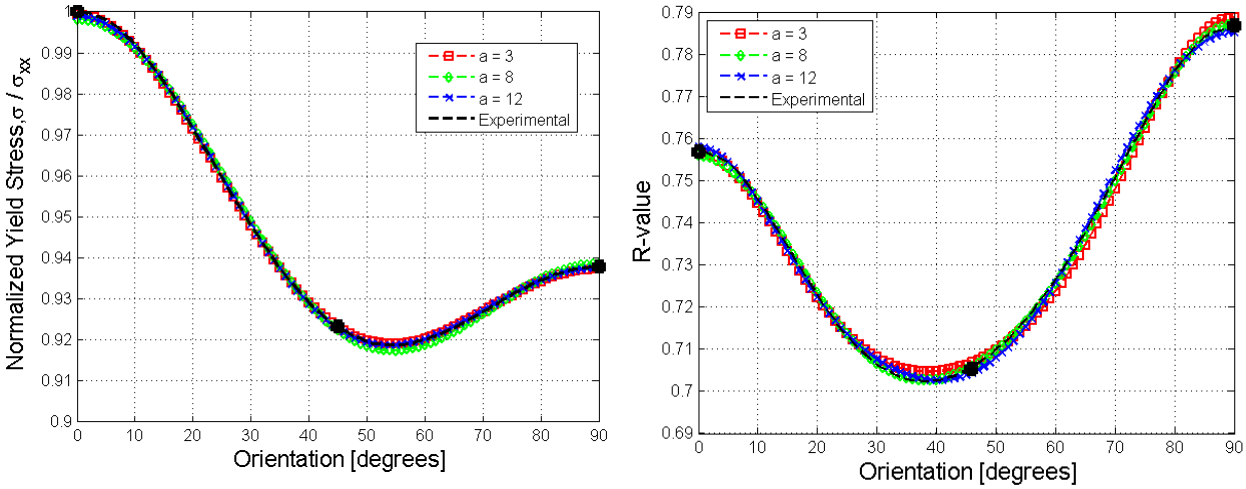

(a) **(b)**

Figure 5.3 - Experimental variations in (a) normalized yield stress and (b) Lankford coefficients as a function of sheet orientation for AA5754-O

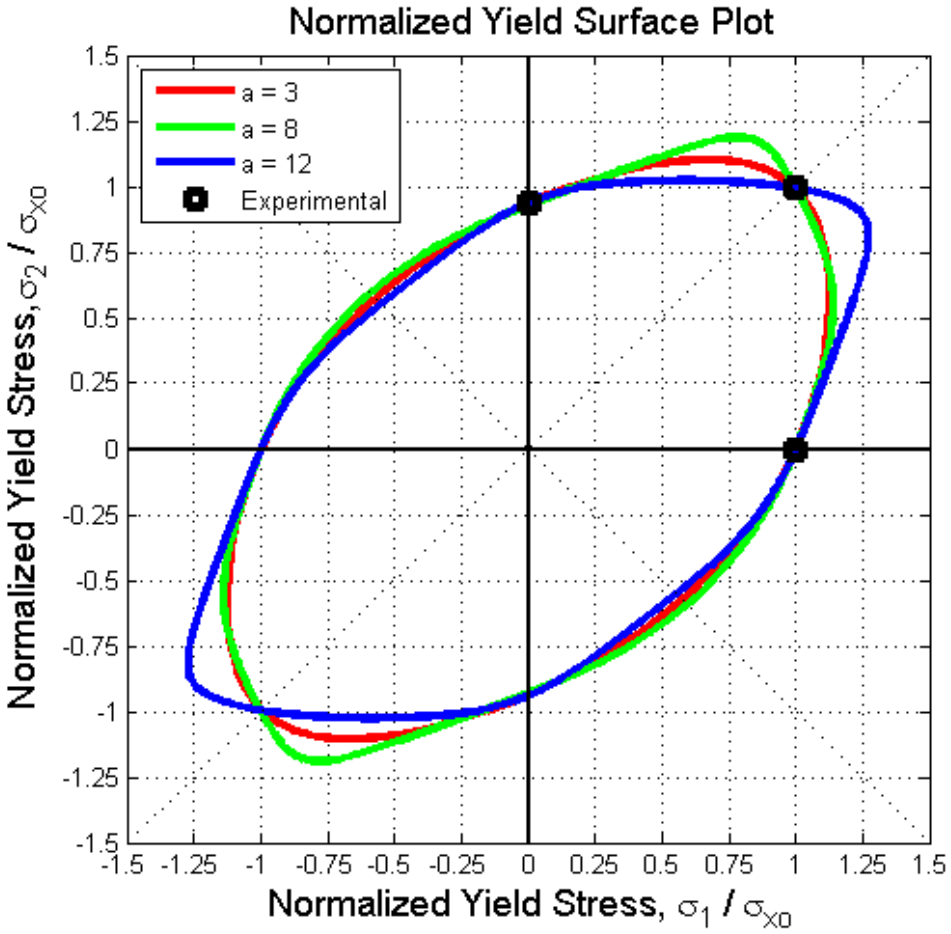

Figure 5.4 - Yield surfaces obtained using CPB06ex2 for AA5754-O for a = 3, 8, and 12

5.3 Finite Element Modeling

In this study, a finite element (FE) model is developed to simulate the axial crushing of a circular crush tube at various velocities using the commercial FE software LS-DYNA. A non-linear explicit dynamic formulation is used throughout this work [58]. The FE model of the circular crush tube is presented in Figure 5.5. The FE model has been constructed to replicate the experimental setup that was presented by Williams *et al.* [77]. The model consists of a crush tube constrained between two steel bosses. The circular crush tube has an average diameter of 73.2mm with a 3.0mm wall thickness and an initial length of 400mm. The crush tube is meshed with 50mm deep boss at the top and bottom of the tube. This simulates the clamping boundary conditions that are present during high-speed axial crush experiments. The bosses are assigned a mass of 560 kg by modifying the density of steel [77]. The top boss is constrained to move only in the axial z-direction and is given an initial velocity of 8.00m/s (28.8km/h). The base boss is constrained in all degrees of freedom. The total simulation time is 40 milliseconds for the considered loading condition. The force-displacement response of the top boss is monitored to obtain the energy absorption characteristics. The elastic material properties are listed in Table 5.3.

The steel bosses are modeled as an elastic material. Eight node brick elements with full selective reduced integration with a mesh size of 2.5mm × 2.5mm × 2.5mm are employed for the bosses. The circular crush tube is meshed using Belytschko-Tsay shell elements to simulate thin sheet deformation. Belytschko-Tsay element formulations are also computationally efficient and give a good level of accuracy for crashworthiness simulations [58]. Seven integration points are used through the element thickness. A mesh size of 2.5mm × 2.5mm is employed through the crush tube. Element deletion is used to simulate failure within the material when the total plastic strain exceeds the failure strain, ε_f. Crush initiators are not used in the circular crush tube. Contact algorithms are placed between the crush tube and the rigid plates to capture the friction of the crush tube folds against the boss. The static and dynamic coefficients of friction are set to 0.45 and 0.40 respectively. Self-contact algorithms are also placed to capture the effects of the aluminum folds stacking onto each other. Accordingly, the static and dynamic coefficients of friction for aluminum on aluminum contact are set to 1.05 and 1.40 respectively [130, 131].

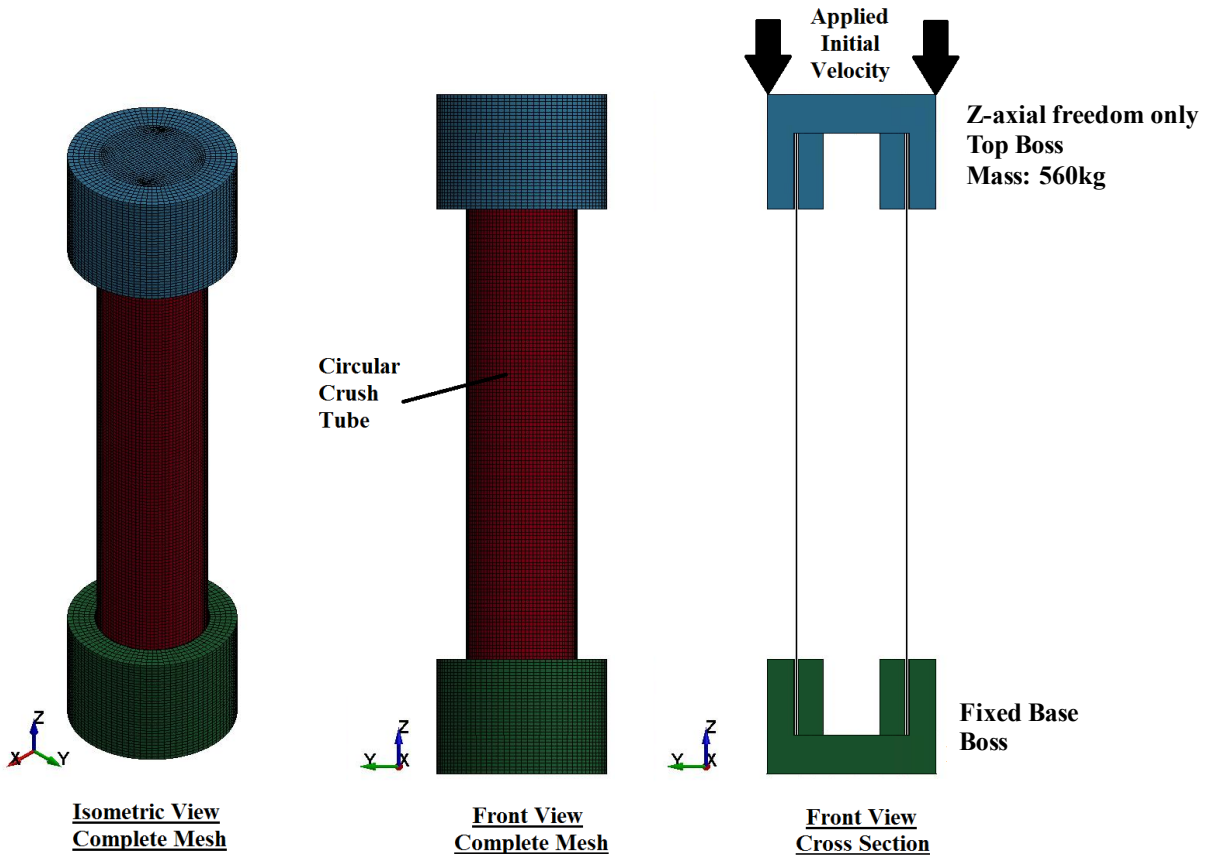

Figure 5.5 - Isometric, front and cross section view of the FE model setup

Table 5.3 - Elastic material properties of aluminum and steel

	Aluminum	Steel
Density [g/cm3]	2.7	7.8
Elastic Modulus [GPa]	67.9	205
Poisson Ratio	0.34	0.3

5.4 Results and Discussion

As soon as the top boss impacts the crush tube, the structure is loaded axially in compression, which transitions into localized deformation. The crush tube exerts a reaction force on the bosses to counter the momentum of the crushing mass. Thus, the energy of the crushing mass is dissipated through the work hardening of the material in the crush tube during deformation. Simulations show that the complex strain paths that develop during axial crush can result in different deformation patterns. These different deformation patterns are known as crush

modes. These crush modes are defined by the symmetry of the folding patterns, such as axi-symmetric, symmetric, and asymmetric. A detailed description on crush modes, can be found in [132, 71, 72]. These different crush modes can result in different crush force and energy absorption responses [132]. In this section, the effects of the yield surface shape, anisotropy (R-value and yield stress) on the peak crush force and energy absorption are investigated. Elemental stress states are also analyzed to identify the dominant strain paths during deformation. Strain paths are identified by the intersection of the maximum and minimum principal stress state with the yield surface. Figure 5.6 presents six major strain paths on the yield surface: (1) Equi-biaxial tension ($\sigma_1 > 0, \sigma_2 = \sigma_1$); (2) in-plane, plane strain under tensile loading $\left(\frac{\partial f}{\partial \sigma} = 0\right)$; (3) uniaxial tension ($\sigma_1 > 0, \sigma_2 = 0$); (4) pure shear ($\sigma_1 > 0, \sigma_2 = -\sigma_1$); (5) uniaxial compression ($\sigma_1 = 0, \sigma_2 < 0$); and (6) equi-biaxial compression ($\sigma_1 < 0, \sigma_2 = \sigma_1$).

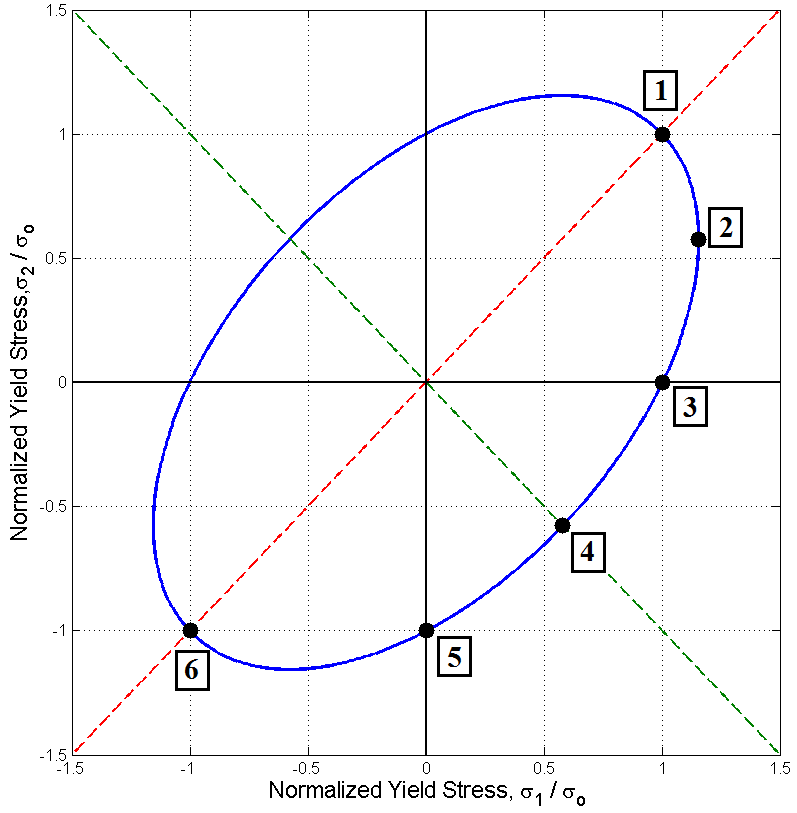

Figure 5.6 - State of stress schematic for normalized yield surface

Eighteen elements are selected at 7.5 mm intervals around the hoop direction of the crush tube (Figure 5.7). Elements are selected at a distance of 95 mm from the top edge to capture the strain paths developed in the second fold. The element stress-state histories are also overlaid onto

the corresponding yield surface, where the stress state is plotted at 0.25millisecond intervals until the folding is complete.

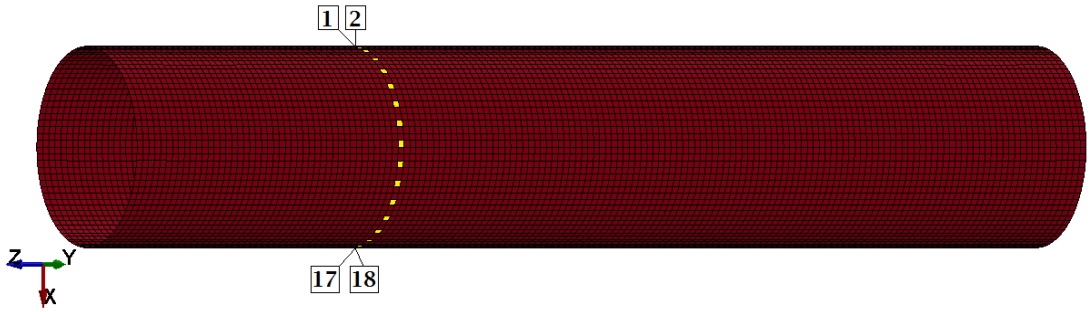

Figure 5.7 - Elemental state stress schematic for hoop direction

Figure 5.8 presents the time lapse of the effective plastic strain contours for a circular crush tube with a homogeneity value of $a = 8$ during the axial crush. In the first 4 milliseconds of crushing, two axi-symmetric folds develop; one on each end of the tube. The first complete fold develops at the top of the crush tube and continues to progressively fold. As the structure continues to deform, the structure transitions from an axi-symmetric mode to a symmetric mode. The structure continues to deform in this symmetric crush mode. Finally, a total of five folds develop; one complete and one incomplete axi-symmetric and two complete and one incomplete symmetric folds.

Figure 5.9 presents the details of the plastic strain contours in the folds. An average plastic strain of 55.1% is developed in this section, while a peak plastic strain of 112% is developed around the outside surface of the axi-symmetric fold. A plastic strain of 172% and 25% is developed on the edge and face of the symmetric fold. The increase in plastic strain development is attributed to the additional strain paths that are not present in axi-symmetric folding.

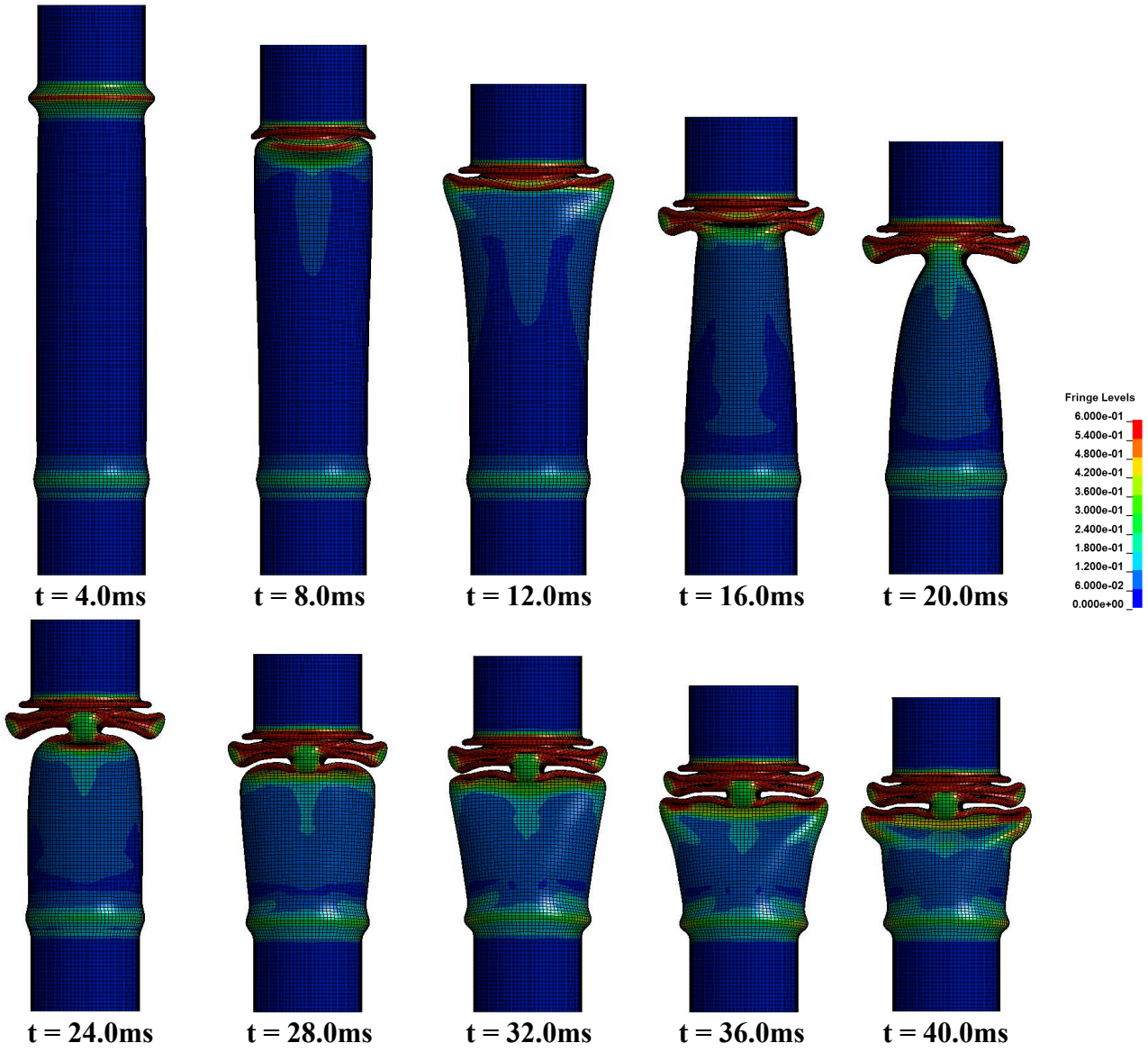

Figure 5.8 - Time lapse (milliseconds) of axial crush simulation with homogeneity coefficient a = 8

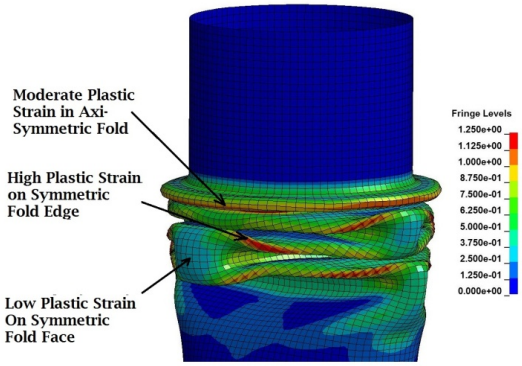

Figure 5.9 - Final plastic strain contours of axial crush tube with homogeneity coefficient a = 8

Figure 5.10 presents a comparison of the final deformation for $a = 8$ with the final deformation of the experimental crush tube [120]. Figure 5.11 presents the crush force and energy absorption response versus time for $a = 8$. The experimental crush force and energy absorption response up to a crush distance of 175mm that was presented in Williams *et al.* [77] is also presented for comparison. A peak crush is observed in both the experiment and simulation response that is attributed to the initial elastic loading before the structure yields to compression. The resulting valleys and peaks in the force displacement response is a result of the progressive folds that initiated from the completion of previous folds. The predicted mean crush force, peak crush force and energy absorption is 81.9kN, 137.9 kN and 14.39 kJ respectively while the experimental mean crush force, peak crush force and energy absorption is 81.0kN, 168.6kN, and 14.3kJ respectively. The force-displacement response has several oscillations in the response, which is attributed to the structural vibrations of the sled-track setup [14]. Thus, the simulation tends to under predict the true experimental peak crush force. The prediction shows good agreement with the valleys and peaks of the experimental force-displacement response. The prediction also shows excellent agreement with the energy absorption response and crush folds. Thus, the anisotropic parameters obtained for a homogeneity value of $a = 8$ predict well the crush response.

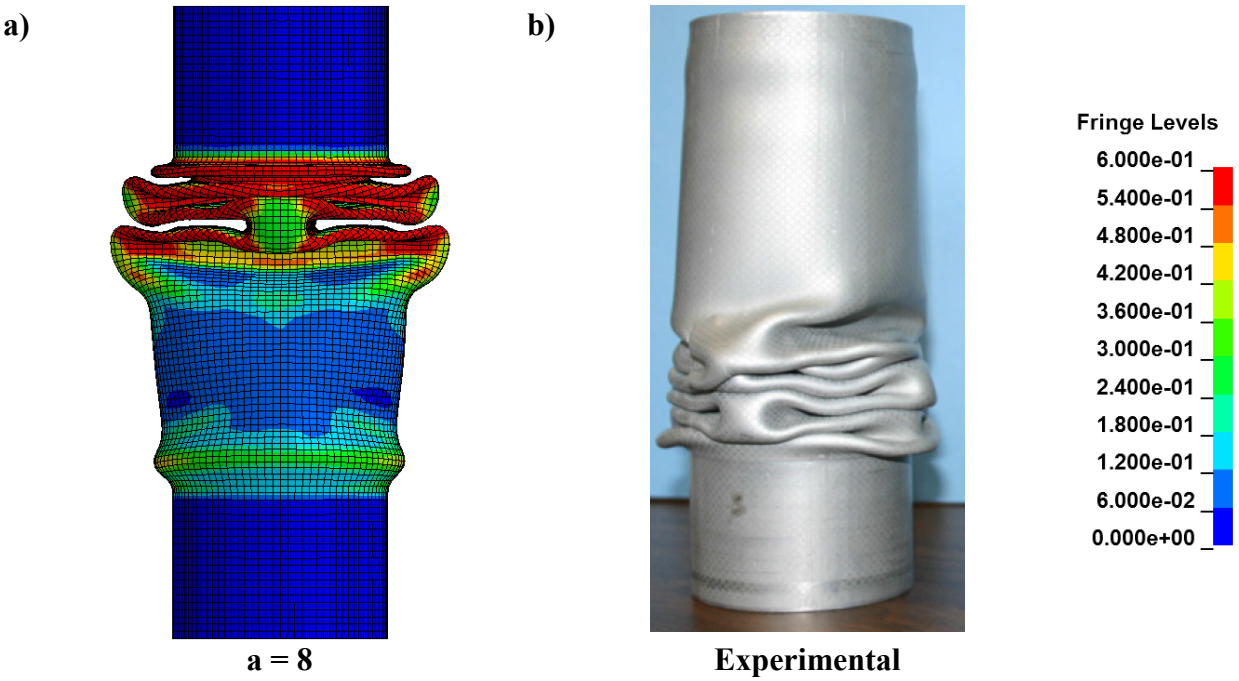

Figure 5.10 - Final crush tube deformation at t = 40.0ms for homogeneity coefficients of (a) a =8 and b) comparison with experiment [120]

a)

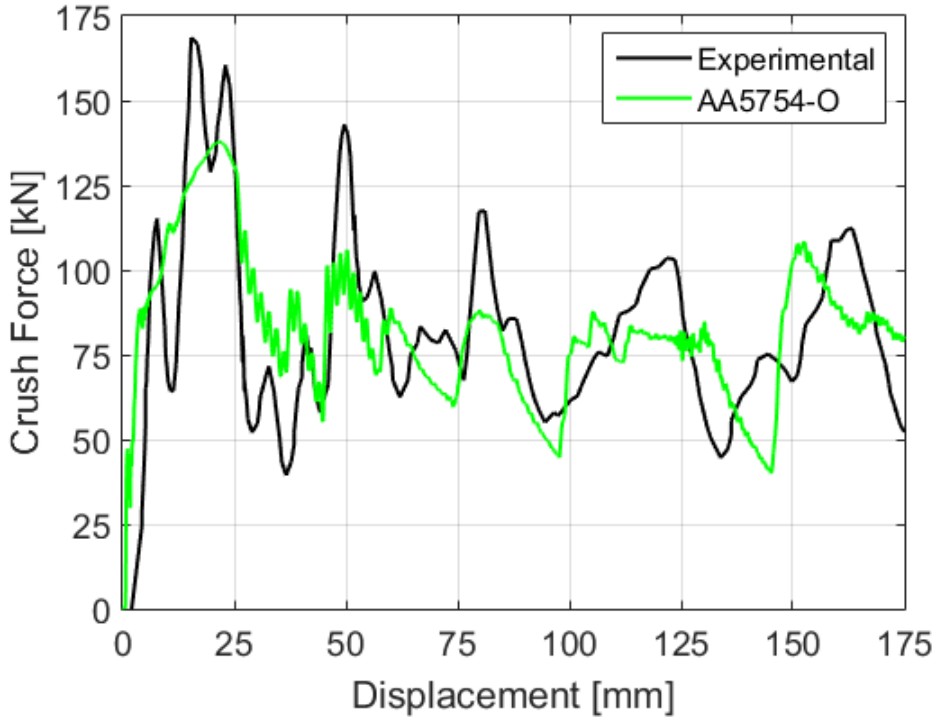

b)

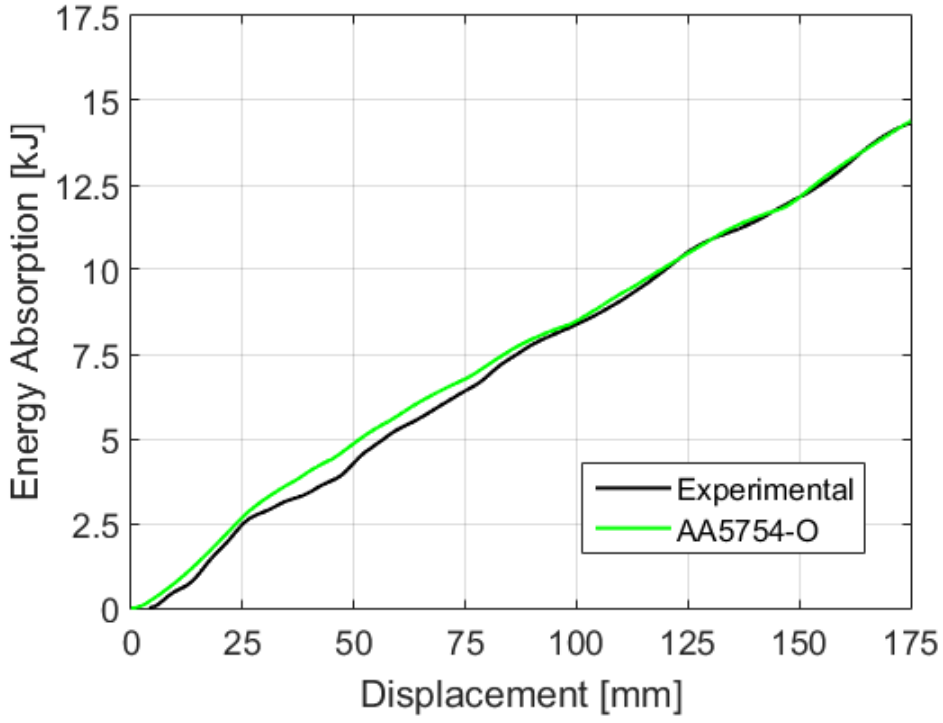

Figure 5.11 - Comparison of experimental [77] and simulated a) crush force and b) energy absorption response for a = 8

Figure 5.12 presents the elemental stress-state history around the hoop path of a fold for the simulation with $a = 8$. Element 1 and 18 correspond to the elements that are located on the face of the first symmetric fold. As expected, upon initial loading, all elements are under the state of uniaxial compression. Once yielding occurs, the loading changes from compression to pure shear. As a symmetric fold forms, a variation in the stress state develops around the circumference. On the face of the symmetric fold, the state of stress transitions quickly to balanced biaxial tension. As one moves away from the symmetric face towards the edge, the state of stress abruptly changes to a combination of pure shear and plane strain (shown in Element 4). Further around the circumference, the elements along the edge of the fold (Elements 7 - 12) transition and remain in a deformation mode that is dominated by plane strain.

5.4.1 Axial Crush Response of Circular Tube with an Isotropic Yield Surface

Figure 5.13 presents the final crush tube deformation using an isotropic von Mises yield criterion. This was accomplished by setting the homogeneity coefficient *a*, in the CPB06ex2 yield function to 2 and the coefficients in the first and second stress transformation to 1.00 and 0.00 respectively. The simulation with the isotropic von Mises yield criterion predicts three complete axis-symmetric folds with one complete and one incomplete diamond fold. Figure 5.14 presents a comparison between the predicted crush force response of the isotropic von Mises model with the complete fitting scheme. The isotropic von Mises model predicts higher mean crush force (83.06kN), lower energy absorption (14.53 kJ) and a similar peak crush force (130.4kN) compared to the complete fitting of AA5754-O with homogeneity coefficient $a = 8$. In the isotropic model, a larger number of folds develop through the axi-symmetric deformation mode to allow for adequate energy absorption. This will have a significant influence on the localization behavior in the folds. Thus, the prediction with the isotropic von Mises model clearly highlights the importance of incorporating anisotropy into predicting the correct folding deformation and resulting crush force response.

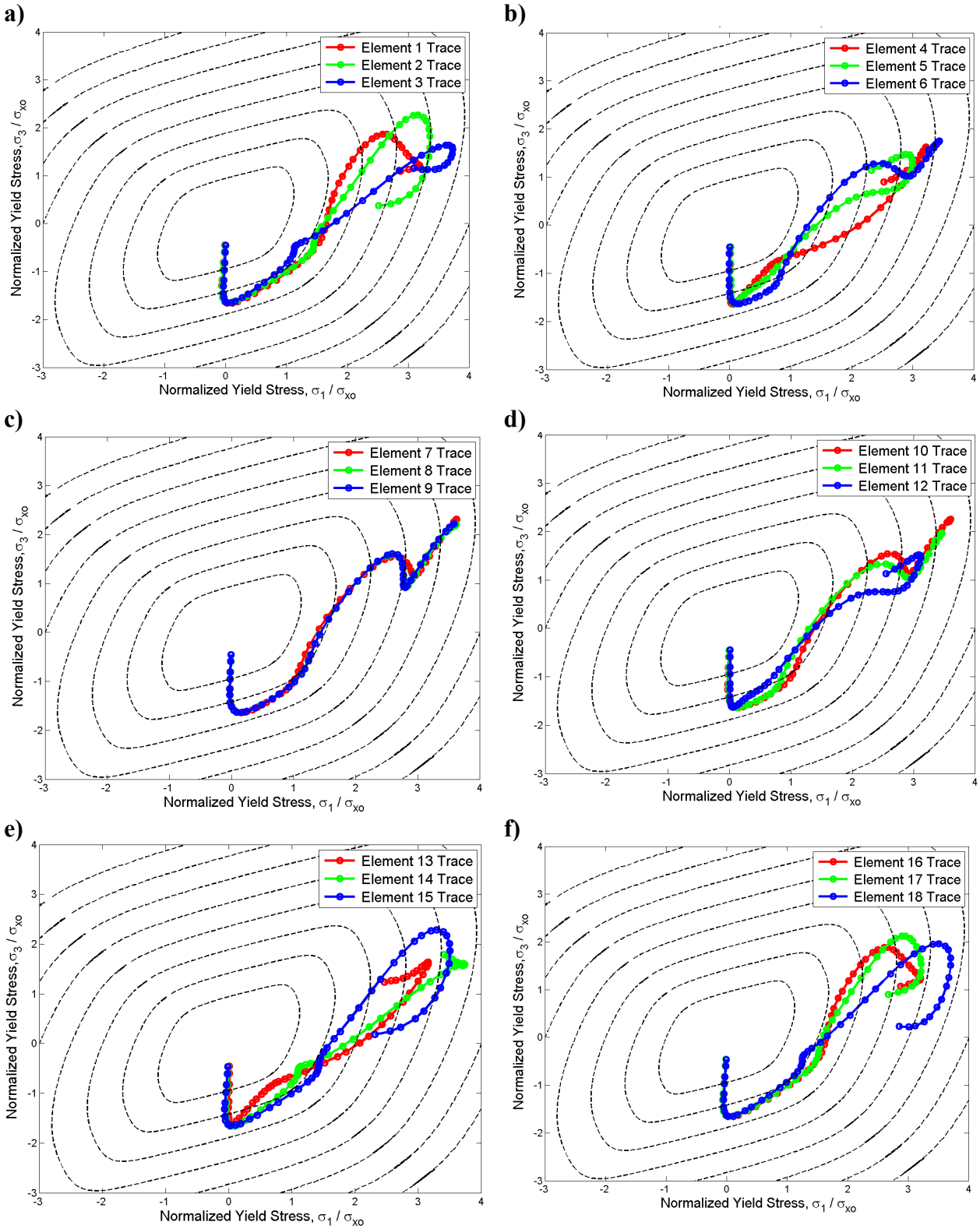

Figure 5.12 - Stress-state history for a = 8 for (a) Elements 1-3, (b) Elements 4-6, (c) Elements 7-9, (d) Elements 10-12, (e) Elements 13-15, and (f) Elements 16-18 along the hoop direction

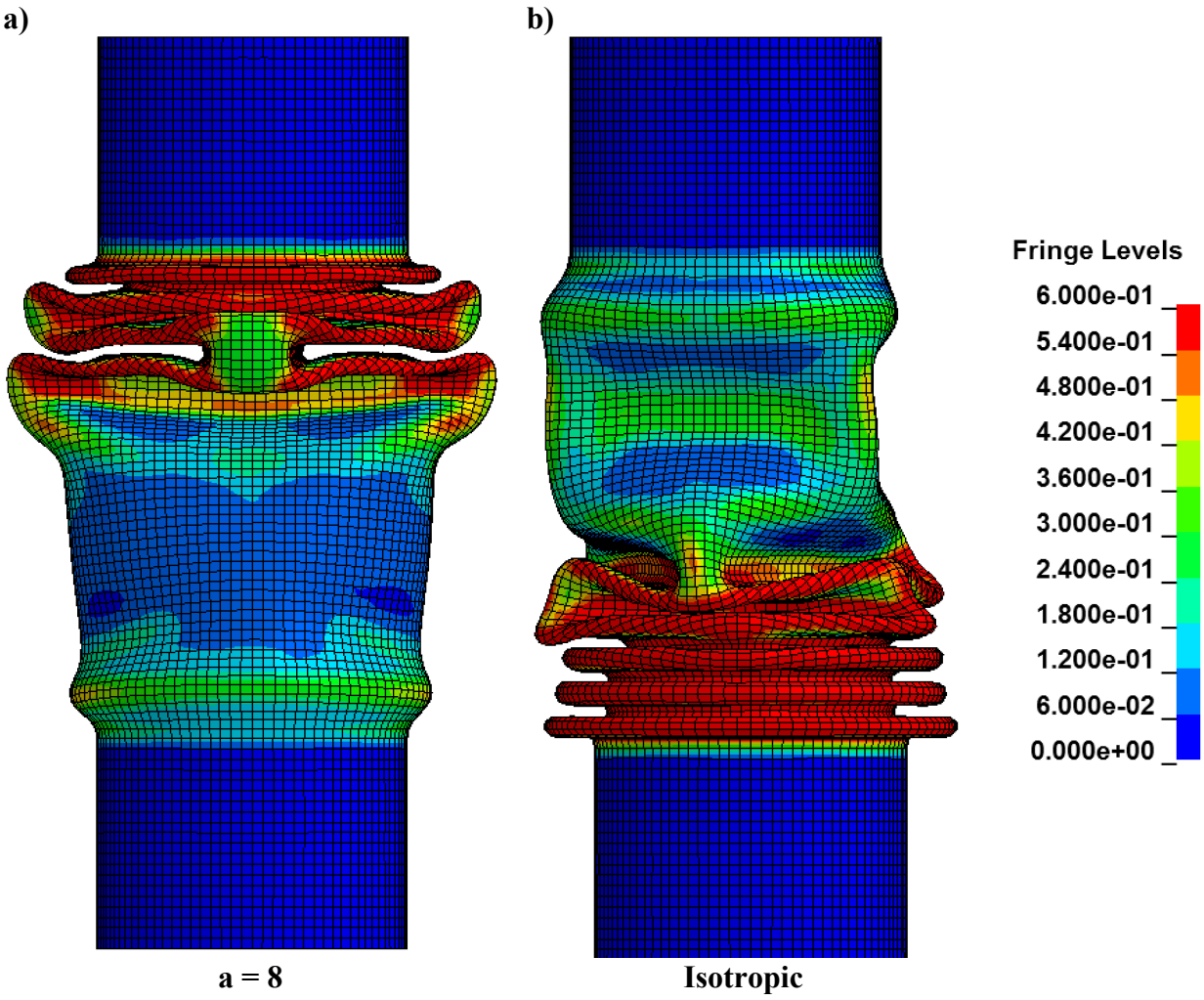

Figure 5.13 - Final crush tube deformation at t = 40.0ms for homogeneity coefficients of (a) a =8 and b) Isotropic von Mises

a)

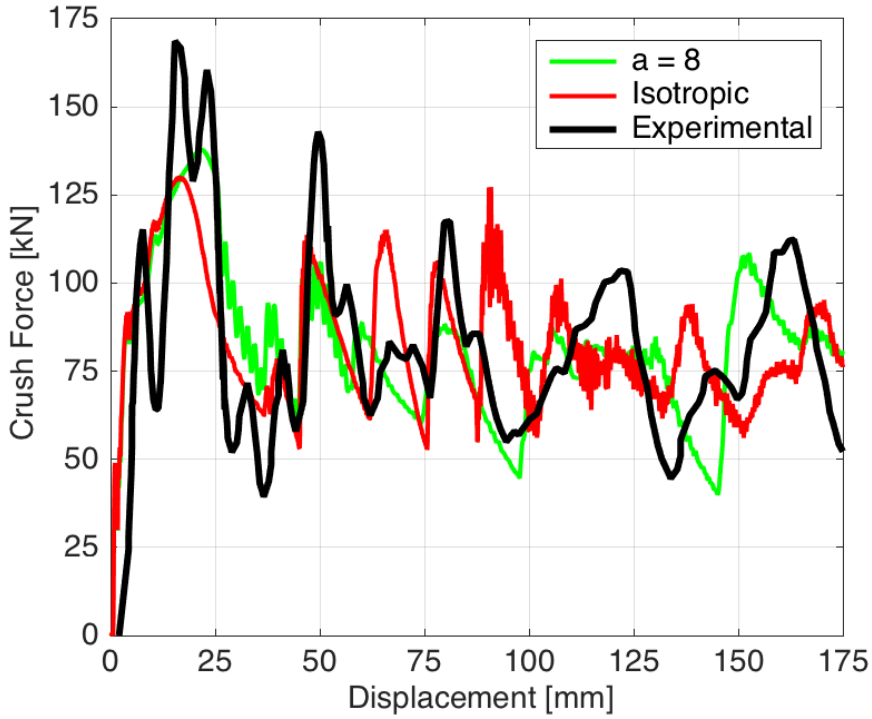

b)

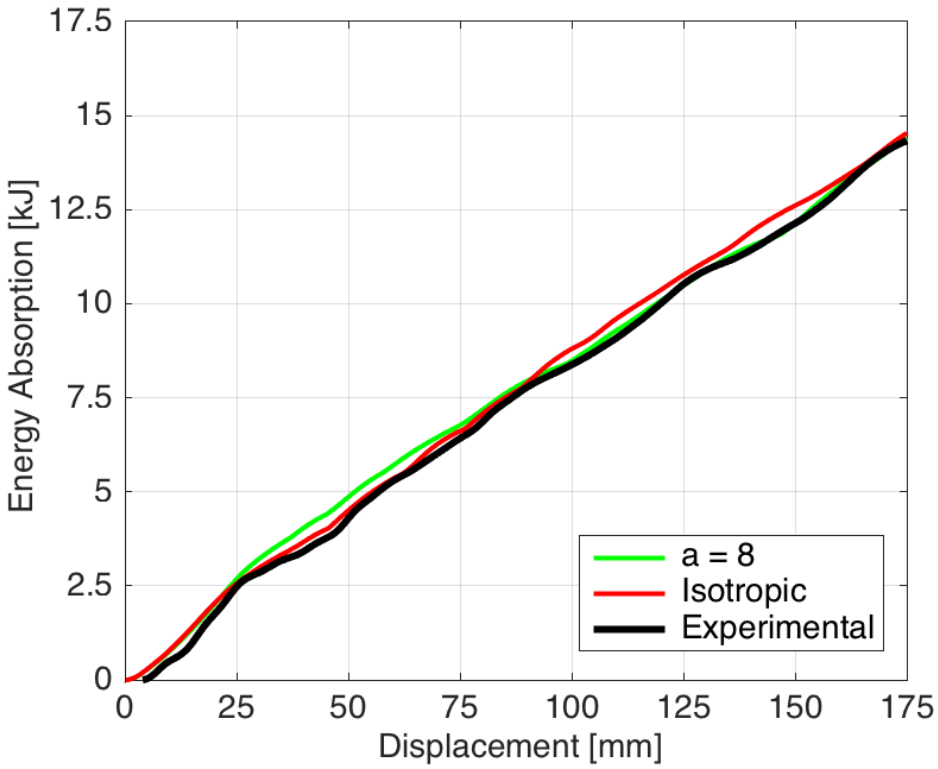

Figure 5.14 - Comparison of experimental [77] and simulated a) crush force and b) energy absorption response for a = 8 and Isotropic von Mises

5.4.2 Axial Crush Response of Circular Tube with Various Homogeneity Coefficients

Figure 5.15 presents the final crush tube deformation for homogeneity coefficients of a = {3, 8, 12}. When $a = 3$, one complete axi-symmetric and two complete symmetric folds form at the top of the crush tube. It also generates an incomplete symmetric fold at the bottom of the tube, which is close to the fixed rigid wall. The simulation with $a = 12$ produces a deformation that is similar to $a = 3$. However, the folds develops in the opposite direction, i.e. one complete axi-symmetric and two complete symmetric folds at the bottom of the crush tube. It also generates a complete symmetric fold at the top of the tube.

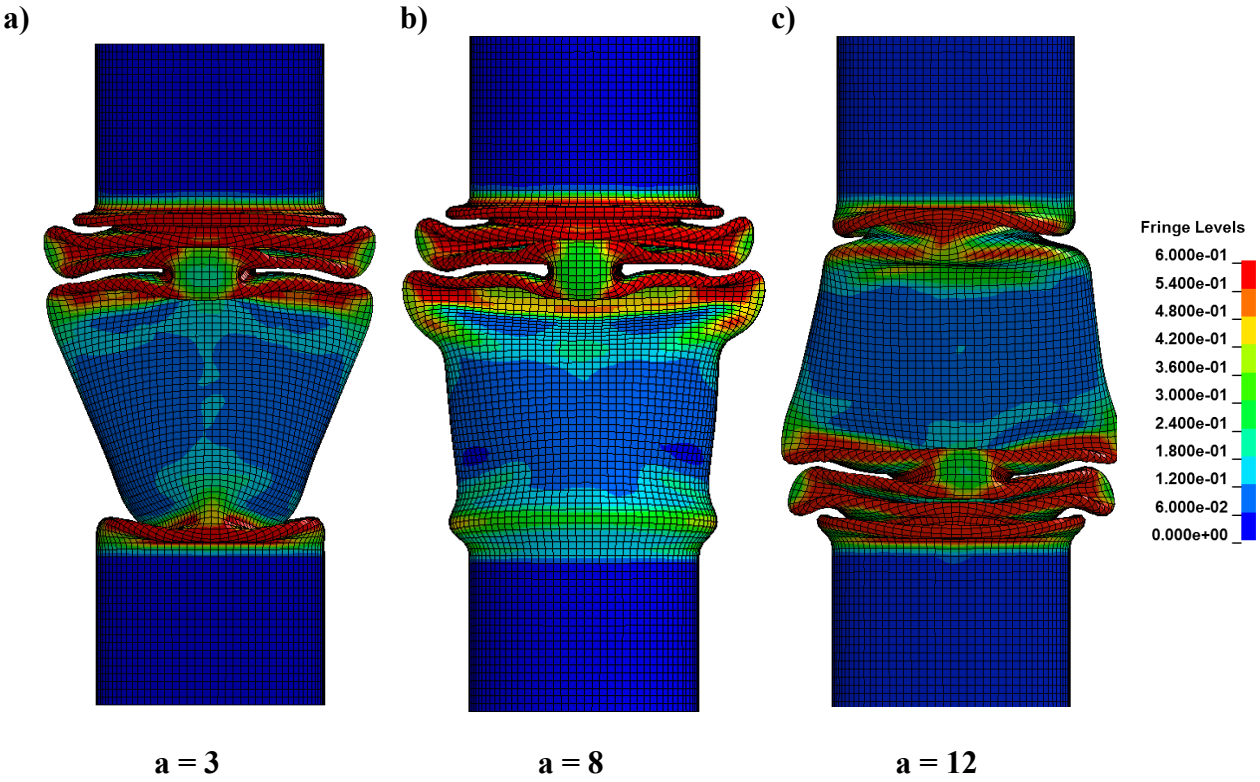

Figure 5.15 - Final crush tube deformation at t = 40.0ms for homogeneity coefficients of (a) a = 3 (b) a =8 (c) a = 12 and comparison with experiments

Figure 5.16 presents a comparison of the resulting force and energy-displacement responses for various homogeneity. Table 5.4 presents a comparison of the developed plastic strains in each crush tube and Table 5.5 presents a comparison of the peak crush force and total energy absorption response for each homogeneity coefficient. Each model shows an average plastic strain of approximately 54 - 55%. However, the plastic strain developed on the edges and faces of the symmetric folds are different. The models with higher homogeneity coefficients ($a = \{8, 12\}$) predicts higher localized plastic strain development, which could lead to failure within the region. Furthermore, the model with a homogeneity coefficient of $a = 8$ predicted the highest peak crush force, while $a = 12$ predicted the lowest peak crush force. Upon initial compressive yielding, the material transitions through a state of pure shear before entering a state of balanced biaxial stress. The model with $a = 12$ predicts a lower peak crush force than all other models because the shear stress regime of the normalized yield surface is lower.

Figure 5.17 and Figure 5.18 present the elemental stress-state history around the hoop path for homogeneity coefficients $a = 3$ and $a = 12$ respectively. Similar to the strain path presented for $a = 8$, the elements enter an initial state of uniaxial compression. Upon this initial yielding, the loading path changes from uniaxial compression to a state of pure shear and then to a state of plane strain. This further demonstrates that the plane strain deformation condition is the main mechanism for axial crushing of circular tubes.

Table 5.4 - Comparison of local plastic strains developed in crush tube with various homogeneity coefficients

Homogeneity Coefficient, a	Average Plastic Strain (%)	Plastic Strain on Edge of Symmetric Fold (%)	Plastic Strain on Face of Symmetric Fold (%)
3	54.9	134	28
8	55.1	172	25
12	54.2	188	24

Table 5.5 - Comparison of peak crush force and energy absorption with various homogeneity coefficients with experimental data

Homogeneity Coefficient, a	Mean Crush Force (kN)	Peak Crush Force (kN)	Energy Absorption (kJ)
3	79.4	132.9	14.02
8	81.9	137.9	14.39
12	76.8	124.8	13.85
Experimental [77]	81.0	168.6	14.33

a)

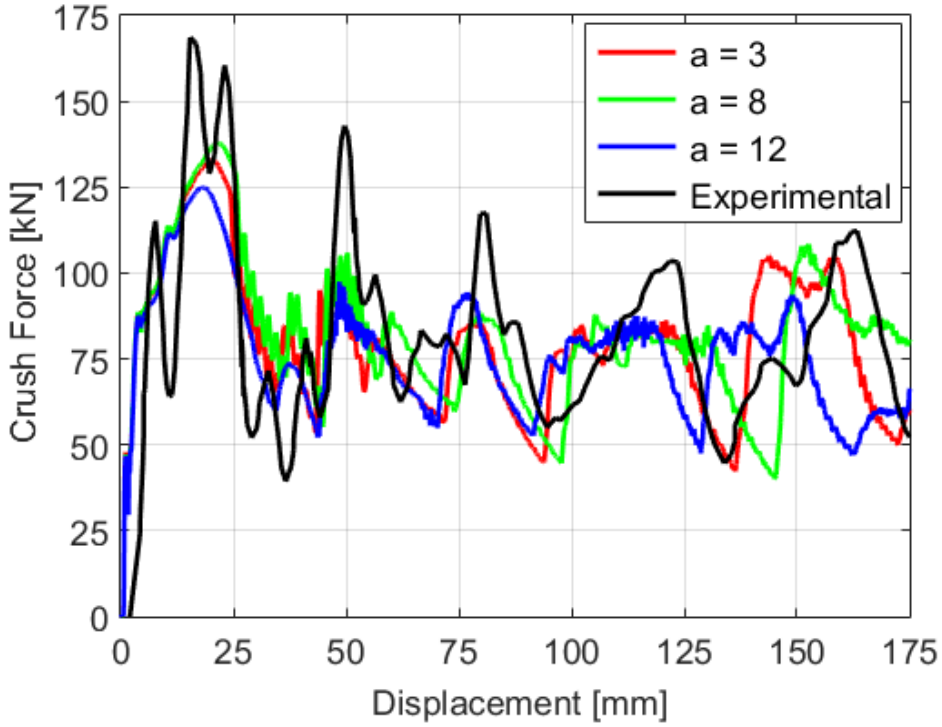

b)

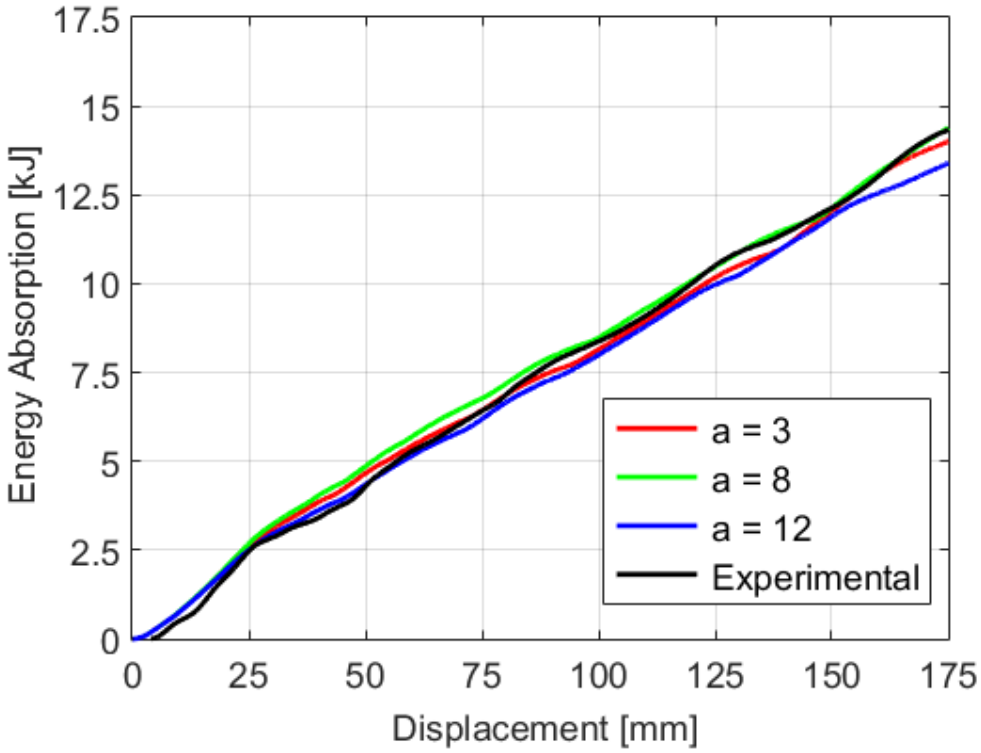

Figure 5.16 - a) Crush force and b) energy absorption response for a = 3, 8, and 12

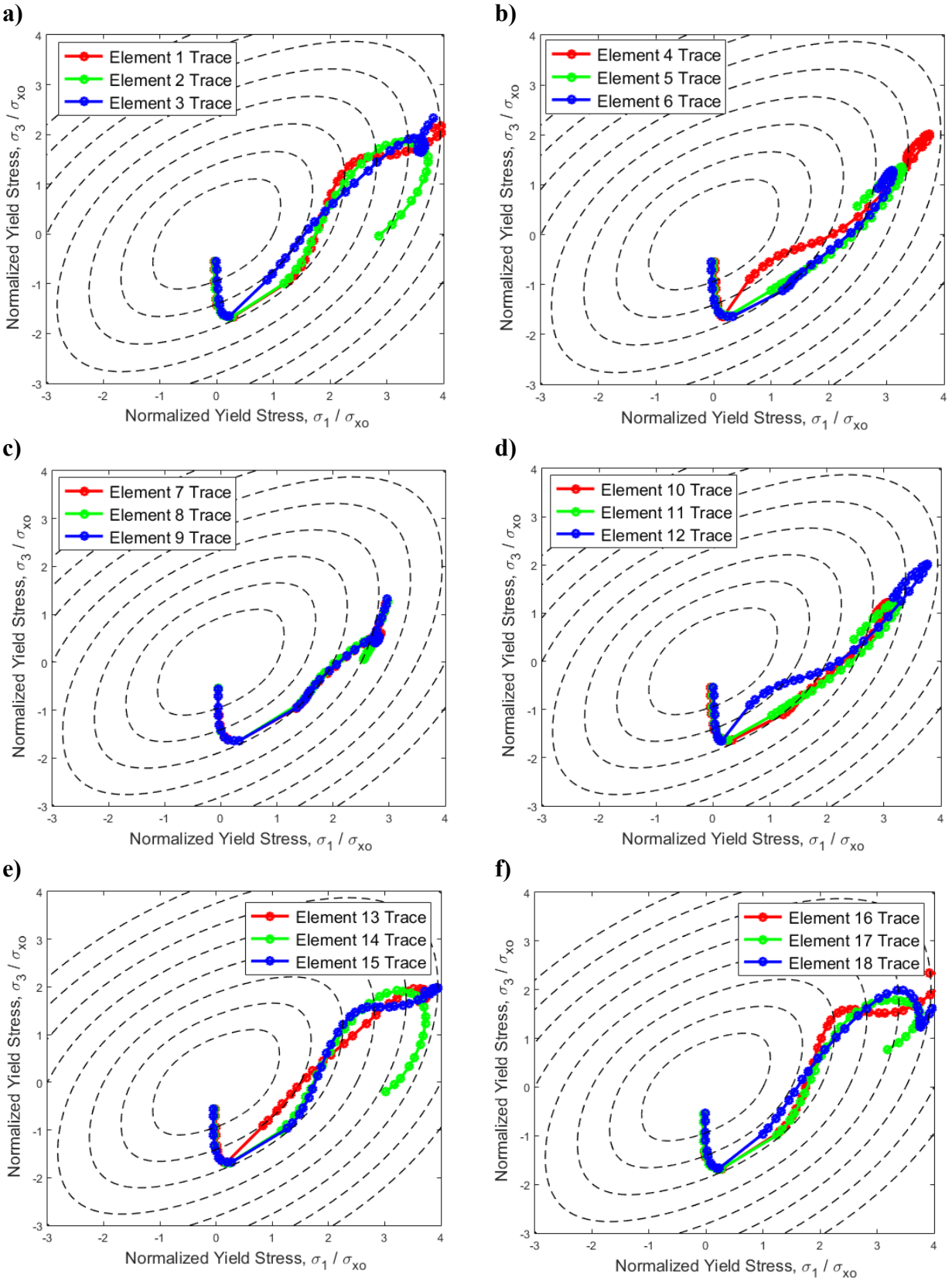

Figure 5.17 - Stress-state history for a = 3 with for (a) Elements 1-3, (b) Elements 4-6, (c) Elements 7-9, (d) Elements 10-12, (e) Elements 13-15 and (f) Elements 16-18 along the hoop direction

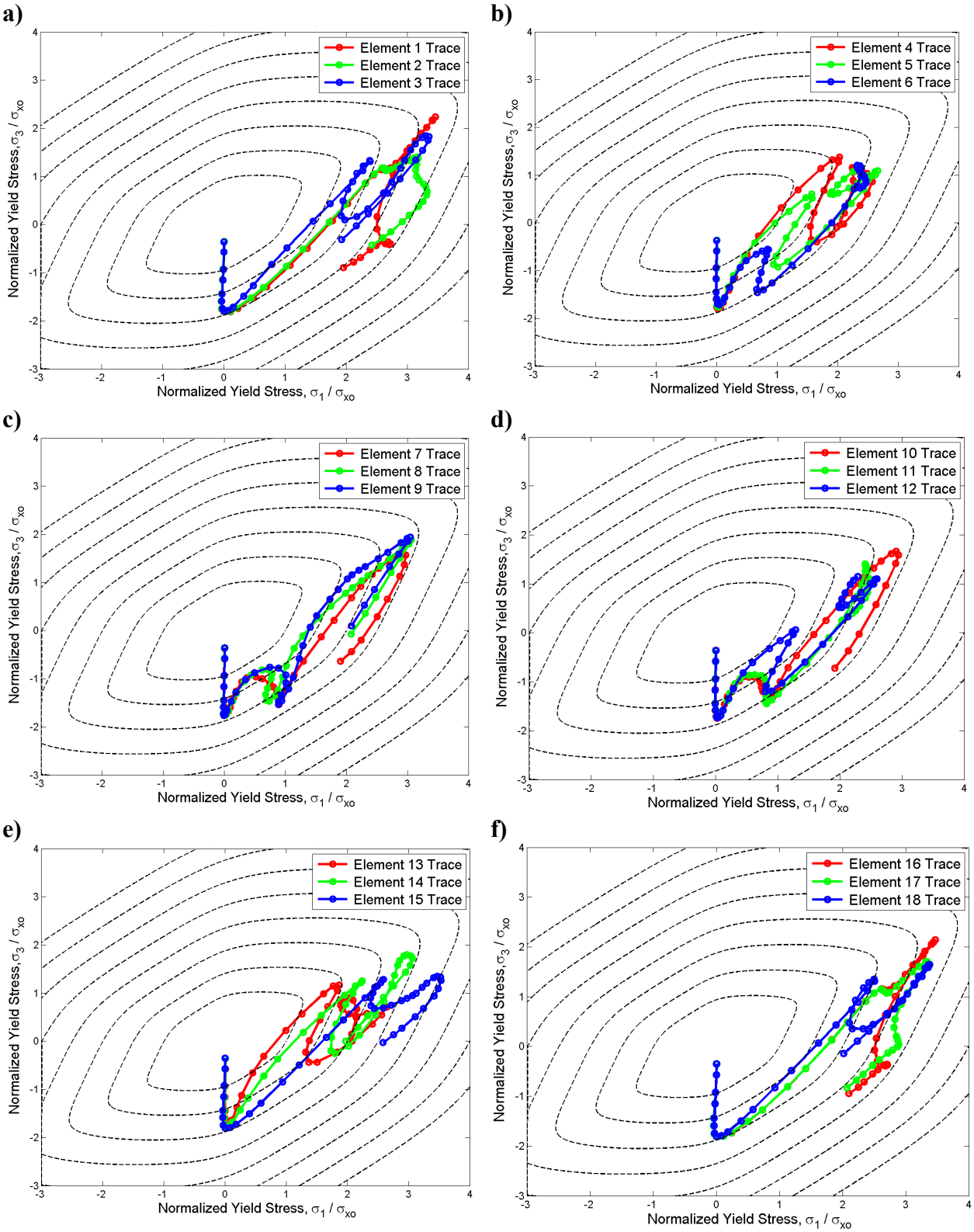

Figure 5.18 - Stress-state history for a = 12 with for (a) Elements 1-3, (b) Elements 4-6, (c) Elements 7-9, (d) Elements 10-12, (e) Elements 13-15 and (f) Elements 16-18 along the hoop direction

5.4.3 Individual Contributions of Material Anisotropy on the Axial Crush Response of Circular Tubes with Homogeneity Coefficient a = 8

In the previous sections, it was demonstrated that the homogeneity coefficient has an effect on the crush response in terms of energy absorption, developed plastic strains and deformation pattern. In this section, the effects of the anisotropy parameters are explored by varying a free anisotropic parameter. For this analysis, a homogeneity coefficient of $a = 8$ is selected because predictions with this homogeneity coefficient show good correlation with experimental results. Three fitting scenarios are explored:

1) Fitting the experimental R-values and yield stresses and varying the biaxial yield stress (known as the **V**arying **B**iaxial **S**tress **F**it Model).
2) Fitting the experimental biaxial yield stress and R-values and varying the yield stresses (known as the **V**arying **Y**ield **S**tress **F**it Model).
3) Fitting the experimental biaxial yield stress and yield stresses and varying the R-values (known as the **V**arying **R**-**V**alue **F**it Model).

The coefficients obtained for fitting each of these different schemes are presented in Table 5.6. The results obtained earlier from fitting the biaxial yield stress, yield stress and R-value as a function of orientation for AA5754-O are also presented for comparison. From here on, these results will be referred to as the complete fit data. The corresponding normalized yield stress and R-values as a function of sheet orientation for each fitting scheme are presented in Figure 5.19, while the normalized yield surface is presented in Figure 5.20. The following section details the influence of each fit on the energy absorption response. Figure 5.21 and Figure 5.22 presents the comparison of the final deformation and resulting crush force and energy-displacement response for each fitting scheme, and the energy absorption responses at a crush distance of 175mm are reported in Table 5.7.

Table 5.6 - Material parameters used in yield functions for different fitting schemes of biaxial yield stress for a = 8

Case	C_{11}	C_{22}	C_{33}	C_{12}	C_{13}	C_{23}	C_{44}
Complete Fit Data	-0.5969	0.3756	0.8482	-1.2344	-0.7846	-0.4337	1.2281
	C_{11}'	C_{22}'	C_{33}'	C_{12}'	C_{13}'	C_{23}'	C_{44}'
	-0.5969	-0.4649	-0.9691	-1.9075	-2.2045	-2.1731	1.5149
Case	C_{11}	C_{22}	C_{33}	C_{12}	C_{13}	C_{23}	C_{44}
VBSF	-9.4423	-9.5903	-10.4326	-10.9089	-9.2113	-9.2997	-1.5282
	C_{11}'	C_{22}'	C_{33}'	C_{12}'	C_{13}'	C_{23}'	C_{44}'
	-9.4423	-7.8409	-7.7007	-9.4097	-9.1296	-8.6018	0.9840
Case	C_{11}	C_{22}	C_{33}	C_{12}	C_{13}	C_{23}	C_{44}
VYSF	-1.8666	-1.0845	-3.5533	-2.9090	-3.5381	-2.2900	1.6576
	C_{11}'	C_{22}'	C_{33}'	C_{12}'	C_{13}'	C_{23}'	C_{44}'
	-1.8666	-2.0267	-1.3005	-0.8229	-2.7878	-2.1284	-1.5355
Case	C_{11}	C_{22}	C_{33}	C_{12}	C_{13}	C_{23}	C_{44}
VRVF	-10.3938	-9.5620	-8.4830	-8.6475	-9.6477	-8.6180	-1.0300
	C_{11}'	C_{22}'	C_{33}'	C_{12}'	C_{13}'	C_{23}'	C_{44}'
	-10.3938	-10.5634	-8.6046	-11.7771	-10.1001	-10.1028	1.4939

Table 5.7 - Comparison of peak crush force and energy absorption for a = 8 with various fitting schemes

Homogeneity Coefficient, a	Fitting Scheme	Mean Crush Force (kN)	Peak Crush Force (kN)	Energy Absorption (kJ)
8	Complete Fit	81.90	137.9	14.39
8	VBSF Model	96.66	140.6	16.83*
8	VYSF Model	74.16	121.4	13.13
8	VRVF Model	84.56	132.6	14.85

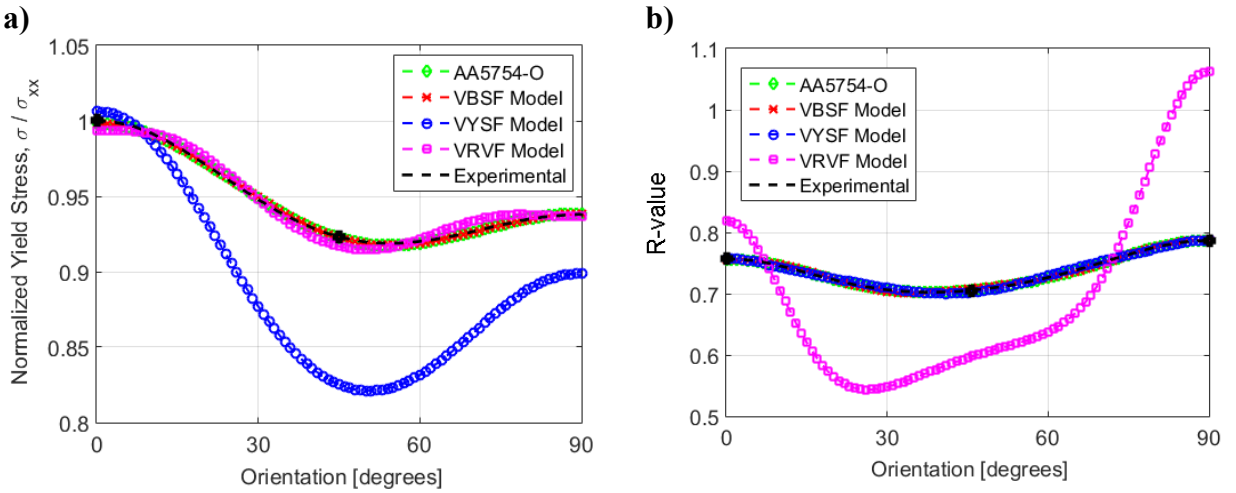

Figure 5.19 - Comparison of (a) normalized yield stress and (b) R-values as a function of sheet orientation for fitting i) AA5754-O, ii) $\sigma_b = 1.15$, iii) VYSF Model and iv) VRVF Model for a = 8

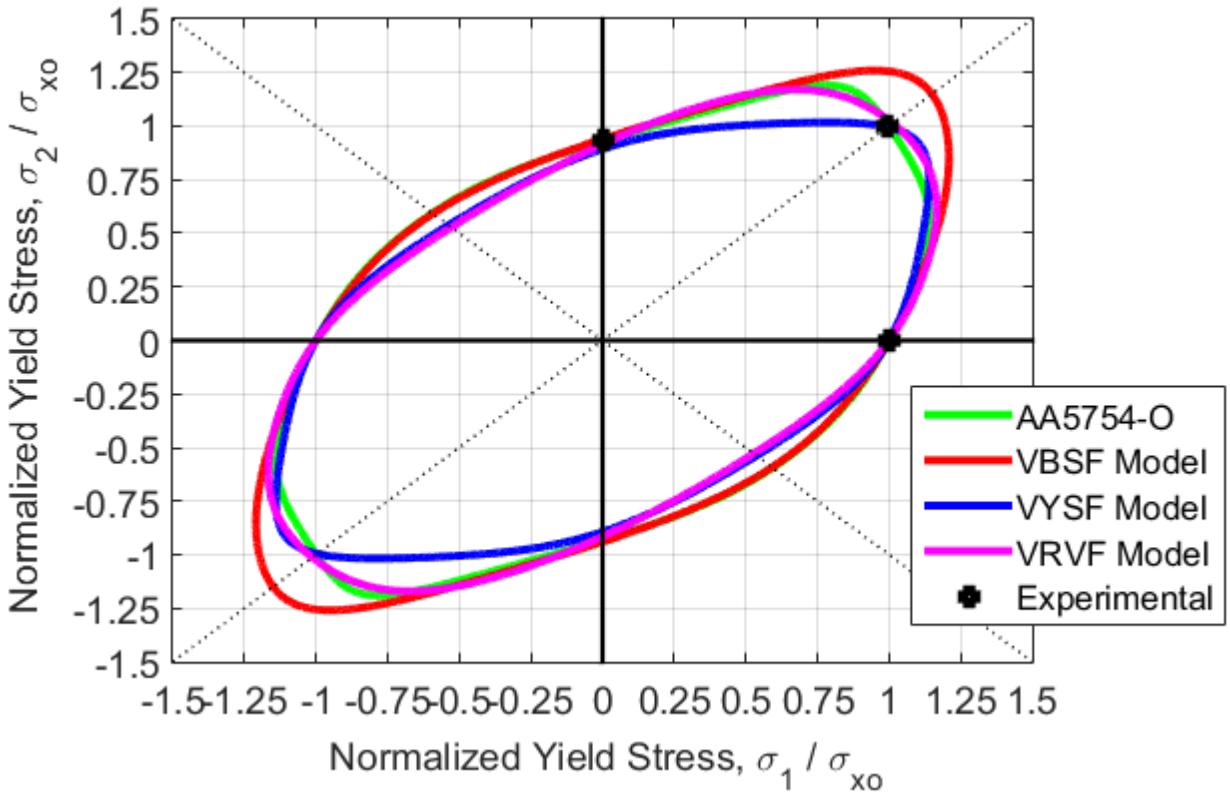

Figure 5.20 - Yield surface plot for fitting i) AA5754-O, ii) $\sigma_b = 1.15$, iii) VYSF Model and iv) VRVF Model for a = 8

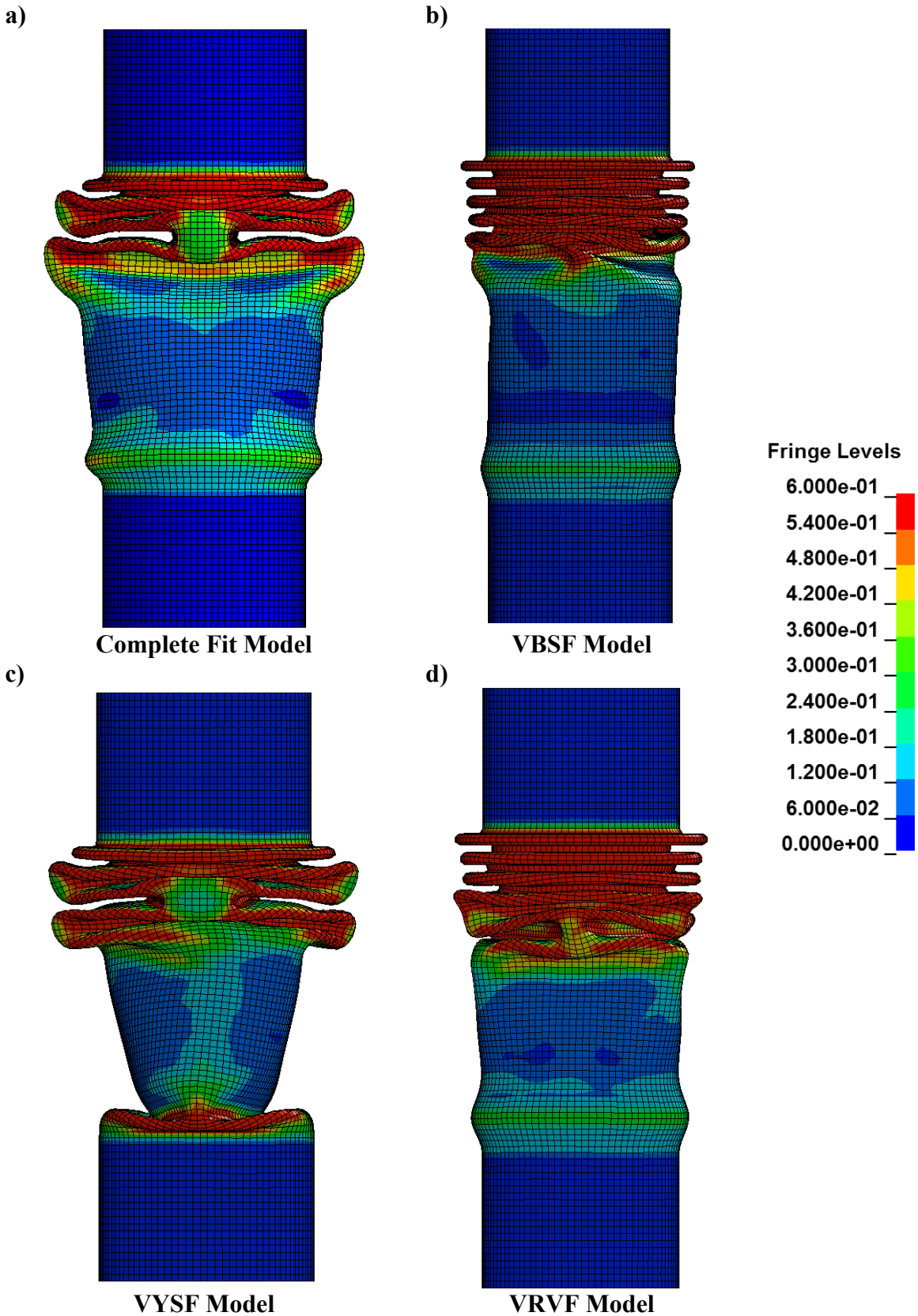

Figure 5.21 - Final crush tube deformation at t = 40.0ms for a) Complete Fit Model, b) VBSF, c) VYSF and d) VRVF for a = 8

a)

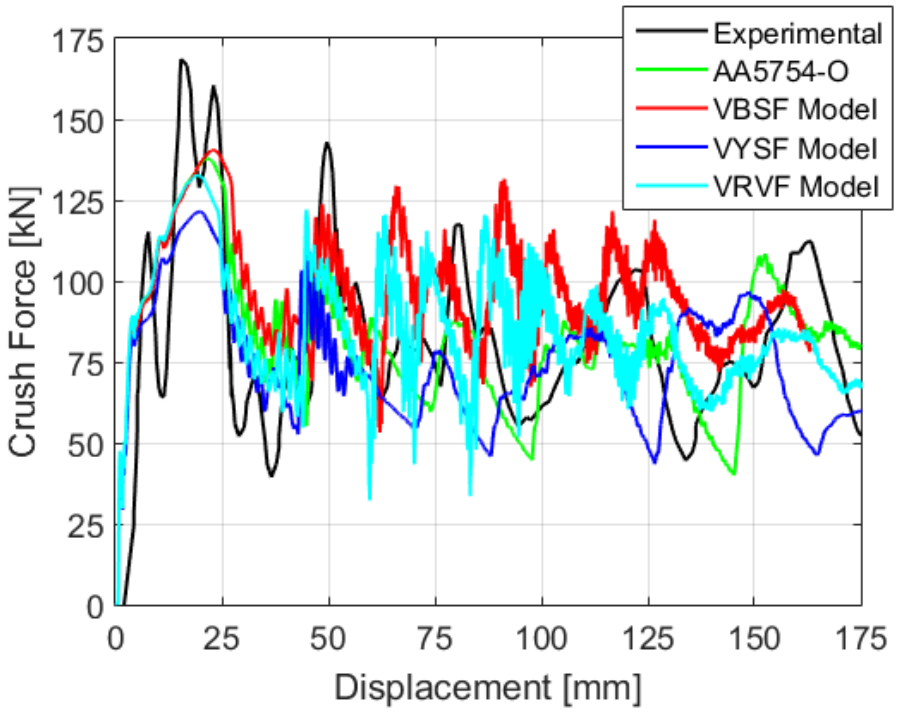

b)

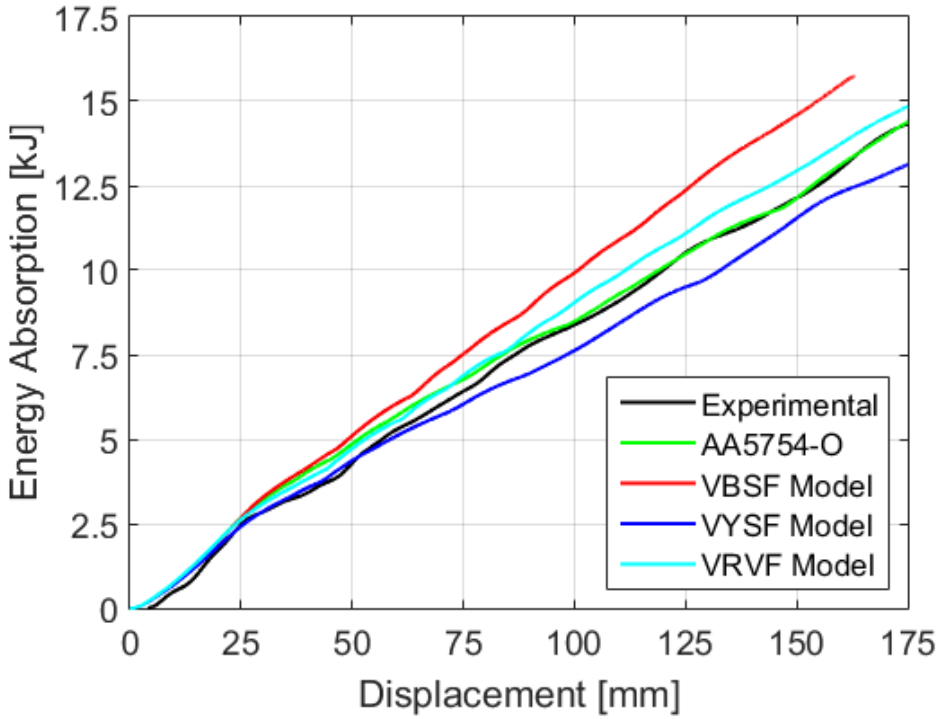

Figure 5.22 - a) Crush force and b) energy absorption response for fitting i) AA5754-O, ii) $\sigma_b = 1.15$, iii) VYSF Model and iv) VRVF Model for a = 8

5.4.3.1 Fitting R-values and Yield Stresses with Varying the Biaxial Yield Stress (VBSF Model)

A normalized biaxial yield stress of $\sigma_b = 1.15$ was selected for this analysis. The overall shape of the yield surface has similar shapes in the uniaxial compression to uniaxial tension region when compared to the complete fit model. However, as expected, varying the biaxial yield stress changes the curvature at the biaxial region. Additionally, it changes the plane strain curvature such that it approaches closer towards the biaxial region. The VBSF Model crush tube produced four complete axi-symmetric folds and an incomplete symmetric fold at the top of the crush tube. It also generates an incomplete axi-symmetric fold at the bottom of the tube. Furthermore, the localized strain contours show different levels developing as a result of the different crush folds.

Figure 5.23 presents the elemental stress-state history around the hoop path for the VBSF Model. Both the VBSF and complete fit model predict similar initial peak crush force (137.9kN vs 140.6kN). Analyzing the yield surface trace, it is seen that the initial load path is dominated by a state of pure compression, which is unaffected by the new yield surface fit. Similarly to the previous stress-states analysis, the structure transitions from a state of pure compression to a state of plane strain. As mentioned earlier, the plane strain region is much closer to the balanced biaxial region. Since the magnitude of balanced biaxial and plane strain region is much larger than previous yield surfaces, higher magnitudes of stresses are developed during the collapse of the structure and thus results in higher plastic work dissipation. This results in a much larger energy absorption (16.83 kJ) and crush force response. It is important to note that the maximum energy absorption measured in the simulation was 15.76 kJ at 163.1mm. Since the energy absorption rate is fairly constant, the total energy absorption at 175mm was extrapolated.

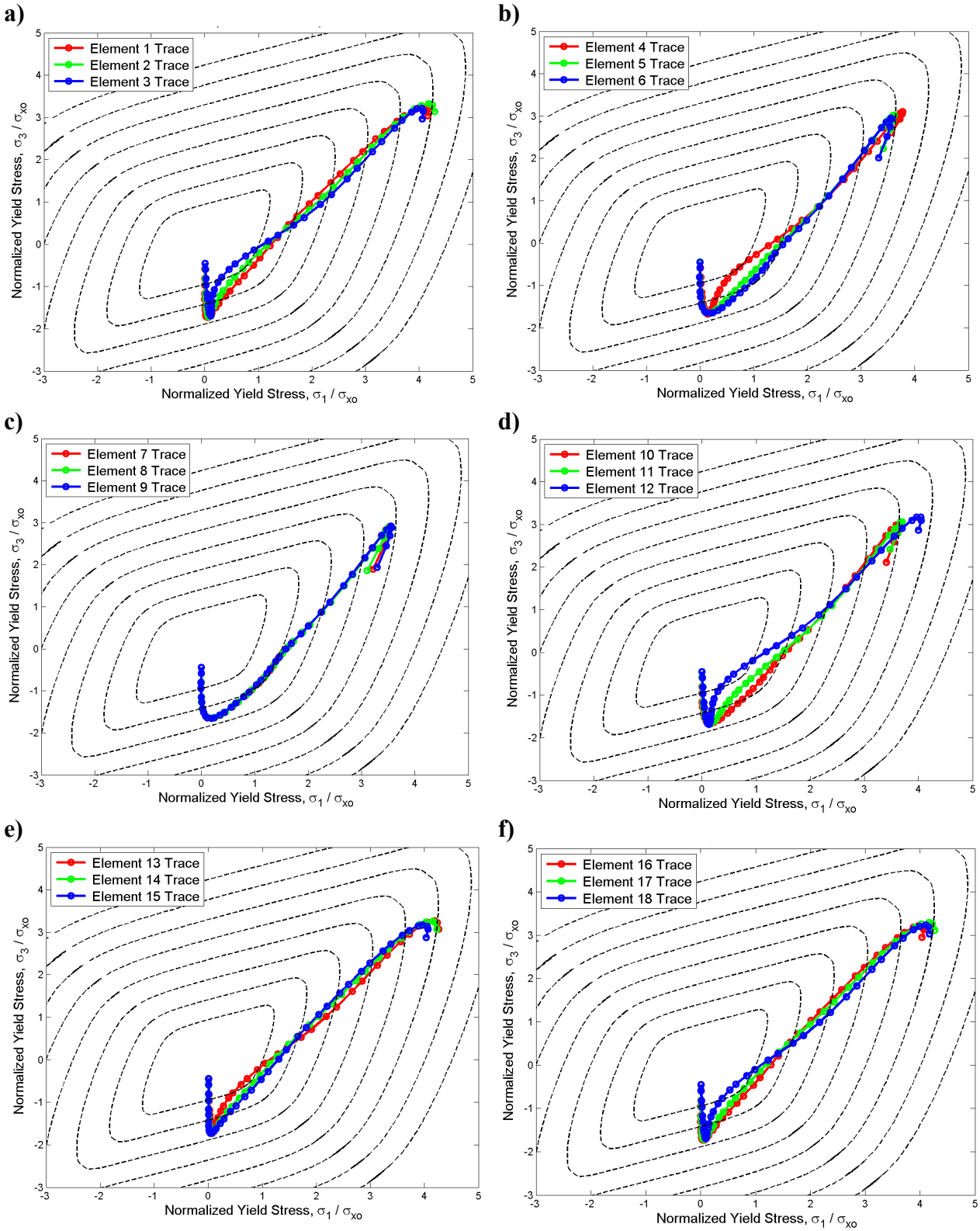

Figure 5.23 - Stress-state history for VBSF Model with a = 8 (a) Elements 1-3, (b) Elements 4-6, (c) Elements 7-9, (d) Elements 10-12, (e) Elements 13-15, and (f) Elements 16-18 along the hoop direction

5.4.3.2 Fitting R-values and Biaxial Yield Stress Varying Yield Stresses (VYSF Model)

The R-values used to generate these coefficients are the same as the R-values obtained for AA5754-O. Figure 5.24 presents the corresponding elemental stress-state history around the hoop direction. The VYSF model produced one complete axi-symmetric fold with three complete and one incomplete symmetric fold. Furthermore, the localized strain contours are unique to this particular set of parameters. This new fitting scheme predicts lower mean crush force (74.16kN), lower energy absorption (13.13kJ) and peak crush force (121.4kN) compared to the complete fit.

Upon initial loading, the loading is a state of pure compression. Since the material model assumes no strength differential, the compressive yield is the same as the tensile yield strength. Thus, the 90^o orientation of the yield stress of the tensile is the same for compression, which is much lower than the complete fitted model. Many examples are presented in literature that demonstrates the positive relationship between the initial yield stress and energy absorption characteristics (i.e., Ref [132]). The VYSF scheme results in a lower initial compressive yield stress and thus results in a lower energy absorption and peak crush force. Further analysis of the elemental stress-state history plot shows the stress state evolves through a state of pure shear. The region of pure shear lies much lower in magnitude compared to the complete scheme, which further contributes to the reduction in energy absorption. The final loading condition transitions to plane strain.

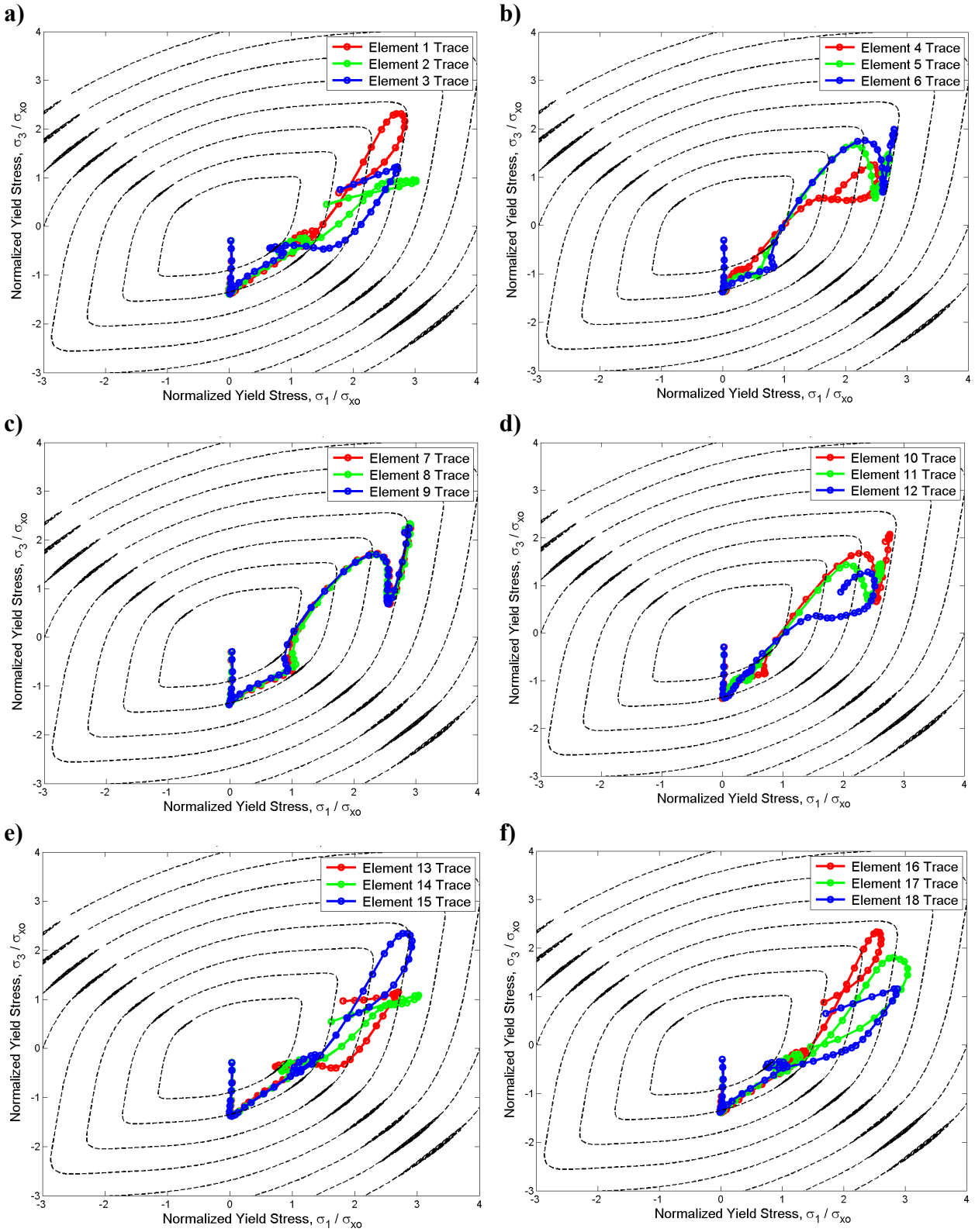

Figure 5.24 - Stress-state history for VYSF Model for (a) Elements 1-3, (b) Elements 4-6, (c) Elements 7-9, (d) Elements 10-12, (e) Elements 13-15 and (f) Elements 16-18 along the hoop direction

5.4.3.3 Fitting Yield Stresses and Biaxial Yield Stress with Varying R-values (VRVF Model)

In this fitting scheme, the normalized yield stress values used to generate these coefficients are the same as those obtained for AA5754-O. Comparing the yield surface of the complete fit of AA5754-O, the VRVF yield surface has similar curvature. However, the VRVF yield surface has a lower yield stress in the pure shear regime and a higher magnitude in the plane strain regime. The new model with varied R-values produces three complete axis-symmetric folds with one complete and one incomplete diamond fold. This new fitting scheme predicts higher mean crush force (84.56kN), more energy absorption (14.85 kJ) and similar peak crush force (132.6kN) compared to the complete fitting of AA5754-O.

Figure 5.25 presents the corresponding elemental stress-state history around the hoop path of the axi-symmetric fold. Figure 5.26 presents the corresponding elemental stress-state history around the hoop path of the diamond fold. Again, the initial loading is a state of pure compression. In the initial folds, the pure compression loading transitions through a state of pure shear to the plane strain. However, instead of unloading elastically, the stress-state transitions back to a state of pure shear. This is due to the significant variations in the R-values. As mentioned earlier, the R-value is a measure of the ratio of the second and third principal strains. In the previous results, the R-values vary mildly, so that the contribution to anisotropy is relatively low and the results are comparable to uniform material behaviour. Furthermore, this results in a uniform elastic unloading behaviour. However, with a large R-value variation in this fitting scheme, a variation exists in the unloading strain path. This incompatibility around the hoop direction causes an internal load that develops shear stress around the circumference during unloading. As a result, the folds developed transition through the pure shear stress state, the material exceeds the yield stress and begins to harden again that results in the extra plastic deformation development and higher energy absorption. The shear stress that develops around the hoop causes an additional loading condition that causes the change from the axi-symmetric crush mode to the diamond crush mode. Analyzing the stress-stress state history of the diamond mode shows a larger pure shear stress contribution in the loading path. However, the stress-state transitions to a state of plane strain that is larger in magnitude than the axi-symmetric mode. This further increases the energy absorption behaviour of the tube.

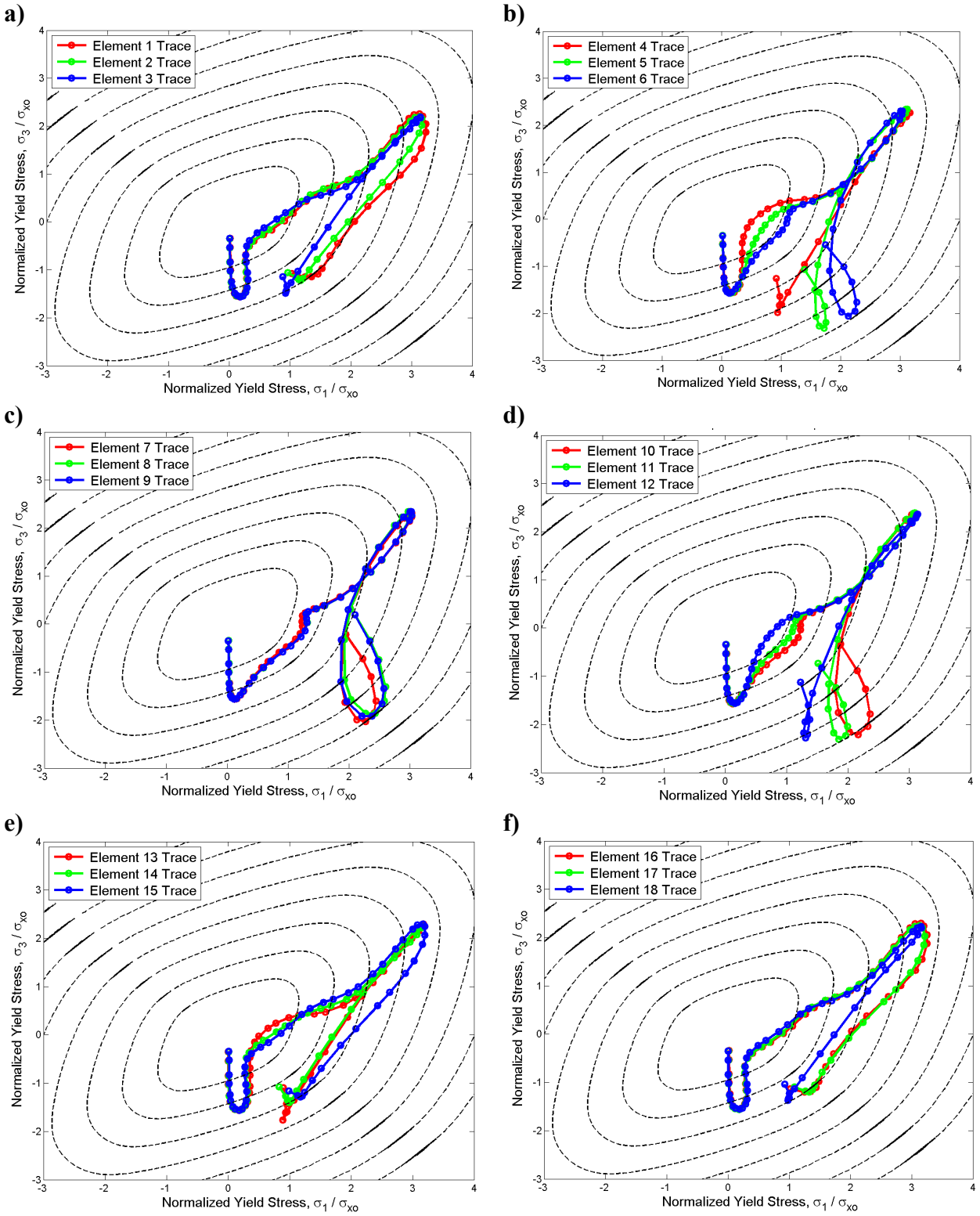

Figure 5.25 - Stress-state history for VRVF Model for (a) Elements 1-3, (b) Elements 4-6, (c) Elements 7-9, (d) Elements 10-12, (e) Elements 13-15 and (f) Elements 16-18 along the hoop direction of axi-symmetric fold

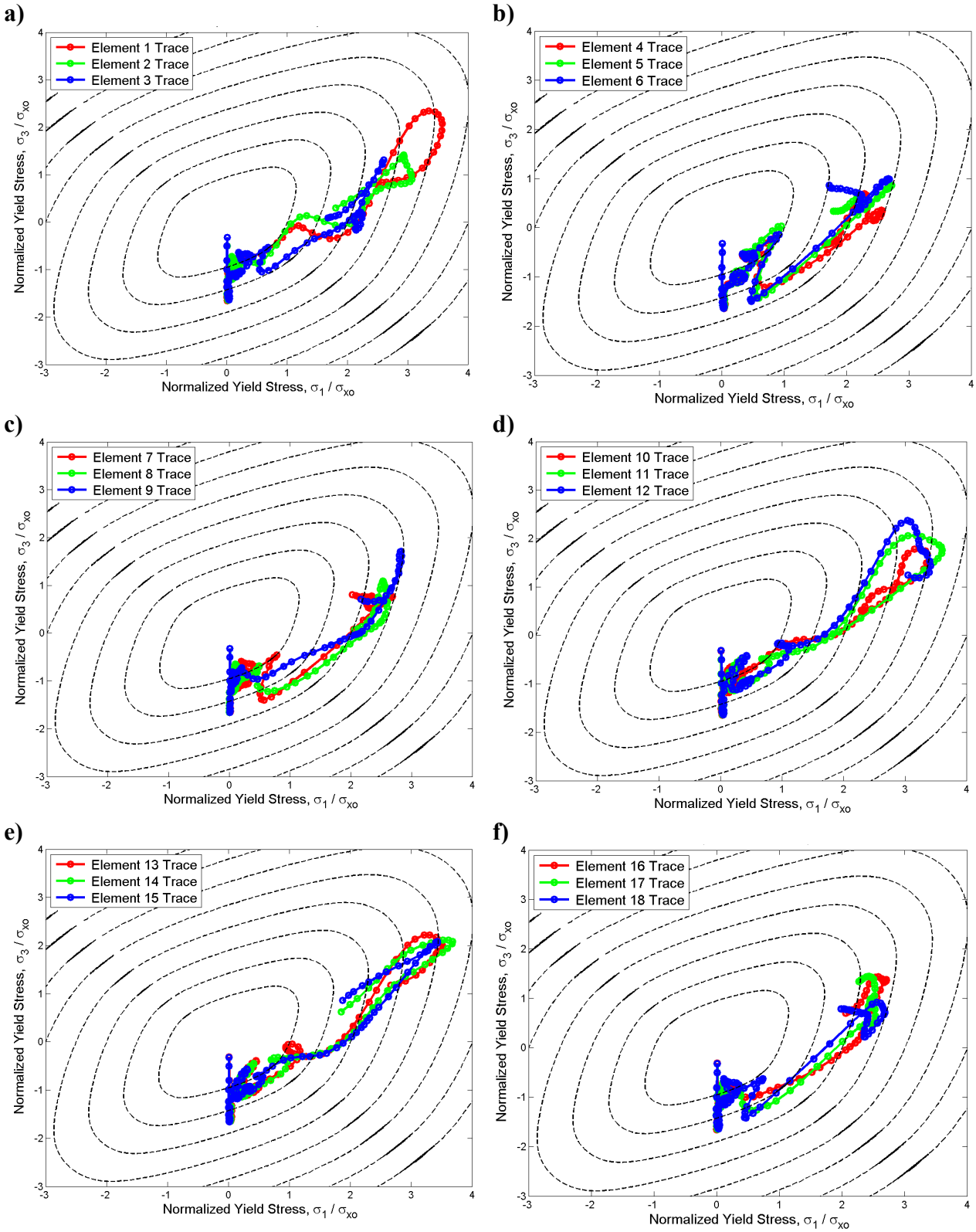

Figure 5.26 - Stress-state history for VRVF Model for (a) Elements 1-3, (b) Elements 4-6, (c) Elements 7-9, (d) Elements 10-12, (e) Elements 13-15 and (f) Elements 16-18 along the hoop direction of diamond fold

5.4.4 Summary of Effects of Yield Surface Shape on Energy Absorption Characteristics

Table 5.8 presents a summary of the energy absorption responses for the three different cases mentioned in Section 5.4. Two dominant points are highlighted and their locations on their respective normalized yield surface: pure shear and plane strain. The corresponding magnitude of each component, with respect to the axes, is calculated as

$$M = \sqrt{{\sigma_1}^2 + {\sigma_2}^2} \qquad (5.1)$$

The yield surface area is also presented in Table 4.2.8. This number is obtained by integrating the yield function, such that

$$A = \int_A f(\sigma_1, \sigma_2) dA \qquad (5.2)$$

Table 5.8 - Summary of effects of the yield surface shape on energy absorption characteristics

Deformation Mode	Pure Shear			Plane Strain			Yield Surface Area	F_{mean} [kJ]	F_{peak} [kJ]	E_{abs} [kJ]
Coordinate	σ_1	σ_2	M	σ_1	σ_2	M				
$a = 3$	0.575	-0.575	0.813	1.127	0.574	1.2648	3.4584	80.98	132.9	14.02
$a = 8$	0.594	-0.594	0.841	1.141	0.555	1.2689	3.5717	81.90	137.9	14.39
$a = 12$	0.551	-0.551	0.779	1.277	0.814	1.5141	3.4877	76.82	124.8	13.40
VBSF Model	0.592	-0.592	0.837	1.209	0.853	1.4795	3.8350	96.66	143.3	16.84
VYSF Model	0.538	-0.538	0.761	1.140	0.749	1.3641	3.2510	74.16	121.4	13.13
VRVF Model	0.527	-0.527	0.745	1.159	0.618	1.3135	3.4704	84.56	132.6	14.85

Figure 5.27 presents the relationship between the normalized yield surface area, location of points of plane strain and pure shear on the energy absorption predictions. A simple linear regression line is also plotted for each component. In these figures, it is shown that the energy absorption of the crush tube is strongly proportional to the total area of the normalized yield surface. Thus, increasing the yield surface area will increase the energy absorption. Dependence also exists between the location of the plane strain and pure shear on the yield surface and the energy absorption. This is a result of these points being the most common strain paths during

axial crushing. The results show a moderate influence on the location of the pure shear state of stress, which is a result of the transitional state of stress from compression to shear.

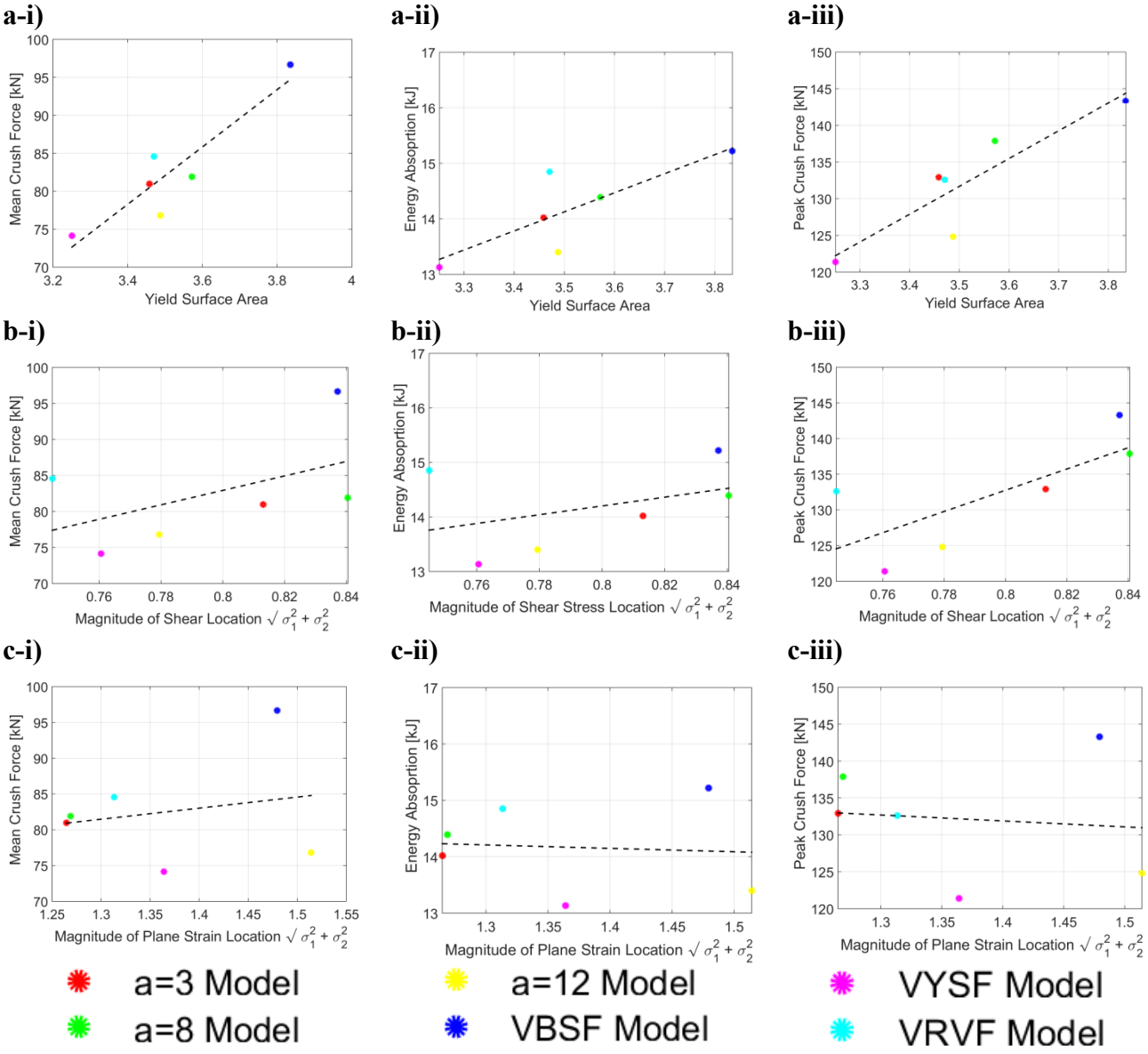

Figure 5.27 - Effect of the (a) normalized yield surface area, (b) shear stress, and (c) plane strain on (i) mean crush force, (ii) energy absorption, (iii) max force

5.5 Chapter Conclusions

In this chapter, the effects of yield surface shape on the energy absorption characteristics of the axial crushing of circular tubes were analyzed. The parameters of CPB06ex2 yield function proposed by Plunkett *et al*. [39] was varied to effects of material anisotropy on the axial impact response. The yield stress and R-values were calibrated to represent experimental anisotropy of AA5754-O sheet for different homogeneity values. This calibration showed that for the same sheet anisotropy, a different yield surface shape could be generated for different homogeneity value. Dynamic simulations were performed and predictions showed good agreement with experimental results for the axial crush of a circular tube. A new stress-state history analysis of crush mechanics was presented to identify the dominate strain paths during axial crush. Furthermore, a systematic study was performed to identify the individual contributions of material anisotropy on the axial crush response. Accordingly, the numerical analysis presented in this study showed that:

- Predictions of axial crush response strongly depend on the shape of the yield surface. Thus, the correct representation of the material anisotropy (yield stresses, R-values, etc.) alone is not sufficient for accurate predictions of axial crush.
- A homogeneity factor of 8 ($a = 8$) for the yield function CPB06ex2 provides the most accurate predictions for axial crushing of aluminum circular tubes.
- For accurate first order predictions of energy absorption (ignoring local fracture), balance biaxial tension is the most important material anisotropy parameter. Accurate characterizations of the yield stress variation are important for predicting the initial and mean crush forces, while accurate characterizations of the R-values are important for predicting the resulting crush modes after initial impact
- Energy absorption capabilities of a material are strongly dependent on the area under the yield surface.

6 DEVELOPMENT OF HIGH CRUSH EFFICIENT, EXTRUDABLE ALUMINUM FRONT RAILS FOR VEHICLE LIGHTWEIGHTING - C.P. Kohar, A. Zhumagulov, A. Brahme, M.J. Worswick, R.K. Mishra, K. Inal (2016). International Journal of Impact Engineering, 95, p. 17-34

This chapter presents the development of a new framework for optimization geometric cross section profiles of front rail geometries that maximizes crash energy absorption characteristics. The new design is coupled with material and process development to provide a component with superior energy absorption and strength characteristics that is commercially sustainable. Simulations of the extrusion crush behaviour are performed using the anisotropic Barlat *et al.* Yld2000 yield function [34]. The simulations are compared to the dynamic crush results for this extrusion. The size of the structure is optimized using the response surface methodology, using artificial neural networks metamodels and simulated annealing optimization techniques. The specific energy absorption (SEA) is used as a single optimization objective function for maximizing energy absorption and minimizing mass. An analytical relationship that relates the SEA function to the crush efficiency is derived to show that a single optimization function parameter may be sufficient for mass minimization. Analysis is performed to identify key extrusion operational parameters and the wall thickness is identified as the most important parameter to control during extrusion. The results of this work have been published in Kohar et al. [133].

6.1 Introduction

Recently, the use of optimization software has served as a valuable tool in improving the crashworthiness performance by coupling these algorithms with finite element simulations [134]. Machine learning and optimization techniques have been applied to such models to increase the crash performance by varying the sizing, topology and topography of the structure. This approach, known as structural optimization through the response surface methodology [12], has been employed to optimize the shape of honeycomb structure to maximize the energy absorption [11]. Through this technique, they have been able to optimize the energy absorption of the structure, while minimizing mass.

In this chapter, an optimization framework for increasing the energy absorption and minimizing mass of an aluminum extrusion profile with a multi-cellular structure as a crush

structure is presented. A multi-cellular aluminum extrusion profile is an excellent candidate for further optimization because the wall thickness – a parameter that strongly correlates with mass as well as energy absorption - can be easily controlled and varied in the manufacturing process. A multi-cavity extruded tube made from an AA7xxx alloy that satisfies the design constraints and meets the crush energy absorption needs for front rail applications in a current production vehicle is then taken as a benchmark for optimization of 6xxx structure in this investigation. The benchmark tube is experimentally crush tested using a dynamic sled apparatus to obtain the experimental energy absorption response. AA6063-T6 extrusion with the same profile is crushed under the same experimental conditions for comparison. The commercial FE software, LS-DYNA, is used to simulate the crush behaviour of the AA6063-T6 structure using measured material anisotropy and high strain rate behaviour data from the extruded tubes as input. The simulation results are compared to experimental results to validate the FE model. New multi-cellular extrusion profiles are developed through FE modeling, manufactured, sled-tested and crush simulation results are compared with experiments. The size of the new multi-cellular extrusion is optimized using the response surface methodology, to further improve the energy absorption characteristics, while the topology and topography is held constant. The sizing of the extrusion is varied using the commercial optimization package, LS-OPT. The specific energy absorption, which maximizes the energy absorption and minimizes the mass, is selected and evaluated as a single optimization objective.

6.2 Experiments

Figure 6.1 presents the cross-section of the baseline extrusion profile. Commercially available AA6063 billets were extruded using a commercial extrusion press and the extruded rails were artificially aged to a T6-temper. Figure 6.2 shows a new multi-cellular four-cell hexagon structure, referred to as UWR4 extrusion profile, which was also extruded. The multi-cellular topology was developed through an optimization of the number of crush elements within the profile envelop (for further details on this approach, the readers are refer to Ref [11, 68, 104]). Each aluminum extrusion profile was cut to a length of 464mm for crush experiments. Table 6.1 presents the length, mass and other data for the tested materials. Table 6.2 lists the chemical composition of the extruded tubes.

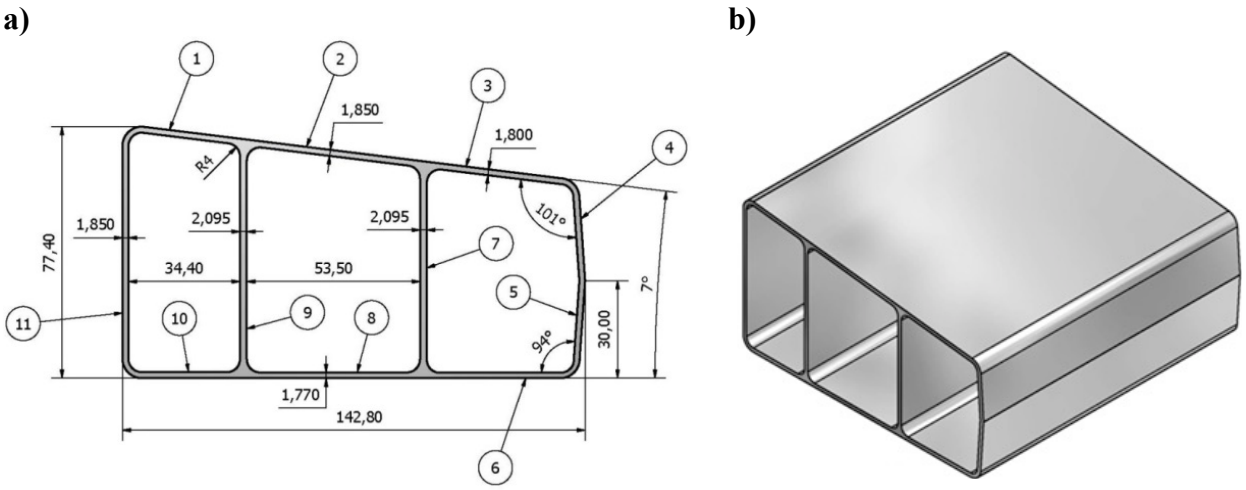

Figure 6.1 - (a) Cross Section and (b) Isometric view of baseline extrusion profile

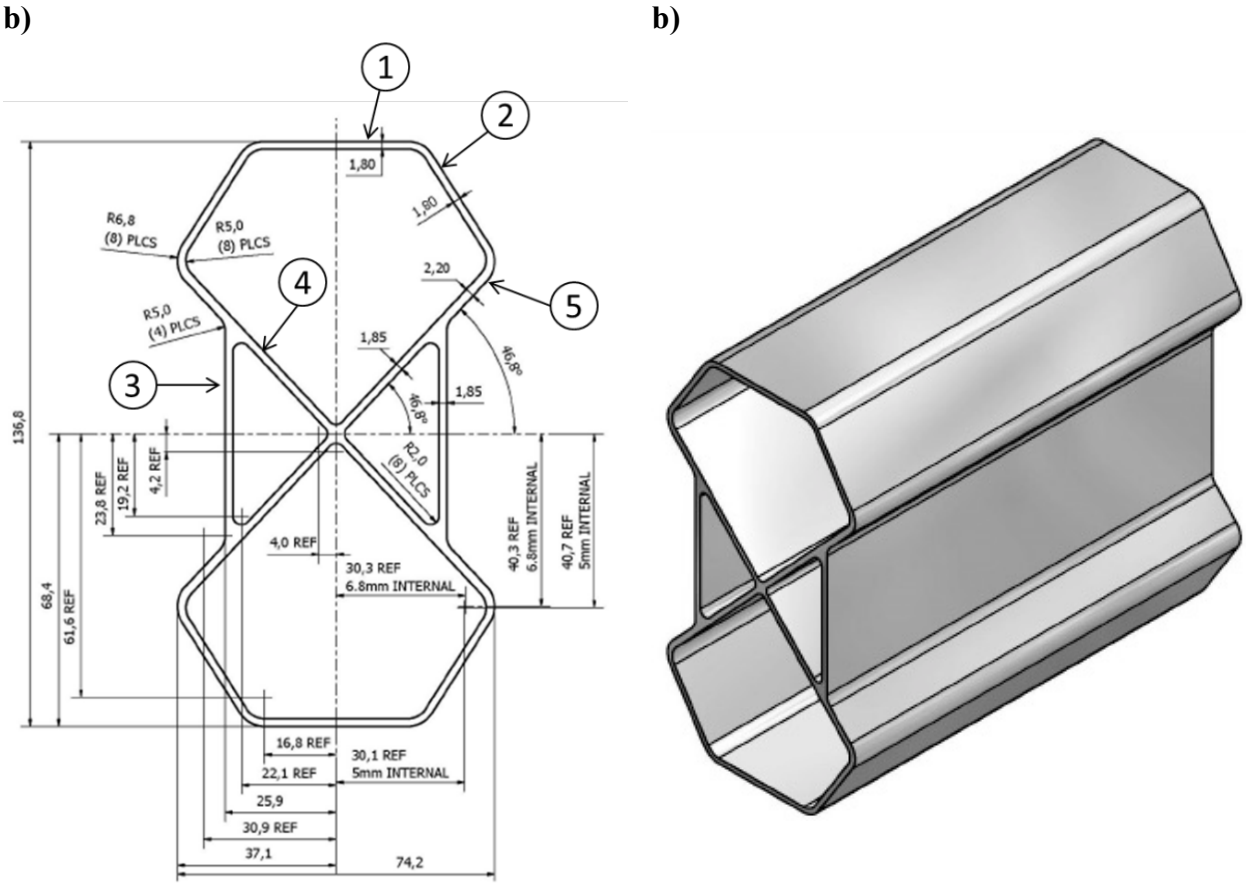

Figure 6.2 - (a) Cross Section and (b) Isometric view of new UW-R4 extrusion profile [103]

Table 6.1 - Extrusion Length, Mass and Specific Length of 7xxx Series and 6063 Extrusions

	Length [mm]	Mass [g]	Specific Length [g/mm]
Baseline 7xxx Profile	464	1494	3.22
Baseline AA6063-T6 profile	464	1295	2.79
UW-R4 AA6063-T6 profile	464	1234	2.66

Table 6.2 - Chemical composition of extrusion AA6063 aluminum alloy (wt%)

Al	Mg	Mn	Fe	Si	Cu	Ti
Bal	0.490	0.029	0.160	0.400	0.010	0.010

Quasi-static uniaxial tensile tests, in accordance with ASTM-E8, were performed using specimens cut along the extrusion direction of the baseline profile to explore the variation in the mechanical behaviour in eleven different locations (as indicated in Figure 6.1). The resulting true stress-true strain curves are shown in Figure 6.3. Some variation existed in the T6-temper mechanical responses. In particular, two stress-strain responses exceeded the average response, due to the variation in the cooling rate of the internal webs (numbered 7 and 9 in Figure 6.1) during the extrusion process. An average stress response was fit to a power-law hardening model [58]. Table 6.3 lists the representative parameters.

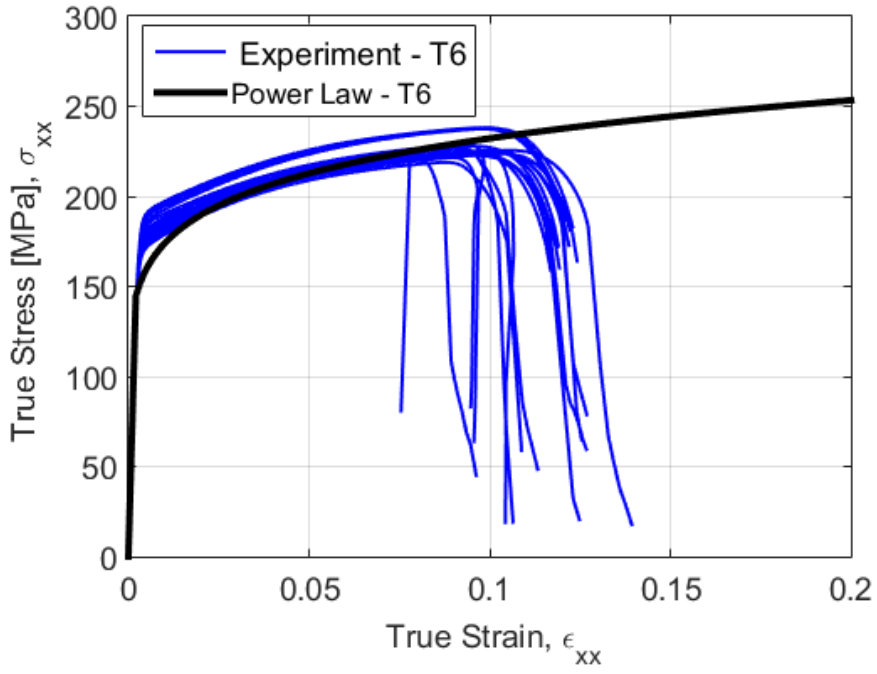

Figure 6.3 - Stress-strain from tensile tests of extrusion AA6063-T6 for various locations at quasi-static strain rate [103]

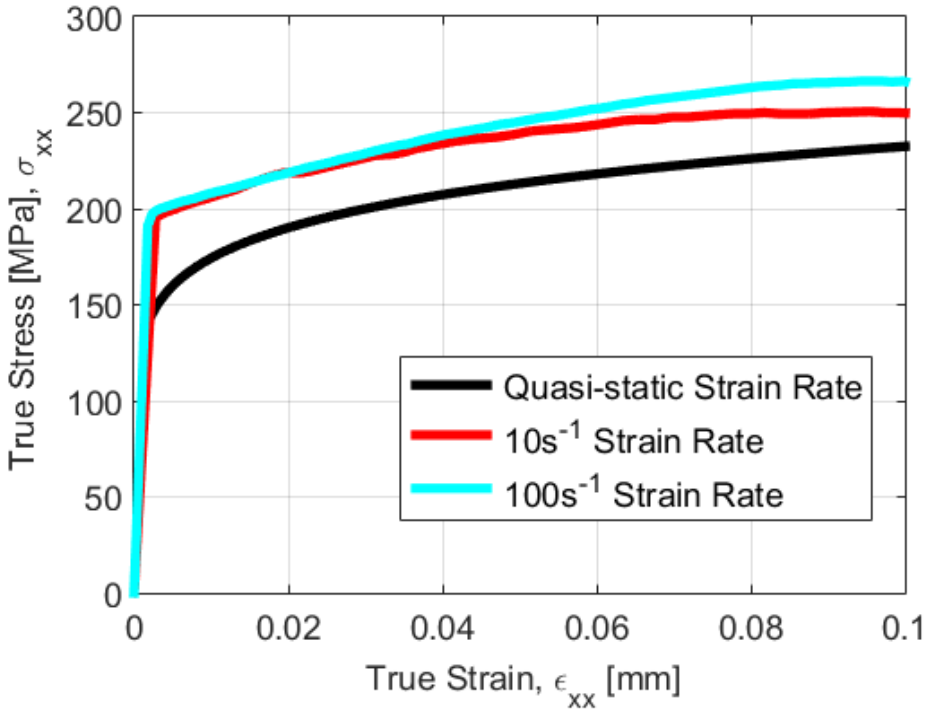

Figure 6.4 - Stress-strain response for quasi-static, 10s^{-1}, 100 s^{-1} strain rates of extrusion AA6063-T6 [103]

Table 6.3 - Power-law hardening parameters for the extruded AA6063 aluminum alloy [103]

	AA6063-T6
K [MPa]	310
n	0.125
ε_0	0.0022

In the experimental work of Hsu and Jones [113] for extruded AA6063-T6, it was reported that this alloy exhibits moderate strain rate sensitivity. Thus, moderate strain rate tensile testing was performed for strain rates of 10/s and 100/s. Miniature dog-bone specimens were cut from the extrusion and pulled in uniaxial tension using a hydraulic intermediate strain rate apparatus. The details about the experimental apparatus and testing procedure are similar to that described in Bardelcik *et al.* [135]. The power law plasticity relation, coupled with the Cowper-Symonds strain rate sensitivity [53], was used to characterize the strain-rate sensitivity. Strain rate sensitivity parameters of $M = 5.60\times10^{10}s^{-1}$ and $P = 12.6$ were calibrated to the moderate strain rate data presented in Figure 4. These values compare well with the experimental values obtained from the work of Hsu and Jones [113] for extruded AA6063-T6, ($M = 9.39\times10^{10}s^{-1}$ and $P = 9.55$).

A schematic of the dynamic crush experimental setup is shown in Figure 6.5. The aluminum extrusions were clamped between steel boss structures and impacted using a sled-track apparatus. Only one profile was tested at a time. The mass of the sled was 855kg and the impacting speed was 8.00 m/s [28.8km/h]. No crush triggers were used for any of the dynamic tests. A 12.7mm [0.50"] plywood sheet was mounted to the end plate to minimize the high frequency noise from the metal-to-metal contact. Aluminum honeycomb blocks were used to dissipate any excessive sled energy in the event of an unforeseen catastrophic failure of the crush tube. This setup provided for a free-crush length of 125mm for each extrusion before the sled-mass would impact the aluminum honeycomb blocks.

Figure 6.6 shows the experimental force-displacement and energy absorption response of the tubes from the dynamic crush experiments. Three repeats were performed for each geometry. The force-displacement response had several oscillations in the response, attributed to the structural vibrations of the sled-track setup [14]. To attenuate the noise, the raw dynamic force-displacement response was post-processed using a SAE CFC 180 filter. Figure 6.7 shows the experimental crushed tubes for each profile. Each experimental crush tube produced a combination of Type-I crush modes during crush [72]. Table 6.4 lists a summary of the energy absorption, mean crush force, peak crush force, and the crush efficiency at different velocities. The mean crush force values of the baseline AA7xxx, baseline AA6063-T6, and UWR4 AA6063-T6 profile are 171.4kN, 92.5kN, and 121.9kN respectively. At 125mm crush distance, the baseline 7xxx Series, baseline AA6063-T6, and UWR4 AA6063-T6 absorbed 20.6kJ, 11.0kJ, and 14.6kJ of energy respectively. The peak crush force values for respective profile are 255.4kN, 161.4kN and 190.0, corresponding to a crush efficiency of 67.1%, 57.3% and 64.2%, respectively. The UWR4 AA6063-T6 tube had a higher mean crush force and energy absorption than the baseline AA6063-T6 tube. Although the peak crush force of the UWR4 AA6063-T6 was higher than that of the baseline AA6063-T6, its crush efficiency was higher. Thus, the UWR4 structure had a superior crush performance than the baseline structure. The Baseline AA7xxx tube had the best crush performance, but it also had the most mass. Therefore, the energy absorption characteristics of the UWR4 needs to be further optimized by varying mass as well as material properties attainable in AA6xxx series alloys to replace the AA7xxx extrusions.

a)

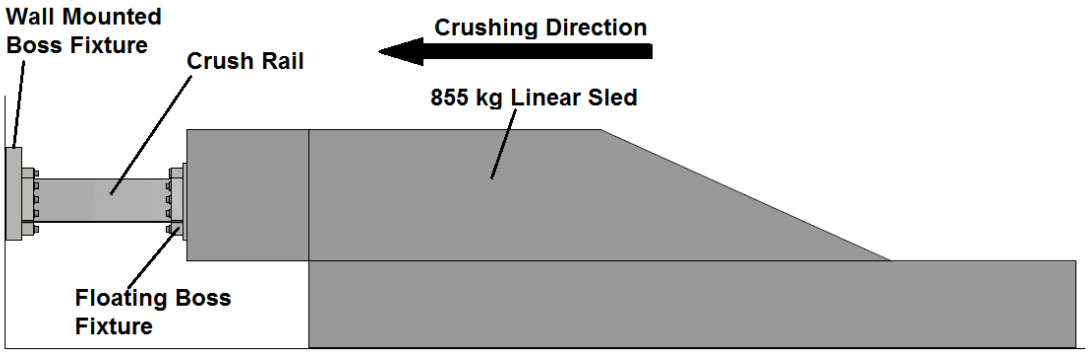

b)

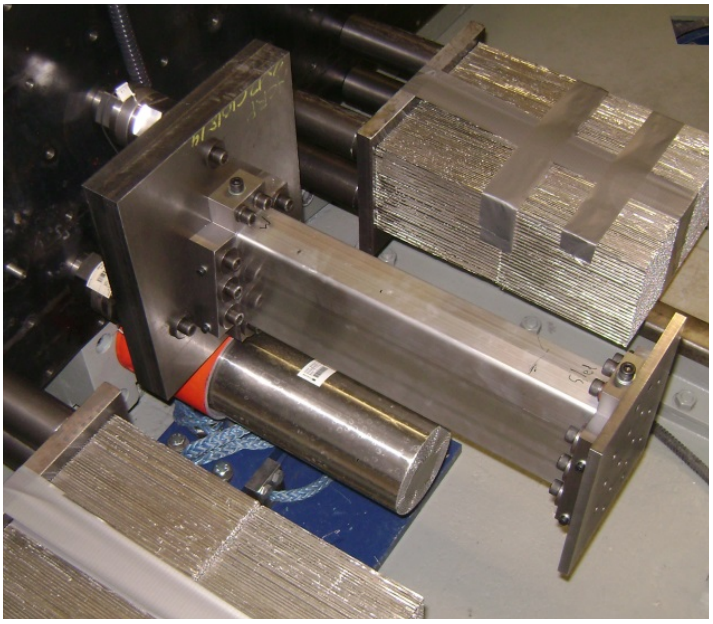

c)

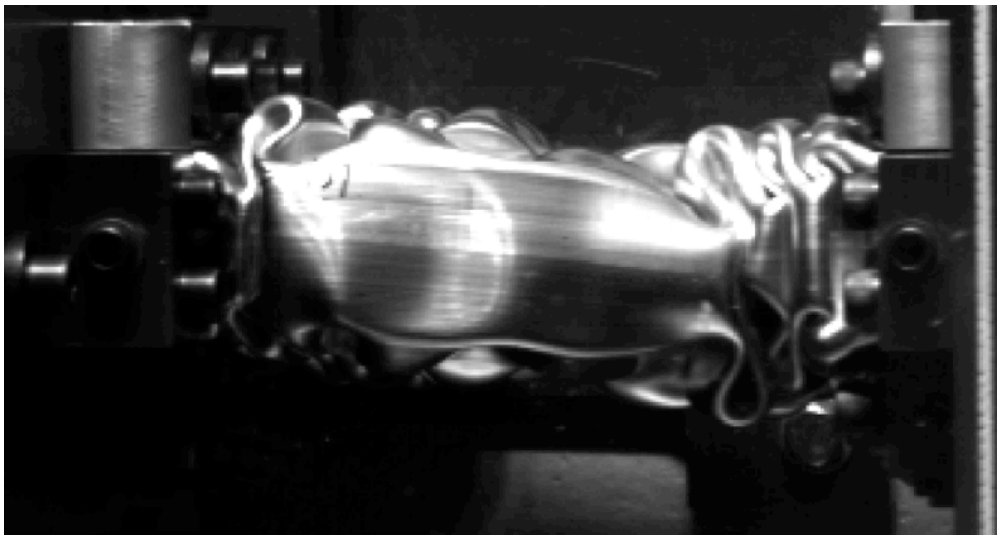

Figure 6.5 - (a) Schematic of the sled-track testing apparatus, (b) experimental setup and (c) tube crushing during impact [103]

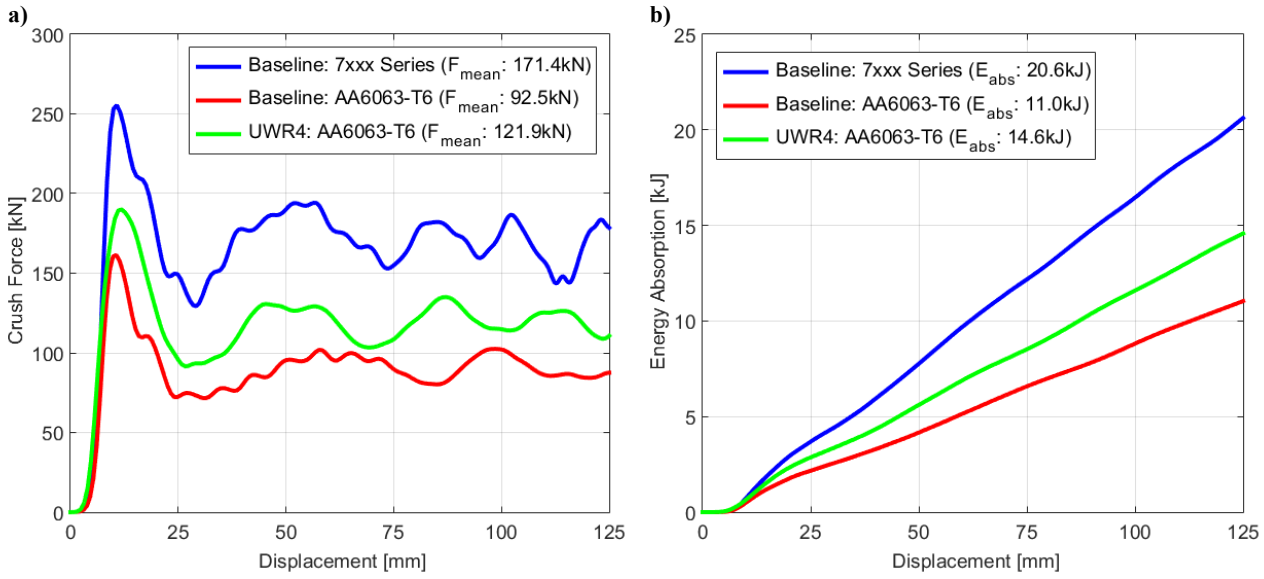

Figure 6.6 - Experimental (a) force-displacement and (b) energy response for Baseline Profile – 7xxx Series, Baseline Profile – AA6063-T6 and UWR4 Profile – AA6063-T6

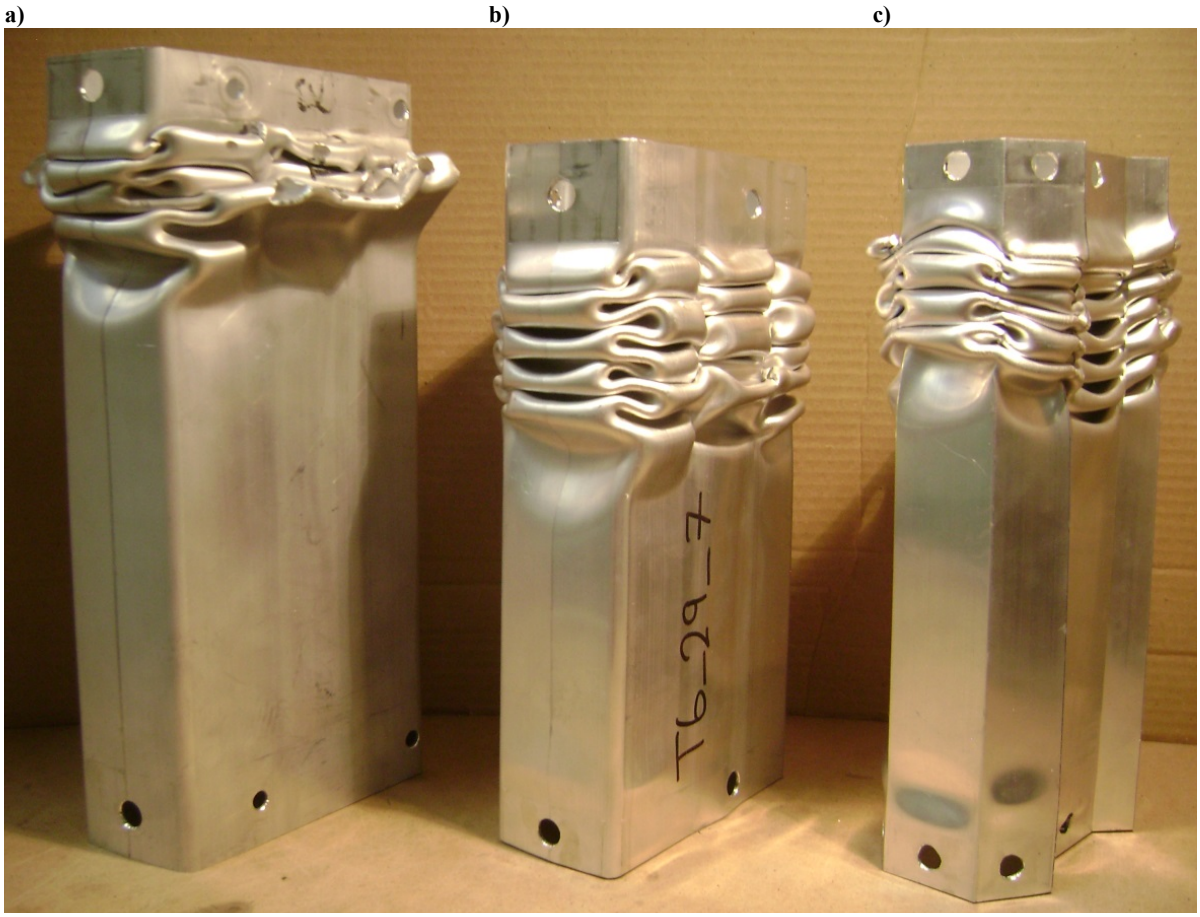

Figure 6.7 - Experimentally crushed (a) Baseline Profile – 7xxx Series, (b) Baseline Profile – AA6063-T6, and (c) UWR4 Profile – AA6063-T6 [103]

Table 6.4 - Summary of Experimental Crush Response for Profiles [103]

	Baseline Profile 7xxx Series	Baseline Profile AA6063-T6	UWR4 Profile AA6063-T6
Energy Absorption [kJ]	20.6	11.0	14.6
Mean Crush Force [kN]	171.4	92.5	121.9
Peak Crush Force [kN]	255.4	161.4	190.0
Crush Efficiency [%]	67.1	57.3	64.2

6.3 Constitutive Modeling

As shown in Chapter 5, both the effects of Lankford coefficients and the yield stress as a function of orientation have a significant effect on simulation predictions of the energy absorption characteristics. The goal of this study is to demonstrate the influences of capturing the anisotropy using a simple anisotropic yield function, such that the computational time is minimal.

The Barlat and Lian (1989) [33] yield function is able to capture the variation of the Lankford coefficients, but does not capture the yield stress variation. As observed both by Jansson *et al.* [136] and Achani *et al.* [116], extruded aluminum alloy AA6063 has a larger Lankford variation than the yield stress variation with respect to the extrusion direction. Using the simple Barlat and Lian (1989) yield function can over emphasize the yield stress variation because it is not directly captured in the yield function. In Achani *et al.* [116], the Yld2000 and Yld2004 yield functions by Barlat *et al.* [34, 35] were evaluated for their applicability for extruded aluminum alloy AA6063-T6. They found that the Yld2004 yield function captured the anisotropy better than the Yld2000 yield function. However, the Yld2004 yield function required 18 parameters to calibrate the yield function, as opposed to the 8 parameters required for the Yld2000 yield function. Furthermore, the Yld2004 yield function requires individual linear stress transformations to be computed, which requires significantly more computational resources. Therefore, the Barlat *et al.* [34] Yld2000 yield criterion is employed through this study because it has good predictive capability with reasonable computational efficiency. The Yld2000 constitutive model [34] is utilized as *MAT_133 (*MAT_BARLAT_YLD2000) in LS-DYNA.

Table 6.5 presents the experimental anisotropy parameters (Lankford Coefficients) and yield stress variations for extruded AA6063-T6 given by Achani *et al.* [116], that are used in this

study. Figure 6.8 presents the normalized (about x-direction) yield surface calculated using the above data. The isotropic von Mises yield surface is also presented for comparison.

Table 6.5 - Experimental Lankford Coefficients and Yield Stress Variation [116]

R_{00}	R_{45}	R_{90}	σ_{00}	σ_{45}	σ_{90}	R_b	σ_b
0.5667	0.3400	2.8567	226.556	207.068	195.88	0.4800	226.556

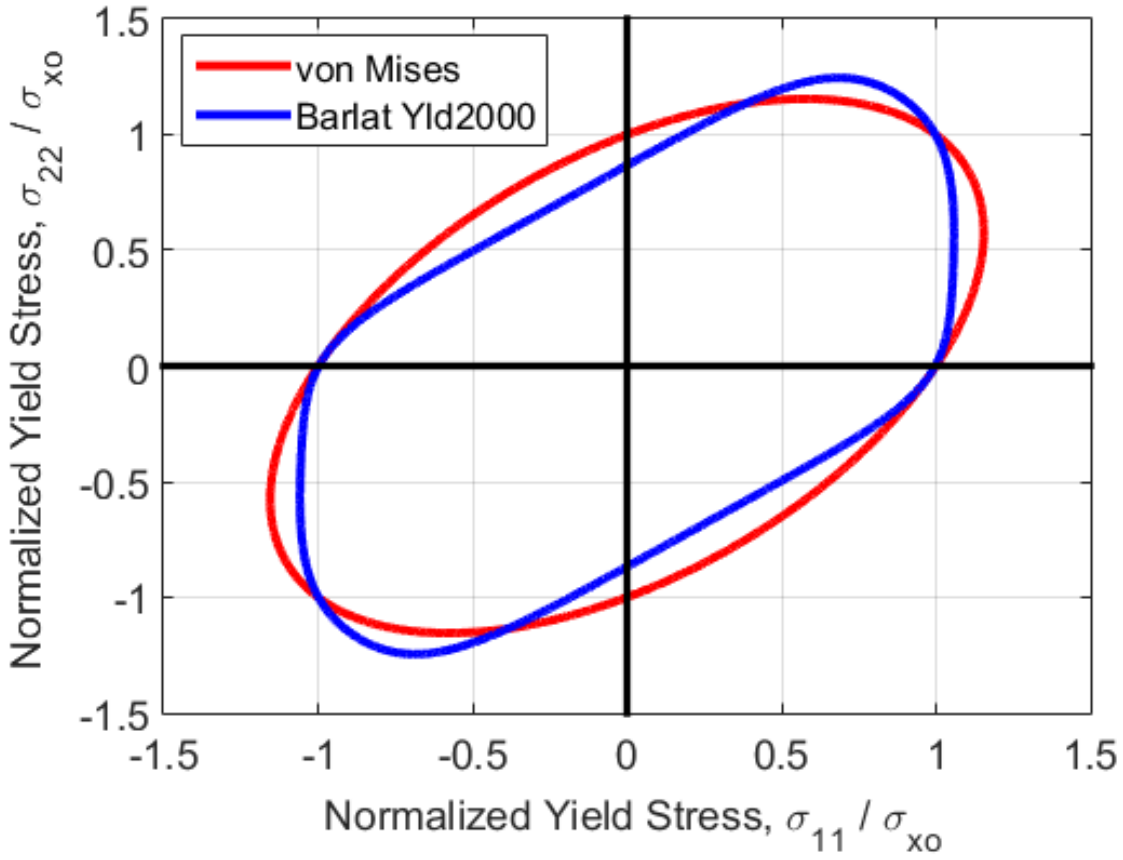

Figure 6.8 - Yield surface shape for the isotropic von Mises and anisotropic Barlat *et al.* Yld2000

6.4 Finite Element Modeling

The axial crushing response of extruded tubes of the baseline AA6063-T6 and UWR4 AA6063-T6 were simulated using a finite element (FE) model. A non-linear explicit dynamic formulation available in the commercial LS-DYNA software FE code was used throughout this work [58]. The FE models for the two profiles are shown in Figure 6.9 and Figure 6.10. The FE mesh was generated using the commercial meshing software Altair Hyperworks Hypermesh. The

FE model setup and comparison with experiments are presented and discussed below and is similar to the approach in Chapter 0.

The FE model consists of the crush tube constrained between two steel bosses. Each crush tube was meshed about the mid-thickness of the profile geometry, which are presented in Figure 6.1 and Figure 6.2. Each of the five unique wall thickness sections (shown in red, blue, brown, magenta and cyan) were individually meshed. The top (yellow) and bottom (green) boss fixtures were individually meshed according to the experimental setup requirements. The top boss was assigned a mass of 855kg by modifying the density of steel. The top boss was constrained axially in the z-direction and was given an initial velocity of 8m/s. The base boss fixture was constrained in all degrees of freedom on the bottom face. A total simulation time of 30 milliseconds was used for this study. The force-displacement response of the top boss was monitored to obtain the energy absorption characteristics. The elastic material properties are listed in Figure 6.6**.**

The steel bosses were modeled as an elastic material. Eight-node brick elements with full selective reduced integration were used to model these components. A mesh size of 2.00mm × 2.00mm × 2.00mm was employed for the bosses. A 6mm region was meshed around the outside of the crush tube to simplify the model. The crush tube was meshed using Belytschko-Tsay shell elements to simulate plane stress deformation. A mesh size of 2.00mm × 2.00mm with 7 through thickness integration points was employed through the crush tube. As presented in Section 5.3, contact algorithms are placed between the crush tube and the rigid plates to capture the friction of the crush tube folds against the bosses. The static and dynamic coefficients of friction were set to 0.45 and 0.40 respectively. Self-contact algorithms were also placed to capture the effects of the folds stacking onto each other. Accordingly, the static and dynamic coefficients of friction for this contact were set to 1.04 and 1.00 respectively [130].

Table 6.6 - Elastic material properties of aluminum and steel

	Aluminum	**Steel**
Density [g/cm^2]	2.70	7.80
Elastic Modulus [MPa]	67900	205000
Poisson Ratio	0.34	0.30

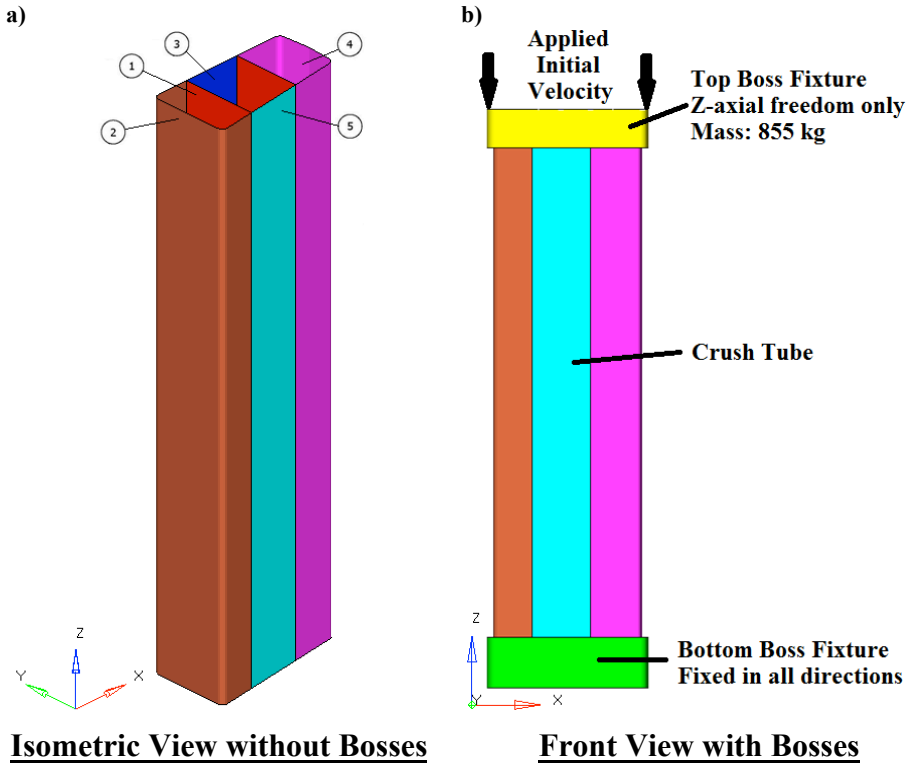

Figure 6.9 - (a) Isometric View without Bosses and (b) Front View with Bosses of Omega Profile

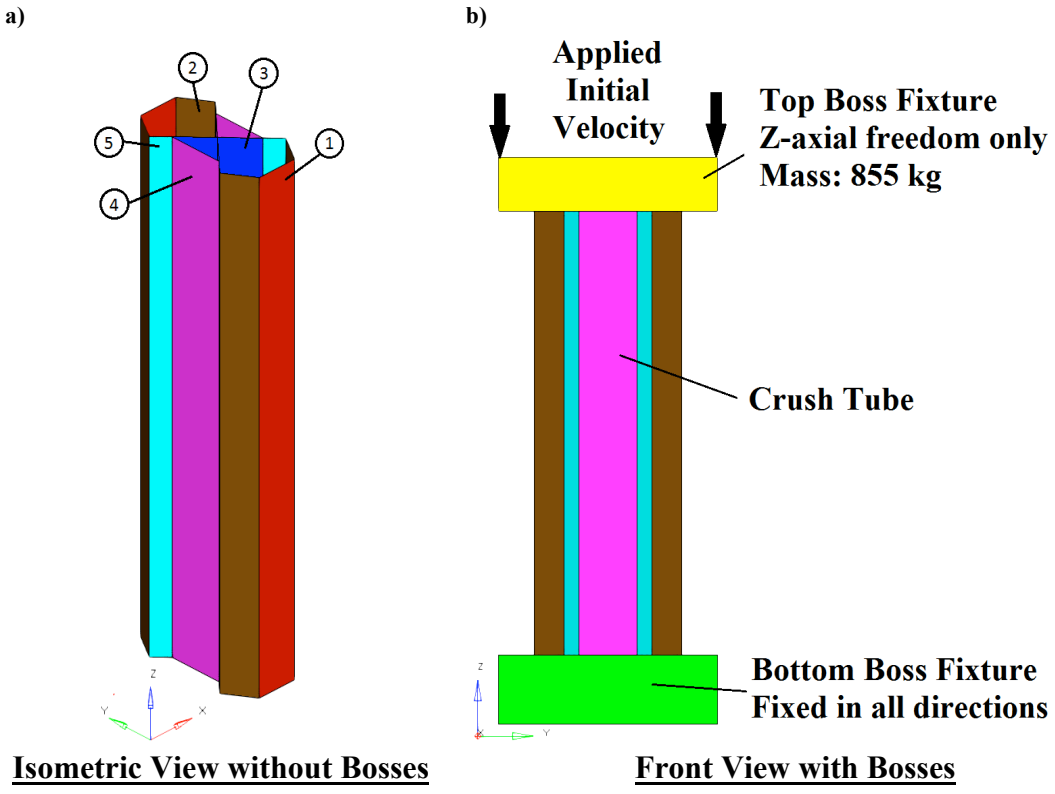

Figure 6.10 - (a) Isometric View without Bosses and (b) Front View with Bosses of UWR4 Profile

6.4.1 Comparison of experiment with simulation

Figure 6.11 presents the predicted effective plastic strain contours for the Baseline Profile – AA6063-T6 and UWR4 – AA6063-T6. The folding patterns of each simulation show good agreement with the experimental deformation. Figure 6.12 presents the force-displacement and energy absorption predications for each profile that was simulated. Each force-displacement response was filtered using a SAE CFC 180 filter. Table 7 and Table 8 presents the predicted mean crush force, energy absorption, peak crush force and crush efficiency for each respective simulated profile. The error, denoted as ΔErr, between the simulation prediction and experiment for each simulated profile is also presented in Table 6.7 and Table 6.8. The error for the Baseline AA6063-T6 mean crush force, peak crush force, energy absorption, and crush efficiency was 7.6%, 5.9%, 2.7%, and 1.0% respectively. The error for the UWR4 AA6063-T6 mean crush force, peak crush force, energy absorption, and crush efficiency was 0.0%, 2.9%, 0.0%, and 1.9% respectively. The overall trend of the force-displacement response and energy absorption-displacement response show good agreement with each experiment. Since the model has good predictive capabilities, it is concluded that the FE model has been constructed properly and is suitable for size optimization.

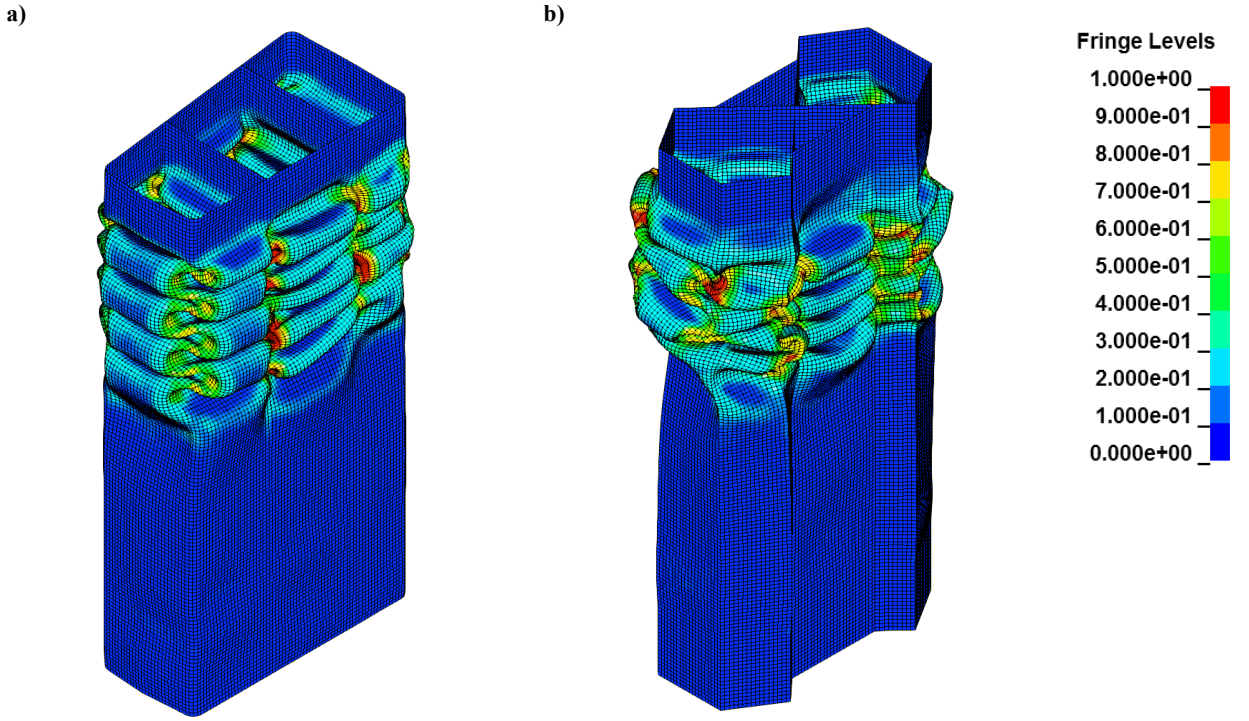

Figure 6.11 - Simulated crush tube effective strain contours for (a) Baseline Profile – AA6063-T6, and (b) UWR4 Profile – AA6063-T6 models

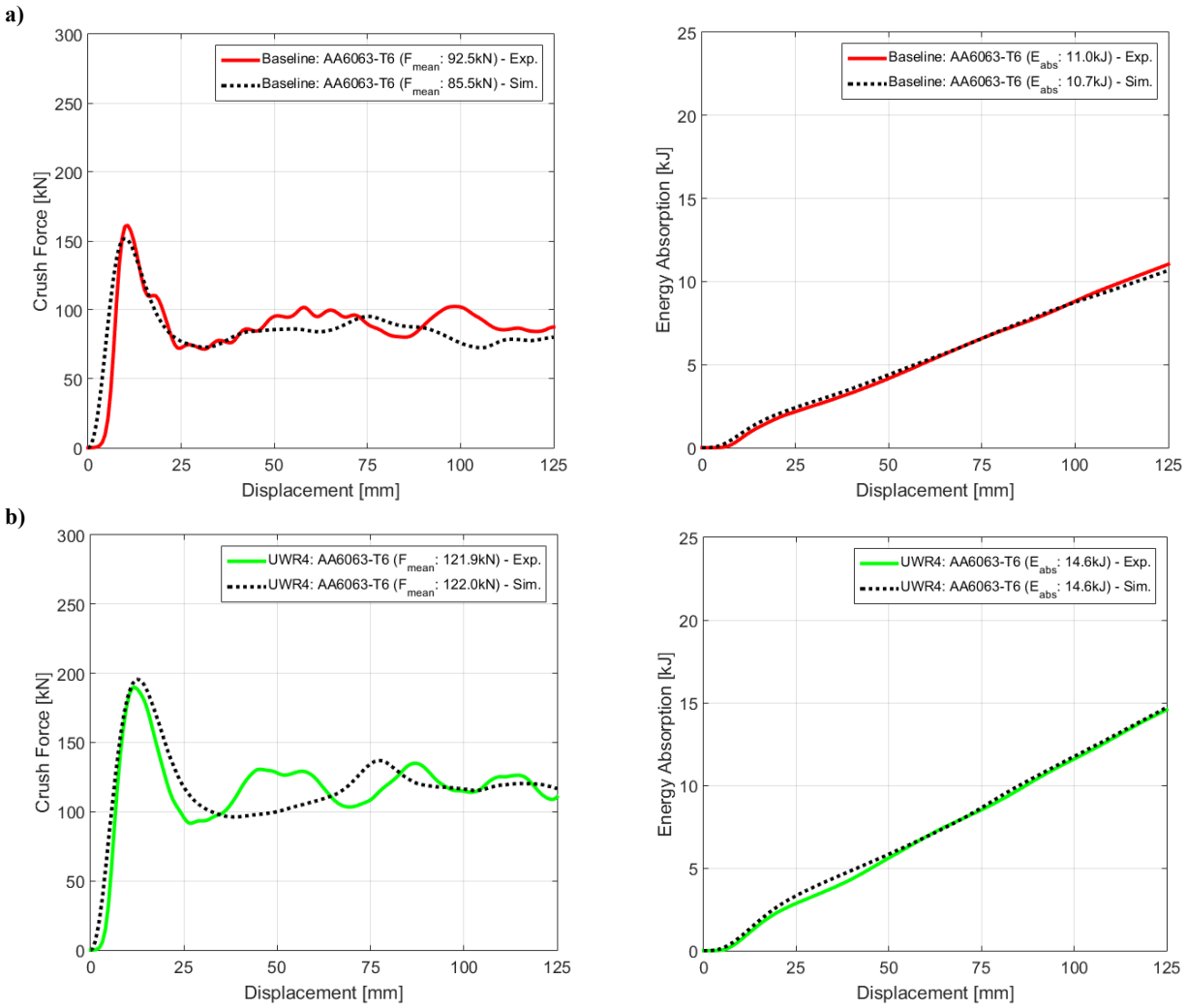

Figure 6.12 - Comparison of simulation and experimental force-displacement and energy absorption response for (a) Baseline Profile - AA6063-T6 and (b) UWR4 Profile - AA6063-T6

Table 6.7 - Numerical, simulation and error for mean crush force, peak crush force, energy absorption and crush efficiency for Baseline AA6063-T6 Profile

	Energy Absorption, E_{abs} [kJ]	Mean Crush Force, F_{mean} [kN]	Peak Crush Force, F_{peak} [kN]	Crush Efficiency
Exp.	11.0	92.5	161.4	57.3
Sim. Prediction	10.7	85.5	151.8	56.3
ΔErr **Exp. To Sim. (%)**	2.7	7.6	5.9	1.0

Table 6.8 - Numerical, simulation and error for mean crush force, peak crush force, energy absorption and crush efficiency for UWR4 AA6063-T6 Profile

	Energy Absorption, E_{abs} [kJ]	Mean Crush Force, F_{mean} [kN]	Peak Crush Force, F_{peak} [kN]	Crush Efficiency
Exp.	14.6	121.9	190.0	64.2
Sim. Prediction	14.6	122.0	195.6	62.3
ΔErr **Exp. To Sim. (%)**	0.0	0.0	2.9	1.9

6.5 Front Rail Optimization Strategy for Thickness

In this section, the framework for the Front Rail Optimization Strategy of Thickness (FROST) Method is detailed. The FROST Method is a numerical framework that was implemented to optimize the size of the UWR4 crush rail. The commercial optimization package LS-OPT was used to perform the optimization procedure.

6.5.1 Framework for Optimization Method

For the optimization of the crush tube, the FROST method begins by decomposing the geometry into individual parts. As shown in Figure 6.10a, the UWR4 crush tube is individually meshed into five unique parts that are composed of shell elements and constrained together. The overall topology is held constant and the size of the structure is optimized. In other words, the focus of the work is constrained to optimizing the thickness of the structure. Each component is assigned its own unique part identification, material and shell element sectional information. Thus, the shell element thickness for each section is parameterized accordingly as t_i with $i = 1…5$. Sets of parameters within this space, which is known as the design of experiments [12], are selected for simulation. Using a linear space filling point selection algorithm, 10 sample sets of thickness combinations (t_i) are selected within these bounds and each combination is simulated. For each set of parameters, the resulting mass and mean crush force is measured and is used as the performance metric for optimization. The optimization function, optimization strategy and constraints are discussed further below.

6.5.1.1 Optimization Objective Function

The objective of this optimization is to minimize the mass while maximizing the mean crush force. To evaluate each design, a performance metric, *P*, must be defined that can encapsulate this objective

$$P(t_i) = f\left(\frac{F_{mean}}{Mass}\right) \qquad (6.1)$$

Since the topology of the structure is fixed and must remain as an extrusion, an approximate linear functional constraint is imposed on the mass of the structure (when neglecting the radii), such that

$$Mass = L\rho \sum_{i=1}^{5} a_i t_i \qquad (6.2)$$

where a_i is dependent on the dimensions of the section of the structure and L is the initial uncrushed length. In the work by Wierzbicki and Abramowicz [72], a formulation that related the kinematic deformations to the energy absorption capabilities in simple Type-I collapse modes using an isotropic rigid-perfectly plastic material behaviour was presented

$$E = \frac{f(\sigma)t^2}{4}\left(16HI_1\frac{b}{t} + 2\pi C + 4I_3\frac{H^2}{b}\right) \qquad (6.3)$$

where $f(\sigma)$ is the material yield stress function. For a perfectly plastic material with rate sensitivity, the material yield stress function is described as

$$f(\sigma) = \sigma_0\left(1 + \left(\frac{V}{3CM}\right)^{\frac{1}{P}}\right) \qquad (6.4)$$

where V is the impacting velocity [114] and σ_0 is the yield stress. By dividing by the total crushing distance, δ, the mean crush force can be determined as

$$F_{mean} = \frac{E}{\delta} = \frac{f(\sigma)t^2}{4\delta}\left(16HI_1\frac{b}{t} + 2\pi C + 4I_3\frac{H^2}{b}\right) \qquad (6.5)$$

Since the crush tube consists of a combination of Type-I collapse elements, this means that the mean crush force response of this crush tube will be at least functionally quadratic with respect to material thickness. The specific energy absorption (SEA) is a common performance metric that is used for evaluating the performance of a crush tube [68]

$$SEA = \frac{E}{Mass} = \frac{F_{mean}\delta}{Mass} \qquad (6.6)$$

Evaluating the performance metric at a given crush displacement, the first performance metric is defined as

$$P_1(t_i) = SEA = \frac{E}{Mass} = \frac{F_{mean}\delta}{Mass} = \frac{\delta\sigma_0}{4L\rho}\sum_{i=1}^{5}\frac{{t_i}^2\left(16H_iI_1\frac{b_i}{t_i} + 2\pi C_i + 4I_3\frac{{H_i}^2}{b_i}\right)\left(1 + \left(\frac{V}{3C_iM}\right)^{\frac{1}{P}}\right)}{a_it_i} \quad (\ 6.7\ )$$

where *i* denotes a section of the profile. This performance metric is a linear function with respect to the wall thickness,t_i, to a first order with a contribution of higher order non-linear functions. Since the structure is a combination of multiple Type-I collapse elements, the objective function will attempt to optimize the section where the local SEA has the greatest influence.

As presented in the work of Marzbanrad *et al.* [7], there are other choices available as an optimization objective function. Another common performance metric, $P_2(t_i)$, is to optimize the crush efficiency of the structure, such that

$$P_2(t_i) = \eta = \frac{F_{mean}}{F_{peak}} \quad (\ 6.8\ )$$

In the work presented in Chapter 4, it was shown that the peak crush response of Type-I collapse elements is linearly proportional to the area of the structure and the flow stress properties of the material

$$F_{peak} \propto Af(\sigma) \quad (\ 6.9\ )$$

Since the topology and the material properties of the extrusion is fixed, the peak force becomes linearly functional, such that

$$F_{peak} = f(\sigma)\sum_{i=1}^{5} a_it_i \quad (\ 6.10\ )$$

Thus, the performance metric for optimizing the crush efficiency takes the form

$$P_2(t_i) = \eta = \frac{F_{mean}}{F_{peak}} = \frac{1}{4}\sum_{i=1}^{5}\frac{{t_i}^2\left(16H_iI_1\frac{b_i}{t_i} + 2\pi C_i + 4I_3\frac{{H_i}^2}{b_i}\right)}{a_it_i} \quad (\ 6.11\ )$$

This performance metric is also to a first order linear function of wall thickness with a contribution of higher order non-linear functions that maximizes the crush force and minimizes the mass.

With two different performance metrics, another method is to develop a multi-objective performance metric, P_3, that is a weighted sum of the individual performance metrics

$$P_3(t_i) = w_1 SEA + w_2 \eta \qquad (6.12)$$

where w_i are individual weights assigned to each parameter. This function is able to not only capture the desired weight minimization, but capture the benefit of optimizing the crush efficiency. However, from the above derivations, the specific energy absorption and crush efficiency have the same functionality. In fact, it is proposed that the specific energy absorption and crush efficiency are directly proportional to each other through Υ, such that

$$\Upsilon = \frac{P_2(t_i)}{P_1(t_i)} = \frac{\eta}{SEA} = \frac{\rho L}{\delta f(\sigma)} \qquad (6.13)$$

For an isotropic power law hardening material, the equivalent perfectly plastic yield stress can be determined as [110]

$$\sigma_0 = \sqrt{\frac{\sigma_y \sigma_{uts}}{n+1}} \left(1 + \left(\frac{V}{3C_i M}\right)^{\frac{1}{P}}\right) \qquad (6.14)$$

where σ_y is the yield stress and σ_{uts} is the ultimate tensile strength. Substituting into the multi-objective optimization function produces

$$P_3(t_i) = \left(w_1 + w_2 \frac{\rho L}{\delta f(\sigma)}\right) SEA \qquad (6.15)$$

It can be concluded that when optimizing the specific energy absorption, the crush efficiency is also optimized. Therefore, it is proposed that selecting only a single objective optimization function is required for minimizing weight and maximizing energy absorption. In this work, the specific energy absorption is selected as the optimization objective function.

6.5.1.2 Optimization Strategy

The response surface method (RSM) was used to develop a metamodel for the optimization of the performance metric [12] [83]. In this application, a metamodel was created that relates the set of material thickness for the structure to the performance metric. The feed-forward multi-layered neural-network, with a single hidden layer, was implemented as the

metamodeling technique to map the material thickness because it provides sufficient complexity to approximate the input-output relationship [93].

Once the metamodel has been generated, an optimization algorithm operates on this function to generate the optimal parameters for the optimization objective. An adaptive simulated annealing (ASA) algorithm was used to perform the optimization procedure on the neural network generated metamodel [137, 138, 90]. The optimization objective consists of a complex trade-off objective function that is highly constrained, which is very well suited for the ASA method [90]. Upon determining an initial optimal solution, a new subspace within the design is generated within the previous design space using the sequential response surface method (SRSM). The new region is generated to encompass the current optimal solution through an adaptive contraction and panning window that are designed to alleviate oscillation and prevent premature convergence [91]. Further iterations and domain reductions are performed until a local optimal solution is obtained for the given problem. This method assures that a local optimal solution is obtained. However, this solution is highly dependent on the accuracy of the metamodel, such that initial domain reductions may exclude a region where better performance could be obtained. This response surface methodology and optimization process was performed using LS-OPT.

6.5.2 Optimization Criteria and Constraints

Several criterion and constraints were placed on the optimization process:

1. An upper and lower bound of 2.40mm and 1.75mm respectively was placed on each thickness parameter to generate UWR4 crush rails that were feasible for extrusion. The lower limit was selected as the lowest extrudable wall thickness for the given size of the profile. The upper limit was determined by limiting the variation of wall thickness to not exceed 40% above the lower limit. The constraints on these design parameters constitute what is commonly known as the design space. Each parameter could vary in discrete increments of 0.01mm.
2. A convergence error, $Err_{converge}$, constraint of 0.01 was imposed on the neural network to ensure that metamodel has predictive capabilities. This means that the error between

the predicted output of the metamodel to the actual output of the simulation for the given input (thickness) parameters must be less than 1%.

3. Newly synthesized topographies should have the same or better performance than the Baseline 7xxx series shape (presented in Figure 1). A newly generated UWR4 crush rail should have a mass less than 1.494 kg and a crush force greater than 171.0kN. If both criteria cannot be satisfied simultaneously, preference was given to satisfying the mass criteria.

The optimization problem of the sizing for the UWR4 crush can be formulated as follows:

$$\begin{cases} \text{Max } \{SEA\ (t_i)\} \\ \text{s.t. Mass} \leq 1.494 \text{ kg (strict)} \\ \quad F_{mean} \geq 171.0 \text{ kN} \\ \quad t_i \in [1.75, 1.76, \ldots, 2.40]\text{mm} \\ \quad Err_{converge} \leq 0.01 \end{cases} \qquad (6.16)$$

6.5.3 Optimization Analysis

The FROST Method was applied to the 8.0m/s explicit dynamic FE model using an isotropic plasticity model (*MAT_LINEAR_PIECEWISE_PLASTICITY). This reduced computational resources required to navigate throughout the design of experiments domain. Once the FROST Method converged to an optimal isotropic solution, a final simulation of the new superior UWR4 sizing was performed using the Yld2000 anisotropic yield function. A sensitivity analysis was performed to identify an operation window for the extrusion tolerances of the new UWR4 profile.

6.5.3.1 Results of Optimization

APPENDIX A.2 presents the test matrix that details the simulation parameters. The energy absorption characteristics of each size combination was measured and also presented in APPENDIX A.2. Figure 6.13 presents the convergence history for each thickness parameter using the isotropic model. The wall thickness for each section specified in Figure 6.2 was used as an initial guess of the optimal sizing.

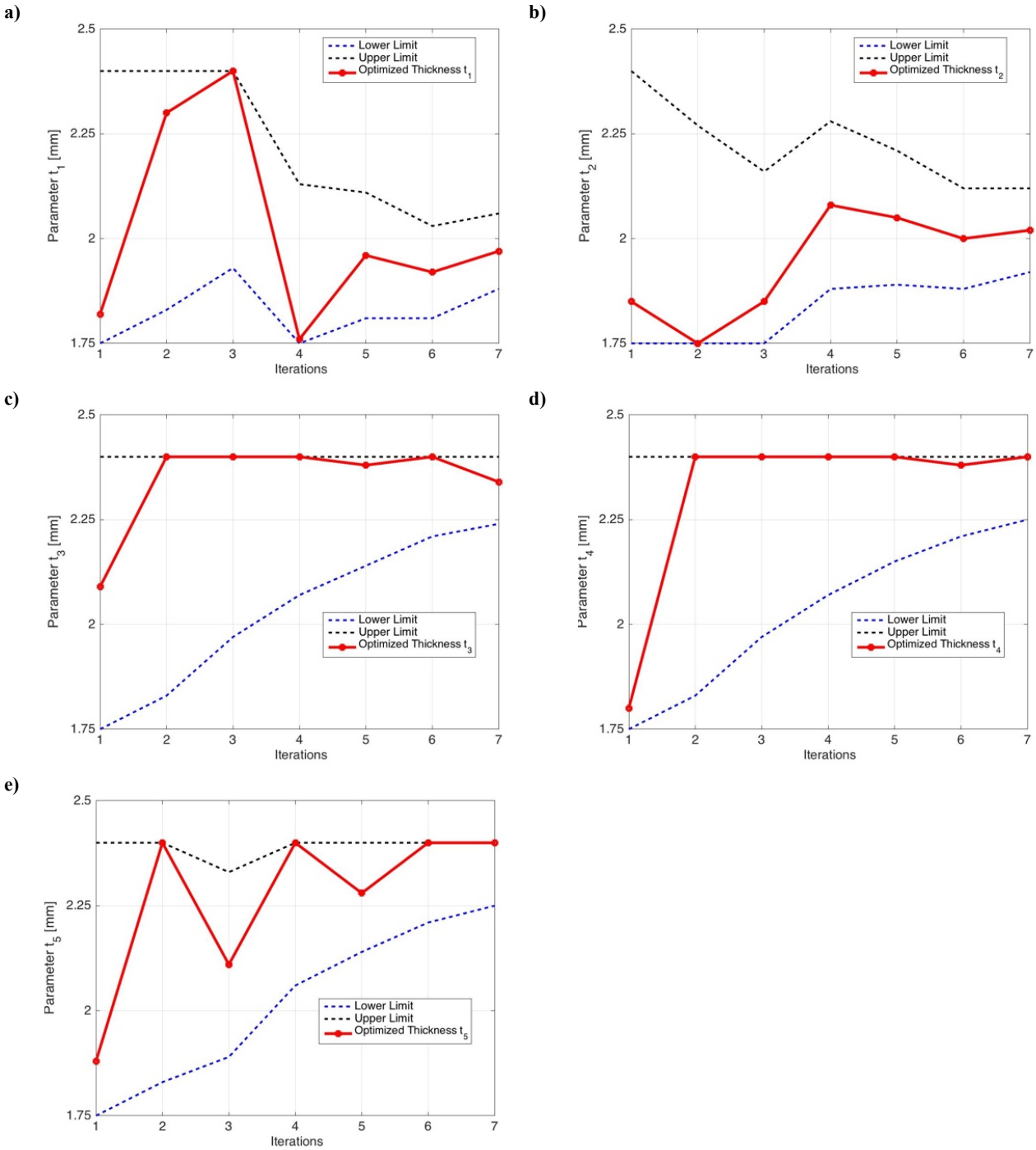

Figure 6.13 - Parameter Convergence Plot of Crush Rail Wall Thickness Parameters (a) t_1, (b) t_2, (c) t_3, (d) t_4 and (e) t_5 using Isotropic Material Model (UWR4)

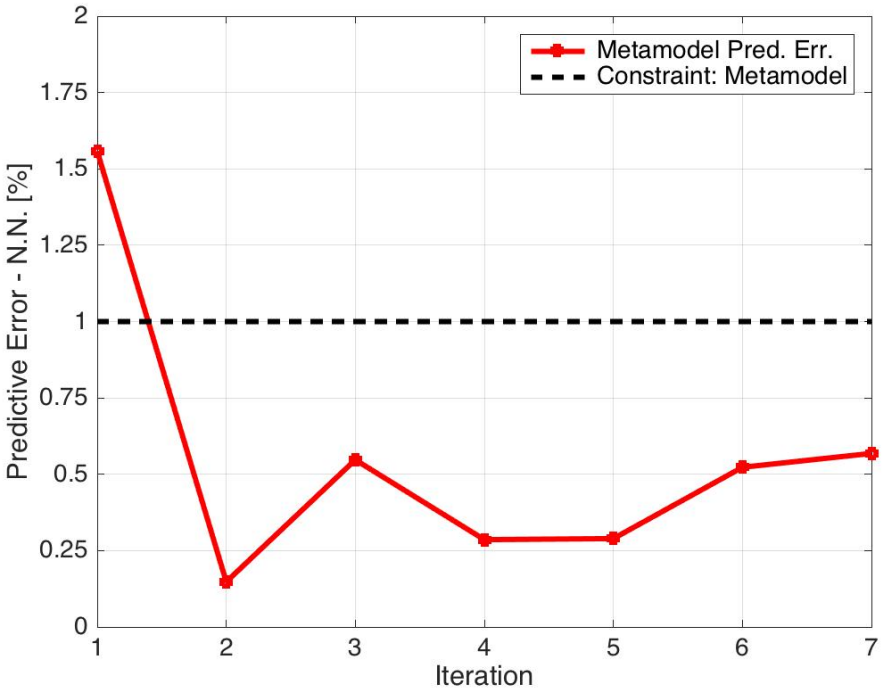

Figure 6.14 - Convergence Plot of Metamodel Prediction Error of Specific Energy Absorption using Isotropic Material Model (UWR4)

a) **b)**

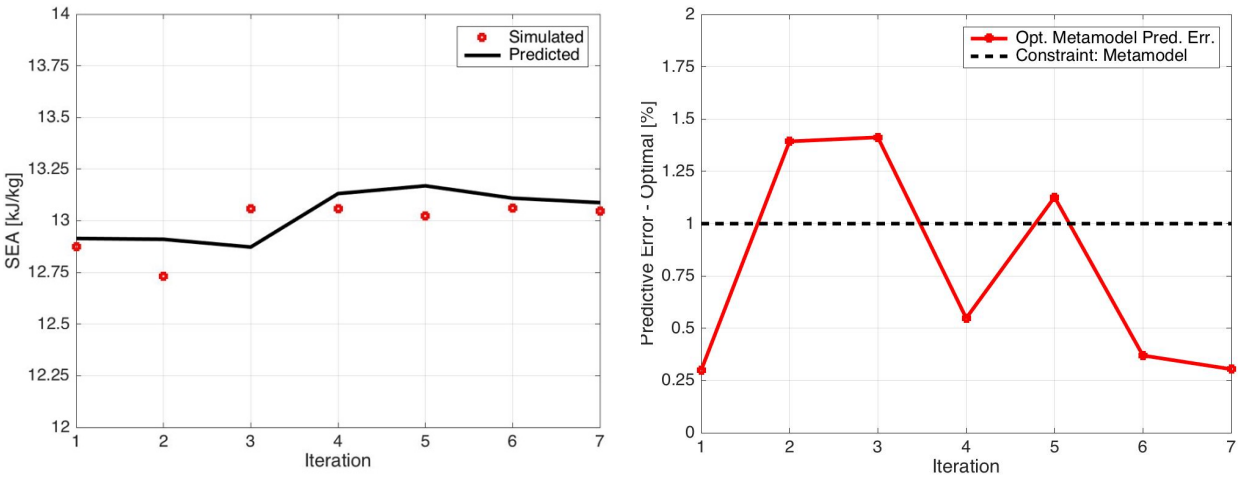

Figure 6.15 - Convergence Plot of a) Predicted and Simulated b) Metamodel Prediction Error of Optimal Specific Energy Absorption using Isotropic Material Model (UWR4)

Table 6.9 presents the initial and final dimensions and mass for the UWR4 model. The isotropic optimization process required a total of 7 iterations to converge to its final configuration. The final mass of the structures converged to a mass of 1.494kg, which corresponds to the limit of the allowable mass constraint imposed. This is a result of SEA being dominant by first order linear functions of wall thickness as presented in Equation 6.7 [74].

Table 6.9 - Initial and Final Topography and Mass

	Initial UWR4 AA6063-T6 Profile	New UWR4 AA6063-T6 Profile
t_1 [mm]	1.82	2.03
t_2 [mm]	1.85	1.97
t_3 [mm]	2.09	2.31
t_4 [mm]	1.80	2.40
t_5 [mm]	1.88	2.40
Mass [kg]	1.234	1.494

A plot of the SEA response surface and contours for the isotropic process are presented in Figure 6.16. Each plot is centered about the final converged set of parameters. The maximum allowable mass limit is imposed on each figure in black. This line indicates the combinations of two parameters that produced a mass of 1.494kg. The final wall thickness configuration from the optimization procedure is also presented in each figure. These figures show that decreasing the mass tends to decrease the SEA of the structure. Again, this is a result of the SEA being dominant by first order linear functions (with higher order terms) of wall thickness. Thus, the optimization objective of maximizing SEA will tend to converge towards the limit of the mass constraints.

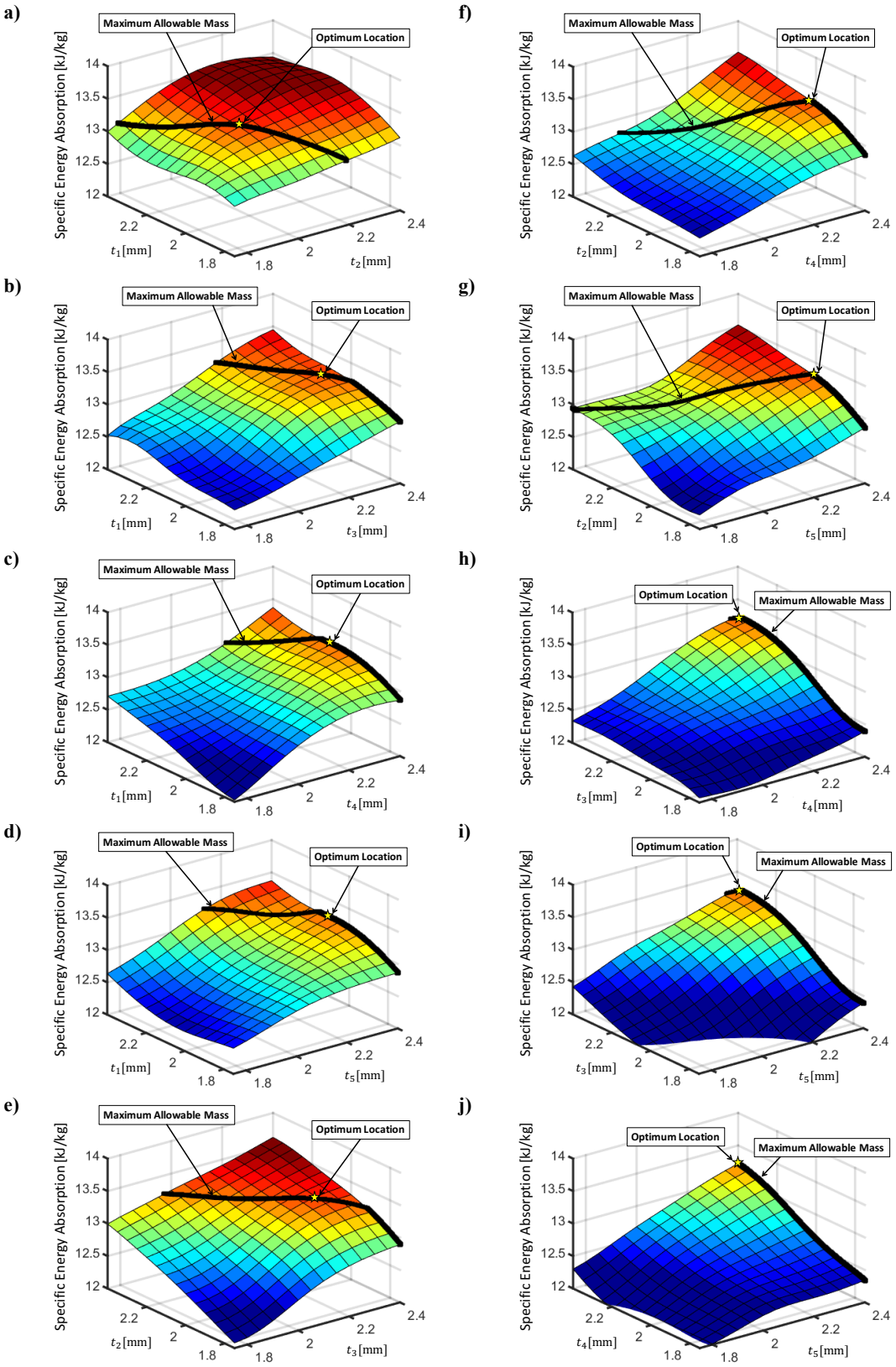

Figure 6.16 - Response surface response plots for specific energy absorption (SEA) of isotropic optimization process

6.5.3.2 Interaction of Specific Energy Absorption and Crush Efficiency

Figure 6.17 presents the specific energy absorption and the crush efficiency results obtained from each simulation during the isotropic optimization process. Each point, shown as a red square with a black box, represents the SEA and crush efficiency for a given point in the design of experiments. Table 6.10 presents a simple linear regression that is plotted through this data. The R^2 value for the regression fit is 0.6013. This means that there is a moderate positive linear relationship between the specific energy absorption and the crush efficiency. Equation 6.13 was evaluated and also presented in Table 6.10 to determine analytical relationship between the specific energy absorption and the crush efficiency. Equation 6.13 was calculated using an ultimate tensile strength calculated at 100% plastic strain ($\sigma_{uts}|_{\bar{\varepsilon}_p=1} = 310MPa$). Since energy absorption is naturally minimized by the structure, the effects of strain rate are calculated by minimizing Equation 6.14 with respect to the geometry, where C_i is calculated as the average macro element length [72]. The difference between the analytical parameter and the regression fit for the isotropic models is 6.7%. This means that, using the isotropic material model, one can directly calculate the crush efficiency of the structure once the specific energy absorption is known. Since the optimization process is guided towards the largest allowable mass, the resulting maximization of the specific energy absorption results will tend to simultaneously increase the maximization of the crush efficiency.

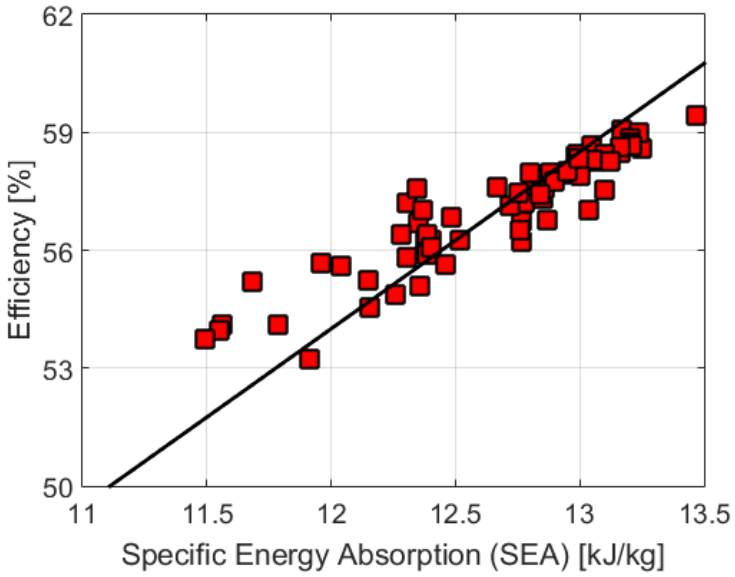

Figure 6.17 - Interaction of Specific Energy Absorption with Crush Efficiency for Isotropic procedure

Table 6.10 - Regression Analysis of the Relationship between Crush Efficiency and Specific Energy Absorption

	Model
Regression Fit Slope $\tilde{m}$ $\left[\frac{kJ/kg}{\%}\right]$	4.50
R^2 Fitting Result	0.6013
Υ, $\left[\frac{kJ/kg}{\%}\right]$	4.20
Difference Between Υ and $\tilde{m}$ [%]	6.7

6.5.3.3 Optimized Anisotropic UWR4 Simulation Results

Figure 6.18 presents the simulated force-displacement and energy absorption response of the new UWR4 sizing using the Yld2000 anisotropic yield function. Table 6.11 presents a summary of the energy absorption characteristics of the new UWR4 profile. The mean crush force, peak crush force, energy absorption and crush efficiency was 148.6kN, 248.9kN, 18.5kJ, and 59.7% respectively. Although the mass constraint was satisfied, the mean crush force criteria was not. Even though a 2.5% decrease in the crush efficiency is observed, the new UWR4 profile has 26.7% more energy absorption and a higher crush force by 21.9% than the initial UWR4 profile when increasing the mass by 21%. Although the mean crush force and energy absorption is 10% and 13% respectively lower than the Baseline 7xxx Series profile, the new UWR4 profile can achieve comparable energy absorption characteristics for the given mass using the AA6xxx-T6 alloy of appropriate strength.

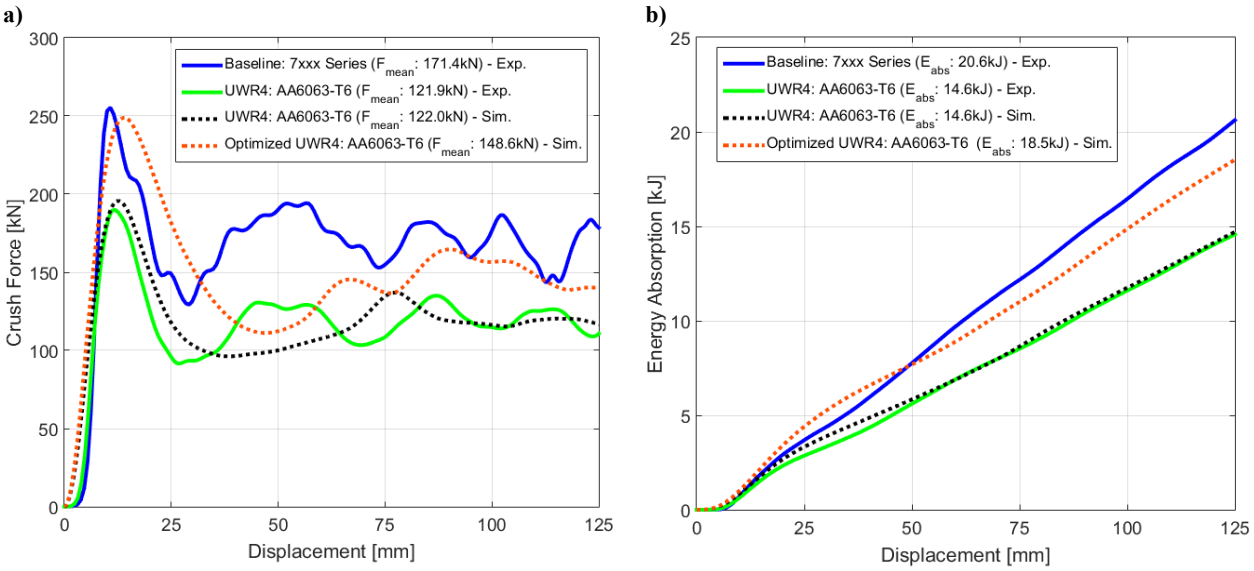

Figure 6.18 - Comparison of (a) Force-Displacement Response and (b) Energy Absorption Response for Baseline 7xxx Series Profile, UWR4 AA6063-T6 profile and new UWR4 AA6063-T6

Table 6.11 - Summary of Energy Absorption Characteristics of New UWR4 AA6063 Profile

	Baseline 7xxx Series – Exp.	UWR4 AA6063-T6 – Exp.	UWR4 AA6063-T6 – Sim.	New UWR4 AA6063-T6 – Sim.	Gains of New UWR4 vs Baseline UWR4
Energy Absorption [kJ]	20.6	14.6	14.6	18.5	+26.7%
Mean Crush Force [kN]	171.4	121.9	122.0	148.6	+21.9%
Peak Crush Force [kN]	255.4	190.0	195.6	248.9	+27.2%
Crush Efficiency [%]	67.1	64.2	62.3	59.7	-2.5%
Mass [kg]	1.494	1.234	1.234	1.494	+21.0%

6.5.3.4 Size Sensitivity Analysis

Figure 6.19 presents a wall thickness sensitivity analysis for the mean crush force, mass, and SEA of the new UWR4 AA6063-T6 profile. The gradient of each response, β_i, is calculated using a first order regression, such that

a) $\beta_o = (\boldsymbol{X}^T\boldsymbol{X})^{-1}\boldsymbol{X}^T F_{mean}$ **b)** $\beta_1 = (\boldsymbol{X}^T\boldsymbol{X})^{-1}\boldsymbol{X}^T Mass$ **c)** $\beta_2 = (\boldsymbol{X}^T\boldsymbol{X})^{-1}\boldsymbol{X}^T SEA$ **(6.17)**

where $\boldsymbol{X} = [t_1, t_2, t_3, t_4, t_5]$. The first order approximation is appropriate to represent the approximation of SEA, which is the primary optimization goal. This analysis shows that mean crush force and mass was most sensitive to the wall thickness Parameter t_3. However, Parameter t_4 had the highest sensitivity to SEA. Parameter t_1 had the lowest sensitivity to the mean crush force and the second lowest sensitivity to any mass increase. As a result, the overall SEA sensitivity to Parameter t_1 was the lowest of all parameters, followed by Parameter t_2. It also shows that Parameters t_5 and t_3 followed after t_4 in order of SEA sensitivity. This was reflected in the convergence history of Figure 13, where Parameters t_4 and t_5 converged to the limit of the bounds. Parameters t_1 and t_2 converged to the lowest combination that produced the largest mass, which produced the largest SEA. Thus, higher quality extrusion process control should be applied to Parameter t_4 to ensure the crush structure absorbs energy in the most efficient manner.

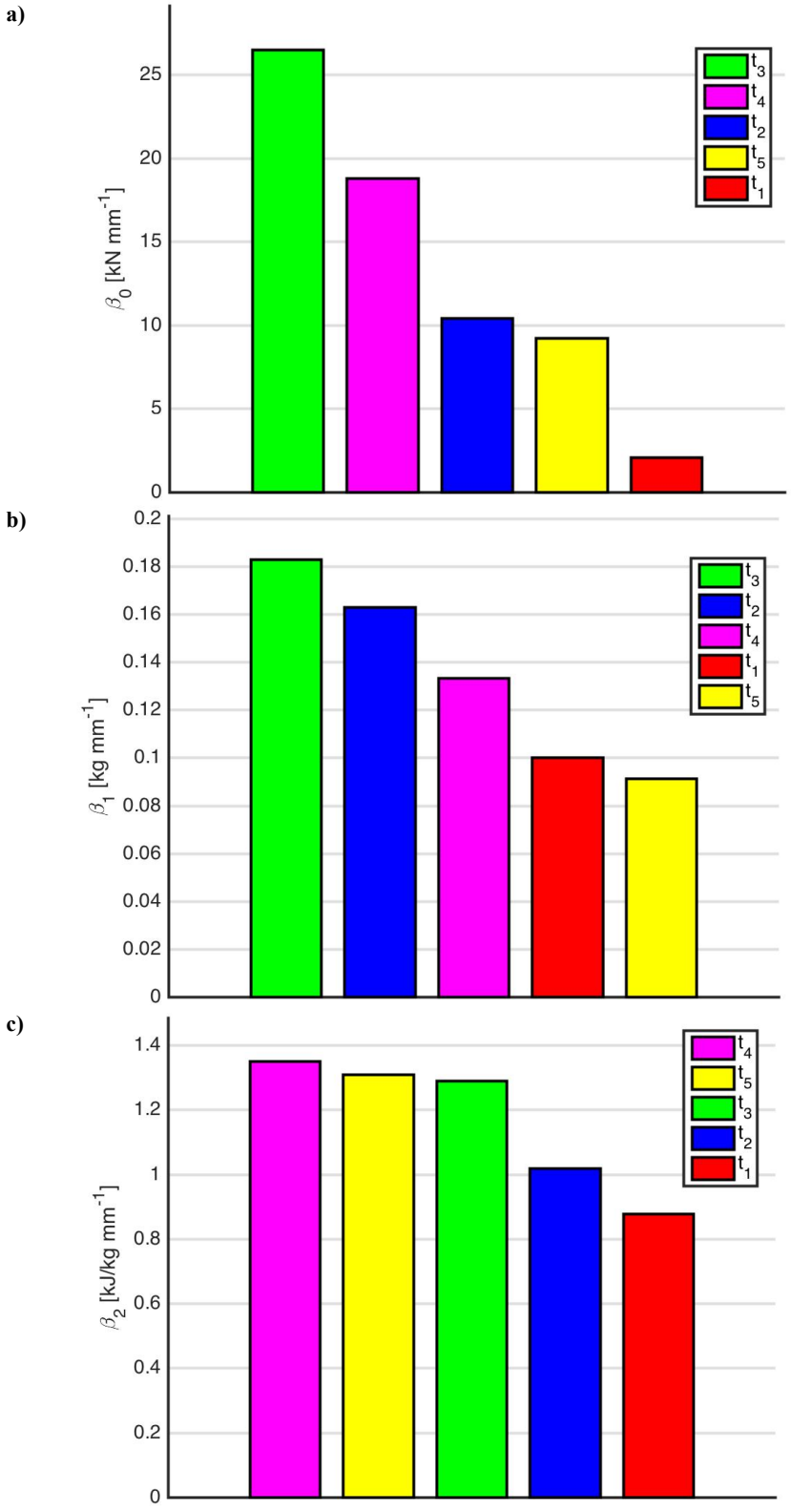

Figure 6.19 - (a) Mean Crush Force, (b) Mass, and (c) SEA Wall Thickness Sensitivity Analysis for New UWR4 AA6063-T6 profile

6.6 Chapter Conclusions

In this chapter, a framework was presented for optimizing the sizing of a multi-cellular aluminum extrusion for automotive crashworthiness applications. New AA6063-T6 aluminum extrusion profiles were designed using finite elements, fabricated and dynamically crushed using a sled-track apparatus. The energy absorption characteristic responses of the AA6063-T6 extrusions were compared to experimental results of a commercially available 7xxx series profile. Constitutive modeling and numerical simulations for these AA6063-T6 extrusions were presented and compared with experimental data. Simulations using the Yld2000 anisotropic yield function showed good agreement with the experiments for different crashworthiness parameters.

In the optimization framework, the response surface methodology, coupled with neural network metamodeling and adaptive simulated annealing optimization scheme, was used to optimize the size to increase the mean crush force and energy absorption. A new superior UWR4 profile was developed that had a higher mean crush force by 21.9% and 26.7% more energy absorption than the initial size of the UWR4 profile. The specific energy absorption was selected as the optimization objective function. The functionality of the specific energy absorption criteria guided the optimization process to the maximum allowable mass. It was shown that the specific energy absorption linearly relates to the crush efficiency and that the optimization of the specific energy absorption function will tend to simultaneously increase the crush efficiency. An analytical relationship was presented in Equation 6.13 that relates the specific energy absorption and crush efficiency, and showed good predictive capabilities. Through a sensitivity analysis of the optimization framework, key size sections were identified for critical extrusion process control to manage the mass and efficiency of the energy absorption characteristics of the profile. This framework allows a 6000-series aluminum alloy, in particular AA6063-T6 family alloy, to have competitive energy absorption characteristics compared to mass-produced 7000-series aluminum profiles.

7 EFFECTS OF COUPLING ANISOTROPIC YIELD FUNCTIONS WITH THE OPTIMIZATION PROCESS OF EXTRUDED ALUMINUM FRONT RAIL GEOMETRIES IN CRASHWORTHINESS - C.P. Kohar, A. Brahme, R.K. Mishra, K. Inal (2017). Under Revision at International Journal of Solids and Structures (IJSS-S-16-01573)

This chapter presents the influences of coupling anisotropic yield functions into the size optimization of extruded front rails to maximize energy absorption characteristics. Finite element simulations of the extrusion crush response are performed using the von Mises [29], Hosford [31] and Barlat *et al.* [35] Yld2004-18p yield functions. Each yield function is implemented into a 2-dimensional plane stress and 3-dimensional element formulation to highlight the modeling differences prior to optimization. The simulations are also compared to the experimental dynamic crush response of the extrusion. The response surface methodology (RSM) with the artificial neural network (ANN) metamodeling technique is coupled with the genetic algorithm (GA) optimization scheme to improve the specific energy absorption (SEA) through maximizing energy absorption and minimizing mass. A constrained and unconstrained mass optimization study is performed to identify the sensitivity of global optimization to yield surface choice. Analytical models are derived to explain the influence of the yield surface on the convergence of optimization. The results highlight the importance of incorporating anisotropic yield functions into the optimization process. The results of this work have been submitted for publication in the International Journal of Solids and Structures [139].

7.1 Introduction

Material anisotropy that is introduced from manufacturing presents an additional complexity that affects model predictive capabilities. Accurate representation of material anisotropy is critical to the successful implementation of numerical simulations as a product development tool. Through virtual design of experimental studies [12], these FE models can be coupled with optimization platforms to improve the design of automotive structures in crashworthiness. In finite element based crashworthiness optimization, the calibration data is generated by simulating the energy absorption response within the design of experiments.

In Chapter 6, a framework was presented for optimizing the sizing of aluminum extrusions, using RSM with an isotropic von Mises yield function, for automotive

crashworthiness. It was shown that specific energy absorption (SEA) could be selected as a single optimization objective function because SEA could be related to the crush efficiency for the axial crushing of extrusions. Nevertheless, this direct relationship between SEA and crush efficiency may not hold when incorporating additional nonlinearities into the optimization problem formulation, such as non-linear material behaviours through anisotropy. This can translate into the over-design of energy absorbing structures through the addition of unnecessary mass.

This chapter presents the study of the influences of incorporating anisotropic yield functions into the optimization process of extruded aluminum front rails. The baseline multi-cellular AA6063-T6 aluminum extrusion presented Figure 6.1 is utilized in this study. The commercial FE software, LS-DYNA, is used to simulate the crush behaviour of the AA6063-T6 structure using different yield functions. The isotropic von Mises [29], Hosford's generalized isotropic [31], and Barlat et al. [35] Yld2004-18p yield function will be used in this study. Employing the Hosford yield function will highlight the influence of yield surface curvature, while the Yld2004-18p will show the influence of incorporating material anisotropy through the Lankford coefficients and yield stress variation along with yield surface curvature. Prior to optimization, it is critical to understand the discrepancies between the 2-dimensional plane stress and 3-dimensional formulations. Thus, simulations of both element formulations for each yield function are presented for comparison. In the proposed optimization framework, a 2-dimensional plane stress formulation of each yield function will be utilized. After convergence, the optimized sizing is simulated using the 3-dimensional element formulation using the Yld2004-18p yield function. The commercial optimization package, LS-OPT, is used to optimize the sizing of the aluminum extrusion using each yield function in the design of experiments. The response surface methodology is employed to optimize SEA as a single optimization objective function for a constrained mass using the ANN metamodeling technique and the GA optimization scheme. The convergence history of the optimization scheme is analyzed to highlight interactions between sizing and energy absorption metrics, such as SEA, crush efficiency, peak crush force and mass. An unconstrained optimization study is also presented to understand the influence yield function on the energy absorption potential for a given topology.

7.2 *Experiments*

In this study, the baseline aluminum profile was dynamically crushed using the linear sled-track apparatus setup presented in Section 6.2 and presented in Kohar et al. [103]. Similar to the extrusion profiles presented previously, the baseline profile was initially produced in a state that was similar to AA6063-T4. An artificially aged treatment at 180°C for 5 hours was performed to generate a T6-temper throughout the entire profile. Figure 7.1 presents uniaxial tensile stress that was presented in Section 6.2 of the previous chapter. Along side is the shear-stress response that was recently presented in the work of Muhammad et al. [41, 42]. ASTM-E8 tensile specimens were used to characterize the tensile response, while shear specimens were to characterize the material in shear. Figure 7.2 presents a schematic of the shear specimen presented in Muhammad et al. [41, 42] that was used to characterize the shear-stress response. The shear-stress response exhibited a softening behavior that arises from microstructural spin and texture evolution as shown in Gasperini et al. [141] and Gracio et al., [142]

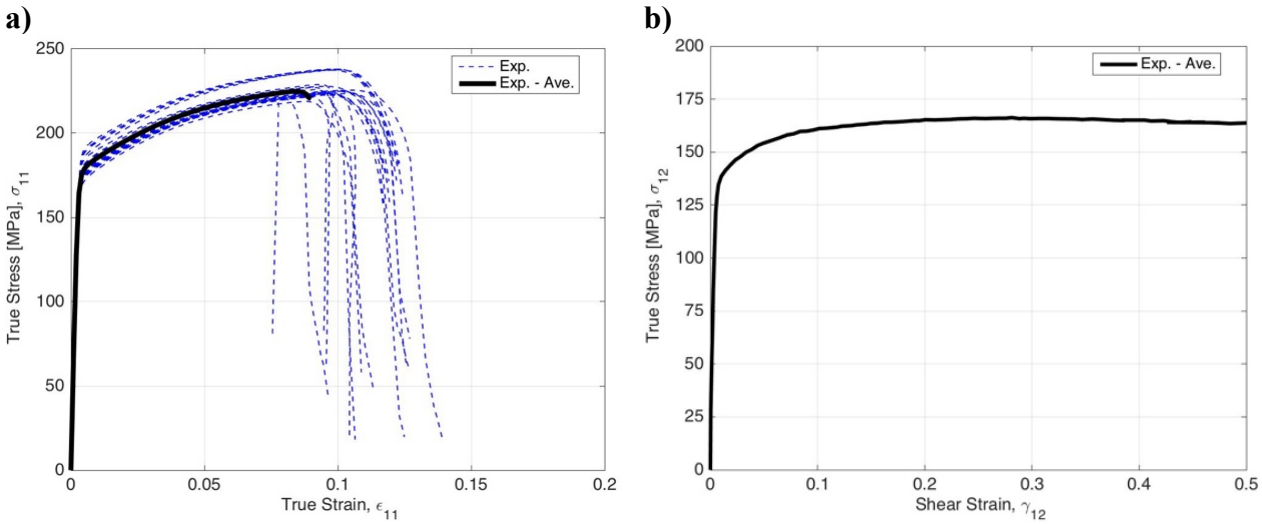

Figure 7.1 - a) Uniaxial tensile [133] and b) Shear stress response [41, 42] of extrusion AA6063-T6

Each aluminum extrusion profile was cut to a length of 525mm for crush experiments and supported using steel boss structures. The mass of the sled was 855kg and the impacting speed was 15.6 m/s [56.0km/h]. A 12.7mm [0.50”] plywood sheet was mounted to the end plate to reduce high-frequency noise during sled impact. Aluminum honeycomb blocks were used to dissipate any excessive sled energy and provided for an uninterrupted crush length of 125mm for each extrusion.

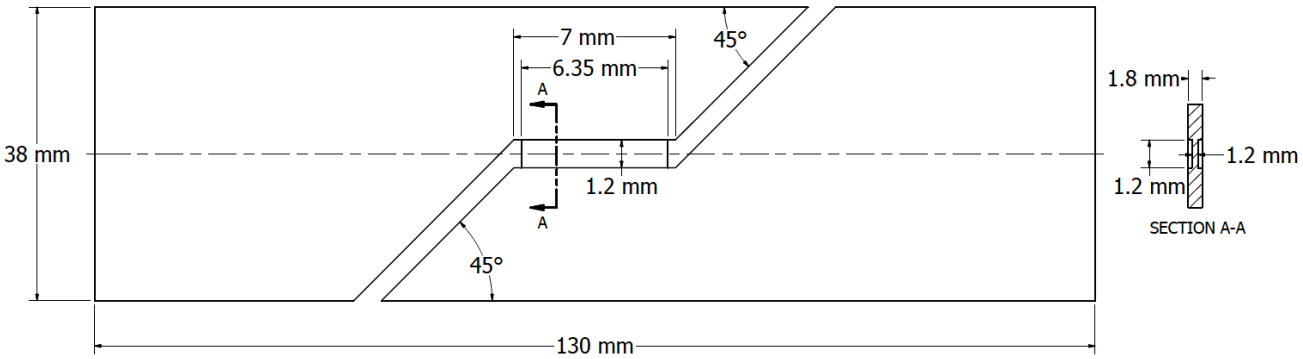

Figure 7.2 - Shear stress specimen used in Muhammad et al., [41, 42] for extruded aluminum AA6063-T6

Figure 7.3 shows the experimental force-displacement and energy absorption response of the extrusion from the dynamic crush experiments. The force-displacement response had several oscillations in the response, attributed to the structural vibrations of the sled-track setup [14]. To attenuate the noise, the raw dynamic force-displacement response was post-processed using an SAE CFC 1000 filter. Four metrics are used to evaluate the energy absorption characteristics of the extrusion: energy absorption, mean crush force, crush efficiency, and specific energy absorption. Table 7.1 lists a summary of the energy absorption, mean crush force, peak crush force, and the crush efficiency at a crush distance of 225mm. Table 7.1 also presents the length and mass of the profile. The mean crush force, peak crush force and crush efficiency of this profile was 94.4kN, 318.7kN, and 29.6%. The energy absorption and specific energy absorption at 225mm was 21.11kJ and 15.19kJ/kg respectively.

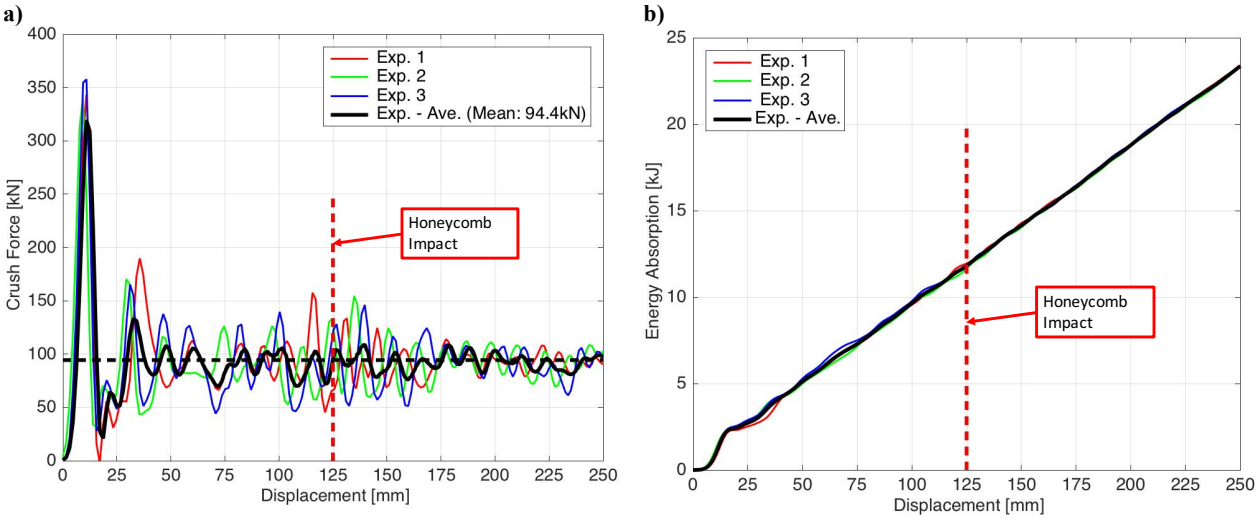

Figure 7.3 - Experimental a) crush force and b) energy absorption response of AA6063-T6 extrusion with test condition of 15.6 m/s

Table 7.1 - Summary of Experimental Crush Response for 15.6 m/s Testing

	15.6m/s
Length [mm]	525
Mass [kg]	1.390
Energy Absorption [kJ]	21.11
Mean Crush Force [kN]	94.4
Peak Crush Force [kN]	318.7
Crush Efficiency [%]	29.6
Specific Energy Absorption [kJ/kg]	15.19

7.3 Constitutive Modeling

In this study, phenomenological-based flow rules are employed to investigate the difference in numerical model predictions and its influence in the optimization procedure. Three different yield criterion are employed in this study: i) Isotropic von Mises yield [29] function, ii) Hosford's [31] generalized isotropic yield function, and iii) Barlat et al. [35] Yld2004-18p yield function. The parameters c_{ij}', c_{ij}'' of the Yld2004-18p yield criteria are determined by fitting the yield stress and Lankford coefficient variation with respect to the extrusion direction. The experimental anisotropy parameters, which is obtained from the work of Achani et al. [116, 140] for extrusion aluminum alloy AA6063-T6 (measured at 5.6% strain), is employed in this work. A summary of the Lankford coefficients and yield stress variation obtained from their experimental work is presented in Table 7.2 and Table 7.3.

Table 7.2 - Experimental Lankford Coefficients [116, 140]

R_{00}	R_{15}	R_{30}	R_{45}	R_{60}	R_{75}	R_{90}	R_b
0.4560	0.2865	0.2080	0.2147	0.4853	1.0807	2.1450	0.4800

Table 7.3 - Experimental Normalized Yield Stress Coefficients [116, 140, 41, 42]

σ_{00} [MPa]	σ_{15}/σ_{00}	σ_{30}/σ_{00}	σ_{45}/σ_{00}	σ_{60}/σ_{00}	σ_{75}/σ_{00}	σ_{90}/σ_{00}	σ_b/σ_{00}	τ_s/σ_{00}
185	0.9697	0.9770	1.0323	1.0427	1.0320	0.9923	1.0000	0.7003

The Yld2004-18p yield function was calibrated using the genetic-evolution scheme for parameter identification [89]. The coefficients are obtained by minimizing an error function (MEF) fit between the predicted response and experimental data for all Lankford coefficients and normalized yield stresses, by a function that is defined as

$$MEF = \sum_{i=1}^{P}\left(\frac{R_{\theta_i} - \hat{R}_{\theta_i}}{R_{\theta_i}}\right)^2 + \sum_{i=1}^{P}\left(\frac{\sigma_{\theta_i} - \hat{\sigma}_{\theta_i}}{\sigma_{\theta_i}}\right)^2 + \left(\frac{\sigma_b - \hat{\sigma}_b}{\sigma_b}\right)^2 + \left(\frac{R_b - \hat{R}_b}{R_b}\right)^2 + \left(\frac{\tau_s - \hat{\tau}_s}{\tau_s}\right)^2 \qquad (7.1)$$

where P is the number of experimental points in different orientations, R_b, R_{θ_i}, σ_{θ_i}, σ_b and τ_s are the experimental measured values and $\hat{R}_b, \hat{R}_{\theta_i}$, $\hat{\sigma}_{\theta_i}$, $\hat{\sigma}_b$, and $\hat{\tau}_s$ are the predicted measurements of the fit. Since no transverse shear experiments were available (i.e. σ_{13}, σ_{23}), the yield stress in shear was assumed to be the same as the yield of in-plane shear. Table 7.4 presents the fitting coefficients for the Yld2004-18p yield function and Table 7.5 presents a comparison between experimental and fitted yield stresses**.** Figure 7.4a and b presents the normalized (about x-direction) yield loci for the von Mises, Hosford, and Yld2004-18p yield functions in the $\sigma_{12} = 0$ plane and $\sigma_{11} = \sigma_{22}$ plane respectively. Figure 7.4c and d presents the variation of the normalized yield stress and Lankford coefficients with respect to extrusion direction for each yield function respectively. The calibrated and experimental anisotropy is also presented for comparison.

Table 7.4 - Yld2004-18p Yield Function Parameters for AA6063-T6

c_{12}'	c_{13}'	c_{21}'	c_{23}'	c_{31}'	c_{32}'	c_{44}'	c_{55}'	c_{66}'
5.2969	4.5420	-3.6766	1.6610	-2.4781	1.0273	0.4335	0.6943	0.6883

c_{12}''	c_{13}''	c_{21}''	c_{23}''	c_{31}''	c_{32}''	c_{44}''	c_{55}''	c_{66}''
3.7938	4.1985	-4.8035	-0.1547	-3.7580	-0.5741	-1.1037	0.8608	0.8668

Table 7.5 - Comparison Between Fitted and Experimental Balanced Biaxial Lankford Coefficient, Normalized Biaxial Yield Stress and Shear Stress for Yld2004-18pYield Functions

	Fitted Parameters			**Experimental Parameters**		
Yield Function	R_b	σ_b/σ_{00}	τ_s/σ_{00}	R_b	σ_b/σ_{00}	τ_s/σ_{00}
Yld2004-18p	0.4733	0.9962	0.7003	0.4800	1.0000	0.7003

7.3.1 Flow Stress Models

Each model uses a flow stress plasticity relation with Cowper-Symonds [53] strain rate sensitivity to describe the flow stress behaviour. Two flow rules are evaluated: Power Law Hardening from the previous Chapter and the Voce [51] hardening law.

Table 7.6 lists the representative parameters that were calibrated from the work in Chapter 6 for aluminum alloy 6063-T6 which is employed in this study. The power law hardening coefficients previously presented in Section 6.2 are presented for reference in Table 7.7. Figure 7.5 presents the comparison between the experimental stress-strain responses and the predictions for each flow stress model. The Voce hardening law calibration has better predictive capabilities of the flow stress behaviour than the power law hardening model. Thus, the Voce hardening law was selected as the flow stress model to be used in further simulations. The Voce law plasticity relation was then coupled with the Cowper-Symonds [53] strain rate sensitivity where $M = 2.46\times10^{10}s^{-1}$ and $P = 8.88$.

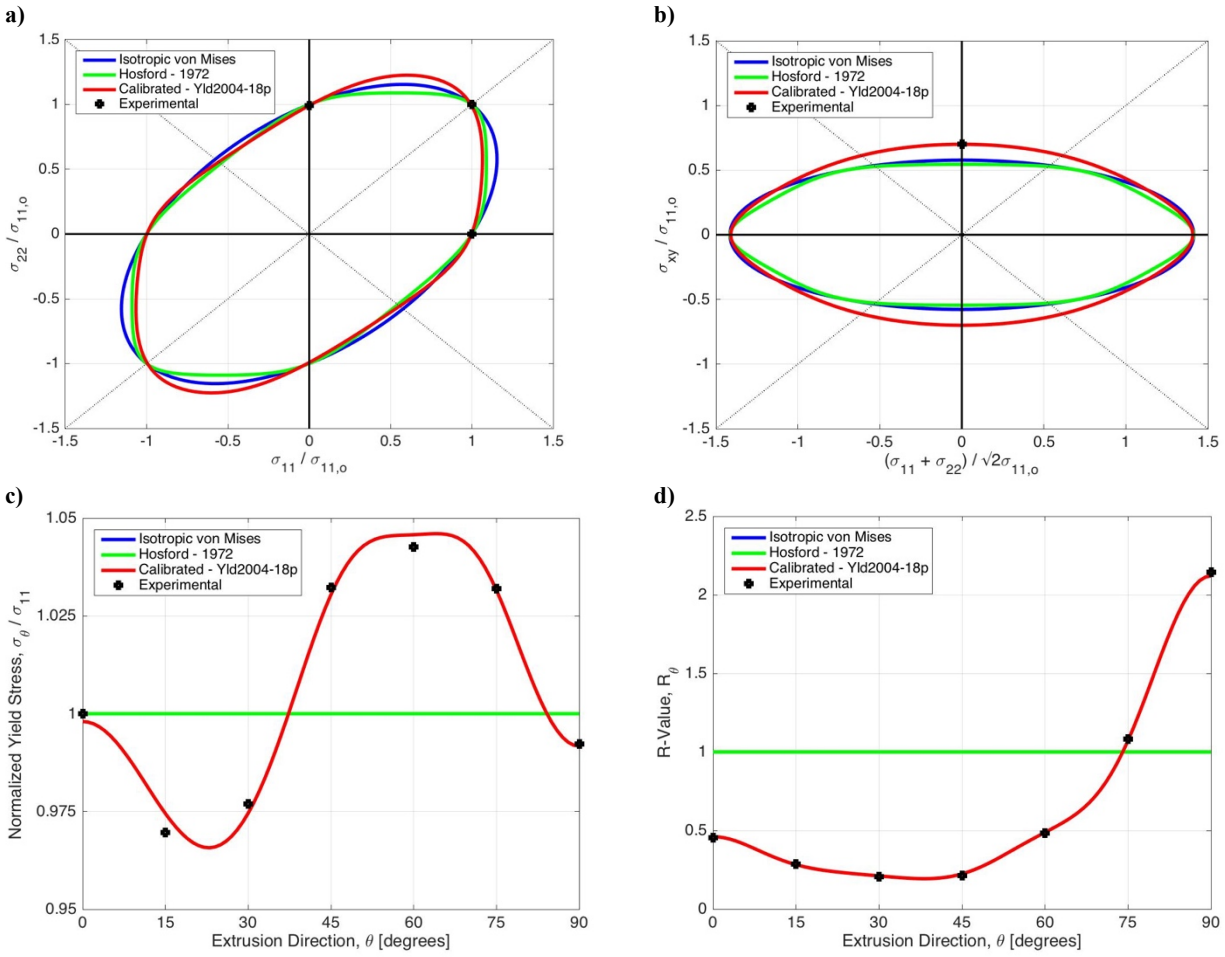

Figure 7.4 - Normalized yield loci in a) $\sigma_{12} = 0$ plane and b) $\sigma_{11} = \sigma_{22}$ plane, c) normalized yield stress variation and d) Lankford coefficient vs extrusion orientation for von Mises [29], Hosford [31], and Barlat et al. [35] Yld2004-18p yield function: comparison: between experimental measurements [140, 116] and calibration

Table 7.6 - Voce hardening parameters of extrusion AA6063-T6 aluminum alloy

	AA6063-T6
σ_0 [MPa]	180
σ_{UTS} [MPa]	235
D	20

Table 7.7 - Power-law hardening parameters of extrusion AA6063-T6 aluminum alloy

	AA6063-T6
K [MPa]	310
n	0.125
ε_0	0.0022

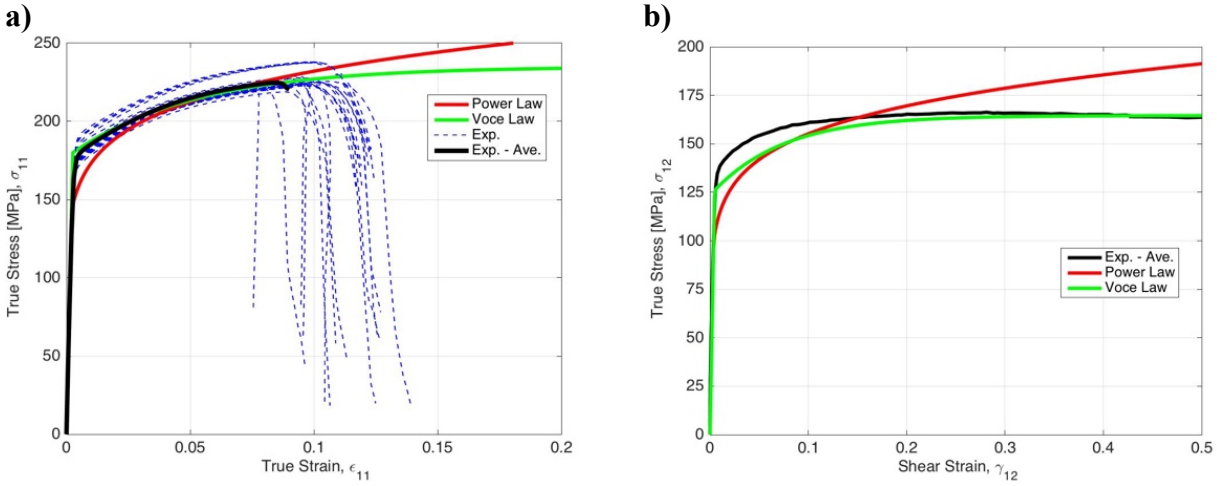

Figure 7.5 - Comparison of different flow stress model fits to a) Uniaxial tensile and b) Shear stress response [41, 42] of extrusion AA6063-T6

7.4 Finite Element Model

A non-linear explicit dynamic formulation of the commercial FE software LS-DYNA was used throughout this work [58]. A total simulation time of 15 milliseconds was used in the crush study. The FE models are shown in Figure 7.6. The FE model consists of the crush tube constrained between the two steel plates (blue and yellow), bosses (green and cyan), and a linear mass (magenta). The elastic material properties for all components are listed in Table 7.8. The bottom steel plate (blue) was constrained at the location of the load cells in all rotational and translational degrees of freedom. The linear mass (shown in magenta) was constrained to prevent lateral motion and given an initial velocity 15.6m/s [56km/h]. The steel bosses, end plates and linear mass were modeled using an elastic material model (*MAT_ELASTIC) and

individually meshed according to the experimental setup requirements. Eight-node hexahedral elements with selective reduced (S/R) integration (ELFORM=2 for *SECTION_SOLID) were used to model these components. The force-displacement response was obtained by monitoring the reaction force on the constrained nodes of the fixed plate (blue) and the displacement of a node on the linear mass (magenta). Contact algorithms were placed between the crush tube, steel plates and bosses, and between the linear mass and floating end plate. Self-contact algorithms were also placed to capture the effects of the folds stacking onto each other. Tied contact algorithms were used on the surfaces of the bosses to the end plates. Details about mesh size for each component can be seen in Figure 7.6.

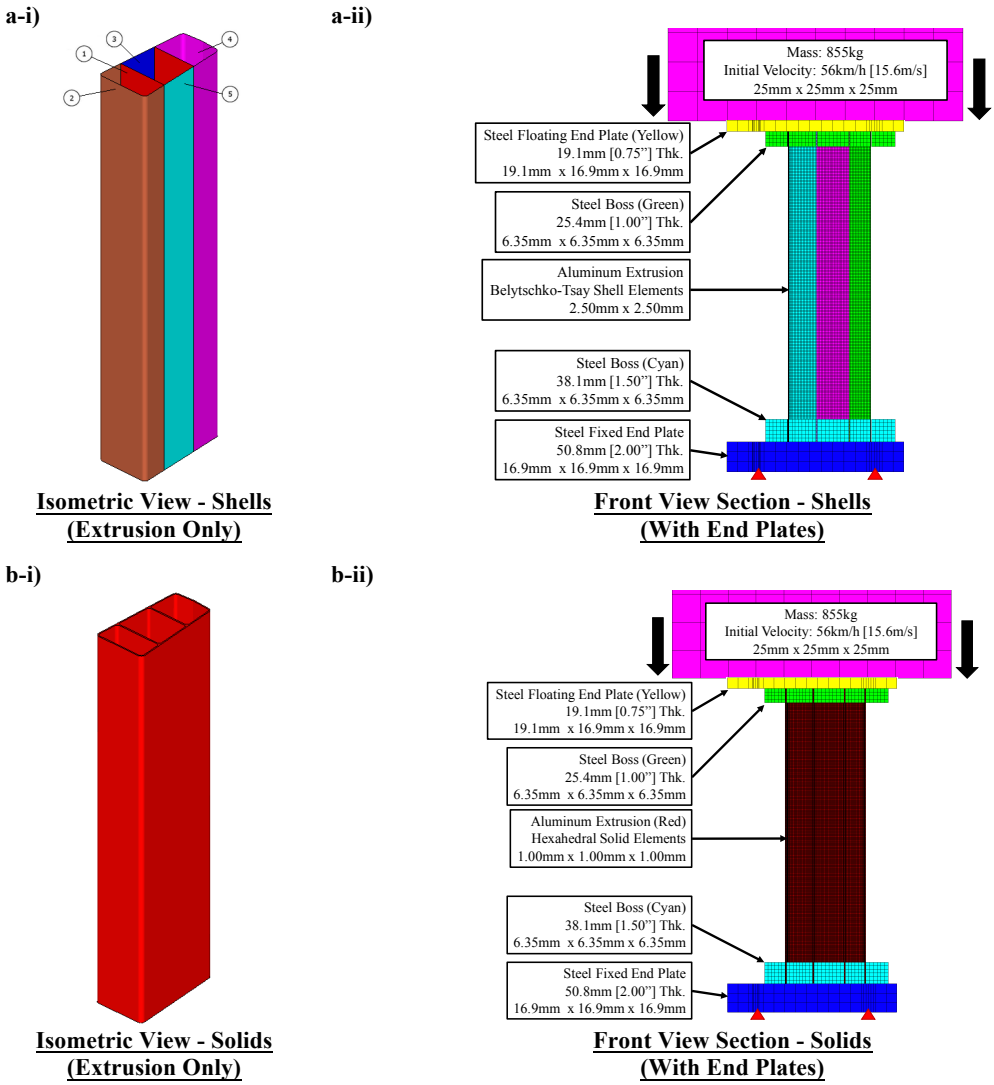

Figure 7.6 - (a) Shell element and (b) Hexahedral element model of FE Model Setup of Crush Tube: i) Isometric View without Bosses and (ii) Front View Section with Bosses

Table 7.8 - Elastic Material Properties of Aluminum and Steel

	Aluminum	Steel
Density [g/cm^2]	2.70	7.80
Elastic Modulus [MPa]	67900	205000
Poisson Ratio	0.34	0.30

Two meshing techniques were applied to the crush tube: solid and shell element modeling. Shell element formulations. For the solid element model, eight-node hexahedral elements with S/R integration were also used to model the geometry of the profile presented in Figure 6.1. A mesh size of approximately 1.00mm × 1.00mm × 1.00mm was employed through the mesh. It was shown in the work of Kohar et al. [104] that two elements through the wall thickness was sufficient to capture the force-displacement response of Type-I crush modes with good accuracy and computational efficiency. For the shell element model, the crush tube is meshed about the mid-thickness of the profile geometry. Each of the five unique wall thickness sections (shown in red, blue, brown, magenta and cyan) are individually meshed. Belytschko-Tsay shell elements (ELFORM=2 for *SECTION_SHELL) were used to simulate plane stress deformation. Table 7.9 presents the prescribed wall thicknesses for each section. A mesh size of 2.50mm × 2.50mm with 7 through-thickness integration points was employed through the crush tube. A total of 45,570 shell elements and 559,650 solid elements were used for each respective modeling technique.

Table 7.9 - Initial Section Thickness

	t_1 [mm]	t_2 [mm]	t_3 [mm]	t_4 [mm]	t_5 [mm]
Baseline	2.10	1.82	1.77	1.80	1.84

7.4.1 Comparison of Experimental and Simulation Crush Data

This section presents a comparison of different constitutive and FE model formulations with experimental energy absorption characteristics. Figure 7.7 and Figure 7.8 presents a comparison of the experimental crushed extrusions with simulation predictions of the plastic strain contours for both 2-dimensional and 3-dimensional formulations. All three constitutive and two FE model formulations predict combinations of Type-I crush modes during crush that agrees well with experimental deformation [72]. Figure 7.9 presents a comparison of the force and energy-

displacement predictions for the various crush rates using the various model formulations. Each predicted response was also filtered using an SAE CFC 1000 filter to allow for a direct comparison with experiments. Table 7.10 summarizes the predicted mean crush force, peak crush force, energy absorption, specific energy absorption and crush efficiency for each model. The error, $\Delta\in_{rr}$, for each simulation is also presented in Table 7.10.

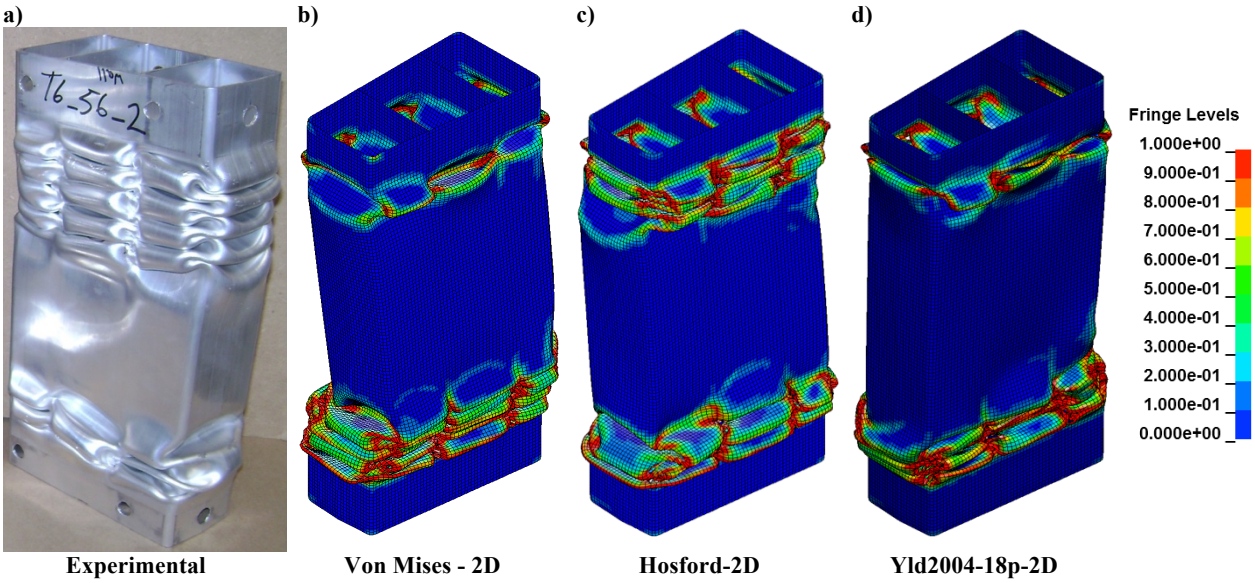

Figure 7.7 - a) Experimental and b) von Mises – 2D, c) Hosford - 2D, and d) Yld2004-18p-2D simulations of plastic strain contours of crush tube

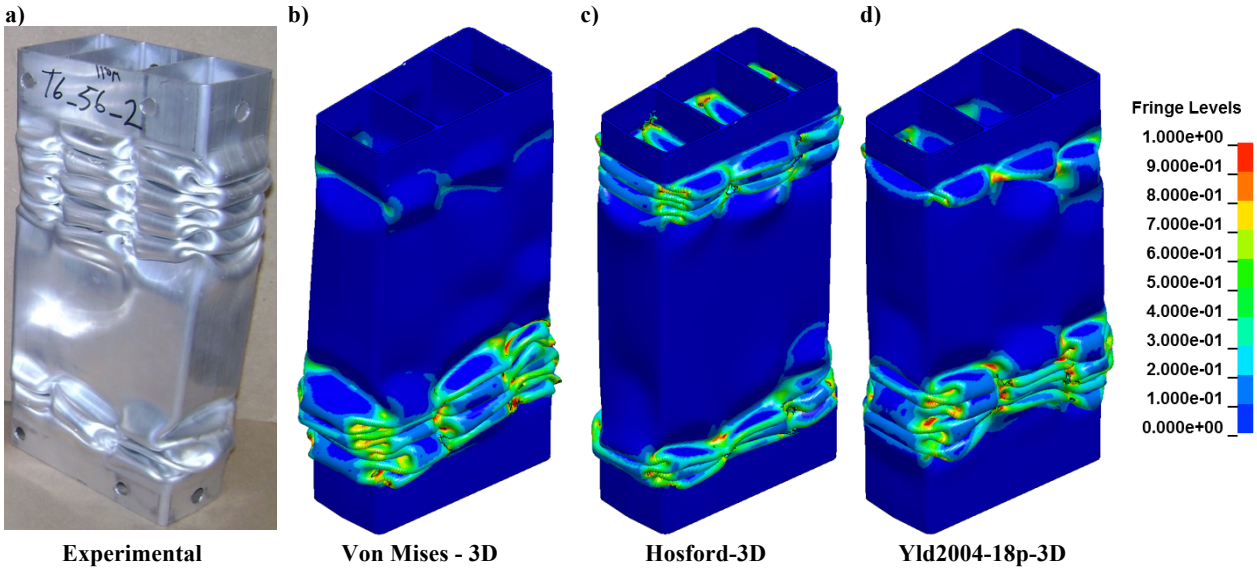

Figure 7.8 - a) Experimental and b) von Mises – 3D, c) Hosford - 3D, and d) Yld2004-18p - 3D simulations of plastic strain contours of crush tube

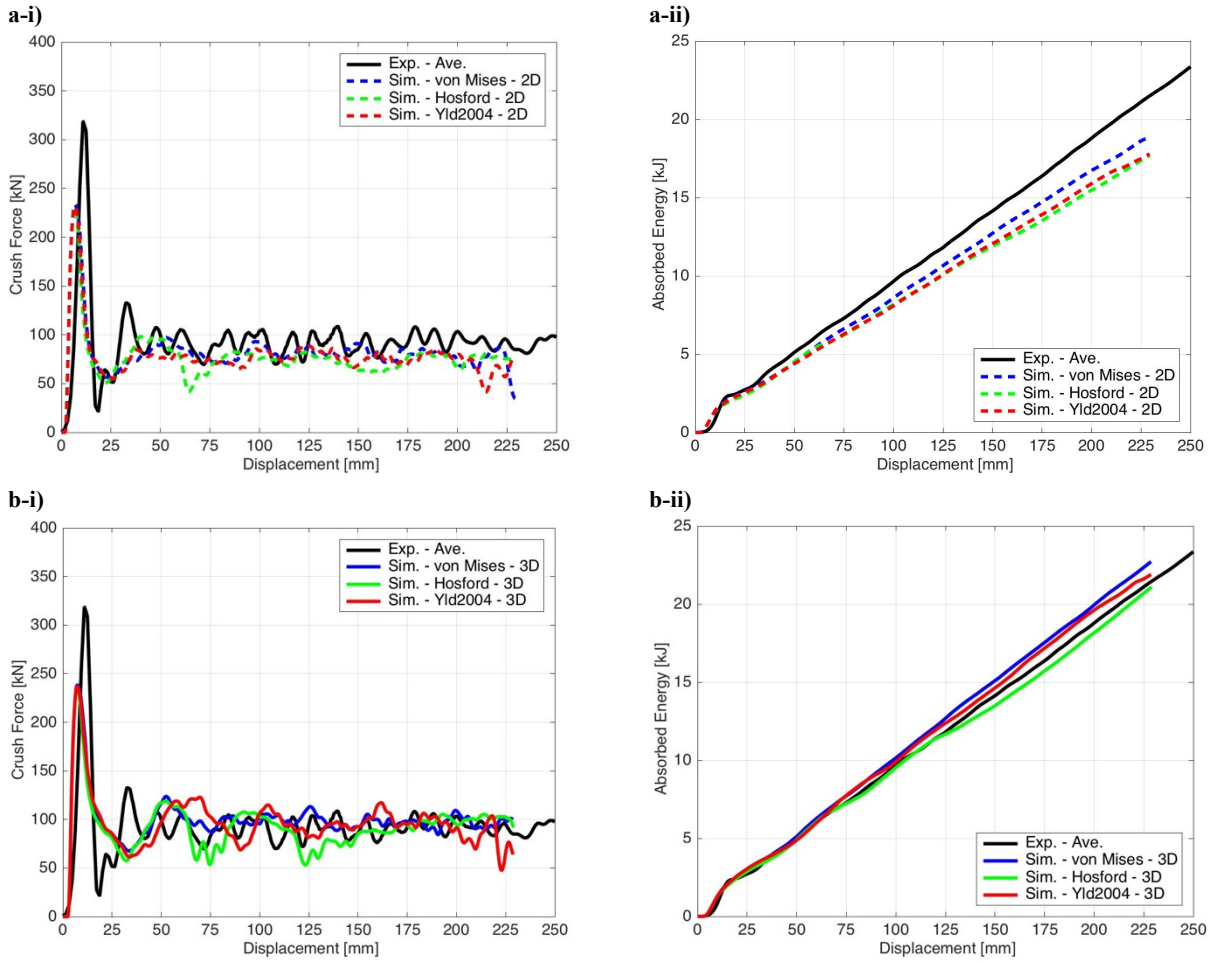

Figure 7.9 - Comparison of experimental and simulated a) 2-dimensional and b) 3-dimensional predictions of i) Crush force and ii) Energy absorption of aluminum extrusion

Table 7.10 - Experimental, simulation time and error for mean crush force, peak crush force, energy absorption, specific energy absorption, crush efficiency for 2D and 3D formulations

		2D Simulations			3D Simulations		
	Exp.	Sim. von Mises 2D	Sim. Hosford 2D	Sim. Yld2004-18p 2D	Sim. von Mises 3D	Sim. Hosford 3D	Sim. Yld2004-18p 3D
Energy Absorption [kJ]	21.11	17.5	17.4	18.6	22.4	20.7	21.6
Mean Crush Force [kN]	94.4	82.1	77.1	77.6	99.4	92.1	95.7
Peak Crush Force [kN]	318.7	233.4	230.0	231.5	238.3	235.1	236.8
Crush Efficiency [%]	29.6	35.1	33.5	33.5	41.7	39.2	40.4
$\Delta\epsilon_{rr}$ **Sim. To Exp. Crush Force (%)**	- -	13.0	18.3	17.8	5.3	2.4	1.4

The von Mises-2D, Hosford-2D, and Yld2004-18p-2D models predicted a crush force of 82.1kN, 77.1kN, and 77.6kN respectively; the difference in prediction error, with respect to the Yld2004-18p-2D models for von Mises-2D and Hosford-2D was +6.5% and -0.6% respectively. The von Mises-3D, Hosford-3D and Yld2004-18p-3D models predicted a mean crush force of 99.4kN, 92.1kN, and 95.7kN respectively. For each FE model formulation, the isotropic von Mises yield function predicted higher mean crush force, while the Hosford yield function predicted the lowest. This is a result of the von Mises having the largest normalized yield surface area in the $\sigma_{12} = 0$ plane, where the deformation mechanisms are dominated by plane-strain and balanced biaxial.

All three 2-dimensional FE model formulations under predict the mean crush and energy absorption by 13.0 – 17.8% for the different yield functions. The 3-dimensional FE model formulations, however, were able to predict the mean crush force between -2.4% and +5.3%. The 3-dimensional FE model utilizing the Yld2004-18p yield function had the best predictive capability with an over prediction error of +1.4%. This is a result of capturing both the through-thickness energy absorption during plastic hinging, and capturing the variation in yield stress and Lankford coefficients. The over-prediction of the crush force can be attributed to not accounting for the post-necking, failure and fracture behaviour in the constitutive model (see Ref. [141, 142, 143]). Incorporating additional experiments [144] with constitutive models that can capture the ductile failure (i.e. Ref. [145, 146, 147, 148]) in aluminum can improve predictions.

Nevertheless, the overall force-displacement response trend and deformation mechanisms are captured by all constitutive models and FE formulations. The isotropic model produces a similar force-displacement response as the anisotropic model with significantly less computational requirements. Since the models have good predictive capabilities for both isotropic and anisotropic models, it is concluded that the FE model has been constructed properly and is suitable for size optimization.

7.5 Optimization Study Using Anisotropic Yield Functions

In this section, the framework for Front Rail Optimization Strategy of Thickness (FROST) Method was applied to the shell element FE model of the aluminum extrusion. Figure 7.10 presents a flowchart of the optimization procedure. In an attempt to achieve global

optimization, the genetic algorithm (GA) optimization procedure without domain reduction was used. As discussed in Section 7.4 and shown in Figure 7.6a, the FE model was decomposed into five unique components where each section thickness was parameterized accordingly as t_i with $i = 1\ldots5$. Each section had an upper and lower bound of 2.25mm and 1.75mm with discrete increments of 0.01mm. The artificial neural network (ANN) metamodel technique was applied with a metamodel convergence error tolerance, $Err_{converge}$, constraint of 1%. A maximum mass constraint of 1.39kg, which corresponded to the mass for the baseline sizing presented in Table 7.9 , was also applied to the optimization process. Furthermore, the sizing presented in Table 7.9 was used as an initial guess for the optimization process. In this study, a single objective optimization (SOO) function of specific energy absorption (SEA) was used. The optimization problem formulation was

$$\begin{cases} \text{Max } \{P_1 = SEA\ (t_i)\} \\ \text{s.t. } \text{Mass} \leq 1.390 \text{ kg} \\ \quad t_i \in [1.75, 1.76, \ldots, 2.25]\text{mm} \\ \quad Err_{converge} \leq 0.01 \end{cases} \qquad (7.2)$$

To reduce the complexity of the FE model used in the optimization process, the end plate and boss fixtures were removed and replaced with translation constraints with a constant velocity of 15.6m/s in the crush direction. Furthermore, the mesh size was increased to 5.00mm × 5.00mm Belytschko-Tsay shell elements with 3 through-thickness integration points. Figure 7.11 and Figure 7.12 present comparisons of the complete shell FE model with the simplified optimization model for energy absorption and folding patterns with experiments. Each simulation was executed with 8 x 2.70 GHz Intel Xeon E5-2680 processors. Overall, the simplified optimization FE model still captured the trends of energy absorption and deformation of the experiments.

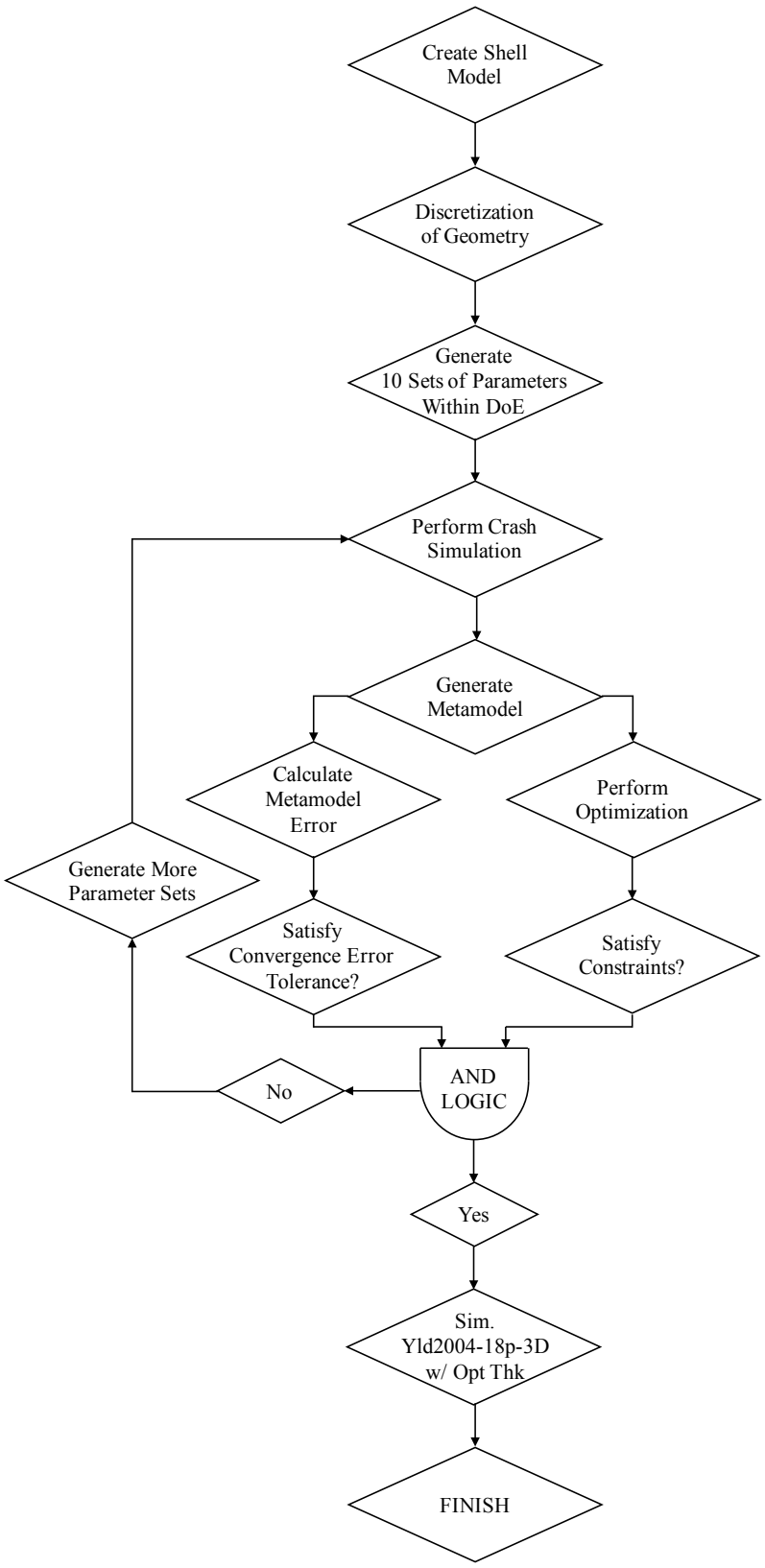

Figure 7.10 - Flowchart of Optimization Procedure

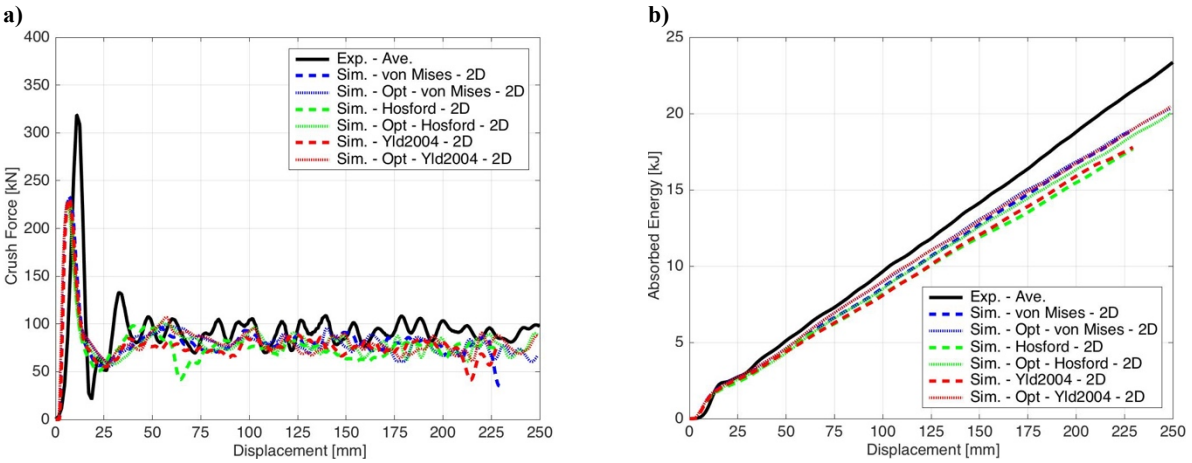

Figure 7.11 - Comparison of experimental and simulated complete and optimization FE model of a) Crush force and b) Energy absorption of aluminum extrusion

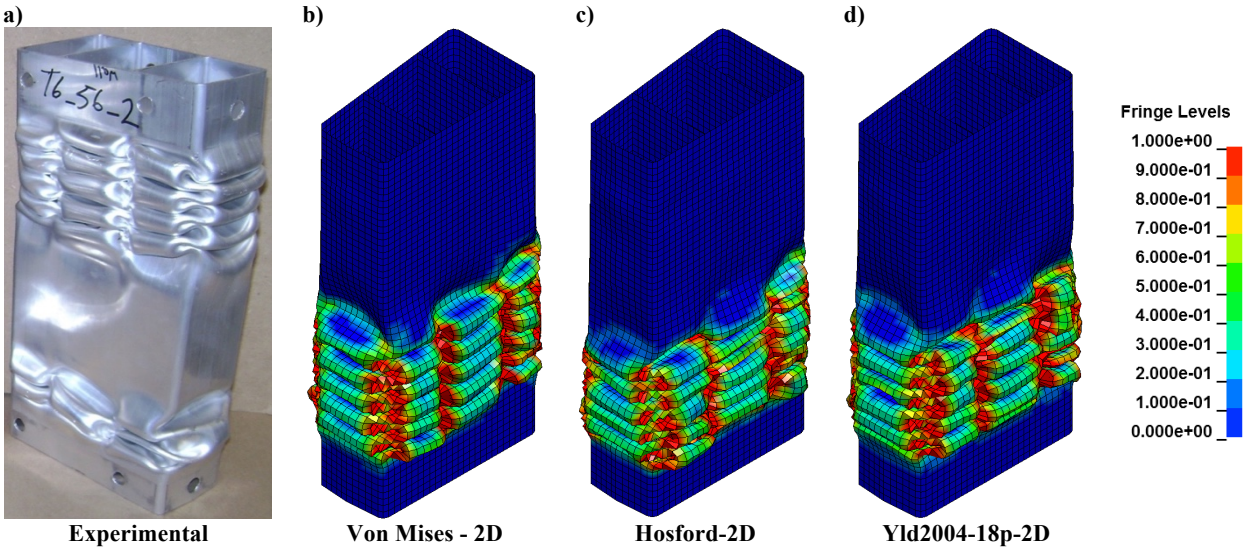

Figure 7.12 - a) Experimental and simplified optimization FE model b) von Mises – 2D – Opt., c) Hosford - 2D – Opt., and d) Yld2004-18p-2D – Opt. simulations of plastic strain contours of crush tube

In the following section, the three yield functions were employed with the GA optimization procedure without domain reduction to improve the SEA of the extrusion. The emphasis of this study will be on the optimization of SEA that employed the Yld2004-18p-2D yield function. A comparison between the optimization results of SEA for different yield functions is presented.

7.5.1 Optimization Results of Yld2004-18p-2D Yield Function with SOO-SEA

Figure 7.13 presents the convergence plot of each individual wall thickness parameter for optimization of SEA using Yld2004-18p-2D. Figure 7.14 presents a convergence plot of the

metamodel predictive error, the optimal SEA and mass of each generated optimal solution, and the predictive error of the metamodel at the optimal sizing. The optimization process converged within 13 iterations to a total mass of approximately 1.39kg with an SEA of 14.26 kJ/kg. Figure 7.15 present plots of the SEA response surface contours for the optimization process that is centered about the optimal sizing. On each plot, a black trace is presented that indicates the combinations of thickness parameters that produce a mass of 1.39kg. Decreasing either thickness parameter will decrease the mass. For this optimization process, the converged optimal solution occurred at the maximum allowable mass; however, global optimization was not achieved. Throughout the parameter domain, there exist multiple solutions that surpass the performance of the converged solution, but they violate the maximum allowable mass. Thus, the maximum allowable mass constraint is limiting global optimization for the constrained topology.

7.5.2 Comparison of Different Yield Functions for Optimization of SEA

In this section, the results of different yield functions on the optimization of SOO Function - SEA is presented. As discussed earlier, the optimization procedure employs a plane stress FE model to reduce the computational requirements. After the optimization procedure completed, an FE model was constructed of each sizing using eight-node hexahedral elements with (S/R) integration and simulated using the Yld2004-18p-3D yield function. Figure 7.16 presents the simulated force and energy-displacement response of the three sizing combinations. Table 7.11 presents the final sizing of the extrusion for the three yield functions and Table 7.12 presents the corresponding energy absorption responses. The simulation response of the initial wall thickness sizing using the Yld2004-18p-3D is also presented for comparison. Figure 7.17 and Figure 7.18 presents the percent difference between the response surfaces for SEA generated by the von Mises and Hosford yield function compared to the Yld2004-18p-2D. It can be observed that differences upwards of +/-15% can be observed with large variations in differences throughout the domain. This results in each yield function generating a unique sizing for each optimization.

The Yld2004-18p-2D optimized extrusion had a mean crush force, peak crush force, energy absorption, and crush efficiency of 98.0kN, 237.5kN, 22.5kJ, and 41.3% respectively. This corresponds to an increase in energy absorption and mean crush force of +4.2% and +2.5% respectively. The Hosford-2D optimized extrusion had a mean crush force, peak crush force, energy absorption, and crush efficiency of 95.4kN, 231.8kN, 21.5kJ, and 41.2% respectively;

this resulted in a minor loss in energy absorption (-0.3%) and mean crush force (-0.5%). The von Mises optimized extrusion had a mean crush force, peak crush force, energy absorption, and crush efficiency of 94.8kN, 238.7kN, 21.3kJ, and 39.7% respectively. This corresponds to a decrease in energy absorption and mean crush force of -1.4% and -0.9% respectively compared to the initial sizing. Comparing the sizing of the von Mises-2D and Yld2004-18p-2D solutions, the Yld2004-18p-2D optimization procedure predicted +3.4% higher crush force and +5.6% energy absorption than the von Mises optimization procedure. In this application, the von Mises optimization process resulted in a sizing that produced lower energy absorption characteristics than the initial sizing.

Although minor changes were observed for the Hosford optimized extrusion, the Hosford sizing improved the crush efficiency by +0.8% through a decrease in the peak crush force by -2.1% compared to the initial sizing. This improvement results from the Hosford yield function capturing the yield surface curvature within the uniaxial, plane strain, and balanced biaxial regime better than the von Mises yield function. Thus, the sizing generated by the Hosford yield function outperformed the sizing of the von Mises. This indicates that the incorporating the non-quadratic yield function exponent can have an influence on size optimization. However, the Yld2004-18p yield function predicted the highest energy absorption characteristics than any other yield function. Again, this is a result of capturing the variation in yield stress and Lankford coefficients in a manner that best represents the material in the local regions of large deformation. This result shows that incorporating material anisotropy can generate additional improvements in energy absorption when coupled with optimization strategies.

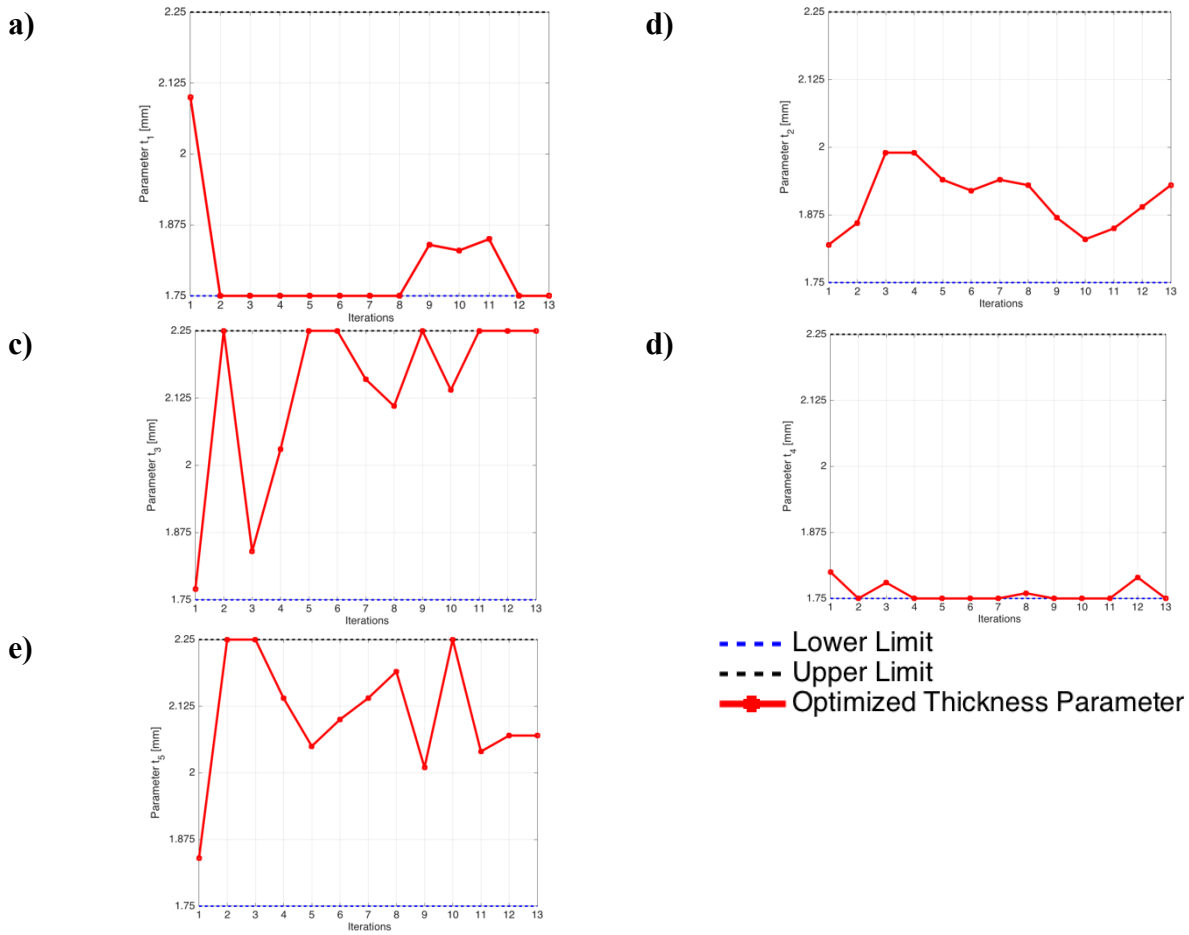

Figure 7.13 - Wall thickness parameters convergence plots of a) t_1, b) t_2, c) t_3, d) t_4 and e) t_5 for SOO Function – SEA using Yld2004-18p-2D yield function with GA and without Domain Reduction

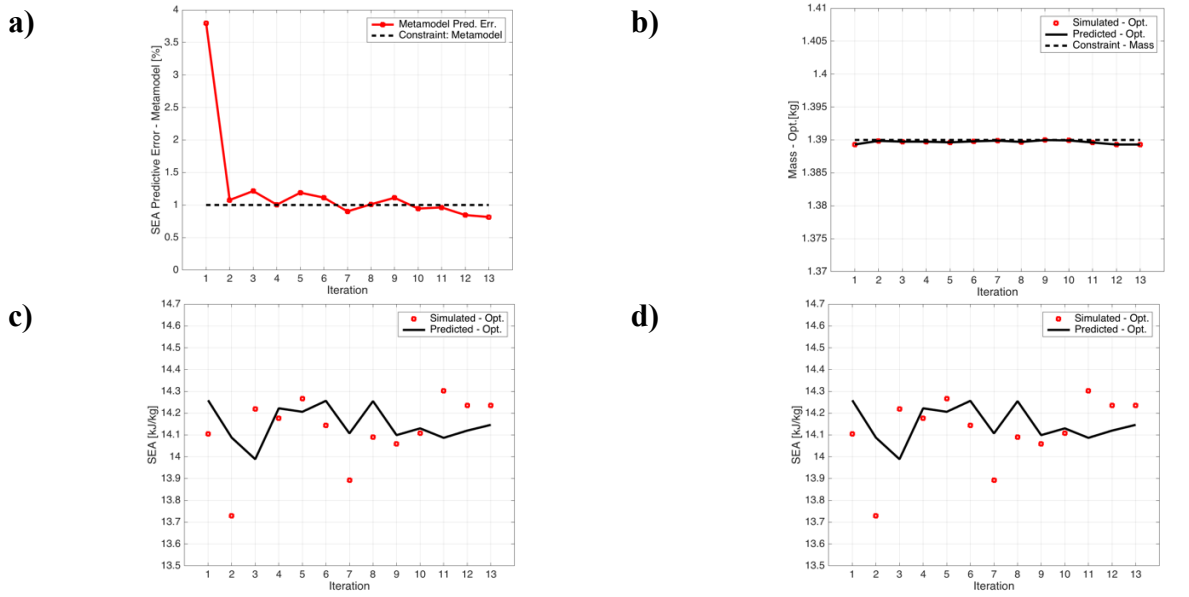

Figure 7.14 - Convergence plot of (a) SEA metamodel predictive error, (b) Mass of optimal sizing, (c) Optimal SEA and (d) Metamodel predictive error for optimal sizing using Yld2004-18p-2D yield function with GA and without Domain Reduction

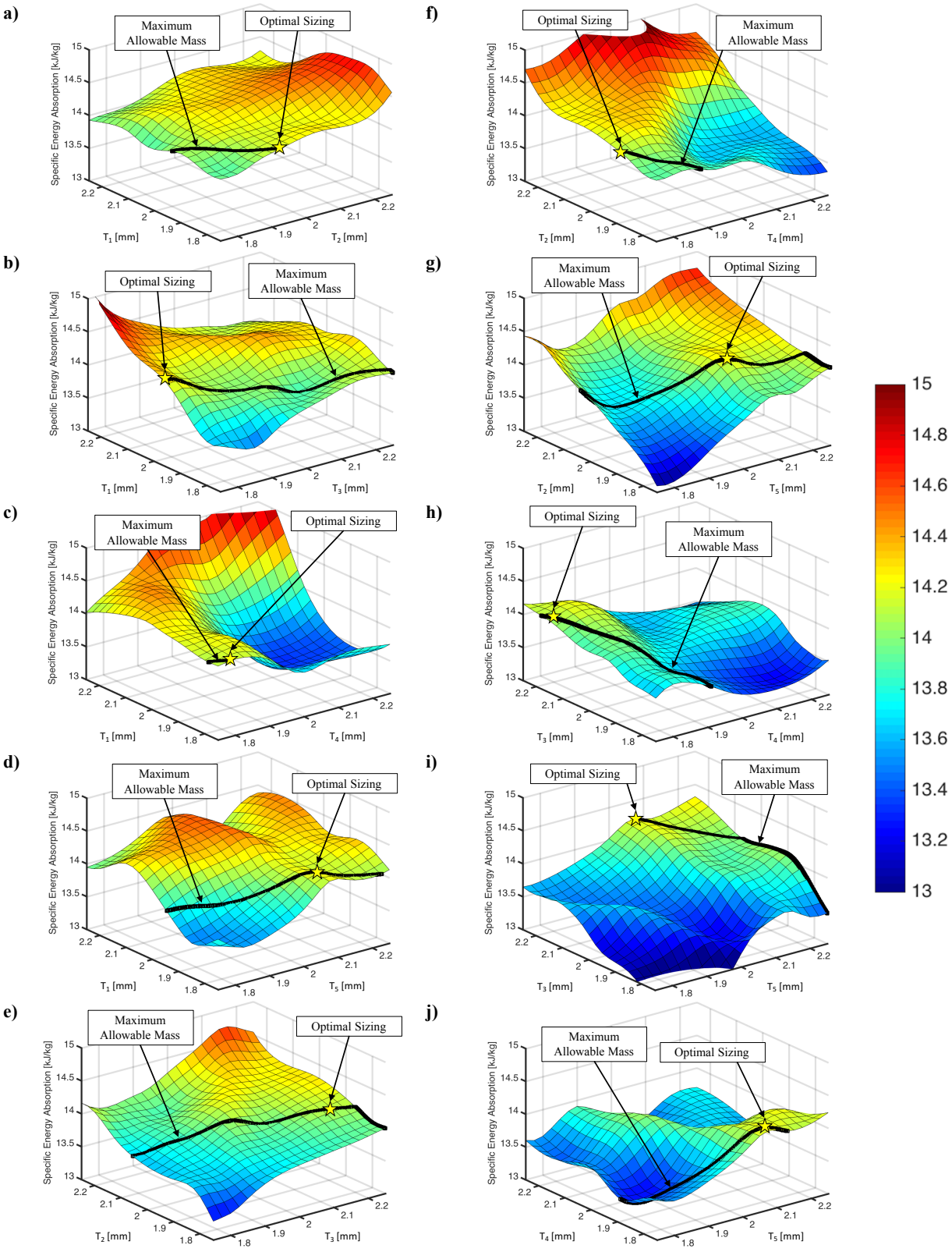

Figure 7.15 - Surface response plots for specific energy absorption (SEA) of Yld2004-18p-2D optimization process with GA and without Domain Reduction

a) b)

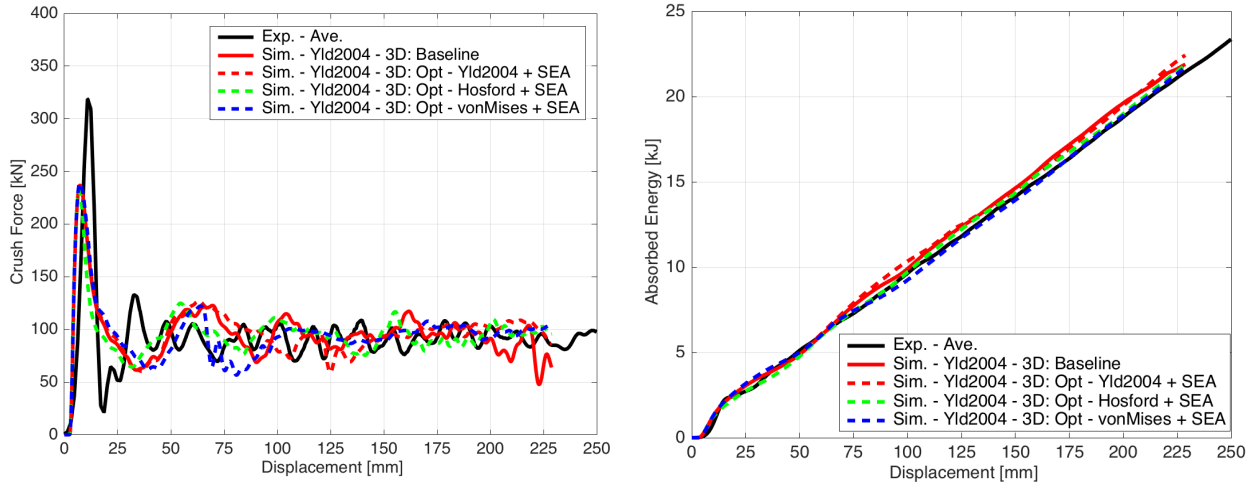

Figure 7.16 - Comparison of experimental and simulated baseline and optimization FE model of a) Crush force and b) Energy absorption of aluminum extrusion using Yld2004-18p-3D

Table 7.11 - Converged wall thicknesses for optimization of SEA for various yield functions using GA w/o Domain Reduction

Yield Function	Problem Formulation	Iter.	t_1 [mm]	t_2 [mm]	t_3 [mm]	t_4 [mm]	t_5 [mm]
Yld2004-18p	Initial Sizing	- -	2.10	1.82	1.77	1.80	1.84
	SOO Function - SEA	13	1.75	1.93	2.25	1.75	2.07
Hosford	SOO Function - SEA	16	1.89	1.75	2.20	1.75	2.25
Von Mises	SOO Function - SEA	5	2.13	1.75	1.78	1.75	2.08

Table 7.12 - Energy absorption response for optimization of SEA for various yield functions using GA w/o Domain Reduction

Yield Function	Problem Formulation	Energy Absorption [kJ]	Mean Crush Force [kN]	Peak Crush Force [kN]	Crush Efficiency [%]
Yld2004-18p	Initial Sizing (Sim.)	21.6	95.7	236.8	40.4
	SOO Function - SEA	22.5	98.0	237.5	41.3
Hosford	SOO Function - SEA	21.5	95.4	231.8	41.2
Von Mises	SOO Function - SEA	21.3	94.8	238.7	39.7

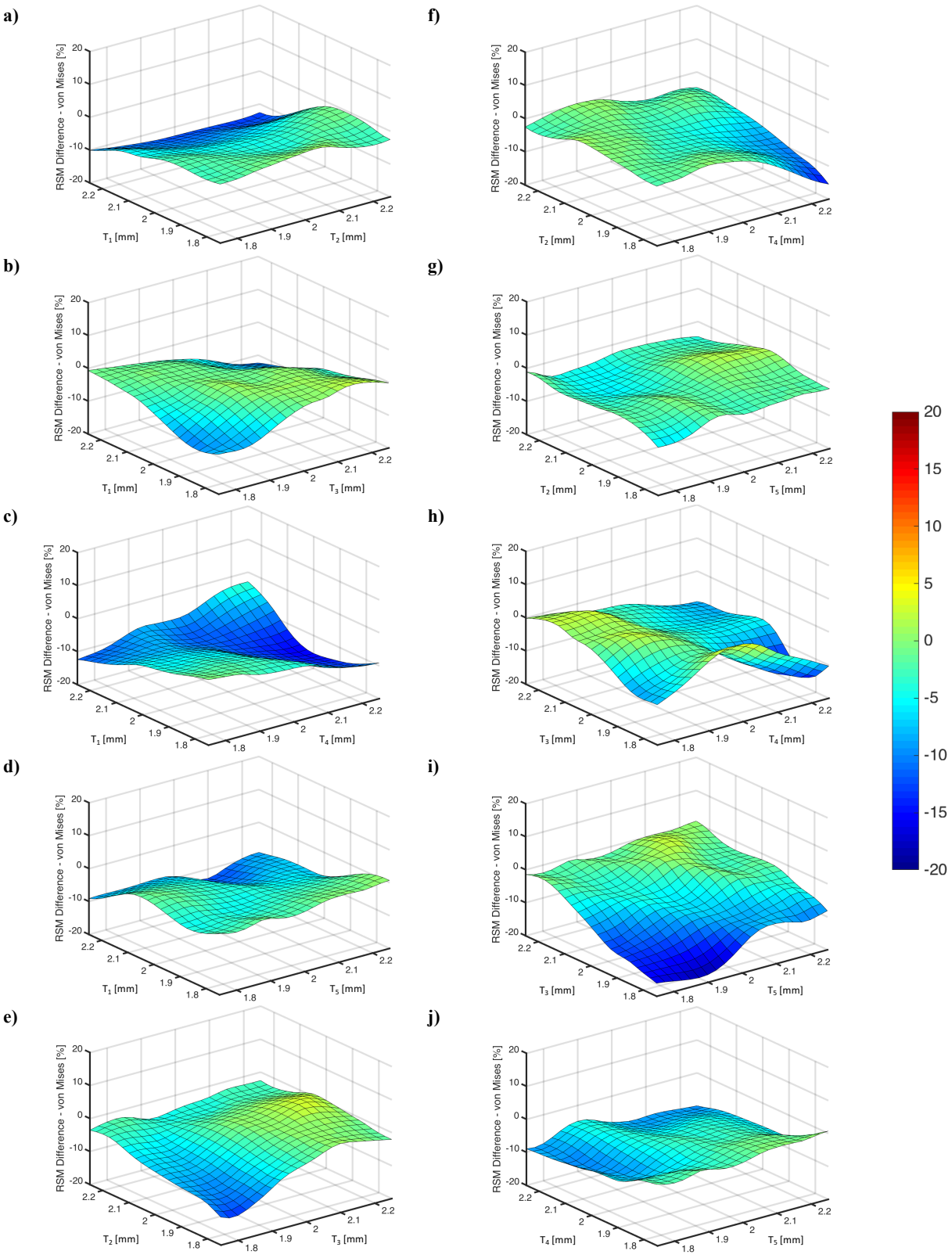

Figure 7.17 - Variation in surface response plots for SEA between Yld2004-18p-2D and Isotropic-2D optimization process with GA and without Domain Reduction

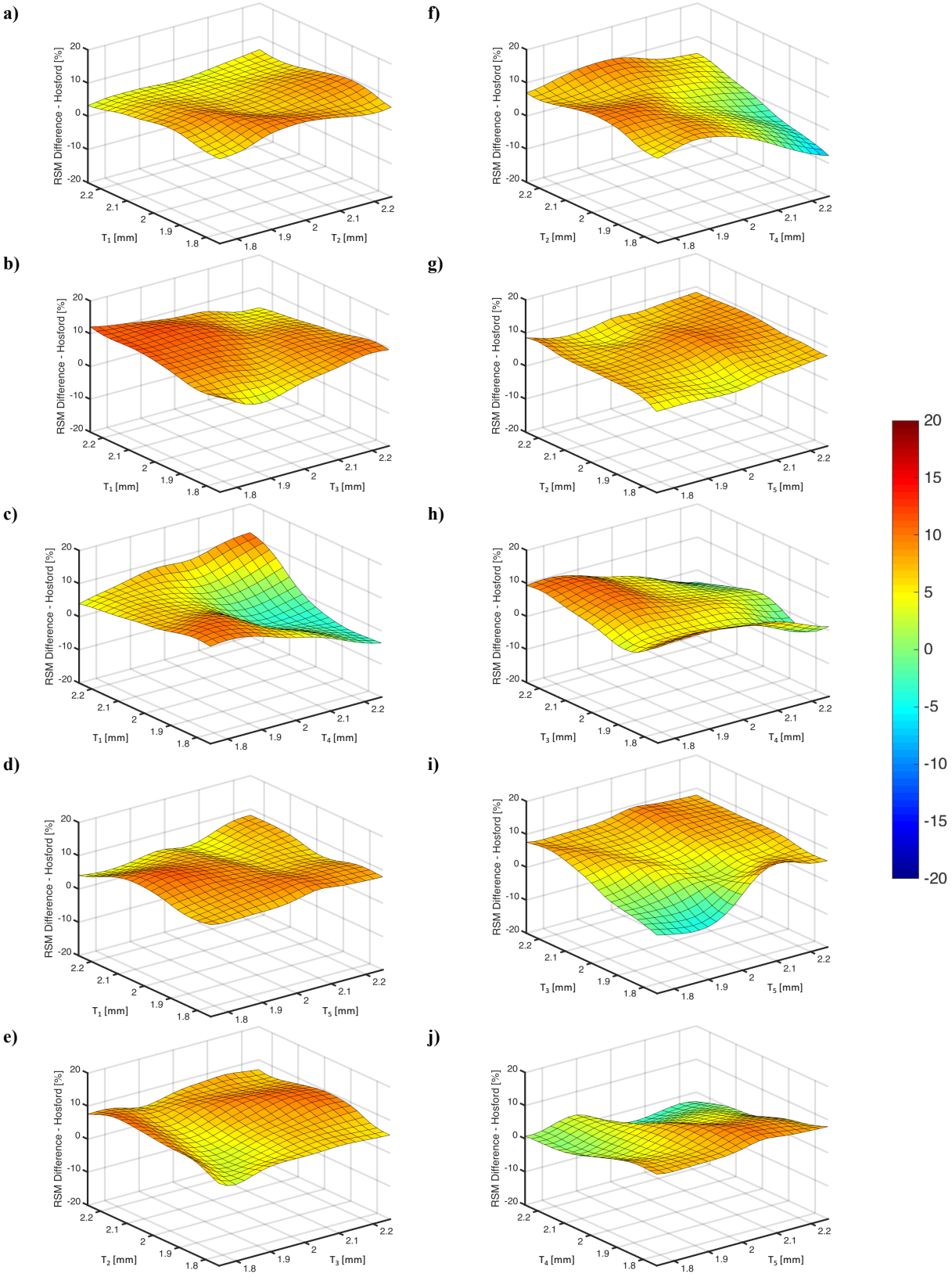

Figure 7.18 - Variation in surface response plots for SEA between Yld2004-18p-2D and Hosford-2D optimization process with GA and without Domain Reduction

7.5.3 Comments about Optimization using Yld2004-18p

Figure 7.19 presents interaction plots of energy absorption characteristics and their sensitivity to mass. In each figure, a solution that violated or satisfied the maximum allowable mass constraint of 1.39 kg was marked in red and green respectively. Figure 7.19a presents the interaction between SEA and crush efficiency. A linear regression with respect to SEA and crush efficiency was performed and presented in Figure 7.19a. The regression analysis generated an R-squared value of $R^2 = 0.9978$ indicating a strong linear correlation between SEA and crush efficiency. Figure 7.19b and c presents the interaction between peak crush force and SEA, and peak crush force and crush efficiency respectively. Although there is no direct relationship between these interactions, inspection of the solutions that satisfy or violate the maximum allowable mass constraint show that all satisfying solutions had at most a peak crush force of approximately 238kN, and that solutions that maximized SEA or crush efficiency occur at this peak crush force limit. Figure 7.19d presents the interaction between peak crush force and mass. Again, a linear regression with respect to peak crush force and crush efficiency was performed with a resulting R-squared value of $R^2 = 0.9983$. The peak crush stress, σ_{PCS}, can be defined by normalizing the peak crush force by the cross section area, as presented in Equation 7.3

$$\sigma_{PCS} = \frac{F_{peak}}{\sum_{i=1}^{5} C_i t_i} \qquad (7.3)$$

Figure 7.19e presents the interaction between the peak crush stress and the mass. For the various mass compositions of the extrusion, the peak crush stress corresponded to 235MPa with a maximum variation of 0.4%; the magnitude of the peak crush stress correlates to the magnitude of the ultimate tensile strength in the extrusion direction. Thus, there exists a direct relationship between a material's ultimate tensile strength and mass constraints in the optimization of extrusions. Utilizing this result can impose additional constraints on the design of experiments domain to could reduce the number of simulations required to perform optimization.

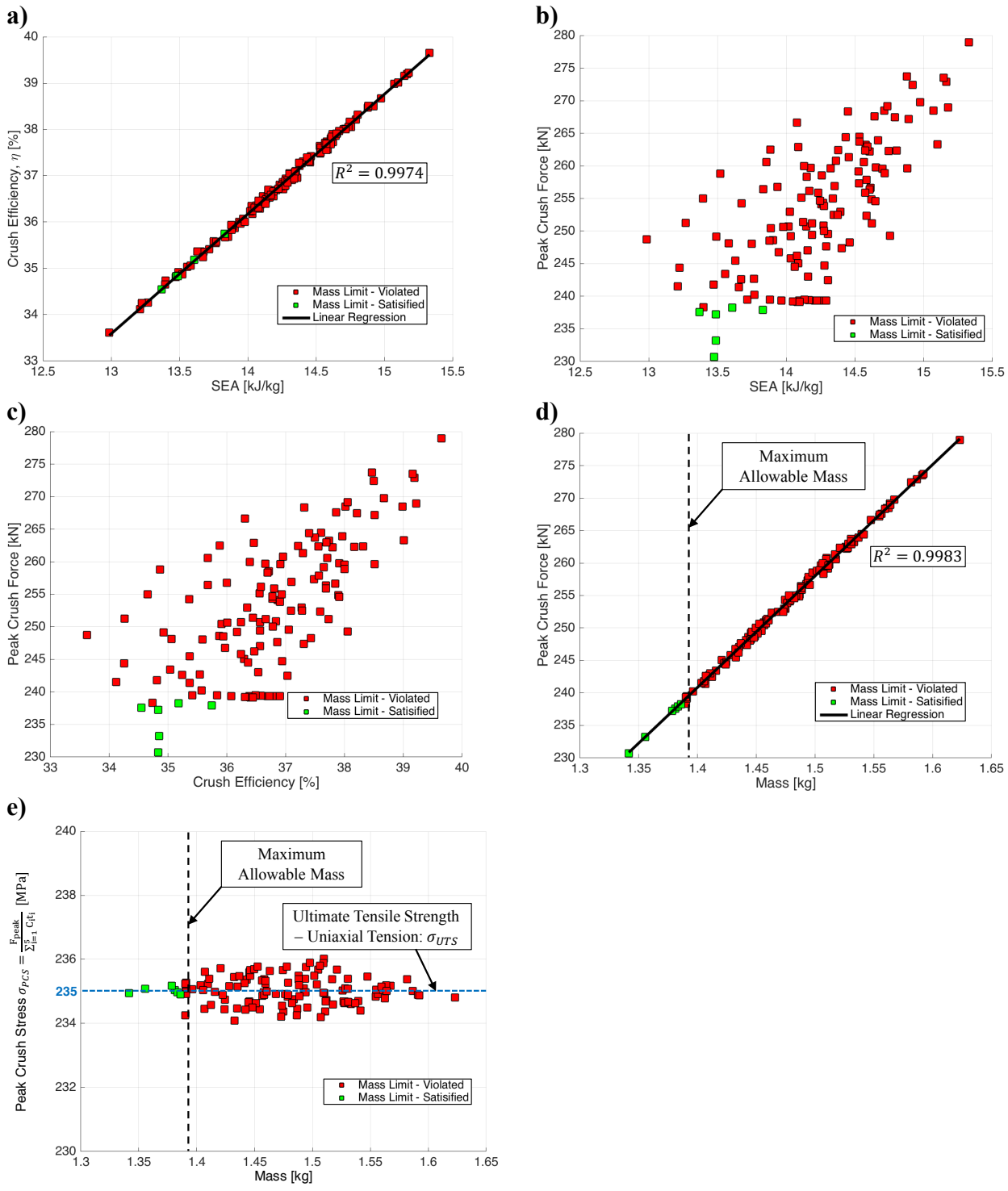

Figure 7.19 - Interaction between a) SEA vs. Crush Efficiency, b) SEA vs. Peak Crush Force, c) Crush Efficiency vs. Peak Crush Force, d) Mass vs. Peak Crush Force, e) Peak Crushing Stress vs. Mass

As suggested earlier, the overall performance of this profile was limited by the mass constraint for SEA optimization. However, relaxing the maximum allowable mass constraint could determine the global optimal SEA and mass for the given topology. Figure 7.20 and Figure 7.21 presents a study of the convergence and influence of maximum allowable mass constraint on optimal SEA for various yield functions. In this study, the GA optimization approach was used to optimize the sizing for SEA, where the maximum allowable mass constraint was varied between 1.39kg to 1.67kg in increments of 0.2kg for each yield function. Varying the maximum allowable mass allows for new combinations of wall thickness parameters to achieve superior SEA that would have been supressed by previous constraints. The value of 1.67kg corresponds to the mass of the profile where all sections had a wall thickness equal to 2.25mm. Table 7.13 presents the final mass and SEA for constrained and unconstrained optimization. For the unconstrained maximum allowable mass, the Yld2004-18p, Hosford, and von Mises yield functions converged to a mass of 1.54kg, 1.62kg, and 1.55kg respectively. In each yield function, the resulting sizing, and thus, the final mass was unique to each yield function. These converged masses represent the limit of size optimization for the given topology of the extrusion. Using the Metamodel of the Yld2004-18p-2D, the Yld2004-18p, Hosford, and von Mises yield functions predict a SEA of 16.24kJ/kg, 15.60kJ/kg, and 14.61kJ/kg respectively. Again, incorporating the yield surface curvature influence through the yield function exponent predicts higher energy absorption than the von Mises yield function. Incorporating the anisotropic variation predicts the best SEA for the given topology. Since each yield function is predicting different limits of sizing for the given topology, this result shows that it would be critical to incorporate an appropriate yield function when performing topology optimization in conjunction with size optimization.

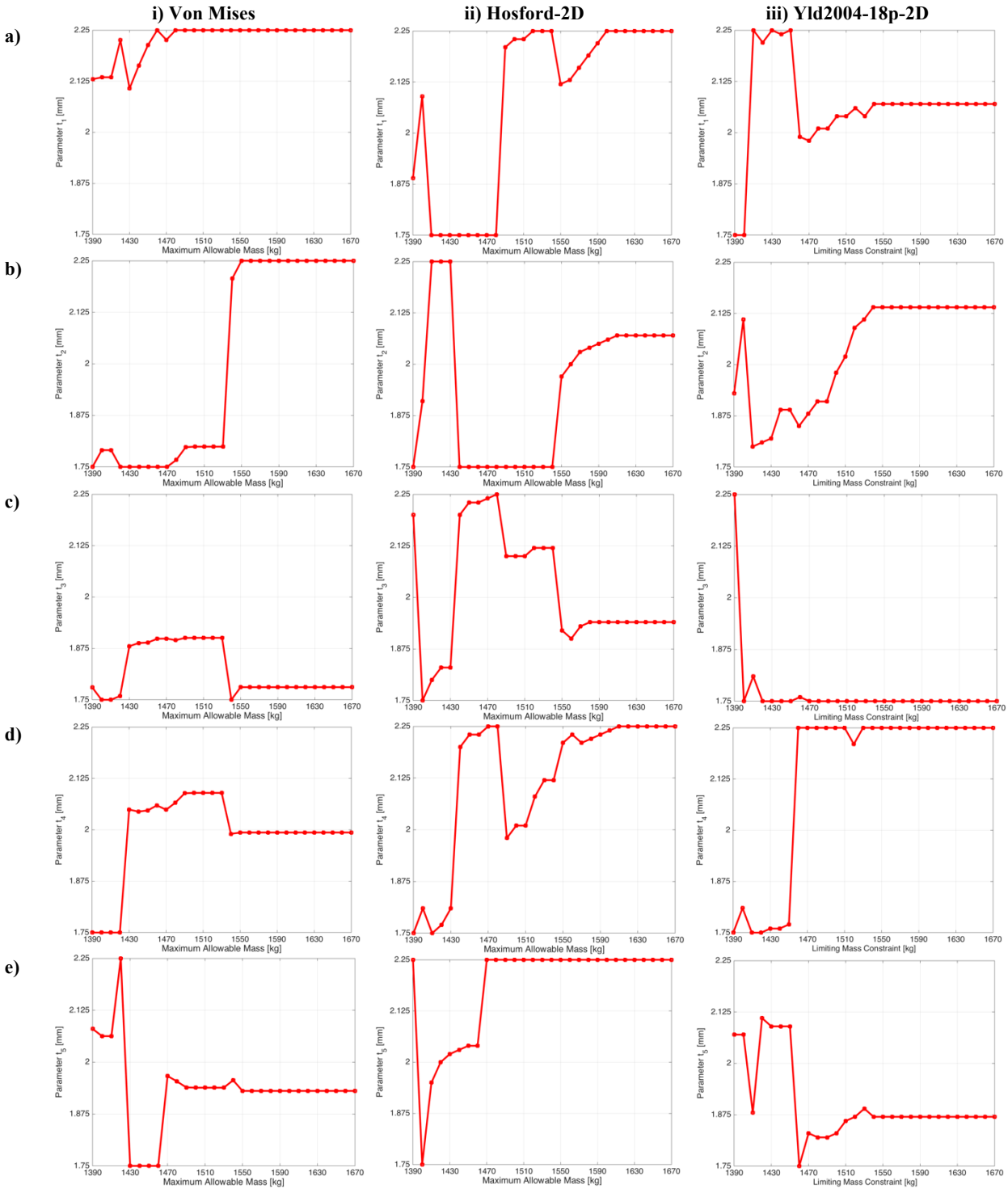

Figure 7.20 - Convergence of a) t_1, b) t_2, c) t_3, d) t_4 and e) t_5 wall thickness parameters for optimizing SEA for various maximum allowable mass constraints

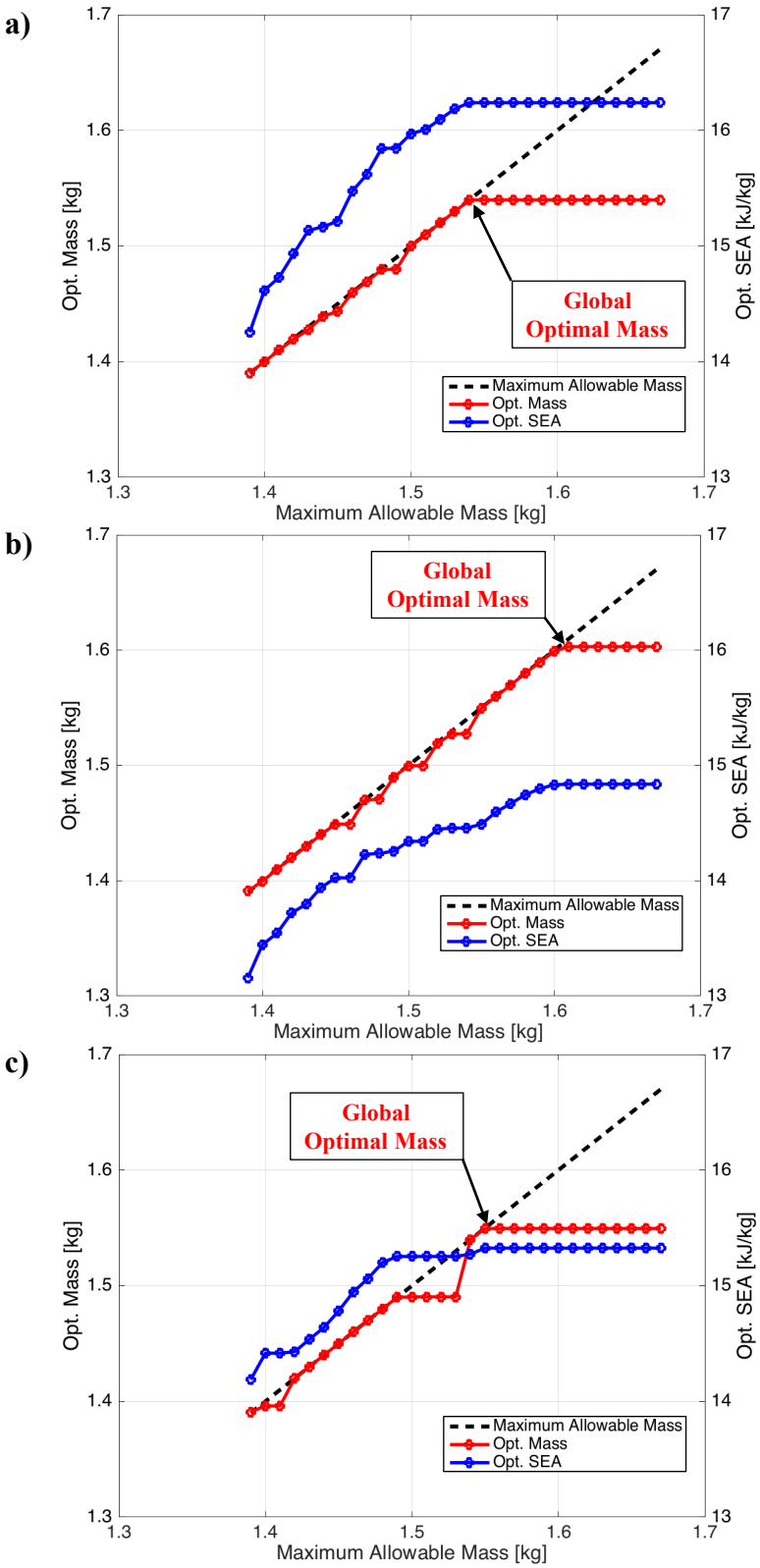

Figure 7.21 - Influence of maximum allowable mass constraint on optimal SEA for various yield functions: a) Yld2004-18p-2D, b) Hosford-2D and c) von Mises-2D yield functions

Table 7.13 - Comparison between constrained and unconstrained mass SEA optimum sizing for various yield

	Constrained Opt.		Unconstrained Opt.			
Yield Functions	**Mass [kg]**	**SEA [kJ/kg]**	**Mass [kg]**	**SEA [kJ/kg]**	**SEA (Yld2004-18p-2D) [kJ/kg]**	**Increase SEA [%]**
Yld2004-18p-2D	1.39	14.26	1.54	16.24	16.24	- -
Hosford-2D	1.39	13.16	1.62	14.83	15.60	3.9
Von Mises-2D	1.39	14.18	1.55	15.32	14.61	10.0

7.6 Analytical Analysis of Coupling Optimization with Anisotropic Yield Functions

For an aluminum extrusion with five independent sections, Chapter 4 presented an analytical relationship from Type-I collapse elements [72] for mean crush force that can be expressed as

$$E_{abs} = F_{mean}\delta = \frac{1}{4}\sum_{i=1}^{5} {t_i}^2 \left(16H_iI_1\frac{b_i}{t_i} + 2\pi C_i + 4I_3\frac{{H_i}^2}{b_i}\right) f(\sigma, t_i)\left(1 + \left(\frac{V}{3C_iM}\right)^{\frac{1}{P}}\right) \qquad (\ 7.4\ )$$

$f(\sigma, t_i)$ is a function dependent on the material yield stress function for mean crush force in a section. Since the topology of the structure was fixed, the mass of the structure

$$Mass(t_i) = L\rho\sum_{i=1}^{5} C_it_i \qquad (\ 7.5\ )$$

where L is the length of the profile and ρ is the density of the material. This assumed that details of the extrusion, such as fillets and radii, were negligible resulting in a linear function with respect to thickness. Thus, the specific energy absorption could be defined as

$$SEA(t_i) = \frac{E_{abs}}{Mass} = \frac{F_{mean}\delta}{Mass} = \frac{1}{4L\rho}\sum_{i=1}^{5} t_i\left(16H_iI_1\frac{b_i}{C_it_i} + 2\pi + 4I_3\frac{{H_i}^2}{C_ib_i}\right) f(\sigma, t_i)\left(1 + \left(\frac{V}{3C_iM}\right)^{\frac{1}{P}}\right) \qquad (\ 7.6\ )$$

The initial work presented in Chapter 4 assumed that $f(\sigma, t_i)$ could be expressed as an equivalent isotropic stress function that were section independent. This resulted in $SEA(t_i)$ being dominated by a first order linear functionality with respect to wall thickness. Thus, optimization of $SEA(t_i)$ would tend to converge towards the limit of imposed mass constraints. However, from the formulation presented in Equation 7.6, the stress function is dependent on wall

thickness. This means that changes in thickness can affect the stress state and strain path, and thus be more influenced by material anisotropy during optimization.

In Chapter 4, the peak crush force was related through

$$F_{peak}(t_i) = \sum_{i=1}^{5} g(\sigma, t_i) C_i t_i \left(1 + \left(\frac{V}{3C_i M}\right)^{\frac{1}{P}}\right) \quad (7.7)$$

where $g(\sigma)$ is a function dependent on the material yield stress function for peak crush force. This assumed that $f(\sigma, t_i)$ and $g(\sigma, t_i)$ were equivalent functions that were section independent. Through the assumption of equivalent isotropic flow stress, the previous formulation for the crush efficiency, $\eta^{(I)}$, could be obtained

$$\eta^{(I)} = \frac{F_{mean}}{F_{peak}} = \frac{1}{4\delta} \sum_{i=1}^{5} t_i \left(16 H_i I_1 \frac{b_i}{t_i C_i} + 2\pi + 4 I_3 \frac{{H_i}^2}{C_i b_i}\right) \quad (7.8)$$

and that the crush efficiency could be related through a constant, $\Upsilon^{(I)}$

$$\Upsilon^{(I)} = \frac{\eta^{(I)}(t_i)}{SEA(t_i)} = \frac{\rho L}{\delta f(\sigma)} \left[\sum_{i=1}^{5} \left(1 + \left(\frac{V}{3C_i M}\right)^{\frac{1}{P}}\right)\right]^{-1} \quad (7.9)$$

However, when assuming material nonlinearities, such as anisotropy, this relationship may not hold. Thus, the crush efficiency is now defined as

$$\eta^{(II)} = \frac{F_{mean}}{F_{peak}} = \frac{1}{4\delta} \sum_{i=1}^{5} \frac{f(\sigma, t_i)}{g(\sigma, t_i)} t_i \left(16 H_i I_1 \frac{b_i}{t_i C_i} + 2\pi + 4 I_3 \frac{{H_i}^2}{C_i b_i}\right) \quad (7.10)$$

and the new relationship between crush efficiency and mean crush force, $\Upsilon^{(II)}$ that is dependent on individual section thicknesses is defined as

$$\Upsilon^{(II)} = \frac{\eta^{(II)}(t_i)}{SEA(t_i)} = \frac{\rho L}{\delta} \sum_{i=1}^{5} \left[g(\sigma, t_i) \left(1 + \left(\frac{V}{3C_i M}\right)^{\frac{1}{P}}\right)\right]^{-1} \quad (7.11)$$

This can be extended to incorporate the influence of the ultimate tensile strength on the peak crush force, such that

$$\Upsilon^{(II)} = \frac{\eta^{(II)}(t_i)}{SEA(t_i)} = \frac{\rho L}{\delta U_o} \sum_{i=1}^{5} \left[h(\sigma, t_i) \left(1 + \left(\frac{V}{3C_i M} \right)^{\frac{1}{P}} \right) \right]^{-1} \quad (7.12)$$

where $h(\sigma, t_i) = U_o \, g(\sigma, t_i)$, where U_o is the ratio of the ultimate tensile strength to the yield in the axial direction (or the extrusion in this application)

$$U_o = \frac{\sigma_{UTS}}{\sigma_{00}} \quad (7.13)$$

7.7 Chapter Conclusions

In this chapter, a framework was presented for size optimization that coupled anisotropic yield functions to increase energy absorption characteristics of multi-cellular aluminum extrusions. Experimental and numerical simulations of the dynamic crush response of AA6063-T6 aluminum extrusions were performed. The isotropic von Mises [29], Hosford's [31] generalized isotropic, and Barlat *et al*. [35] Yld2004-18p yield function were employed for both 2-dimensional plane stress and 3-dimensional FE formulations to simulate the dynamic crush response. The isotropic von Mises yield function FE models predicted higher mean crush force, while the Hosford yield function predicted the lowest because the von Mises yield function had the largest normalized yield surface area. The 3-dimensional FE model formulations were able to capture more accurately the experimental energy absorption characteristics than the 2-dimensional FE models. All three 2-dimensional FE model formulations under predicted the mean crush and energy absorption by 13.0 – 17.8% for the different yield functions. The 3-dimensional FE model utilizing the Yld2004-18p yield function had the best predictive capability with an over prediction error of +1.4%. This was a result of capturing both the through-thickness energy absorption during plastic hinging, and capturing the variation in yield stress and Lankford coefficients. All yield functions using different FE formulations predicted similar combinations of Type-I crush modes that agreed well with experimental deformation and captured the overall trend of the force-displacement response. Thus, the 2-dimensional FE models could be used in the optimization framework to generate sizing configurations and then simulated using a 3-dimensional FE formulation for accurate predictions.

In the optimization framework, the response surface methodology (RSM) employed the artificial neural network (ANN) metamodeling technique to predict energy absorption

characteristics with respect to extrusion section wall thickness for each yield function. The genetic algorithm (GA) optimization procedure was utilized in an attempt to achieve global optimization with a maximum allowable mass constraint. Applying a complex yield function during the optimization process resulted in better energy absorption characteristics than solutions using simplified yield functions. Incorporating the effect of the non-quadratic yield function exponent alone improved optimization process for constrained optimization of SEA. Using the Yld2004-18p yield function, an optimal extrusion configuration predicted an increase in energy absorption and mean crush force of +4.2% and +2.5% respectively for a constrained mass of 1.39kg when using specific energy absorption (SEA) as a single optimization objective function.

Analytical models were derived to explain the influence of the yield surface on the convergence of optimization. It was shown that there exists a direct relationship between a material's ultimate tensile strength and mass constraints in the optimization of extrusions. Utilizing this result can impose additional constraints on the design of experiments domain to could reduce the number of simulations required to perform optimization. When removing the maximum allowable mass constraint, each yield function resulted in a unique size configuration and ultimately different masses and SEA. These converged masses represented the limit of size optimization for the given topology of the extrusion. Since each yield function predicted different limits of sizing for the given topology, this result showed that it would be critical to incorporate an appropriate yield function when performing topology optimization in conjunction with size optimization. SEA can be further enhanced by 10% when coupling anisotropic yield functions and relaxing mass constraints. These results show that incorporating material anisotropy can generate additional improvements in energy absorption when coupled with optimization strategies.

8 A NEW MULTI-SCALE FRAMEWORK TO INCORPORATE MICROSTRUCTURE EVOLUTION INTO PHENOMENOLOGICAL PLASTICITY - C.P. Kohar, J.L. Bassani, A. Brahme, R.K. Mishra, K. Inal (2017).

Anisotropy has been shown to be an important factor in the predictive capabilities of finite element simulations of the axial crush of lightweight alloys. Micromechanics-based computational models, such as crystal plasticity, have served as a powerful tool over phenomenological-based models for their ability to predict initial and evolution of anisotropy. However, these micromechanics-based models are often sacrificed for much faster phenomenological models that do not capture microstructure evolution. In this chapter, a new multi-scale framework is presented to incorporate microstructure evolution into phenomenological plasticity. Crystal plasticity is used to calibrate yield functions and microstructural evolution in a phenomenological manner using only a uniaxial tensile response and an electron backscatter diffraction (EBSD) map. Both single crystal and polycrystalline mechanical properties are calibrated and predicted by the new framework. The constitutive framework is implemented in the commercial finite element software, LS-DYNA, to simulate the localization behaviour and axial crush response of extruded aluminum AA6063-T6 and sheet aluminum AA5754-O. These simulations highlight the importance of capturing microstructural evolution in the simulation of large deformation in lab-scale components. Furthermore, this multi-scaling technique highlights the ability to accurately predict macroscopic properties without the need of extensive experimentation. The results of this work are currently in preparation for a two-part publication to the International Journal of Plasticity.

8.1 Introduction

The initial anisotropy is typically introduced into the material during the manufacturing process. Polycrystalline materials, such as aluminum, also exhibit deformation-induced anisotropy as a result of microstructural development, such as crystallographic reorientation, during finite deformation [149]. The crystal plasticity is a physics-based constitutive model that computes the crystallographic slip that results from dislocation glide [19]. Crystal plasticity simulations are typically calibrated to an electron backscatter diffraction (EBSD) map and a

single uniaxial stress-strain curve. Once calibrated, crystal plasticity can be used to predict microstructural evolution and localization behaviour during large deformations.

Although crystal plasticity constitutive models have been implemented into finite element frameworks (i.e. [46, 18, 24]), they are currently too computationally expensive to simulate lab-scale components with complete microstructural information [25]. This gives rise to the development of phenomenological constitutive models that are derived from fitting a mathematical function, called a yield function, to the macroscopic anisotropy that is observed experimentally. Even though phenomenological plasticity models are computationally efficient, these models typically do not capture the microstructural evolution that develops during large plastic strain [13]. In the work of Ghaffari Tari *et al.* [48], the CPB06ex3 [36, 39] yield function, which utilizes three stress transformations, was calibrated for the evolution of Lankford coefficients and yield stress variation in magnesium alloy AZ31B for proportional strain paths. However, this procedure of calibrating the initial and evolutionary anisotropic behaviours requires an extensive experimental testing program and may not be appropriate for non-proportional or complex strain paths that arise during forming or crush [16].

Attempts have been made to bridge phenomenological models to predictions from crystal plasticity to enhance the ability to predict strain path effects without extensive experimentation. In the work of Inal, Mishra and Cazacu [152], crystal plasticity was used to generate Lankford coefficients and yield stress variation from a single 2D EBSD map of the initial microstructure and a single uniaxial tensile stress-strain response. These predictions were then used to calibrate the CPB06ex2 [36, 39] yield function and thus, reducing the need for mechanical testing. However, this bridging of crystal plasticity theory to phenomenological modeling did not allow for microstructural evolution during off-axis loading or non-proportional strain paths. Recently, Muhammad et al [41, 42] demonstrated that crystal plasticity models can accurately capture the texture evolution in complex strain paths, such as simple shear.

Bassani and Pan [26] proposed a phenomenological-based texture evolution (PBTE) model that relates the rotation of the orthotropic axes of anisotropy to the plastic shear components in a phenomenological manner. Bassani and Pan [26] calibrated their model to experimental measurements of orthotropic spin during off-axis (with respect to the rolling direction) loading in uniaxial tensile and predicted the mechanical response under different loading conditions. The

results of their work show promise in the ability of phenomenological models to capture detailed microstructural information in an efficient manner. However, the experimental framework proposed by Kim and Yin [149], and Bunge and Nielsen [153], to generate these measurements for orthotropic spin is extensive and time-consuming. This model only captures the microstructural spin and cannot capture the strengthening from weak textural components [13]. Furthermore, this constitutive model has not been implemented for use in a commercial finite element framework to simulate large deformation in lab-scale components.

In this chapter, a new multi-scale framework from crystal plasticity to phenomenological plasticity with microstructural evolution is presented. This new framework employs the crystal frameworks presented in Inal et al. [17, 152] to determine the initial anisotropy variation for use in a yield function. The non-quadratic multi-transformation yield function proposed by Cazacu, Plunkett and Barlat [36, 39] is used throughout this work to capture the initial variations in anisotropy with a high degree of accuracy. Measurements of the orthotropic axis evolution are generated by crystal plasticity following the test program proposed by Kim and Yin [149], and Bunge and Nielsen [153]. The objective of this framework is to calibrate the phenomenological-based texture evolution constitutive model using only a single uniaxial stress-strain response and an EBSD scan via crystal plasticity. The constitutive framework for phenomenological-based texture evolution is implemented into a user-defined material subroutine (UMAT) in the commercial FE software LS-DYNA using incremental plasticity theory. This new implementation is compared to the results previously published by Bassani and Pan [26], which utilized the quadratic yield function proposed by Hill (1948) [30]. Once verified, this new framework is used to calibrate three materials: single cube face-centered cubic crystal, polycrystalline extruded aluminum AA6063-T6, and polycrystalline sheet aluminum AA5754-O. The single cube face-centered cubic crystal simulation is used to highlight the ability of the constitutive model to capture microstructure evolution. The polycrystalline materials are used to demonstrate the capability of this constitutive model to predict the behaviour of aluminum alloys used in the automotive industry. Lastly, finite element simulations of uniaxial tensile specimens and axial crush are performed using the phenomenological-based texture evolution model. Macroscopic and localization behaviours, such as strain at fracture and energy absorption characteristics, are predicted and compared to experiments.

8.2 Constitutive Model

This section details the constitutive models and frameworks that are utilized for the phenomenological-based texture evolution model proposed by Bassani and Pan [26]. The framework for extracting and calibrating the microstructure evolution is also presented. The phenomenological-based texture evolution model is implemented into a User Defined Material Subroutine (UMAT) in the non-linear explicit dynamic formulation of the commercial finite element software LS-DYNA [58]. The phenomenological-based texture evolution model requires calibration from crystal plasticity. The crystal plasticity framework presented in Inal *et al.* [18] with the power law and Chang-Asaro [28] hardening model is employed in this work. This allows for the capability to simulate complex, non-trivial deformations that occur during the forming or crash behaviour of lab-scale components. The phenomenological-based texture evolution model follows the cutting plane algorithm that was formulated by Chung and Richmond [59] and Yoon et al. [37] and used by Abedrabbo et al. [60] for incremental plasticity formulations. A detailed derivation and algorithm procedure of this new formulation is presented. Two yield functions are used for the phenomenological-based texture evolution model: the quadratic yield function proposed by Hill (1948) [30] and the non-quadratic multi-transformation yield function proposed by Cazacu, Plunkett and Barlat [36, 39]. The Hill (1948) yield function is initially used to verify the new implementation of this model, while the Cazacu, Plunkett and Barlat [36, 39] yield function is used to calibrate and predict the response of single and polycrystalline materials for further study.

8.2.1 Calibrating Microstructure Evolution during Deformation

The measurement of the orthotropic axis evolution follows the experimental frameworks as proposed by Kim and Yin [149], and Bunge and Nielsen [153]. The orthotropic axis is defined as the sample symmetry axis of an orientation distribution function (ODF). An ODF can be obtained from 2D electron backscatter diffraction (EBSD) map of the initial microstructure, which can generate crystallographic orientations in 3-dimensional Bunge Euler space $(\theta_1, \Phi, \theta_2)$, which is the texture of the material [155], with respect to the rolling direction (RD) and transverse direction (TD). A pole figure is a 2-dimensional representation in polar space (R_i, θ_j) of the 3-dimensional Euler angles with respect to the sample frame on crystallographic planes,

where the frequency of orientations is represented by intensity $W(R_i, \theta_j)$ in bins with respect to R_i and θ_j , such that $0 \leq R_i \leq 1$ and $0 \leq \theta_j \leq 2\pi$.

Figure 8.1 presents a schematic of the simulation procedure that is adopted from Kim and Yin [149] to generate the calibration data for microstructure evolution. Each microstructure is rotated about the normal direction axis to the rolling/extrusion direction at various angles, which simulates cutting a specimen at different orientations. Each rotated microstructure is simulated using crystal plasticity at various uniaxial tensile strain levels. During each stage of deformation, the material orthotropic axis is recorded through analysis of the pole figures. This will show the evolution of the material axis with respect to plastic deformation. These measurements of the orthotropic axis will serve as the calibration data for the phenomenological evolution parameters, η_{oi} and ξ_i. A similar procedure can be performed about the transverse direction and rolling/extrusion direction to obtain the microstructural spin for the out-of-plane components.

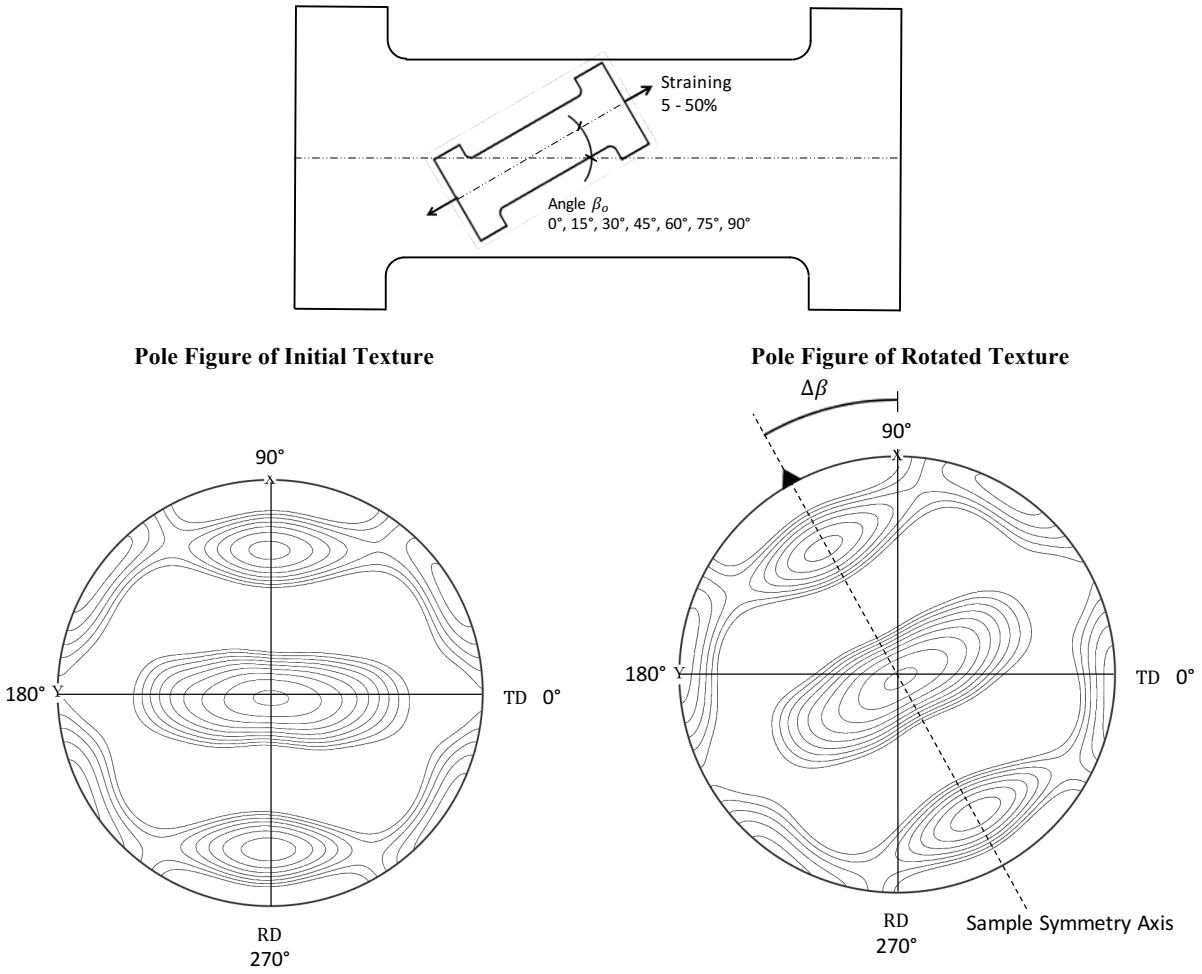

Figure 8.1 - Schematic of Orthotropic Material Axis Rotation From Pole Figure Rotation

The angle of the orthotropic axis from the sample reference direction, β, is determining by rotating the pole figure and measuring the degree of symmetry through an error function. The local pole figure symmetry error is computed as the difference in intensities about an axis of symmetry, β_k

$$\varphi_{ijk} = \left|W(R_i, \theta_j + \beta_k) - W(R_i, 2\pi - (\theta_j + \beta_k))\right| \qquad (8.1)$$

The total error in symmetry, Ψ_k is calculated as

$$\Psi_k = \sum_{i=1}^{N}\sum_{j=1}^{M} \frac{\left|W(R_i, \theta_j + \beta_k) - W(R_i, 2\pi - (\theta_j + \beta_k))\right|}{\left({R_i}^2 - {R_{i-1}}^2\right)\left(\theta_j - \theta_{j-1}\right)} \qquad (8.2)$$

where N and M are the number of bins used to discretize the polar domain of the pole figure. The angle of the orthotropic axis occurs when the total error function is minimal. Figure 8.2 presents a sample analysis of sheet aluminum AA5754-O that was initially rotated 30° from the rolling axis and deformed 5% strain in uniaxial tension, where the final angle of the orthotropic axis is $\beta = 116.6°$.

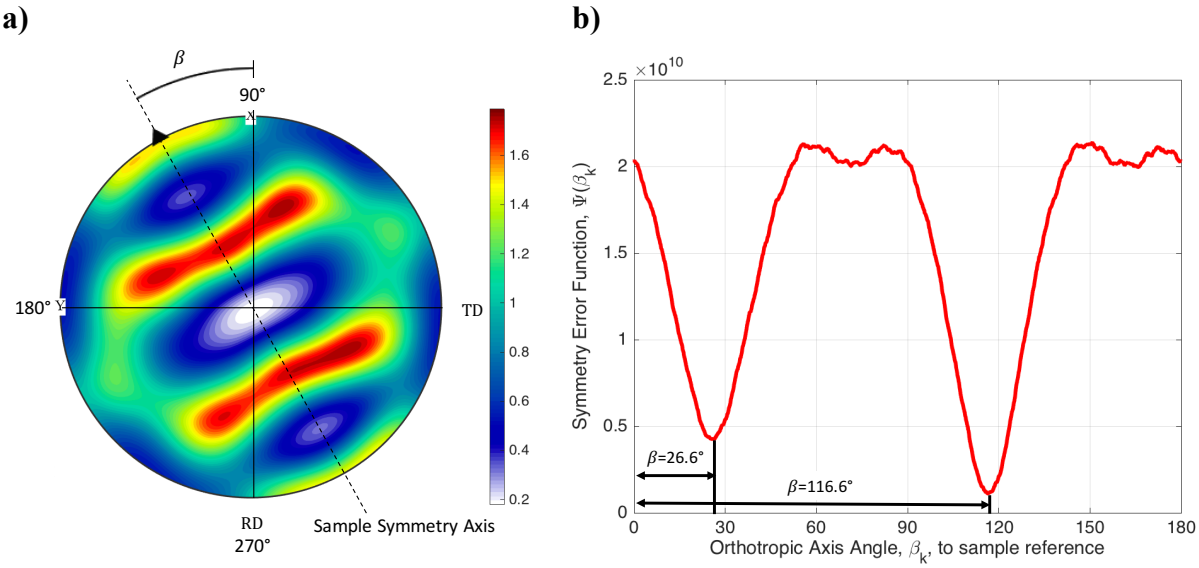

Figure 8.2 - Schematic of Orthotropic Material Axis Rotation From Pole Figure Rotation

8.2.2 Implementation into an Incremental Plane Stress Finite Element Formulation

The constitutive framework for phenomenological-based texture evolution is implemented into a user-defined material subroutine (UMAT) in the commercial FE software LS-DYNA. A non-linear explicit dynamic formulation for stress analysis is used throughout this work [58]. The

stress integration scheme follows the cutting plane algorithm that was formulated by Chung and Richmond [59] and Yoon et al. [37] and used by Abedrabbo et al. [60]. The stress integration scheme is presented as an incremental form of rate-independent plasticity using an associative flow rule. The elasto-plastic constitutive equations for this model are

$$\boldsymbol{\Delta D} = \boldsymbol{\Delta D}^{*} + \boldsymbol{\Delta D}^{\boldsymbol{P}} \quad (8.3)$$

$$\boldsymbol{\Delta \sigma} = \boldsymbol{L}^{el} : \boldsymbol{\Delta D}^{*} \quad (8.4)$$

Associative flow rule: $$\boldsymbol{\Delta D}^{\boldsymbol{P}} = (\Delta \bar{\varepsilon}^{P}) \frac{\partial \Phi}{\partial \boldsymbol{\sigma}} = (\Delta \bar{\varepsilon}^{P}) \frac{\partial \Phi}{\partial \boldsymbol{\Sigma}} \frac{\partial \boldsymbol{\Sigma}}{\partial \boldsymbol{\sigma}} \quad (8.5)$$

Yield Function: $$\Phi \leq 0 \quad (8.6)$$

Normality Rule: $$\Delta \bar{\varepsilon}^{P} \geq 0 \quad (8.7)$$

where $\frac{\partial \Phi}{\partial \boldsymbol{\Sigma}}$ are the yield function dependent derivatives on the orthotropic axis.

In the UMAT implementation, for a given iteration in time, $\boldsymbol{t}$, the next increment in the stretch, $\boldsymbol{\Delta D_{t+1}}$, is an input into the subroutine, the current stress state, $\boldsymbol{\sigma_t}$, and material history is also known, and the subroutine requires the stress state, $\boldsymbol{\sigma_{t+1}}$, at the next increment in time. Following the cutting plane algorithm, a trial stress is calculated for the next iteration of stress, $\boldsymbol{\sigma}_{\boldsymbol{t+1}}^{(\boldsymbol{i})}$, where i is the current iteration of the trial stress, assuming that the increment in stretch is elastic, such that

$$\boldsymbol{\Delta D}_{t+1}^{*\,(i)} = \boldsymbol{\Delta D}_{t+1} \quad (8.8)$$

$$\boldsymbol{\Delta D}_{t+1}^{\boldsymbol{p}\,(i)} = \mathbf{0} \quad (8.9)$$

$$\bar{\varepsilon}_{t+1}^{\boldsymbol{p}\,(i)} = \bar{\varepsilon}_{t}^{\boldsymbol{p}} \quad (8.10)$$

$$\Delta \bar{\varepsilon}^{p\,(i)} = 0 \quad (8.11)$$

and that the trial stress is

$$\boldsymbol{\sigma}_{t+1}^{(i)} = \boldsymbol{\sigma}_{t} + \boldsymbol{L}^{el} : \boldsymbol{\Delta D}_{t+1}^{*\,(i)} = \boldsymbol{\sigma}_{t} + \boldsymbol{L}^{el} : \boldsymbol{\Delta D}_{t+1} \quad (8.12)$$

The trial stress is used to determine if the material yields, through the calculation of the yield function

$$\Phi^{(i)}\left(\boldsymbol{\sigma}_{t+1}^{(i)}, \bar{\varepsilon}_{t+1}^{\boldsymbol{p}\,(i)}, \boldsymbol{\Delta D}_{t+1}\right) = \sigma_{eq}{}^{(i)}\left(\boldsymbol{\sigma}_{t+1}^{(i)}, \bar{\varepsilon}_{t+1}^{\boldsymbol{p}\,(i)}\right) - \bar{\sigma}\left(\bar{\varepsilon}_{t+1}^{\boldsymbol{p}\,(i)}, \boldsymbol{\Delta D}_{t+1}\right) \leq 0 \quad (8.13)$$

If the condition in Equation 8.13 is satisfied, then the initial assumption of an elastic trial stress is correct and the stress state and material history is returned

$$\boldsymbol{\sigma}_{t+1} = \boldsymbol{\sigma}_{t+1}^{(i)}, \qquad \bar{\varepsilon}_{t+1}^{\boldsymbol{p}} = \bar{\varepsilon}_{t+1}^{\boldsymbol{p}\ (i)}, \qquad \beta_{t+1} = \beta_{t+1}^{(i)}, \qquad \Delta D_{33,t+1} = \Delta D_{33,t+1}^{(0)} \tag{8.14}$$

If the condition is not satisfied, then the trial stress is iterated on the plastic multiplier using an iterative scheme

Trial Stress Update:
$$\boldsymbol{\sigma}_{t+1}^{(i+1)} = \boldsymbol{\sigma}_{t+1}^{(i)} - \boldsymbol{L}^{el} : \Delta \boldsymbol{D}_{t+1}^{\boldsymbol{P}\ (i+1)} = \boldsymbol{\sigma}_{t+1}^{(i)} - \boldsymbol{L}^{el} : \left(\Delta \bar{\varepsilon}^{p\ (i)}\right) \frac{\partial \Phi\left(\boldsymbol{\sigma}_{t+1}^{(i)}\right)}{\partial \boldsymbol{\sigma}} \tag{8.15}$$

with

Effective Plastic Strain Update:
$$\bar{\varepsilon}_{t+1}^{p\ (i+1)} = \bar{\varepsilon}_{t+1}^{p\ (i)} + \Delta \bar{\varepsilon}^{p\ (i)} \tag{8.16}$$

and

Orthotropic Axis Update:
$$\beta_{t+1}^{(i+1)} = \beta_{t+1}^{(i)} + \Delta \beta^{(i)}(\bar{\varepsilon}^{p\ (i)}) \tag{8.17}$$

The increment in effective plastic strain, $\Delta \bar{\varepsilon}_{t+1}^{p\ (i+1)}$, is determined through a first order Taylor series expansion of $\Phi\left(\boldsymbol{\sigma}_{t+1}^{(i)}, \bar{\varepsilon}_{t+1}^{\boldsymbol{p}\ (i)}, \boldsymbol{\Delta D}_{t+1}\right)$ such that

$$\Phi^{(i+1)}\left(\boldsymbol{\sigma}_{t+1}^{(i+1)}, \bar{\varepsilon}_{t+1}^{p\ (i+1)}, \Delta \boldsymbol{D}_{t+1}\right) = \Phi^{(i)}\left(\boldsymbol{\sigma}_{t+1}^{(i)}, \bar{\varepsilon}_{t+1}^{\boldsymbol{p}\ (i)}, \Delta \boldsymbol{D}_{t+1}\right) + \frac{d\Phi^{(i)}\left(\boldsymbol{\sigma}_{t+1}^{(i)}\right)}{d\boldsymbol{\sigma}} : \left(\boldsymbol{\sigma}_{t+1}^{(i+1)} - \boldsymbol{\sigma}_{t+1}^{(i)}\right) + \left(\frac{d\Phi^{(i)}\left(\bar{\varepsilon}_{t+1}^{p\ (i)}, \boldsymbol{\Delta D}_{t+1}\right)}{d(\Delta \bar{\varepsilon}^{p})}\right)\left(\bar{\varepsilon}_{t+1}^{p\ (i+1)} - \bar{\varepsilon}_{t+1}^{p\ (i)}\right) \tag{8.18}$$

where the scheme converges when the yield function criteria satisfies a prescribed tolerance

$$\Phi^{(i+1)}\left(\boldsymbol{\sigma}_{t+1}^{(i+1)}, \bar{\varepsilon}_{t+1}^{p\ (i+1)}, \boldsymbol{\Delta D}_{t+1}\right) \leq \varepsilon_{tol} \approx \mathbf{0} \tag{8.19}$$

Since β_{t+1} is a function of $\Delta \bar{\varepsilon}^{p}$ and ε_{tol} is selected to be a small number (10^{-6}), and substituting

$$\Phi^{(i)}\left(\boldsymbol{\sigma}_{t+1}^{(i)}, \bar{\varepsilon}_{t+1}^{p\,(i)}, \Delta\boldsymbol{D}_{t+1}\right) = -\left(\frac{\partial \sigma_{eq}{}^{(i)}\left(\boldsymbol{\sigma}_{t+1}^{(i)}\right)}{\partial \boldsymbol{\Sigma}}\left(\frac{\partial \boldsymbol{\Sigma}\left(\boldsymbol{\sigma}_{t+1}^{(i)}\right)}{\partial \boldsymbol{\sigma}} + \frac{\partial \boldsymbol{\Sigma}\left(\boldsymbol{\sigma}_{t+1}^{(i)}\right)}{\partial \beta}\frac{\partial \beta\left(\boldsymbol{\sigma}_{t+1}^{(i)}\right)}{\partial \boldsymbol{\sigma}}\right)\right) : \left(\boldsymbol{\sigma}_{t+1}^{(i+1)} - \boldsymbol{\sigma}_{t+1}^{(i)}\right) - \left(\frac{\partial \sigma_{eq}{}^{(i)}}{\partial \boldsymbol{\Sigma}\left(\boldsymbol{\sigma}_{t+1}^{(i)}\right)}\frac{\partial \boldsymbol{\Sigma}\left(\boldsymbol{\sigma}_{t+1}^{(i)}\right)}{\partial \beta}\frac{\partial \beta}{\partial(\Delta\bar{\varepsilon}^{p})} - \frac{\partial \bar{\sigma}^{(i)}}{\partial(\Delta\bar{\varepsilon}^{p})}\right)\left(\Delta\bar{\varepsilon}^{p\,(i)}\right) \quad (8.20)$$

Substituting the rearrangement of Equation 8.15 for $\left(\boldsymbol{\sigma}_{t+1}^{(i+1)} - \boldsymbol{\sigma}_{t+1}^{(i)}\right)$

$$\Phi^{(i)}\left(\boldsymbol{\sigma}_{t+1}^{(i)}, \bar{\varepsilon}_{t}^{\boldsymbol{p}}, \Delta\boldsymbol{D}_{t+1}\right) = -\frac{\partial \sigma_{eq}{}^{(i)}\left(\boldsymbol{\sigma}_{t+1}^{(i)}\right)}{\partial \boldsymbol{\sigma}} : \boldsymbol{L}^{el} : \Delta\bar{\varepsilon}^{p\,(i)}\frac{\partial \Phi^{(i)}\left(\boldsymbol{\sigma}_{t+1}^{(i)}\right)}{\partial \boldsymbol{\sigma}} - \left(\left(\frac{\partial \sigma_{eq}{}^{(i)}\left(\boldsymbol{\sigma}_{t+1}^{(i)}\right)}{\partial \boldsymbol{\Sigma}}\right)\left(\frac{\partial \boldsymbol{\Sigma}\left(\boldsymbol{\sigma}_{t+1}^{(i)}\right)}{\partial \beta}\right)\left(\frac{\partial \beta\left(\boldsymbol{\sigma}_{t+1}^{(i)}\right)}{\partial \boldsymbol{\sigma}}\right)\right) : \boldsymbol{L}^{el} : \Delta\bar{\varepsilon}^{p\,(i)}\frac{\partial \Phi^{(i)}\left(\boldsymbol{\sigma}_{t+1}^{(i)}\right)}{\partial \boldsymbol{\sigma}} \quad (8.21)$$

$$- \left(\frac{\partial \sigma_{eq}{}^{(i)}}{\partial \boldsymbol{\Sigma}\left(\boldsymbol{\sigma}_{t+1}^{(i)}\right)}\frac{\partial \boldsymbol{\Sigma}\left(\boldsymbol{\sigma}_{t+1}^{(i)}\right)}{\partial \beta}\frac{\partial \beta}{\partial(\Delta\bar{\varepsilon}^{p})} - \frac{\partial \bar{\sigma}^{(i)}}{\partial(\Delta\bar{\varepsilon}^{p})}\right)\left(\Delta\bar{\varepsilon}^{p\,(i)}\right)$$

The expansion of $\frac{\partial \beta\left(\boldsymbol{\sigma}_{t+1}^{(i)}\right)}{\partial \boldsymbol{\sigma}}$ from Equation 2.96 leads to a term that is proportional to $\Delta\bar{\varepsilon}^{p\,(i)}$. Thus, the expansion of Equation 8.21 yields a quadratic equation with respect to $\left(\Delta\bar{\varepsilon}^{p\,(i)}\right)$. Since the time step is internally controlled within LS-DYNA by the Courant-Friedrichs-Lewy stability criterion [82], the time step size is sufficiently small ($\Delta t \approx 10^{-8}s$) that the higher order terms of the Taylor series expansion can be neglected. Therefore, $\left(\Delta\bar{\varepsilon}^{p\,(i)}\right)^{2} \approx 0$ leading to

$$\left(\left(\frac{\partial \sigma_{eq}{}^{(i)}\left(\boldsymbol{\sigma}_{t+1}^{(i)}\right)}{\partial \boldsymbol{\Sigma}}\right)\left(\frac{\partial \boldsymbol{\Sigma}\left(\boldsymbol{\sigma}_{t+1}^{(i)}\right)}{\partial \beta}\right)\left(\frac{\partial \beta\left(\boldsymbol{\sigma}_{t+1}^{(i)}\right)}{\partial \boldsymbol{\sigma}}\right)\right) : \boldsymbol{L}^{el} : \Delta\bar{\varepsilon}^{p\,(i)}\frac{\partial \Phi^{(i)}\left(\boldsymbol{\sigma}_{t+1}^{(i)}\right)}{\partial \boldsymbol{\sigma}} \approx 0 \quad (8.22)$$

This linearizes the formulation such that the increment can be solved using the Newton-Raphson method

$$\Delta\bar{\varepsilon}^{p\,(i)} = \frac{\Phi^{(i)}\left(\boldsymbol{\sigma}_{t+1}^{(i)}, \bar{\varepsilon}_{t+1}^{\boldsymbol{p}\,(i)}, \Delta\boldsymbol{D}_{t+1}\right)}{\frac{\partial \Phi^{(i)}\left(\boldsymbol{\sigma}_{t+1}^{(i)}\right)}{\partial \boldsymbol{\sigma}} : \boldsymbol{L}^{el} : \frac{\partial \Phi^{(i)}\left(\boldsymbol{\sigma}_{t+1}^{(i)}\right)}{\partial \boldsymbol{\sigma}} - \frac{\partial \Phi^{(i)}\left(\boldsymbol{\sigma}_{t+1}^{(i)}\right)}{\partial \boldsymbol{\Sigma}\left(\boldsymbol{\sigma}_{t+1}^{(i)}\right)}\frac{\partial \boldsymbol{\Sigma}\left(\boldsymbol{\sigma}_{t+1}^{(i)}\right)}{\partial \beta}\frac{\partial \beta}{\partial(\Delta\bar{\varepsilon}^{p})} + \frac{\partial \bar{\sigma}^{(i)}\left(\bar{\varepsilon}_{t+1}^{p\,(i)}, \boldsymbol{\Delta D}_{t+1}\right)}{\partial(\Delta\bar{\varepsilon}^{p})}} \quad (8.23)$$

where the plastic strain increments are

$$\boldsymbol{D}_{t+1}^{\boldsymbol{p}\ (i+1)} = \Delta \boldsymbol{D}_{t+1}^{\boldsymbol{p}\ (i)} + \left(\Delta \bar{\varepsilon}^{p\ (i)}\right) \frac{\partial \Phi^{(i)}\left(\boldsymbol{\sigma}_{t+1}^{(i)}\right)}{\partial \boldsymbol{\sigma}} \quad (8.24)$$

For a plane stress orthotropic material, $\frac{\partial \beta}{\partial (\Delta \bar{\varepsilon}^{p})}$ can be determined by Equation 2.96

$$\frac{\partial \beta\left(\boldsymbol{\sigma}_{t+1}^{(i)}\right)}{\partial (\Delta \bar{\varepsilon}^{p})} = -\Bigg(\eta_{o3} + \xi_3 \left(\left(\frac{\partial \sigma_{eq}{}^{(i)}\left(\boldsymbol{\sigma}_{t+1}^{(i)}\right)}{\partial \Sigma_{\mathbf{22}}} \right)^2 - \left(\frac{\partial \sigma_{eq}{}^{(i)}\left(\boldsymbol{\sigma}_{t+1}^{(i)}\right)}{\partial \Sigma_{\mathbf{11}}} \right)^2 \right) \Bigg) \frac{\partial \sigma_{eq}{}^{(i)}\left(\boldsymbol{\sigma}_{t+1}^{(i)}\right)}{\partial \Sigma_{\mathbf{12}}} \quad (8.25)$$

At the end of the iteration scheme

$$\boldsymbol{\sigma}_{t+1} = \boldsymbol{\sigma}_{t+1}^{(i+1)}, \qquad \bar{\varepsilon}_{t+1}^{\boldsymbol{p}} = \bar{\varepsilon}_{t+1}^{\boldsymbol{p}\ (i+1)}, \qquad \beta_{t+1} = \beta_{t+1}^{(i+1)}, \qquad \Delta \boldsymbol{D}_{t+1}^{\boldsymbol{P}} = \Delta \boldsymbol{D}_{t+1}^{\boldsymbol{p}\ (i+1)} \quad (8.26)$$

8.2.3 Stress Integration Algorithm

This section details the stress integration scheme used in the finite element simulations. For models without the plane stress assumption, the through thickness strain calculations are neglected. For models without microstructure evolution, $\beta = \text{constant}$, $\Delta\beta = \frac{\partial \beta}{\partial (\Delta \bar{\varepsilon}^{p})} = 0$, and for all time. The steps in the stress integration scheme arthate as follows

(1) Subroutine entry with known values of $\boldsymbol{\sigma}_t, \Delta \boldsymbol{D}_{t+1}, \bar{\varepsilon}_t^{\boldsymbol{p}}, \beta_t, \Delta t_{t+1}$
(2) Perform an elastic predictor

$\Delta D_{33,t+1}^{(0)} = \frac{\upsilon(\Delta D_{22,t+1} + \Delta D_{11,t+1})}{\upsilon - 1}$	Calculate an initial through thickness strain
$\boldsymbol{\sigma}_{t+1}^{(0)} = \boldsymbol{\sigma}_t + L^{el} : \Delta \boldsymbol{D}_{t+1}$	Assume an initial elastic increment
$\bar{\varepsilon}_{t+1}^{\boldsymbol{p}\ (0)} = \bar{\varepsilon}_t^{\boldsymbol{p}}$	Assume that plastic slip has not changed
$\beta_{t+1}^{(0)} = \beta_t$	Assume there is no orthotropic rotation
$\bar{\sigma}^{(0)} = \bar{\sigma}\left(\bar{\varepsilon}_{t+1}^{\boldsymbol{p}\ (0)}, \Delta \boldsymbol{D}_{t+1}\right)$	Calculate a new flow stress
$\boldsymbol{\Sigma}^{(0)} = \boldsymbol{\Sigma}\left(\boldsymbol{\sigma}_{t+1}^{(0)}, \beta_{t+1}^{(0)}\right)$	Calculate the intermediate stress

$\sigma_{eq}{}^{(\mathbf{0})} = \Phi(\boldsymbol{\Sigma}^{(0)})$ Calculate the anisotropic yield function on the orthotropic axis

(3) Check yielding

$$\Phi^{(\mathbf{0})} = \sigma_{eq}{}^{(\mathbf{0})} - \bar{\sigma}^{(0)} \leq 0$$

i. IF TRUE: then the material is elastic

$\bar{\varepsilon}^{\boldsymbol{p}}_{t+1} = \bar{\varepsilon}^{\boldsymbol{p}}_{t+1}{}^{(0)}$

$\boldsymbol{\sigma}_{t+1} = \boldsymbol{\sigma}^{(0)}_{t+1}$

$\beta_{t+1} = \beta^{(0)}_{t+1}$

$\Delta D_{33,t+1} = \Delta D^{(0)}_{33,t+1}$

GO TO Step (6)

ii. ELSE: CONTINUE The material is plastic

(4) Perform Incremental Plasticity

i. Set an incremental counter $i = 0$ and total plastic strain increment $\Delta\bar{\varepsilon}^{p\,(0)} = 0$

ii. Calculate the plastic corrector

$$\Delta\bar{\varepsilon}^{p\,(i)} = \frac{\Phi^{(i)}\left(\boldsymbol{\sigma}^{(i)}_{t+1}, \bar{\varepsilon}^{\boldsymbol{p}}_{t}, \Delta\boldsymbol{D}_{t+1}\right)}{\frac{\partial\Phi^{(i)}\left(\boldsymbol{\sigma}^{(i)}_{t+1}\right)}{\partial\boldsymbol{\sigma}} : \boldsymbol{L}^{el} : \frac{\partial\Phi^{(i)}\left(\boldsymbol{\sigma}^{(i)}_{t+1}\right)}{\partial\boldsymbol{\sigma}} - \frac{\partial\Phi^{(i)}\left(\boldsymbol{\sigma}^{(i)}_{t+1}\right)}{\partial\boldsymbol{\Sigma}\left(\boldsymbol{\sigma}^{(i)}_{t+1}\right)} \frac{\partial\boldsymbol{\Sigma}\left(\boldsymbol{\sigma}^{(i)}_{t+1}\right)}{\partial\beta} \frac{\partial\beta}{\partial(\Delta\bar{\varepsilon}^{p})} + \frac{\partial\bar{\sigma}^{(i)}\left(\bar{\varepsilon}^{p\,(i)}_{t+1}, \boldsymbol{\Delta D}_{t+1}\right)}{\partial(\Delta\bar{\varepsilon}^{p})}}$$

$$\bar{\varepsilon}^{p\,(i+1)}_{t+1} = \bar{\varepsilon}^{p\,(i)}_{t+1} + \Delta\bar{\varepsilon}^{p\,(i)}$$

$$\boldsymbol{\Delta D}^{\boldsymbol{p}\,(i+1)}_{t+1} = \boldsymbol{\Delta D}^{\boldsymbol{p}\,(i)}_{t+1} + \left(\Delta\bar{\varepsilon}^{p\,(i)}\right)\frac{\partial\Phi^{(i)}\left(\boldsymbol{\sigma}^{(i)}_{t+1}\right)}{\partial\boldsymbol{\sigma}}$$

iii. Calculate the new orientation

$$\Delta\beta^{(i)} = -\left(\eta_{o3} + \xi_3\left(\left(\frac{\partial\sigma_{eq}{}^{(i)}\left(\boldsymbol{\sigma}^{(i)}_{t+1}\right)}{\partial\Sigma_{\mathbf{22}}}\right)^2 - \left(\frac{\partial\sigma_{eq}{}^{(i)}\left(\boldsymbol{\sigma}^{(i)}_{t+1}\right)}{\partial\Sigma_{\mathbf{11}}}\right)^2\right)\right)\left(\frac{\partial\sigma_{eq}{}^{(i)}\left(\boldsymbol{\sigma}^{(i)}_{t+1}\right)}{\partial\Sigma_{\mathbf{12}}}\right)\Delta\bar{\varepsilon}^{p\,(i)}$$

$$\beta^{(i+1)}_{t+1} = \beta^{(i)}_{t+1} + \Delta\beta^{(i)}$$

iv. Update the stress, intermediate stress, yield function, and flow stress

$$\boldsymbol{\sigma}^{(i+1)}_{t+1} = \boldsymbol{\sigma}^{(i)}_{t+1} - \boldsymbol{L}^{el} : \left(\Delta\bar{\varepsilon}^{p\,(i)}\right)\frac{\partial\Phi\left(\boldsymbol{\sigma}^{(i)}_{t+1}\right)}{\partial\boldsymbol{\sigma}}$$

$$\boldsymbol{\Sigma}^{(i+1)} = \boldsymbol{\Sigma}\left(\boldsymbol{\sigma}_{t+1}^{(i+1)}, \beta_{t+1}^{(i+1)}\right)$$

$$\bar{\sigma}^{(i+1)} = \bar{\sigma}\left(\bar{\varepsilon}_{t+1}^{\boldsymbol{p}\ (i+1)}, \Delta\boldsymbol{D}_{t+1}\right)$$

$$\sigma_{eq}{}^{(i+1)} = \Phi(\boldsymbol{\Sigma}^{(i+1)})$$

v. Convergence Check

$$\Phi^{(i+1)} = \sigma_{eq}{}^{(i+1)} - \bar{\sigma}^{(i+1)} \leq \varepsilon_{tol}$$

where ε_{tol} is an error tolerance that is set to 10^{-6}.

IF FALSE: $i = i + 1$ and GO TO ((4)ii)

ELSE: CONTINUE

(5) Update states to converged values

$$\bar{\varepsilon}_{t+1}^{\boldsymbol{p}} = \bar{\varepsilon}_{t+1}^{\boldsymbol{p}\ (i)}$$

$$\boldsymbol{\sigma}_{t+1} = \boldsymbol{\sigma}_{t+1}^{(i)}$$

$$\beta_{t+1} = \beta_{t+1}^{(i)}$$

$$\Delta D_{33,t+1} = \Delta D_{33,t+1}^{(0)} + \frac{(2v-1)\left(\Delta D_{33,t+1}^{P\ (i)}\right)}{v-1}$$

(6) Exit Stress Integration Subroutine

8.2.4 Validation of the Implementation

The proposed model formulation was implemented into LS-DYNA and compared to the previous simulations results and experimental measurements reported in Bassani and Pan [26]. The Hill (1948) anisotropic yield function was employed to allow for a consistent comparison. Table 8.1 and Table 8.2 presents the phenomenological hardening parameters, yield stress variation, and the yield function coefficients.

Table 8.1 - Hardening Parameters for Validation Model

E [GPa]	$\boldsymbol{\nu}$	**K [MPa]**	$\boldsymbol{\varepsilon_0}$ $\boldsymbol{(10^{-3})}$	**n**	$\boldsymbol{\dot{\varepsilon}_0}$ $\boldsymbol{(10^{-3})}$
200	0.3	211.6	0.740	0.125	1.00

Table 8.2 - Coefficients for Hill (1948) Yield Function and Yield Stress Variation [156] for Validation Model

s_1	s_2	s_3	c_1	c_2	c_3	c_6
1.06	1.06	0.59	0.780	1.000	1.000	0.958

The yield function was calibrated for three stress states: i) Transverse tension $s_1 = \frac{\Sigma_{22}}{\Sigma_{11}} = 1.06$, ii) Balanced biaxial tension $s_2 = \frac{\Sigma_b}{\Sigma_{11}} = 1.06$, and iii) Shear $s_3 = \frac{\Sigma_{12}}{\Sigma_{11}} = 0.59$ [156]. Along with the criteria Σ_{11} uniaxial requirement (i.e. $\Phi_{H48}(\Sigma_{11} = 1, \bar{\sigma} = 1, \Sigma_{22} = \Sigma_{12} = 0) = 0$), this yields four nonlinear simultaneous equations that can solved using be Newton-Raphson to identify the coefficients. Figure 8.3 presents a comparison of the predicted flow stress and the plastic strain with the experimental measurements [157]. Figure 8.4 presents a comparison between the current implementation, the previous simulations results and experimental measurements reported in Bassani and Pan [26]. Overall, the proposed model shows excellent agreement in predicting the orthotropic rotation and flow stress response.

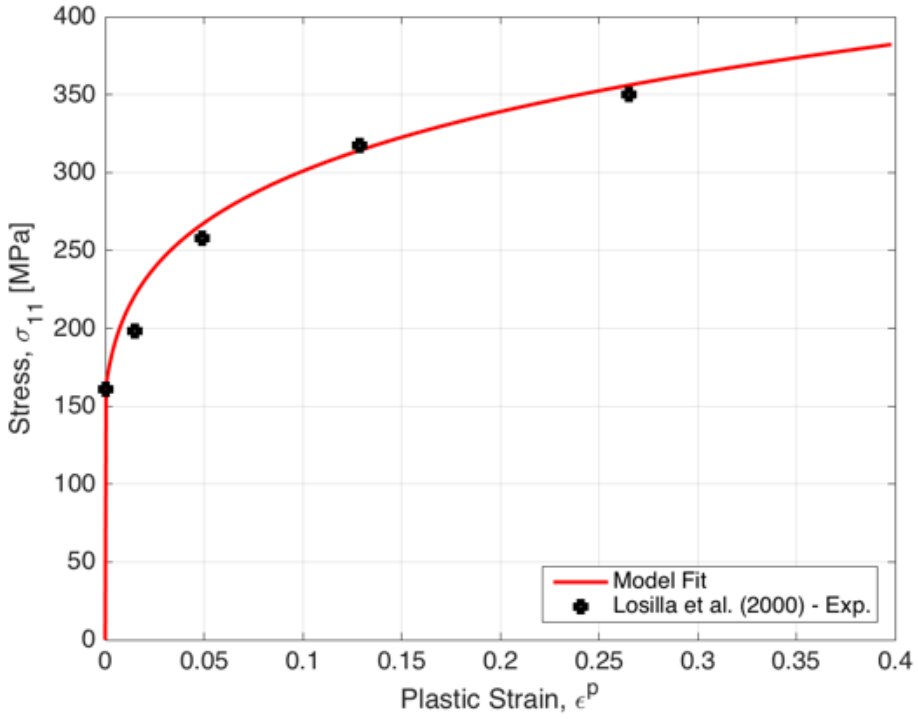

Figure 8.3 - Comparison of Flow Stress vs Plastic Strain: Experiment [157] vs Simulation

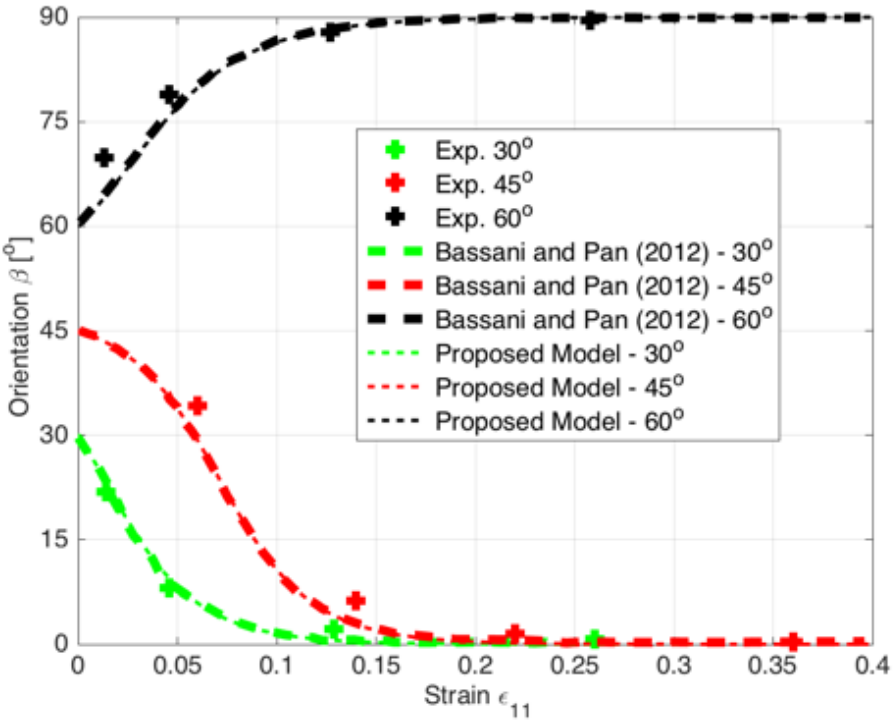

Figure 8.4 - Comparison of Current Implementation with Previous Implementation and Experimental Results [26]

8.3 Material characterization

This section presents the calibration of the phenomenological-based texture evolution model to three FCC materials: single crystal cube, polycrystalline rolled sheet AA5754-O and polycrystalline extruded AA6063-T6. Following the framework presented in Inal et al. [152], the phenomenological-based texture evolution models for each material are calibrated to the material anisotropy and yield loci generated from crystal plasticity.

8.3.1 Single Crystal Cube Texture

8.3.1.1 Calibration of Single Crystal FCC Cube

Figure 8.5 presents the pole figure representation of single crystal FCC cube. The pole figures were generated using MATLAB MTEX 4.3.2 analysis software [158]. Table 8.3 presents single crystal hardening parameters obtained from Brahme et al. [40] used for single crystal FCC cube. Table 8.4 presents the phenomenological hardening parameters that were calibrated to the uniaxial stress-strain response in the 0°-direction. Figure 8.6 presents a comparison between the phenomenological model and crystal plasticity for uniaxial and normalized stress response for

0°-direction. Both the phenomenological model with and without evolution use the same hardening coefficients and show good agreement with crystal plasticity. This is a result of the initial orientation having symmetry about the 0° and 90° axes that results in no microstructure evolution during deformation. In a similar behaviour, no microstructure evolution was generated for an initial orientation of 45° due to symmetry. To calibrate the yield function, crystal plasticity was used the generate the yield locus in the $\sigma_{12} = 0$ and $\sigma_{11} = \sigma_{22}$ planes. The CPB06 yield function with five transformations was used as the phenomenological yield function to accurately capture the yield surface curvature. Figure 8.7 presents the normalized yield locus and calibrated yield function in both planes. The coefficients used for the CPB06 yield function are presented in APPENDIX A.3.

Using the framework for measuring microstructural evolution outlined in Section 8.2.1, the single crystal cube was rotated at increments of 15° and simulated under uniaxial tension along the rolling direction. The orthotropic symmetry axis was measured through the (111) pole figure at various strain levels during deformation. Figure 8.8 presents the 30° rotated single crystal cube texture during deformation. It can be observed from the pole figure intensities that the orthotropic axis is rotating towards the 0°-direction during deformation. This rotation is induced by the resolved shear stress on the slip systems rotating the crystal from misalignment.

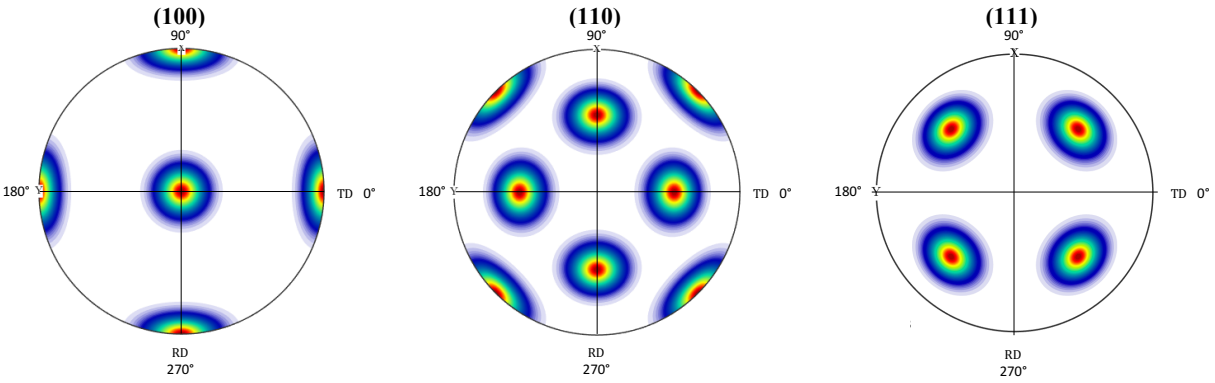

Figure 8.5 - Initial Pole Figures for Single Crystal FCC Cube Texture Simulations

Table 8.3 - Crystal Plasticity Power Law Parameters For Single Crystal FCC Cube Simulations [40]

Model	C_{11} [GPa]	C_{12} [GPa]	C_{44} [GPa]	τ_0 [MPa]	h_0 [MPa]	n_{xp}	m_{xp}	q
Power	230	132	60	12.5	3125	0.370	0.002	1.00

Table 8.4 - Phenomenological Plasticity Hardening Parameters For Single Crystal FCC Cube Simulations

E [GPa]	ν	K [MPa]	ε_0 (10^{-3})	n_{ph}	$\dot{\varepsilon}_0$ (10^{-3})
145.1	0.4191	496.66	0.4103	0.368	1.00

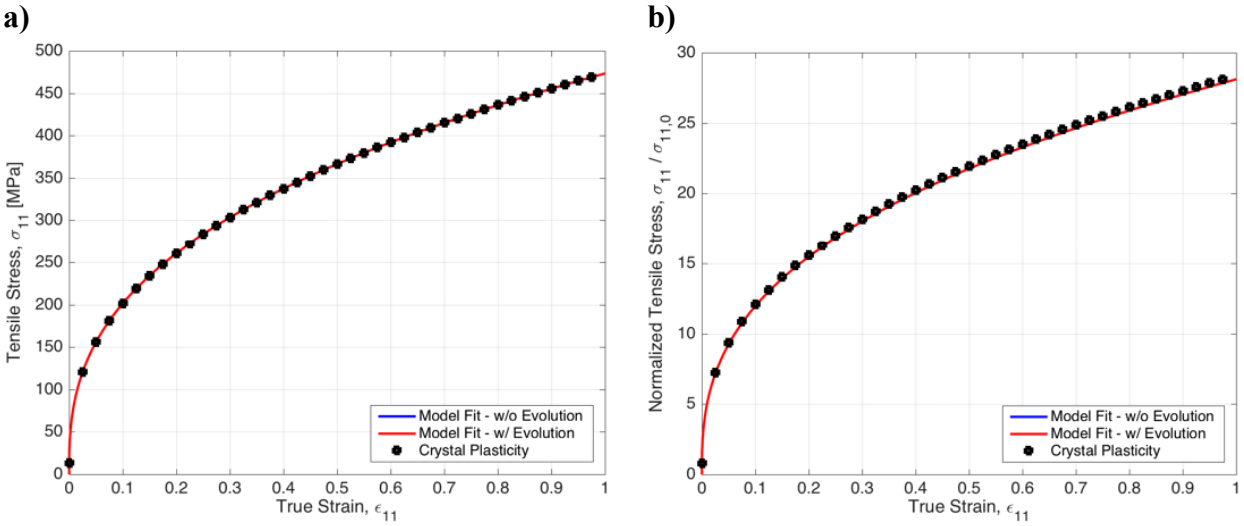

Figure 8.6 - a) Uniaxial and b) Normalized Stress-Strain Response for 0°-direction to the Rolling Direction (RD) for Single Crystal FCC Cube

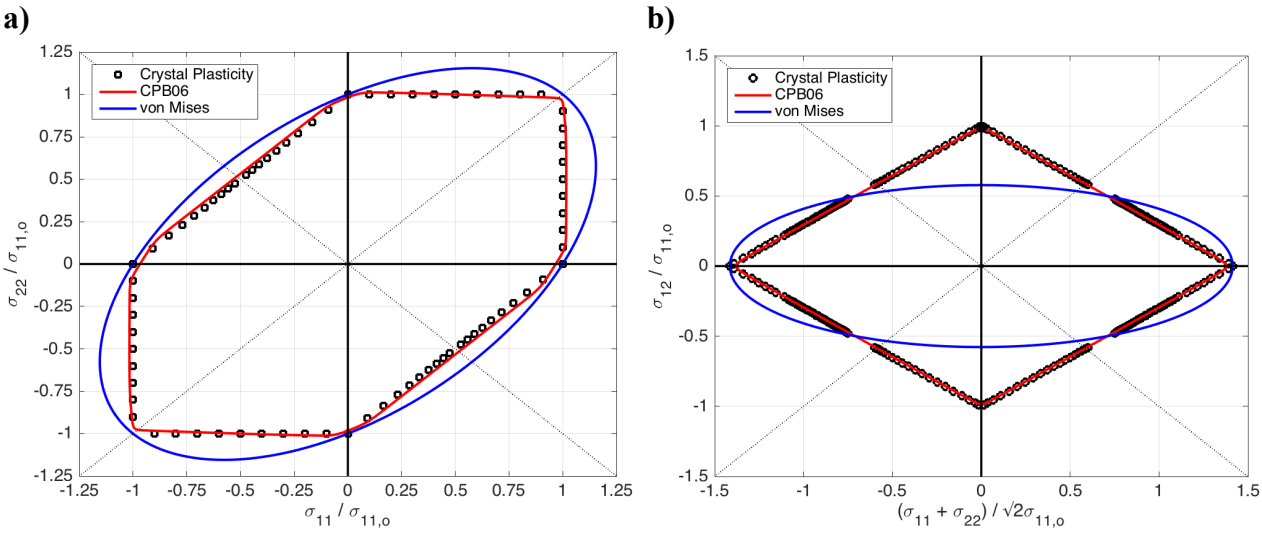

Figure 8.7 - Normalized Yield Loci in a) $\sigma_{12} = 0$ plane and b) $\sigma_{11} = \sigma_{22}$ plane for Single Crystal FCC cube

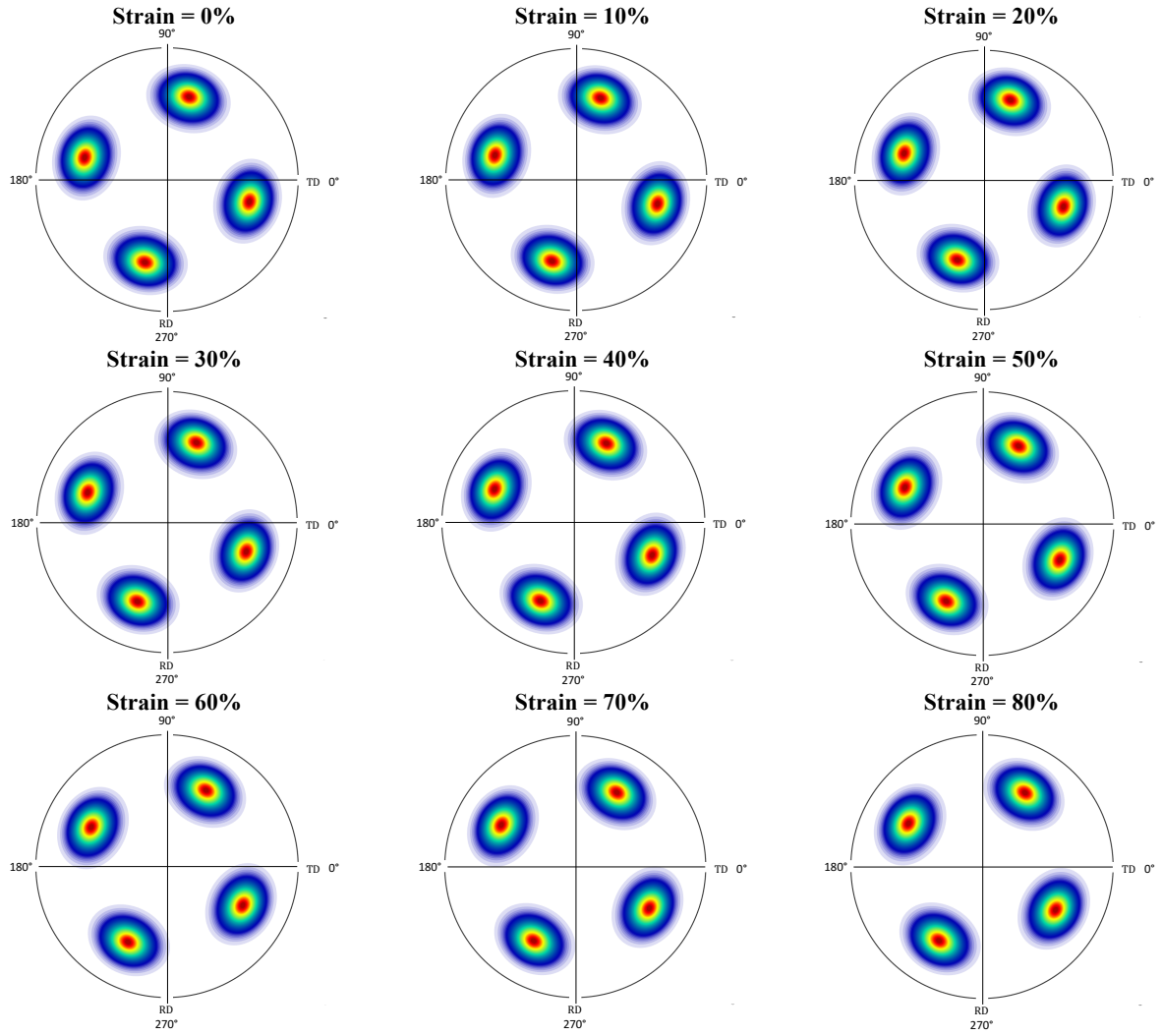

Figure 8.8 - (111) Pole Figure of 30° Rotated Single Crystal FCC Cube Calculated from an ODF at Various Strain Levels Generated From Crystal Plasticity Simulations

Figure 8.9 presents the orthotropic axis evolution generated by crystal plasticity as a function of uniaxial strain levels for various initial offset angles. The phenomenological model with evolution was calibrated to the orthotropic axis evolution using non-linear regression. The error function, $\epsilon_{rr,\beta}$, for calibrating the orthotropic axis evolution is defined as the error between the measured orthotropic axis from crystal plasticity, $\beta_{xp}(\beta_0, \varepsilon_{11})$ and the orthotropic axis predicted using the phenomenological model, $\beta_{ph}(\beta_0, \varepsilon_{11})$, such that

$$\epsilon_{rr,\beta} = \sum \left(\beta_{xp}(\beta_0, \varepsilon_{11}) - \beta_{ph}(\eta_{o3}\ \xi_3, \beta_0, \varepsilon_{11})\right)^2 \qquad (\ 8.27\ )$$

where the error function is minimized with respect to the parameters for phenomenological microstructural evolution, η_{o3} and ξ_3. The parameters for microstructure evolution of single

crystal FCC cube are presented in Table 8.5. The resulting orthotropic axis rotation predictions from the phenomenological model with and without evolution are also presented in Figure 8.9. Excellent agreement is observed between the orthotropic axis rotation generated from crystal plasticity with the phenomenological model with evolution.

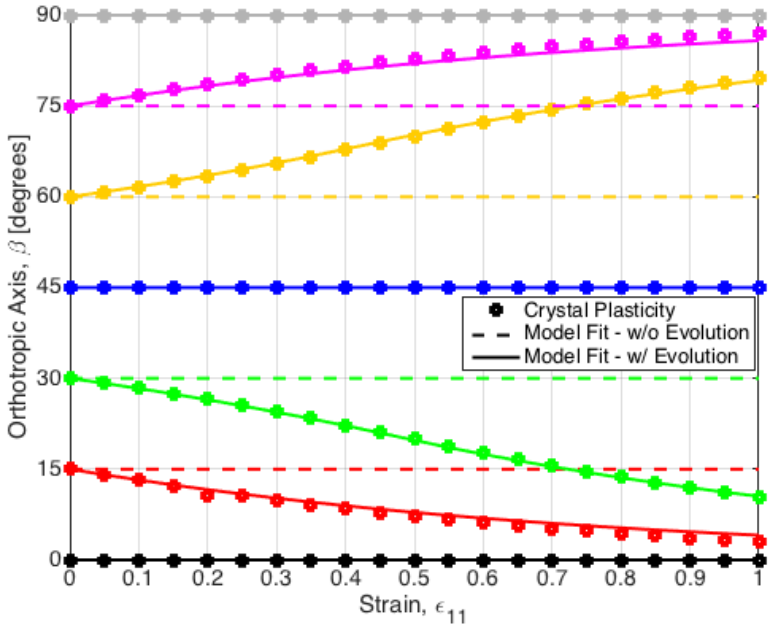

Figure 8.9 - Single Crystal FCC Cube Orthotropic Axis Evolution as a Function of Uniaxial Normal Strain, ε_{xx}: Measurements Generated from Crystal Plasticity and Calibrated using Phenomenological Model

Table 8.5 - Phenomenological Microstructural Evolution Parameters for Single Crystal FCC Cube Simulations

Model	η_{o3} (10^{-4})	ξ_3
w/o Evolution	0.0000	0.0000
w/ Evolution	-2.026	1.0658

8.3.2 Prediction of Uniaxial Tension for Single Crystal Cube

Figure 8.10 presents the normalized tensile and shear stress response of single crystal FCC cube texture during uniaxial tension using crystal plasticity. The orthotropic axis is rotated with initial offset angles in 15° increments and simulated under constrained uniaxial tension; a prescribed uniaxial strain is imposed ($D_{11} = \dot{\varepsilon}$), the shear strain components are constrained $D_{12} = 0$, while the remaining normal strain components are free to deform. A symmetric response in the stress is observed about the 45° orientation, such that the crystal plasticity stress-strain response of 30° and 60° are the same; the same observations is made between 15° and 75°. The stress-strain response of the single crystal simulations exhibits abrupt changes in the flow

stress response, which is a result of the crystal lattice rotation from induced plastic spin. As a result of the constrained shear components, large shear stresses are developed from the resulting sharp yield loci/surface of the single crystal textures. As discussed in Section 8.3.1.1, only the microstructure evolution and the initial yield stress through the crystal plasticity generated yield loci are used to calibrate the phenomenological model. Thus, the resulting stress-strain response from the phenomenological model with and without microstructural evolution are predictions of the crystal plasticity response. The predictions for each initial orthotropic axis using the phenomenological model are also presented in Figure 8.10. The model with microstructure evolution is able to simultaneously capture the overall trends of the tensile and shear stress response. Furthermore, the phenomenological model with microstructural evolution is able to capture the crystal lattice rotation effect through the rotation of the orthotropic axis.

8.3.3 Prediction of Simple Shear for Single Crystal Cube

Figure 8.11 presents the normalized tensile and shear stress response of single crystal FCC cube texture during simple shear using crystal plasticity and the phenomenological models. A prescribed constant shear strain rate is imposed ($D_{12} = \dot{\varepsilon}$), while the planar normal strain components are constrained ($D_{11} = D_{22} = 0$) with the through thickness free to deform. The phenomenological model with microstructure evolution predicts well the shear-strain response generated by crystal plasticity, while the classical approach to phenomenological modeling over-predicts the response. Furthermore, the phenomenological model with evolution is able to capture the prominent Swift effect in the normal stress components (see Ref. [159, 160, 161]) and the abrupt changes due to crystal lattice rotation that occur in single crystal deformation.

a-i) Normalized Tensile Stress - 15° rotated

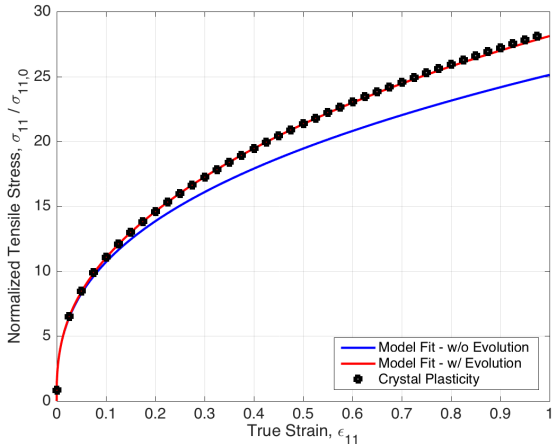

ii) Normalized Shear Stress - 15° rotated

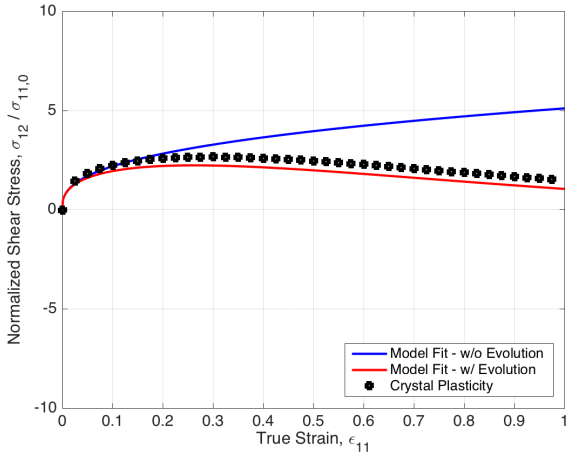

b-i) Normalized Tensile Stress - 30° rotated

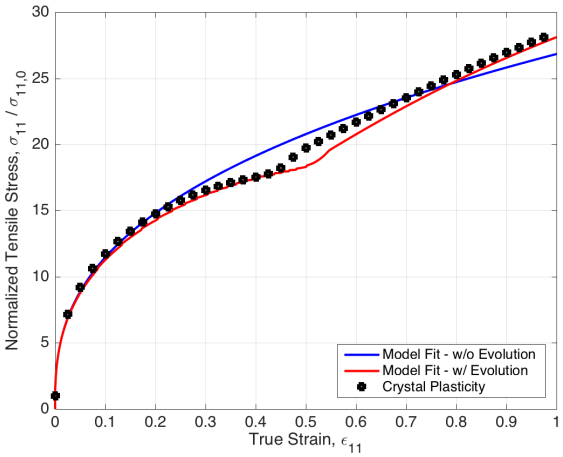

ii) Normalized Shear Stress - 30° rotated

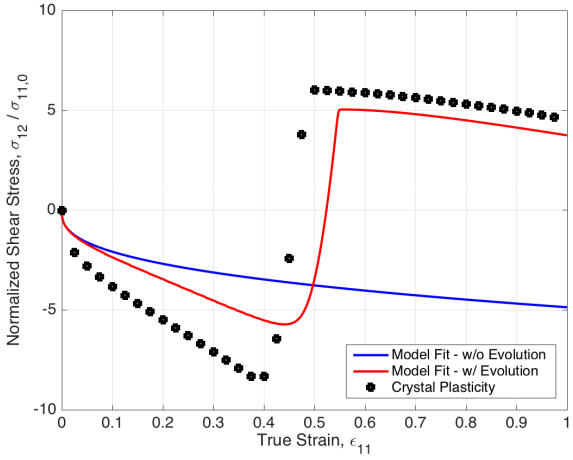

c-i) Normalized Tensile Stress - 45° rotated

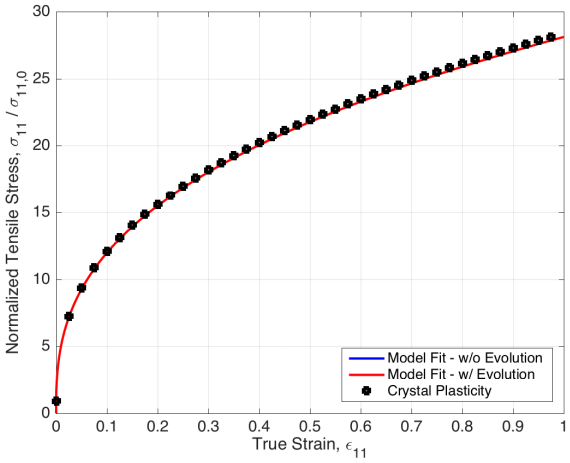

ii) Normalized Shear Stress - 45° rotated

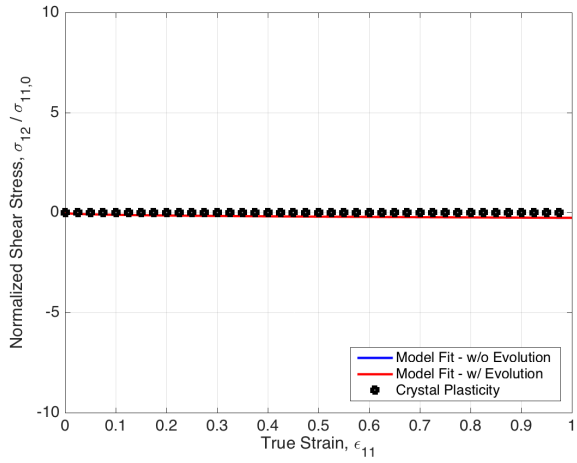

d-i) Normalized Tensile Stress - 60° rotated

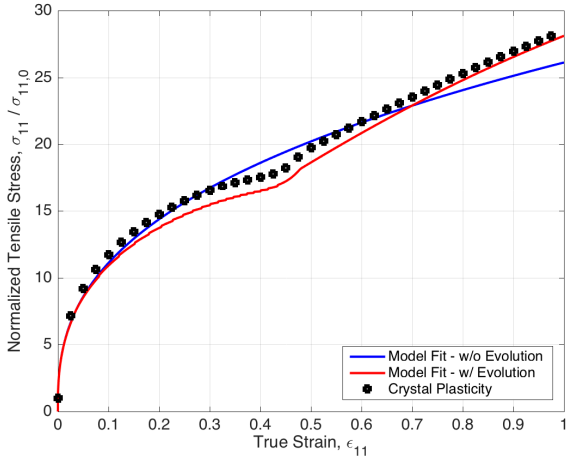

ii) Normalized Shear Stress - 60° rotated

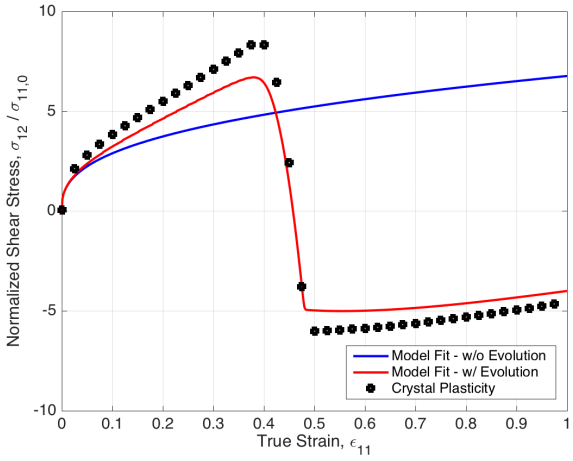

e-i) Normalized Tensile Stress - 75° rotated

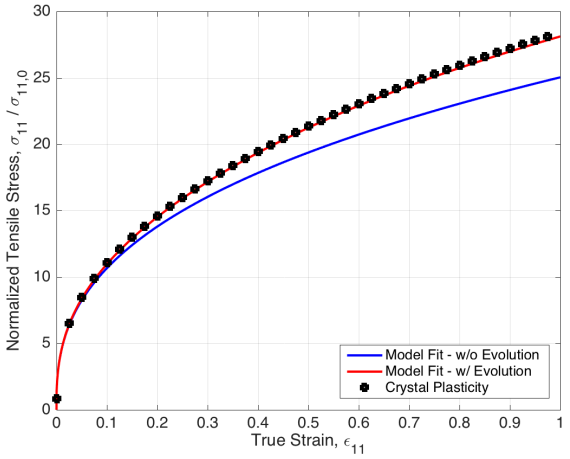

ii) Normalized Shear Stress - 75° rotated

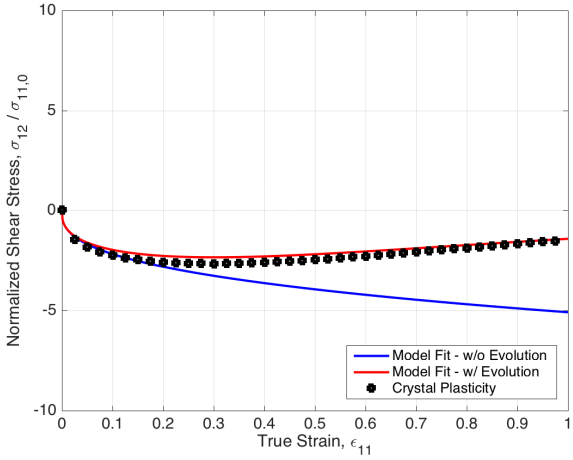

f-i) Normalized Tensile Stress - 90° rotated

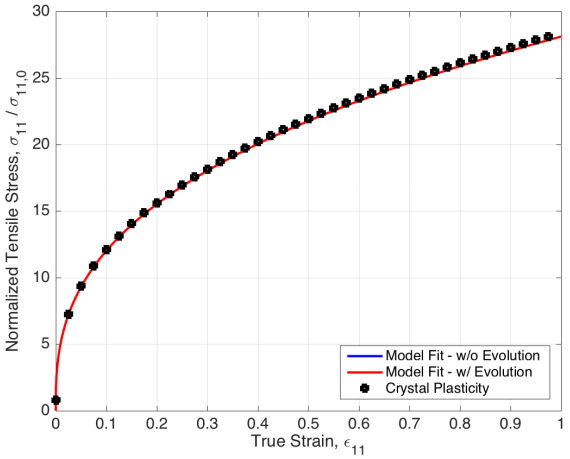

ii) Normalized Shear Stress - 90° rotated

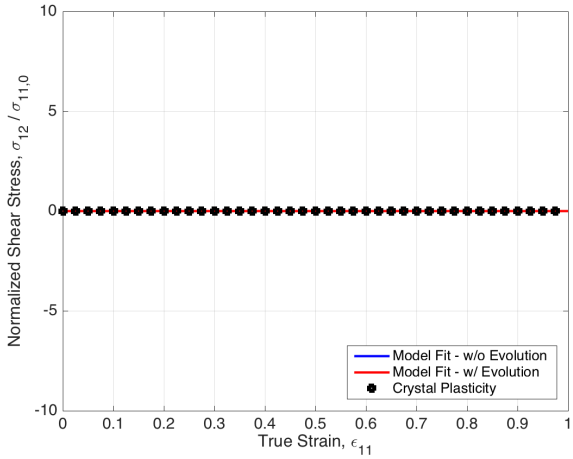

Figure 8.10 - Normalized i) Tensile and ii) Shear Stress Response of Single Crystal FCC Cube Texture During Constrained Uniaxial Tension for Initial Offset angles a) 15°-direction, b) 30°-direction, c) 45°-direction, d) 60°-direction e) 75°-direction, f) 90°-direction

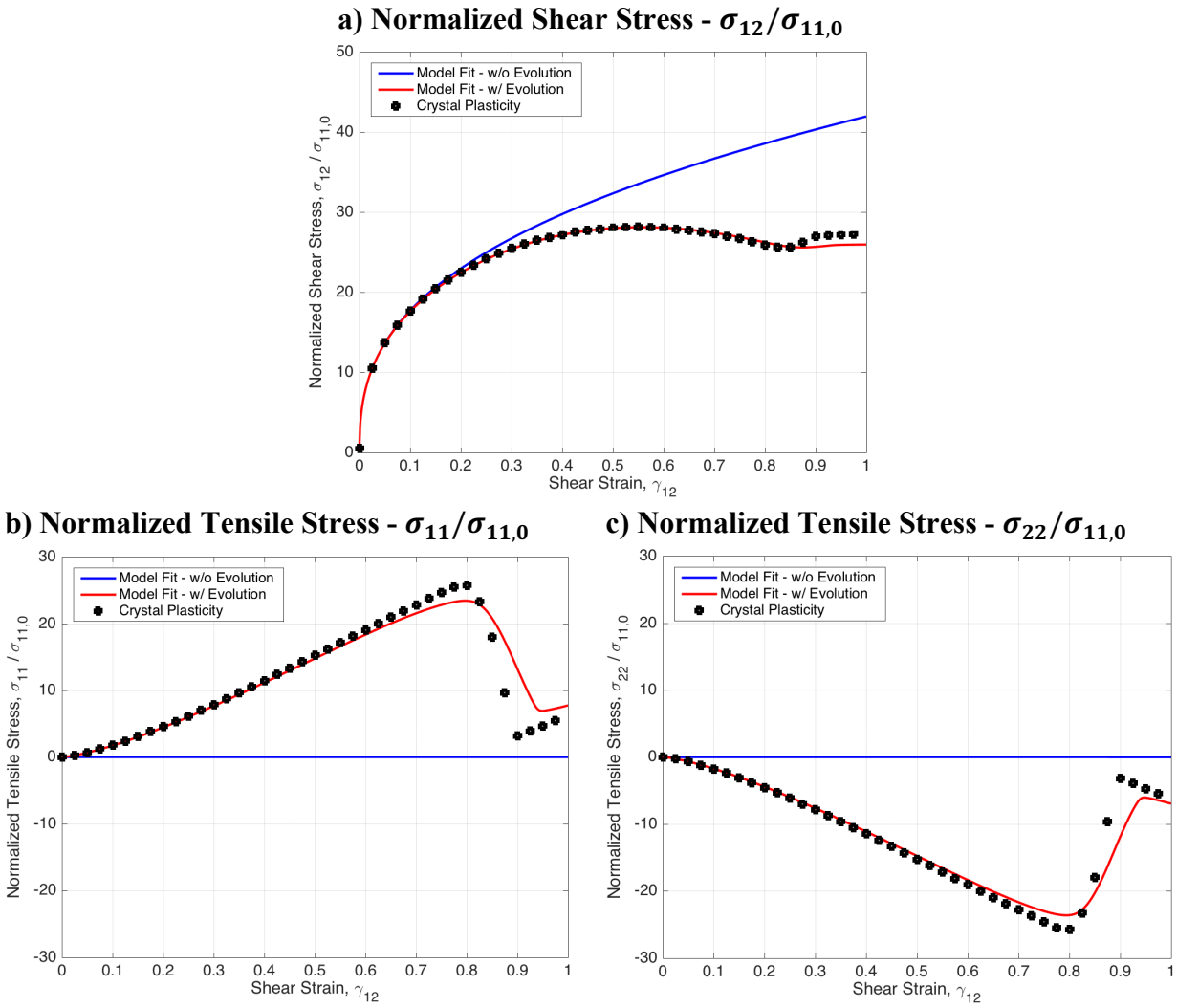

Figure 8.11 - Normalized a) Shear Stress ($\sigma_{12}/\sigma_{11,0}$), b) Tensile Stress ($\sigma_{11}/\sigma_{11,0}$), and c) Tensile Stress ($\sigma_{22}/\sigma_{11,0}$) for Single Crystal FCC Cube Texture During Simple Shear

8.3.4 Polycrystalline Extruded Aluminum AA6063-T6

Figure 8.12 presents a microstructure EBSD map of extruded aluminum AA6063-T6 from the work by Muhammad et al. [41, 42] and pole figures that are used for the crystal plasticity simulations. The synthetic microstructure was constructed from the EBSD map with orthotropic symmetry.

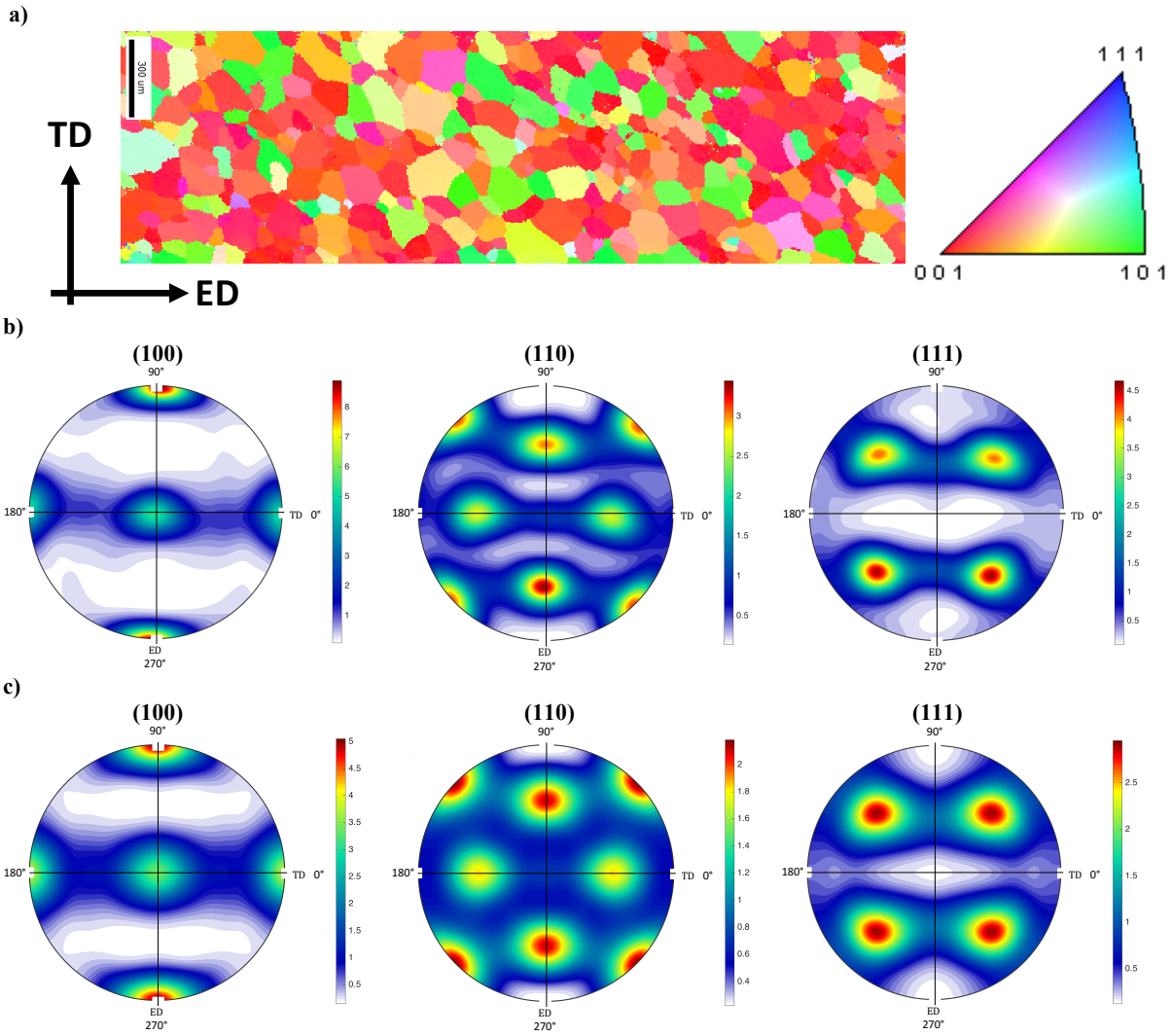

Figure 8.12 - a) EBSD map b) Measured Microstructure and c) Synthetic Microstructure of Extruded AA6063-T6 Microstructure

The hardening coefficients for the crystal and phenomenological plasticity models were obtained by calibrating the stress-strain response to the quasi-static experimental response of AA6063-T6 that was presented in Kohar et al. [103, 104] in the 0°-direction to the extrusion direction (ED). Figure 8.13 presents the experimental results of Kohar et al. [103, 104] and the calibrated stress-strain response that was produced by crystal and phenomenological plasticity for extruded AA6063-T6. Table 8.6 and Table 8.7 presents the crystal plasticity and phenomenological hardening parameters for extruded aluminum AA6063-T6. The Cowper-Symonds rate sensitivity parameters for extruded AA6063-T6 obtained from Kohar et al. [139] are presented and used for this work.

Table 8.6 - Chang-Asaro Crystal Plasticity Hardening Parameters For Extruded AA6063-T6

Model	C_{11} [GPa]	C_{12} [GPa]	C_{44} [GPa]	τ_0 [MPa]	τ_s [MPa]	h_0 [MPa]	h_s [MPa]	q
Chang-Asaro	104.55	52.28	26.14	68.5	87.0	113.0	68.5	1.00

Table 8.7 - Phenomenological Voce Hardening Parameters For Extruded AA6063-T6

E [GPa]	ν	σ_0 [MPa]	σ_u [MPa]	D	M (10^{10}) $[s^{-1}]$	P
69.7	0.33	176.4	235.8	20.98	2.46	8.88

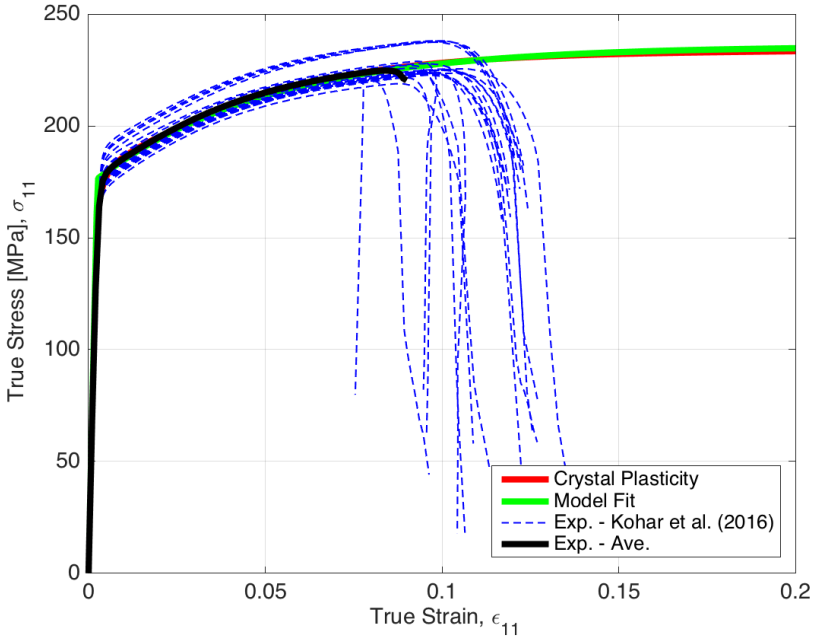

Figure 8.13 - Experimental [133], Crystal plasticity, Phenomenological uniaxial tensile stress-strain response of extruded aluminum AA6063-T6

The CPB06 yield function with three transformations was used as the phenomenological yield function to accurately capture the anisotropy of the material. The yield function was calibrated to the normalized uniaxial yield stress and Lankford coefficient variation with respect to the extrusion direction that was generated by crystal plasticity. Furthermore, the normalized shear yield stress variation was also calibrated with respect to the extrusion direction. Figure 8.14 presents the normalized yield locus from crystal plasticity and calibrated CPB06 yield function in both planes, normalized uniaxial yield stress, Lankford coefficient and shear stress variation for extruded aluminum AA6063-T6. The measurements of anisotropy were obtained at a plastic

work level of 5 MPa. The coefficients used for the CPB06 yield function are presented in APPENDIX A.4.

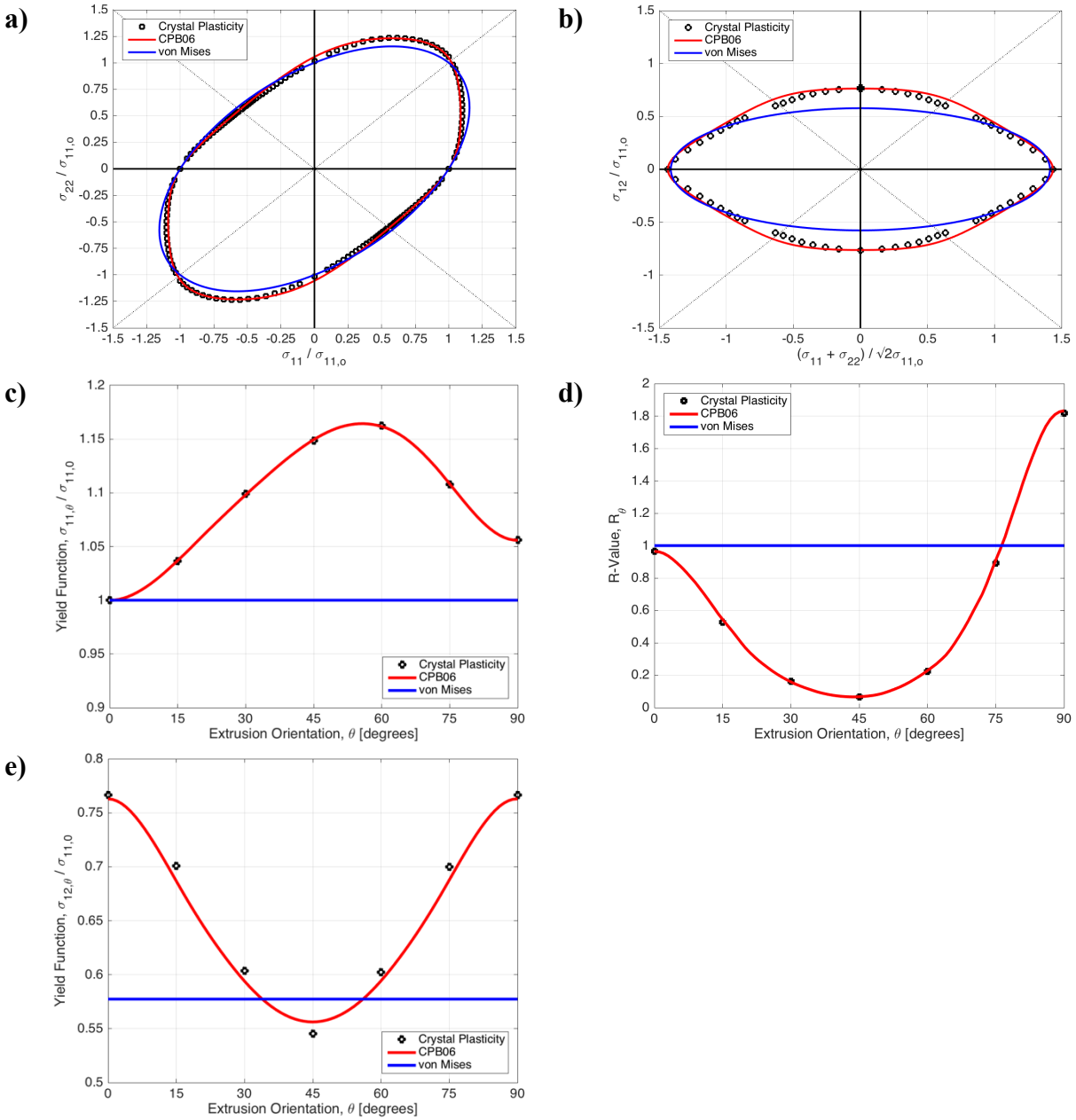

Figure 8.14 - Normalized Yield Loci in a) $\sigma_{12} = 0$ plane, b) $\sigma_{11} = \sigma_{22}$ plane, c) Normalized Yield Stress Variation, d) Lankford Coefficients, and e) Normalized Shear Stress Variation for Polycrystalline Extruded Aluminum AA6063-T6: Comparison Between Crystal and Phenomenological Plasticity at 5MPa Work Levels

Using the framework for measuring and calibrating microstructural evolution outlined in Section 8.2.1 and 8.3.1.1, the polycrystalline AA6063-T6 was rotated at increments of 15° and simulated under uniaxial tension along the extrusion direction. Figure 8.15 presents the orthotropic axis rotation generated by crystal plasticity. As discussed in Bassani and Pan [26], the sense of the rotation depends on the initial angle, β_o, is greater or less than a critical angle that is typically equal to 45°. However, the results from crystal plasticity present multiple critical angles where a change of direction occurs in extruded aluminum AA6063-T6. To capture this trend, an additional even functional component and parameter, $\xi_{3,2}$, is introduced into η_i for calibration, such that

$$\eta_3 = \eta_{o3} + \xi_{3,1}\left(\left(\frac{\partial \Phi}{\partial \Sigma_{22}}\right)^2 - \left(\frac{\partial \Phi}{\partial \Sigma_{11}}\right)^2\right) + \xi_{3,2}\left(\left(\frac{\partial \Phi}{\partial \Sigma_{22}}\right)^4 - \left(\frac{\partial \Phi}{\partial \Sigma_{11}}\right)^4\right) \quad (8.28)$$

The resulting predictions from the phenomenological model with and without evolution are also presented in Figure 8.15. Table 8.8 presents the parameters for the microstructural evolution of polycrystalline extruded AA6063-T6. Figure 8.16 presents the simple shear stress response of polycrystalline extruded AA6063-T6 using crystal plasticity and the phenomenological models. Again, the phenomenological model with evolution is able to capture reduction in shear stress predicted by crystal plasticity, while the classical approach to phenomenological modeling over-predicts the response. Figure 8.17 presents a comparison between the rotation of the orthotropic axis using crystal plasticity and the phenomenological models. The predictions are also compared with experimental EBSD and pole figure measurements from Muhammad et al. [41, 42]. Both the crystal plasticity and phenomenological-based texture evolution models capture the rotations of the axes and show good agreement to the experimental measurement.

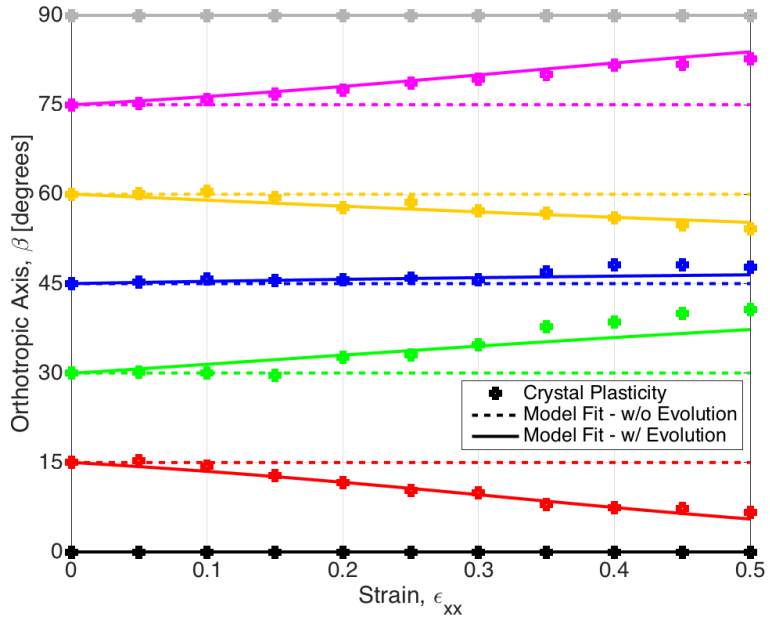

Figure 8.15 - Polycrystalline Extruded Aluminum AA6063-T6 Orthotropic Axis Evolution as a Function of Uniaxial Normal Strain, ε_{xx}: Measurements Generated from Crystal Plasticity and Calibrated using Phenomenological Model

Table 8.8 - Phenomenological Microstructural Evolution Parameters for Extruded Aluminum AA6063-T6

Model	η_{o3}	$\xi_{3,1}$	$\xi_{3,2}$
w/o Evolution	0.0000	0.0000	0.0000
w/ Evolution	-0.1326	-3.5300	-5.6665

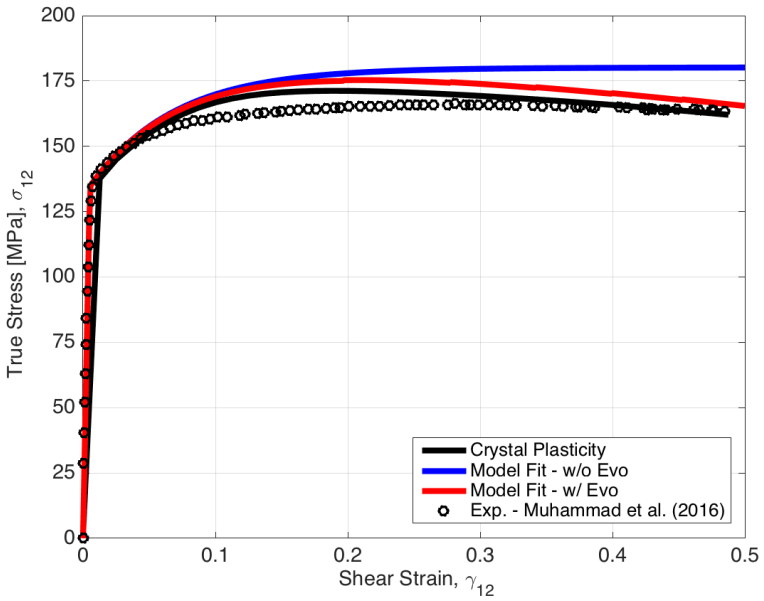

Figure 8.16 - Experimental [41, 42], Crystal Plasticity, and Phenomenological Predictions of Stress-Strain Response for Simple Shear of Extruded Aluminum AA6063-T6

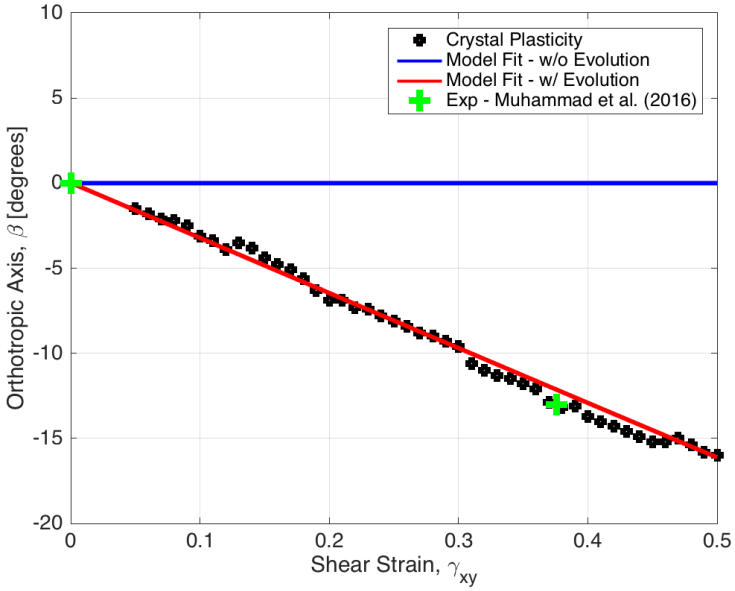

Figure 8.17 - Experimental [41, 42], Crystal Plasticity, and Phenomenological Predictions of Orthotropic Axis Rotation during Simple Shear for Extruded Aluminum AA6063-T6

8.3.5 Polycrystalline Sheet Aluminum AA5754-O

Figure 8.18 presents a microstructure EBSD map of sheet aluminum AA5754-O from the work by Brahme et al. [40] and pole figures that are used for the crystal plasticity simulations. The synthetic microstructure was constructed from the EBSD map without orthotropic symmetry. In the work of Brahme et al. [40], the crystal plasticity hardening coefficients were calibrated to the experimental stress-strain response obtained through X-ray diffraction by Iadicola et al. [162]. In this work, the PBTE model will be used to predict the experimental axial crush response of circular AA5754-O tubes presented in Williams et al. [77]. Figure 8.19 presents the experimental results of Williams et al. [77] and the calibrated stress-strain response that was produced by crystal and phenomenological plasticity. The experimental work stress-strain response by Iadicola et al. [162] is also presented.

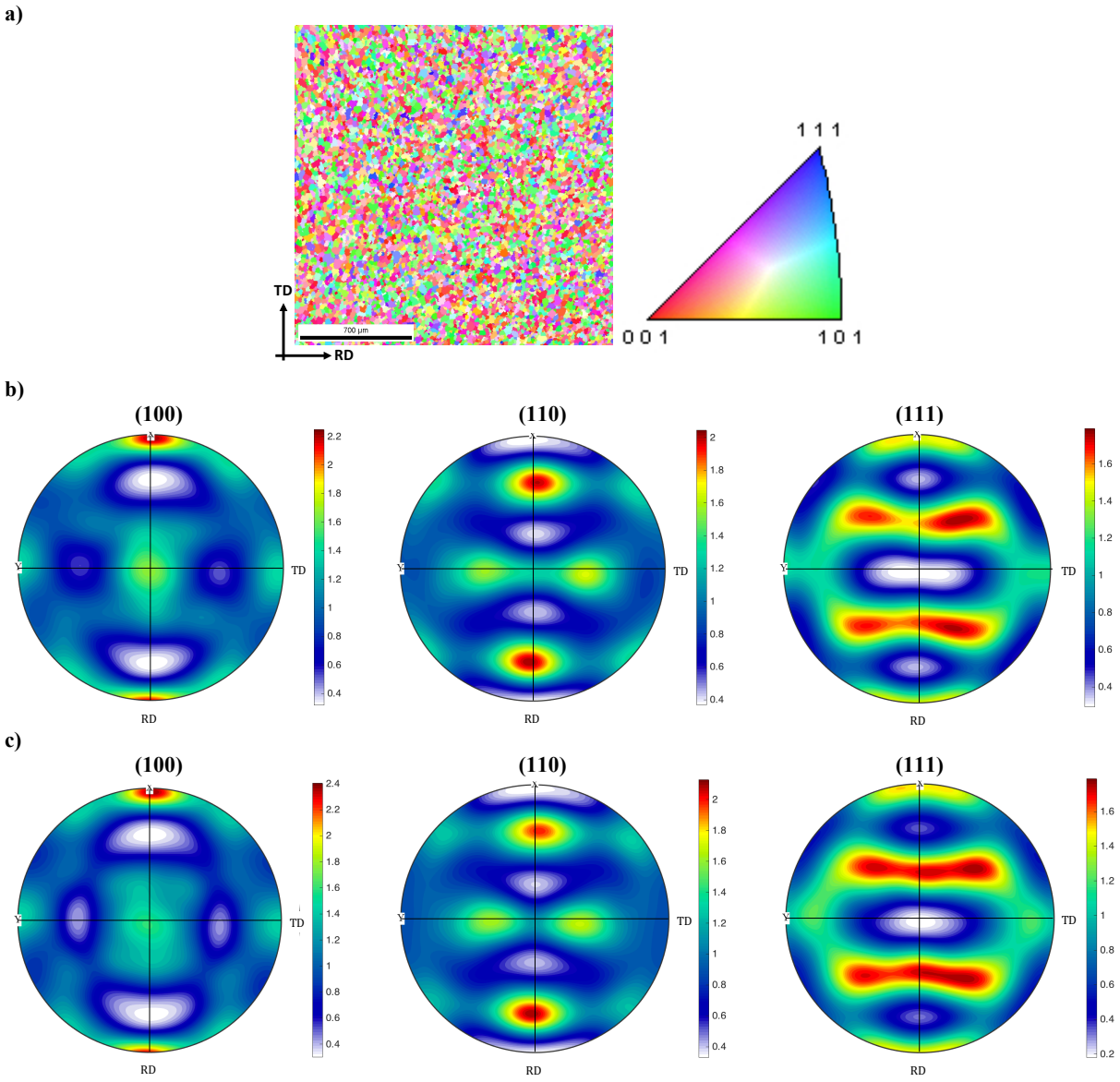

Figure 8.18 - a) EBSD map b) Measured Microstructure and c) Synthetic Microstructure of Rolled Sheet AA5754-O Microstructure

The Johnson-Cook rate sensitivity parameters for sheet aluminum AA5754-O obtained from Salisbury et al. [129] are presented and used for this work. Table 8.9 and Table 8.10 presents the crystal plasticity and phenomenological hardening parameters for sheet aluminum AA5754-O. The Johnson-Cook rate sensitivity parameters for sheet aluminum AA5754-O obtained from Salisbury et al. [129] are presented and used for this work.

Table 8.9 - Chang-Asaro Crystal Plasticity Hardening Parameters For Sheet Aluminum A5754-O

Model	C_{11} [GPa]	C_{12} [GPa]	C_{44} [GPa]	τ_0 [MPa]	τ_s [MPa]	h_0 [MPa]	h_s [MPa]	q
Chang-Asaro	104.55	52.28	26.14	40.0	91.0	100.0	0.4	1.00

Table 8.10 - Phenomenological Voce Hardening Parameters For Sheet Aluminum A5754-O

E [GPa]	ν	σ_0 [MPa]	σ_u [MPa]	D	$\dot{\varepsilon}_0$ (10^{-3}) $[s^{-1}]$	C
69.7	0.33	112.9	296.8	10.27	3.30	0.0102

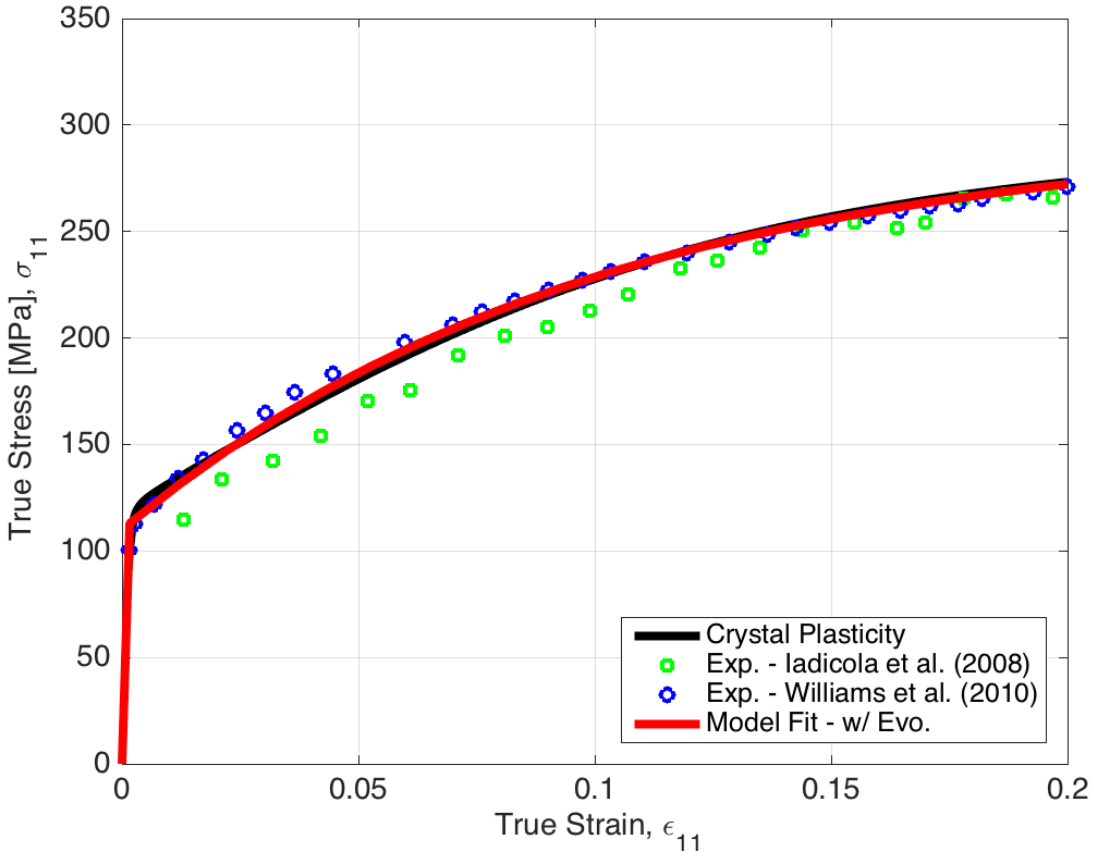

Figure 8.19 - Experimental [162, 77], Crystal plasticity, Phenomenological Uniaxial Tensile Stress-Strain Response of Sheet Aluminum AA5754-O

Figure 8.20 presents the normalized yield locus and calibrated yield function in both planes, normalized uniaxial yield stress, Lankford coefficient and shear stress variation for sheet aluminum AA5754-O. The measurements of anisotropy were obtained at a plastic work level of 5 MPa. The coefficients used for the CPB06 yield function are presented in APPENDIX A.5.

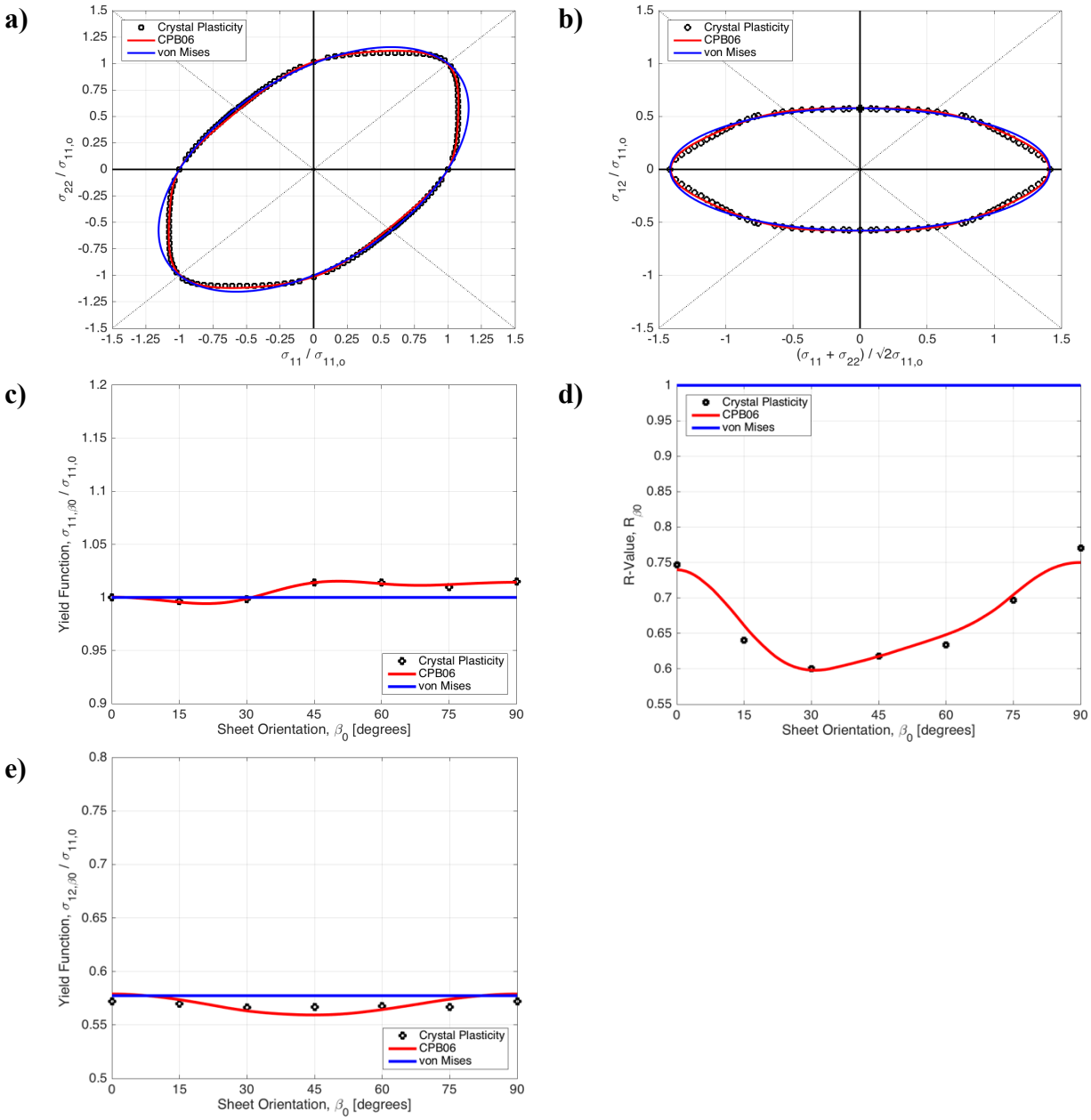

Figure 8.20 - Normalized yield loci in a) $\sigma_{12} = 0$ plane, b) $\sigma_{11} = \sigma_{22}$ plane, c) normalized yield stress variation, d) Lankford coefficients, and e) normalized shear stress variation for polycrystalline sheet aluminum AA5754-O: comparison between crystal and phenomenological plasticity at 5MPa plastic work level

Figure 8.21 presents the orthotropic axis rotation generated by crystal plasticity The resulting predictions from the phenomenological model with and without evolution are also presented in Figure 8.21. Table 8.11 presents the parameters for phenomenological microstructural evolution of sheet aluminum AA5754-O.

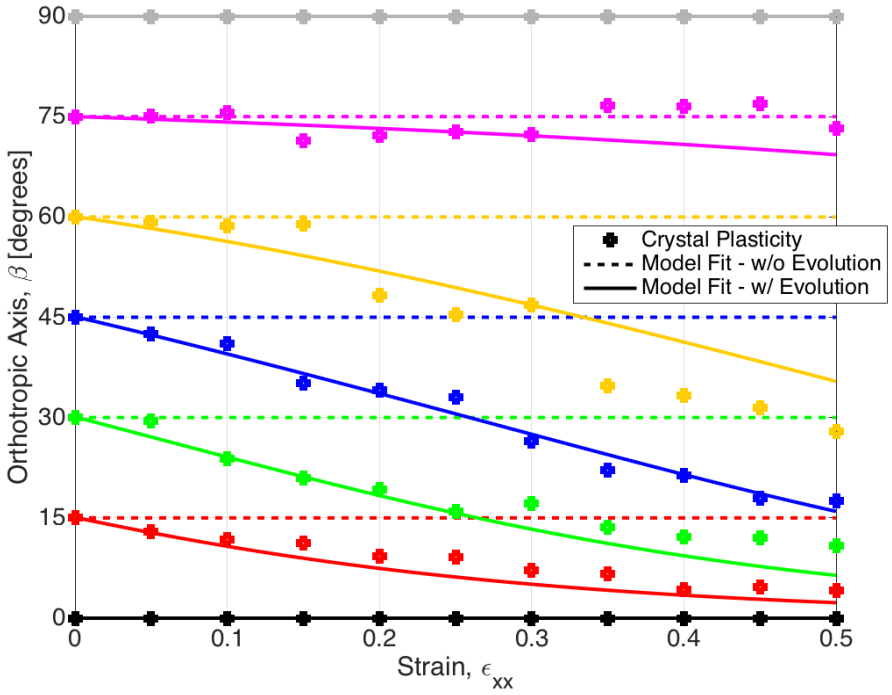

Figure 8.21 - Polycrystalline sheet aluminum AA5754-O Orthotropic Axis Evolution as a Function of Uniaxial Normal Strain, ε_{xx}: Measurements Generated from Crystal Plasticity and Calibrated using Phenomenological Model

Table 8.11 - Phenomenological Microstructural Evolution Parameters for Sheet Aluminum AA5754-O

Model	η_{o3}	$\xi_{3,1}$	$\xi_{3,2}$
w/o Evolution	0.0000	0.0000	0.0000
w/ Evolution	1.3871	0.5054	-1.0224

8.4 Finite Element Models

In this study, finite element (FE) models were created to simulate large deformation and localization in aluminum. FE models were created to simulate the uniform elongation and post-necking behaviour of the uniaxial tensile specimens of AA6063-T6. FE models were also created to simulate the dynamic axial crushing response of an extruded aluminum AA6063-T6 structure and a sheet aluminum AA5754-O circular tubes. This study uses the FE model of the extruded aluminum AA6063-T6 structure presented in Section 7.4 of Chapter 7. A 3D FE model is created to simulate the dynamic crush response of sheet aluminum AA5754-O circular tubes.

8.4.1 Finite Element Model of Uniaxial Tensile Specimen of Extruded Aluminum AA6063-T6

Figure 8.22 presents the quarter-symmetry FE model of the uniaxial tensile specimen. The specimen geometric dimensions were in accordance with the ASTM-E8 standard that was presented in Chapter 6. For quarter symmetry, the gauge length 82.147mm, width of 6.35mm and thickness of 1.00mm. Eight-node hexahedral elements with selective reduced (S/R) integration (ELFORM=2 for *SECTION_SOLID) were used throughout the model. The mesh features $0.20mm \times 0.20mm \times 0.20mm$ elements in the gauge section and a total of 71,540 solid elements. One end of the specimen was fully constrained, while a velocity-controlled boundary condition was applied on the other. To create a quarter-symmetric model, XZ-planar symmetry was applied along the length face and XY-planar symmetry was applied to the bottom face. Since the explicit dynamic formulation was used, a time scaling by a factor of 1000 was used to allow for a reasonable computational time.

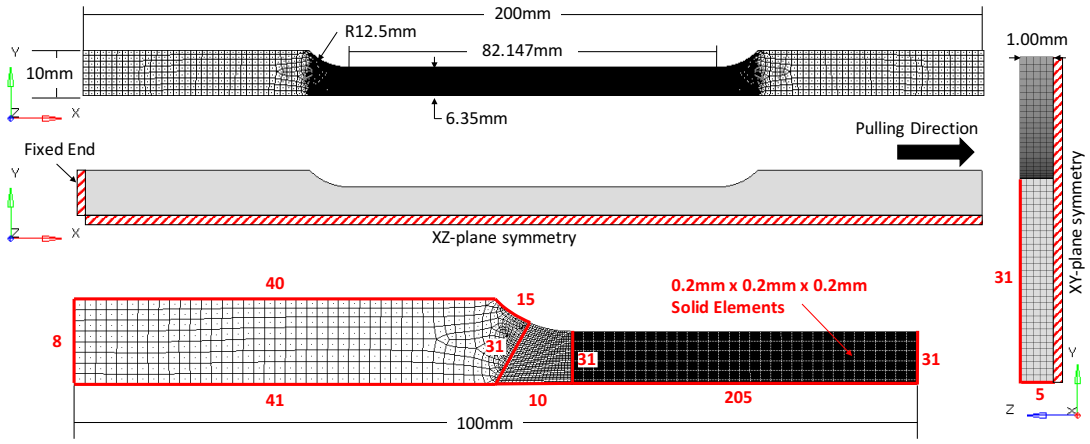

Figure 8.22 - FE Model of ASTM-E8 Uniaxial Tensile Specimen

8.4.2 3D Finite Element Model of Sheet Aluminum AA5754-O Circular Tube in Axial Crush

Figure 8.23 presents the FE model used in the simulation of the axial crush of the circular tube. The construction of this FE model follows the experimental setup in Williams et al. [77] and a similar setup as presented Section 7.4 of Chapter 7. The FE model consists of a 76.2mm [3.00”] outer diameter circular crush tube (red) constrained between the two steel plates (blue and yellow), bosses (green and cyan), and a linear mass (magenta). The initial length and a wall

thickness of the crush tube was 400mm and 3.00mm respectively. The mass of the linear sled was 560kg and an initial velocity of 30.6km/h [8.5m/s]. Similar to the previous section, the elastic material properties of all components in this FE model are listed in Table 5.3. Eight-node $1.50mm \times 1.50mm \times 1.50mm$ hexahedral elements with S/R integration were used to model the axial crush tube. The rolling direction was aligned with the axial crush direction.

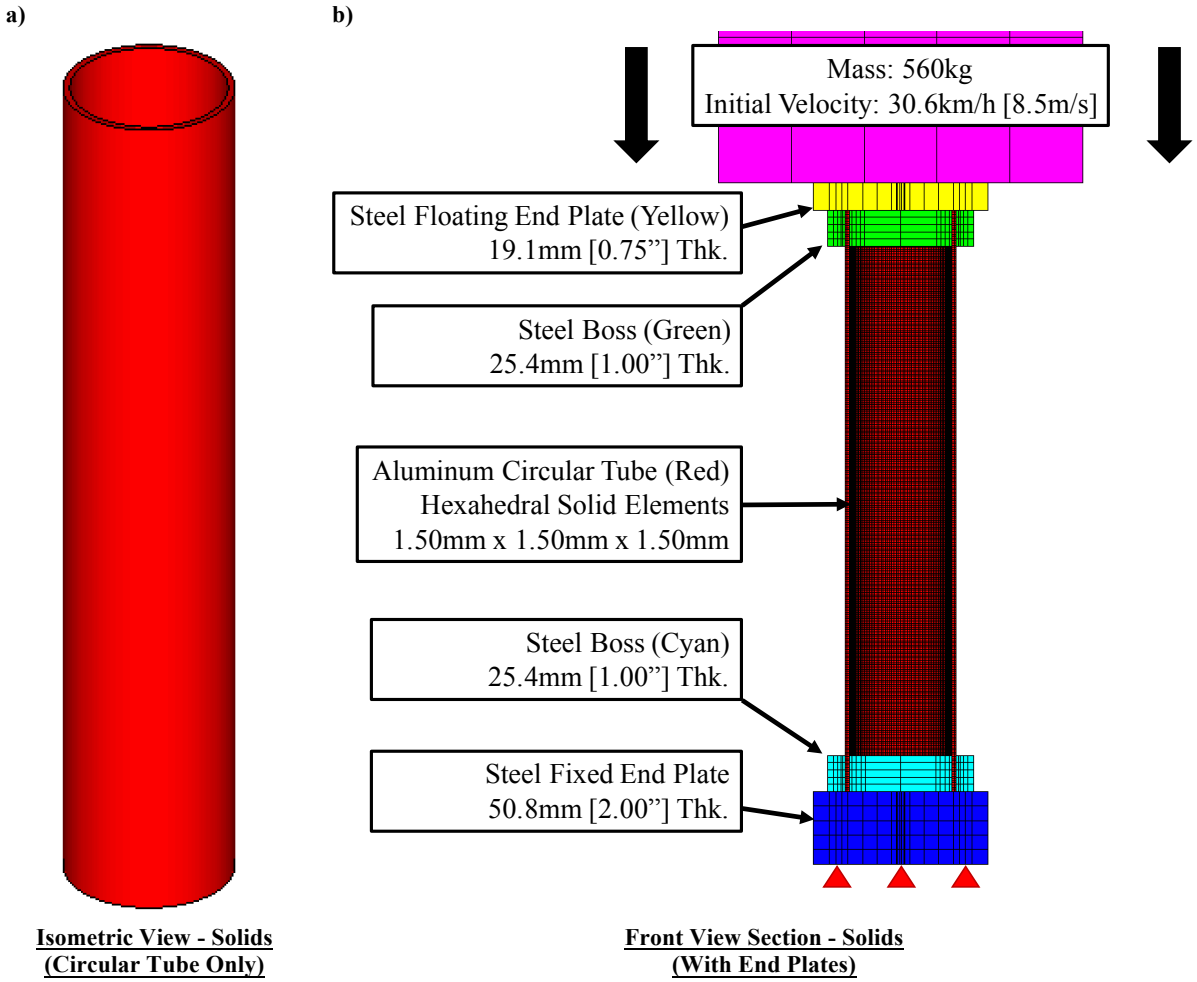

Figure 8.23 - (a) Isometric View without Bosses and (b) Front View Section with Bosses

8.5 Results and Discussion

8.5.1 Uniaxial Tensile Specimen of Extruded Aluminum AA6063-T6

Figure 8.24 presents the predicted true stress – true strain response of the uniaxial tensile specimen with and without microstructure evolution. The experimental true stress – true strain response, crystal plasticity, and single element predictions are also presented in Figure 8.24. Both simulations of the uniaxial tensile specimen show good correlation to the experimental

response in the uniform elongation range and initiation of post-uniform elongation. In the post-necking regime, a minor difference is observed between the macroscopic stress-strain response with and without microstructure evolution. This minor deviation is a result of the microstructure evolution. Figure 8.25 presents a contour plot of the microstructure evolution at a true strain of 0.123, which is a representative value of the experiments at fracture. It can be seen that large rotations in excess of ±20° about the normal direction are generated during necking.

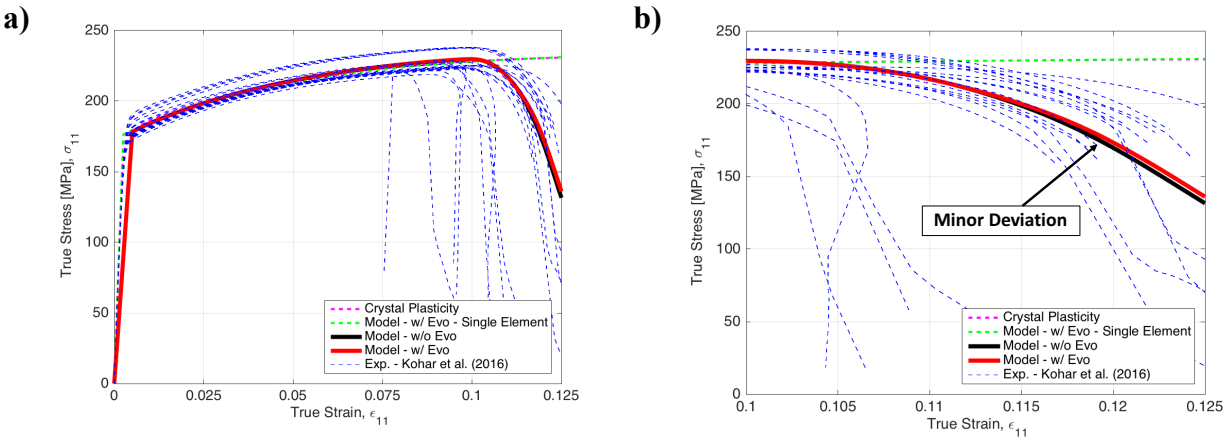

Figure 8.24 - Comparison of Uniaxial Tensile Specimen Stress-Strain Response to Experimental [133], Crystal plasticity, and Single Element Phenomenological Response for Extruded Aluminum AA6063-T6: a) Complete Stress-strain Response and b) Post-necking Response

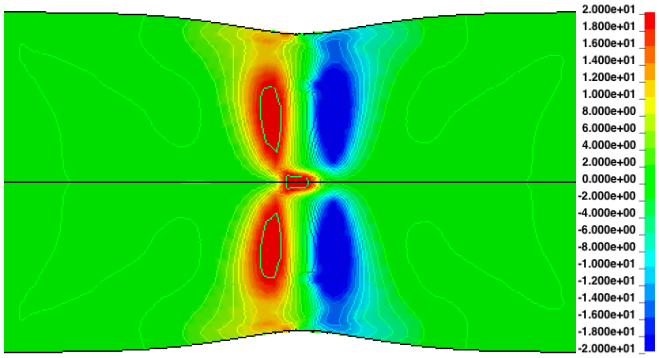

Figure 8.25 - Contours of Rotation (About Normal Direction) During Necking for Extruded Aluminum AA6063-T6 ($\varepsilon_{11} = 0.123$)

Although minor deviations were observed in the macroscopic stress-strain response, these large rotations can influence the strain field and stress state during localization. Table 8.12 presents a summary of results for uniaxial tensile specimen simulations with and without evolution during localization at a macroscopic true strain of 0.123 ($\varepsilon_{11} = 0.123$). A set of elements $1.00mm \times 1.00mm \times 1.00mm$ within the necking region, containing the highest strains, were selected in this analysis. The peak principal and the corresponding minor and equivalent (von Mises) are

presented. The average values throughout this section are also presented in Table 8.12. Two common dimensionless invariants are used to describe the stress state at fracture: stress triaxiality and Lode angle [141, 145, 147, 163, 164]. Stress triaxiality is defined as

$$\eta = \frac{1}{3}\frac{I_1}{\sqrt{3J_2}} \qquad (8.29)$$

where I_1 is the first invariant of the Cauchy stress tensor and J_2 is the second deviatoric invariant of the Cauchy stress tensor. Lode angle, ξ, is a non-dimensional parameter that describes the loading condition (i.e.: tensile, compression, shear, plane strain) through the invariants of the stress tensor (J_2 and J_3 stress invariants)

$$\xi = \operatorname{acos}\left(\frac{3\sqrt{3}}{2}\frac{\mathrm{J}_3}{\mathrm{J}_2{}^{\frac{3}{2}}}\right) \qquad (8.30)$$

The stress triaxiality and Lode angle at the peak principal strain and average throughout the section is also presented in Table 8.12. This table shows significant differences in the stress-strain and sizable differences in the local strains.

Table 8.12 - Summary of Results for Uniaxial Tensile Specimens Simulations With and Without Evolution ($\varepsilon_{11} = 0.123$)

	Model Without Evolution	Model With Evolution	Difference	%
Major Principal Strain – Peak	1.3306	1.2439	0.0867	7.0
Minor Principal Strain – Peak	-1.0960	-1.0044	-0.0916	9.1
Effective Strain – Peak	1.4201	1.3196	0.1005	7.6
Stress Triaxiality – Peak	0.9988	0.8805	0.1183	13.4
Lode Angle – Peak	-0.1286	-0.4750	0.3464	72.9
Major Principal Strain – Average	0.9213	0.9116	0.0097	1.1
Minor Principal Strain – Average	-0.7133	-0.7049	-0.0084	1.2
Effective Strain – Average	0.9671	0.9566	0.0105	1.1
Stress Triaxiality – Average	0.5294	0.5046	0.0248	4.9
Lode Angle – Average	-0.2070	-0.3970	0.1900	47.9

8.5.2 Extruded Aluminum AA6063-T6 Structure in Axial Crush

Using the fracture results from the previous section, simulations of the dynamic axial crushing response of an extruded aluminum AA6063-T6 structure were performed using the

anisotropic model with and without evolution. A simple element deletion framework, where an element is removed from the finite element model when the equivalent strain at fracture is reached, was used to simulate fracture in the structure. Figure 8.26 presents a comparison of the force and energy-displacement predictions for each model to the experimental response. Each predicted response was filtered using an SAE CFC 1000 filter to allow for a direct comparison with experiments. Table 8.13 summarizes the predicted mean crush force, peak crush force, energy absorption, and crush efficiency for each model. Figure 8.27 presents a comparison of the experimental crushed extrusions with simulation predictions of effective strain contours. The anisotropic model with and without evolution predicted a mean crush force of 96.4kN and 97.6kN respectively. This corresponds to a model over-prediction of +2.1% and +3.4% respectively. Both models capture well the overall trend and energy absorption characteristics of this structure. This result highlights the ability to accurately predict macroscopic energy absorption characteristics of lab-scale components using a crystal plasticity-based phenomenological framework using only an EBSD scan and a single uniaxial tensile experiment. Figure 8.28 presents simulated local orthotropic axis rotations about the local normal, extrusion and transverse axes. Large rotations in excess of ±10° are generated during folding that can influence the localization behaviour. During crush, fracture can develop and propagate throughout the structure. In the element deletion framework to simulate fracture, the mass of the element is also removed when the element is deleted. This changes the mass of the component, $m(t)$, of the component as a function of time. The volume fraction evolution of fracture is defined as

$$V_f(\mathrm{t}) = \left(1 - \frac{m(t)}{m_o}\right)\left(\frac{L_o}{d_{max}}\right) \qquad (\ \mathbf{8.31}\ )$$

where m_o is the initial mass, L_o is the initial length, and d_{max} is the final crush distance. Figure 8.29 presents the volume fraction evolution of fracture throughout the structure The evolution model predicts lower energy absorption due to the lower fracture strains and higher rate of fracture, which limits the energy absorption through the reduction of the local plastic work capability.

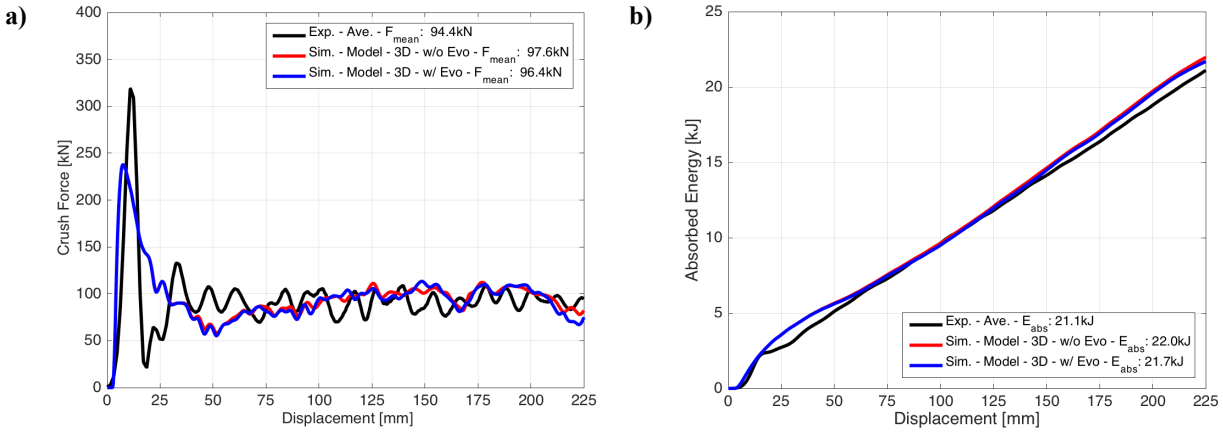

Figure 8.26 - Comparison of Experimental and Simulated a) Crush force and b) Energy absorption of Extruded Aluminum AA6063-T6 crush tube

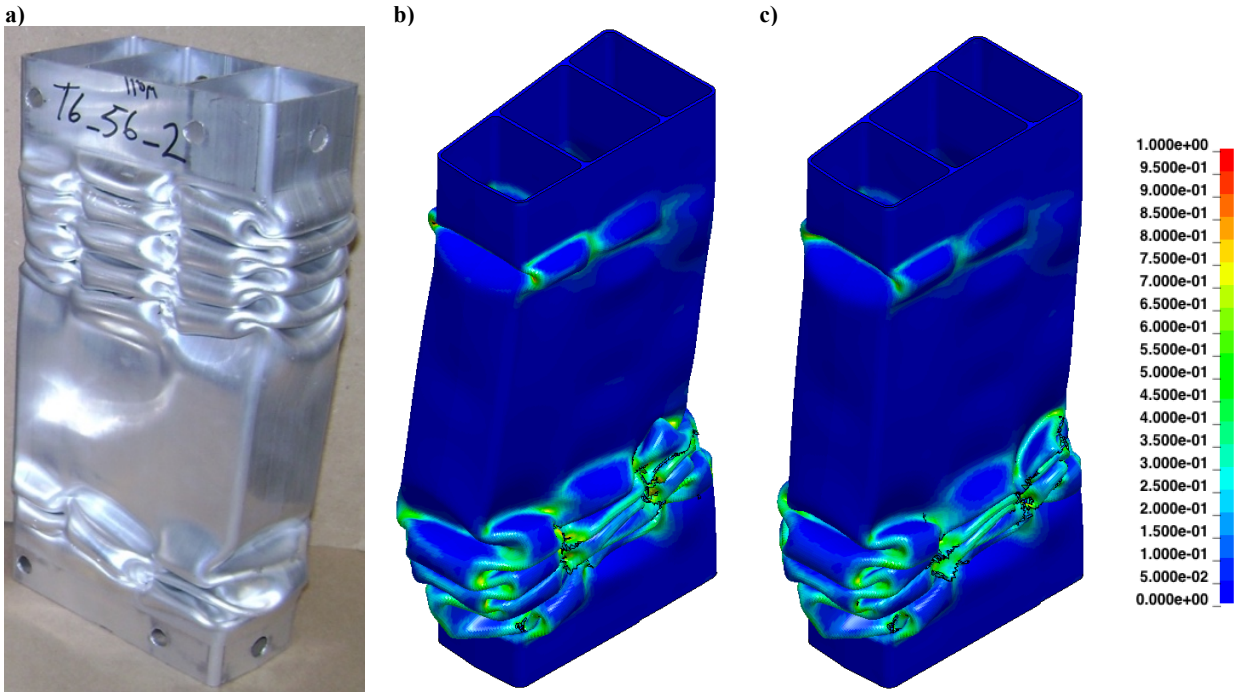

Experimental | **Anisotropic Model – w/o Evolution** | **Anisotropic Model – w/ Evolution**

Figure 8.27 - a) Experimental and b) Anisotropic Model w/o Evolution and c) Anisotropic Model w/ Evolution Simulations of Effective Strain Contours of Extruded Aluminum AA6063-T6 Crush Tube

Table 8.13 - Summary of Results for Extruded Aluminum AA6063-T6 Crush

	Mean Crush Force (kN)	Peak Crush Force (kN)	Crush Efficiency (%)	Energy Absorption (kJ)
Anisotropic – w/o Evolution	97.6	237.7	41.1	22.0
Anisotropic – w/ Evolution	96.4	237.7	40.6	21.7
Experimental	94.4	318.7	29.6	21.1

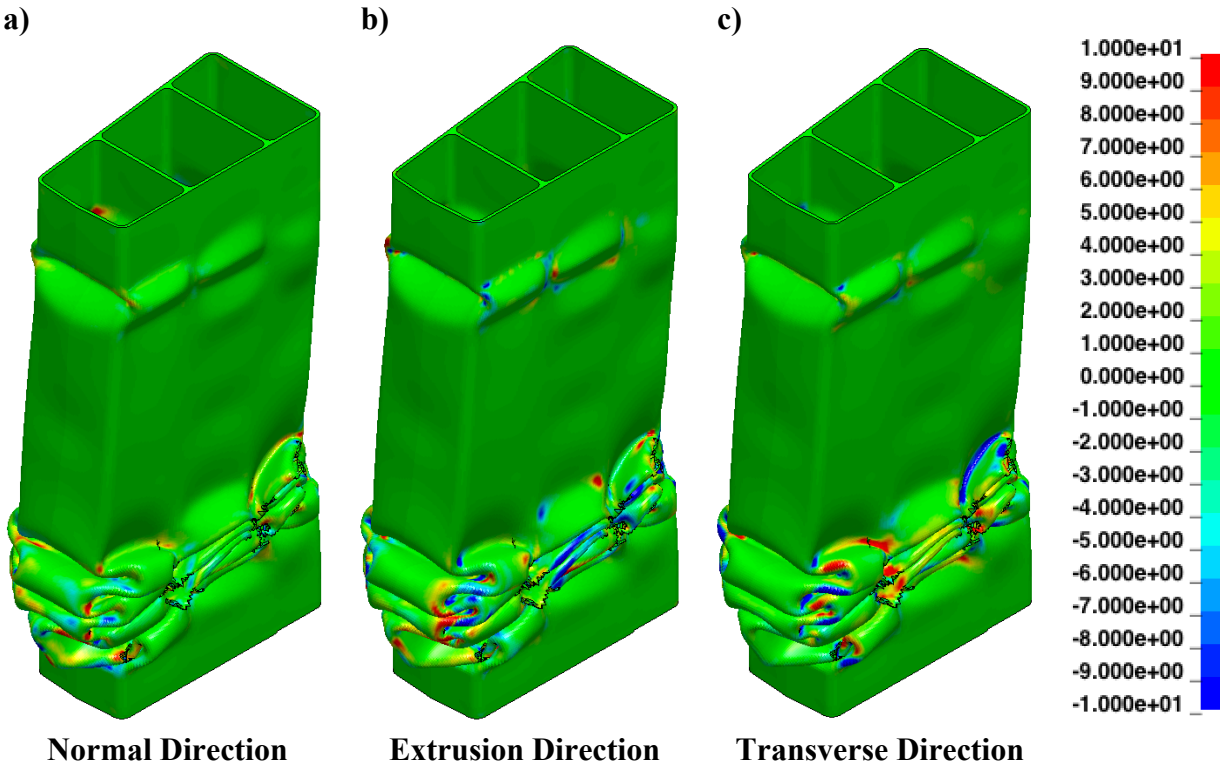

Figure 8.28 - Simulated Rotation of Local Orthotropic Axis [degrees] about Sheet a) Normal, b) Extrusion and c) Transverse Direction of Extruded Aluminum AA6063-T6 Extrusion Crush Tube

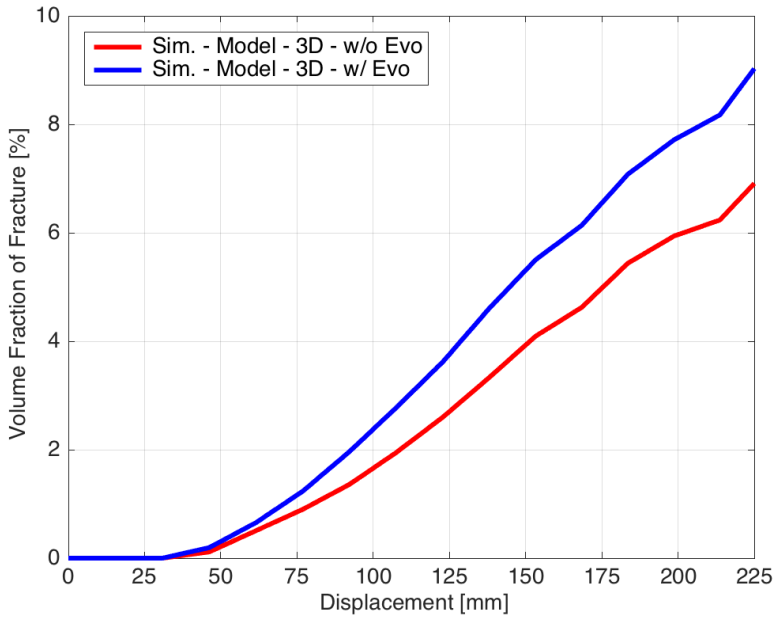

Figure 8.29 - Predicted Volume Fraction Evolution of Fracture of Extruded Aluminum AA6063-T6 Extrusion Crush Tube During Crush

8.5.3 Sheet Aluminum AA5754-O Circular Tube in Axial Crush

8.5.3.1 Comparison of Experimental and Simulation Crush Data

This section presents a comparison between experimental and simulated energy absorption characteristics. Figure 8.30 presents a comparison of the experimental [77] and simulated crush force and energy absorption response. Three simulation conditions were performed: isotropic (von Mises) and anisotropic model with and without microstructural evolution. Table 8.14 presents a summary of the energy absorption responses. Figure 8.31 presents a comparison of the deformation patterns between the experimental and simulated responses. The isotropic (von Mises) model over-predicts both the mean crush force (86.7kN vs 81.0kN) and energy absorption response (15.2kJ vs 14.3kJ). Both anisotropic models predict very similar energy absorption (14.5kJ) and crush force (82.8kN) responses and both show good agreement with the experimental response. This result again highlights the ability to accurately predict macroscopic energy absorption characteristics of lab-scale components using a crystal plasticity-based phenomenological framework. Figure 8.32 presents simulated local orthotropic axis rotations about the local normal, rolling and transverse axes. Again, large rotations in excess of ±20° are generated during folding.

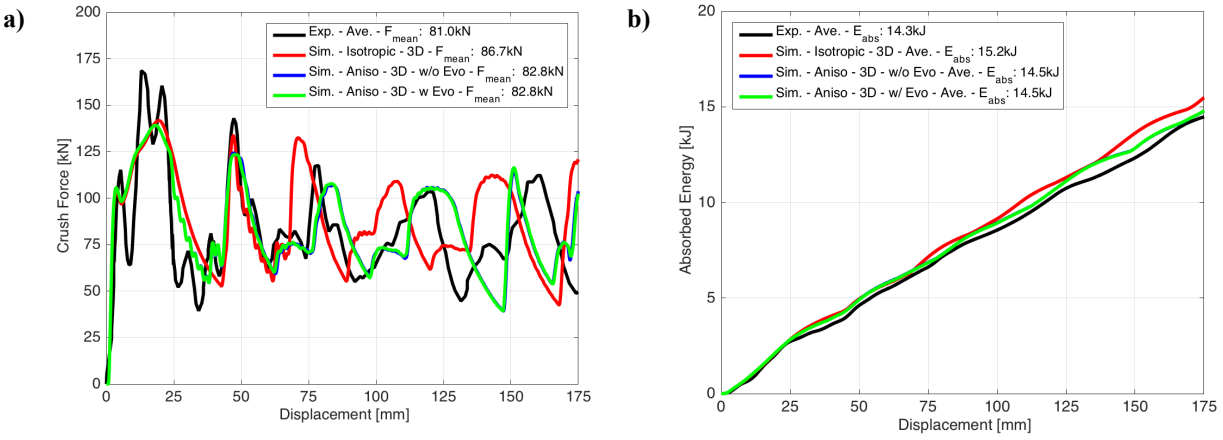

Figure 8.30 - Comparison of Experimental [77] and Simulated a) Crush force and b) Energy Absorption of Sheet Aluminum AA5754-O Circular Tubes

Table 8.14 - Summary of Results for Sheet Aluminum AA5754-O Circular Tube Crush

	Mean Crush Force (kN)	Peak Crush Force (kN)	Energy Absorption (kJ)
Isotropic	86.7	141.7	15.2
Anisotropic – w/o Evolution	82.8	139.1	14.5
Anisotropic – w/ Evolution	82.8	139.1	14.5
Experimental [77]	81.0	168.6	14.3

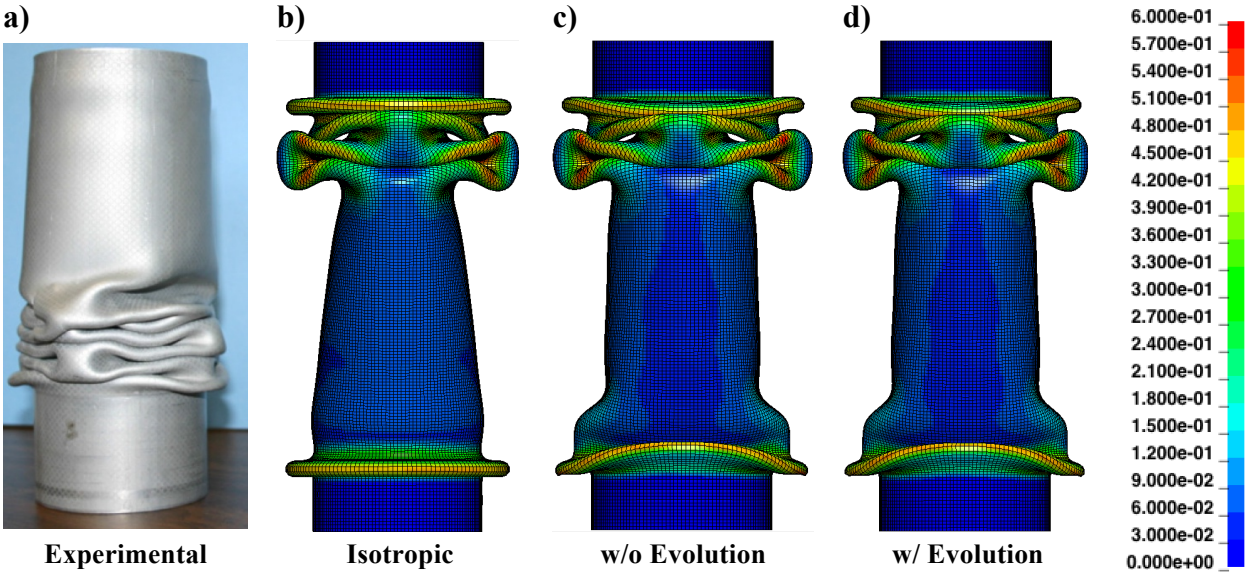

Figure 8.31 – Comparison of Crush Deformation Patterns from a) Experimental [120] and Simulated (effective strain) Contours from b) Isotropic, c) Anisotropic – Without Evolution and d) Anisotropic – With Evolution

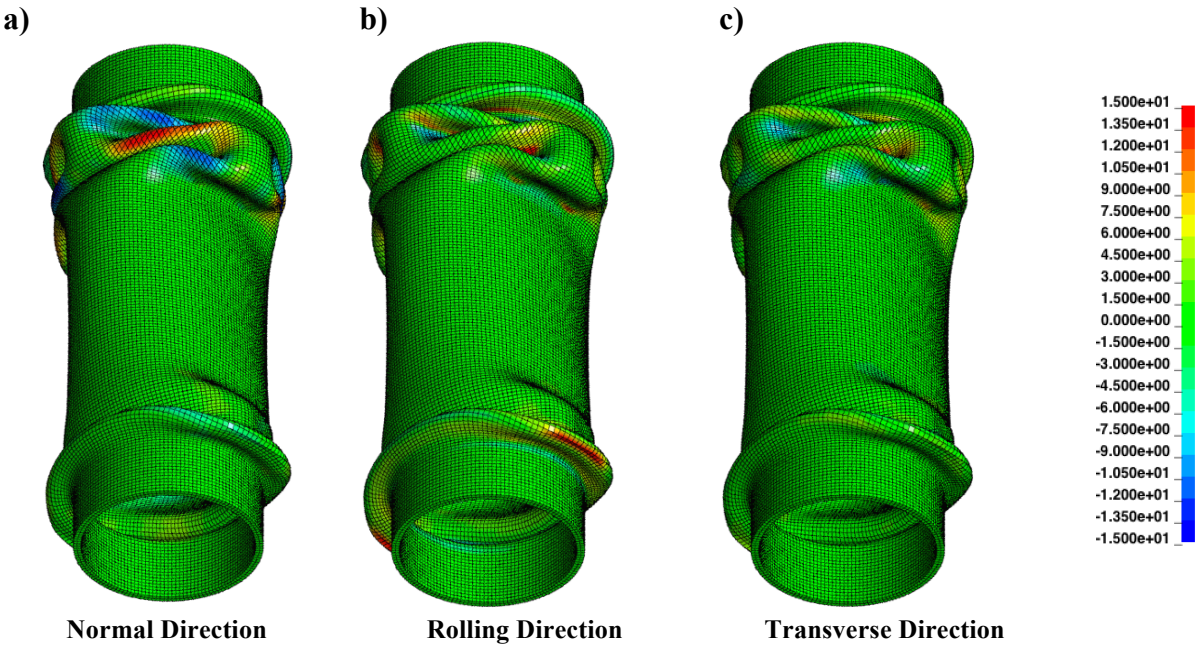

Figure 8.32 – Simulated Rotation of Local Orthotropic Axis [degrees] about Sheet a) Normal, b) Rolling and c) Transverse Direction of Sheet Aluminum AA5754-O Circular Tube

8.5.4 Influence of Varying Sheet Orientation on Energy Absorption

In the previous section, the rolling direction was aligned with the axial crush direction in all simulations ($\beta_o = 0^o$). The anisotropic models with and without microstructural evolution showed similar predictions in energy absorption characteristics and similar crush patterns compared to the isotropic simulation. However, since large orthotropic rotations were predicted with the evolution model, it is plausible that these large rotations could influence the energy absorption response when the sheet orientation is not aligned in a favourable manner. In other words, there could exist an optimal sheet orientation predicted by the anisotropic model with and without evolution.

In this section, the local sheet orientation, β_o, was varied in order to identify an optimal orientation for maximum crush force. This study replicates the process of rotating the aluminum sheet prior to fabrication. By rotating the sheet, the material's resistance to bending and stretching by thinning can increase, which results in an increase in energy absorption. The significance of this study is that an optimal sheet orientation can improve the energy absorption characteristics without increasing the mass of the structure. Since isotropic models are insensitive to the direction of loading, isotropic models cannot be used to identify an optimal sheet orientation. Using the anisotropic model with and without evolution, the initial sheet orientation was varied between 0° and 90° in increments of 15° and simulated using the same boundary conditions.

Figure 8.33 and Table 8.15 presents the variation of the mean crush force with respect to the initial sheet orientation. From the sampled points, the anisotropic model without and with microstructure evolution predicted that the optimal sheet orientation occurs at 30^o and 60^o respectively. Assuming that the experimental behaviour follows the response of the most detailed model (with evolution), the model without evolution over-predicts the model with evolution by 0.8%. More importantly, the difference between the models with evolution at 30^o and 60^o is 1.3%. These differences can be further amplified if the rate of microstructure evolution is higher (in the case of the validation material presented in Section 8.2.4).

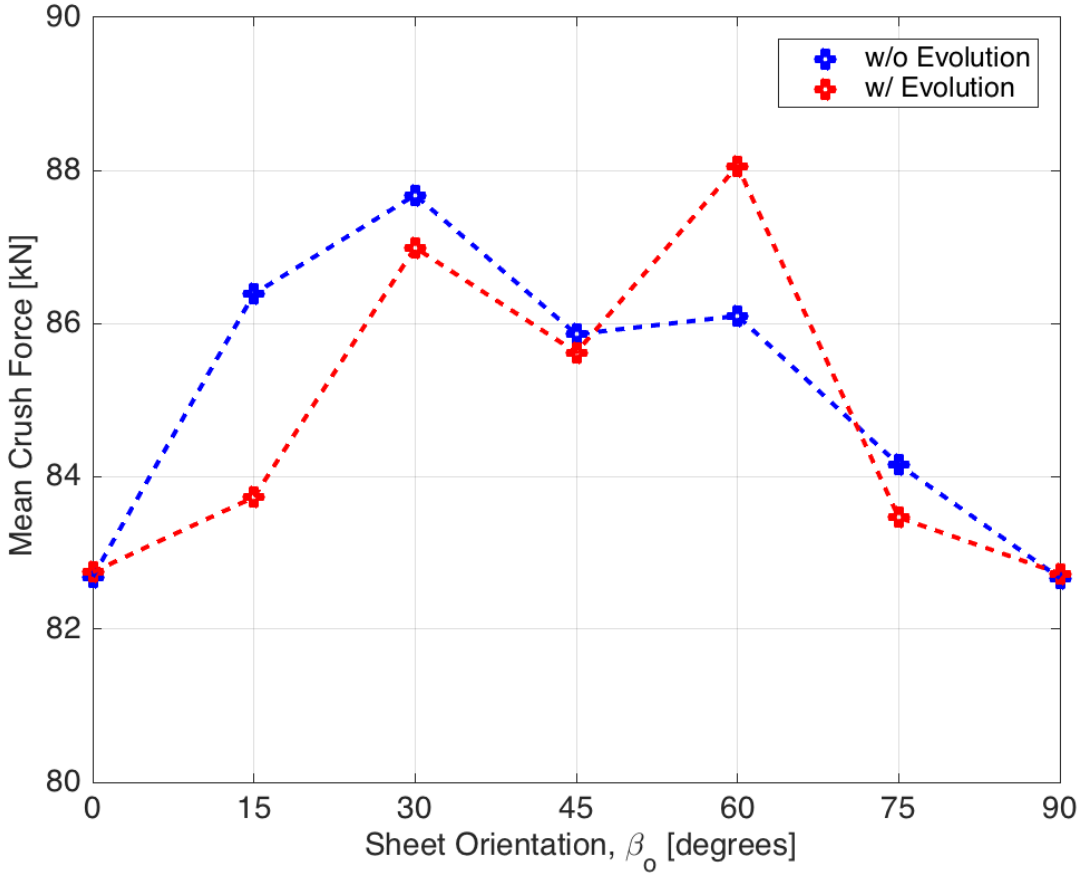

Figure 8.33 – Mean Crush Force Response Variation vs Initial Sheet Orientation, $\boldsymbol{\beta_o}$

Table 8.15 - Mean Crush Force Response Variation vs Initial Sheet Orientation

Initial Sheet Orientation, $\boldsymbol{\beta_o}$	**Anisotropic – w/o Evolution**	**Difference from Baseline w/o $\boldsymbol{\beta_o} = 0^o$ [%]**	**Anisotropic – w/ Evolution**	**Difference from Baseline w/ Evolution $\boldsymbol{\beta_o} = 0^o$ [%]**	**Difference Between w/ and w/o Evolution**
0	82.8	0.0	82.8	0.0	0.0
15	86.4	4.3	83.4	0.7	-3.6
30	87.7	5.9	87.0	5.1	-0.8
45	85.9	3.7	85.6	3.4	-0.4
60	86.1	4.0	88.1	6.4	2.3
75	84.2	1.7	83.5	0.8	-0.8
90	82.7	-0.1	82.7	-0.1	0.0

8.6 Chapter Conclusions

In this chapter, a new multi-scale framework was proposed to incorporate microstructure evolution into phenomenological plasticity. Crystal plasticity was used to calibrate phenomenological yield functions to initial anisotropic variation. Crystal plasticity was also used to generate measurements of microstructural evolution through simulations of off-axis uniaxial tension. This framework was used to calibrate the initial anisotropy and microstructure evolution of single cube face-centered cubic crystal, polycrystalline extruded aluminum AA6063-T6, and polycrystalline sheet aluminum AA5754-O with good agreement to experiments. The PBTE model was able to capture the softening behaviour observed experimentally in simple shear of extruded AA6063-T6 through rotation of the orthotropic axes.

The constitutive framework was implemented into the commercial FE software, LS-DYNA, to simulate uniaxial tensile specimens during large deformation and the axial crush response of aluminum structures. Simulations of simple uniaxial tension of extruded aluminum AA6063-T6 showed large microstructure evolution that generated significant differences in the strain field, stress state and ultimately, strain at fracture in the neck. These differences in prediction of fracture strains translated into differences in the prediction of energy absorption characteristics and fracture behaviour of extruded aluminum AA6063-T6 during axial crush. In the application of sheet aluminum AA5754-O, large microstructure evolution is predicted during axial crush. The phenomenological-based texture evolution model was able to identify an optimal sheet orientation that would provide higher energy absorption without increasing the mass of the structure. These works all highlight the ability to predict macroscopic energy absorption characteristics of lab-scale components using a crystal plasticity-based phenomenological framework using only an EBSD scan and a single uniaxial tensile experiment.

9 CONCLUSIONS AND FUTURE WORK

9.1 Key Conclusions

The objective of this work was to enhance the energy absorption characteristics of aluminum front crush rail for mass-production mid-size vehicles through the development and coupling of optimization frameworks with advanced constitutive modeling techniques. A new framework for optimizing the mechanical and geometrical properties of these crush structures was presented. A new numerical framework for phenomenological-based texture evolution for measuring and calibrating microstructural evolution, which bridges crystal plasticity to phenomenological plasticity, was also presented. As a result of this work, a new understanding of the individual and coupled influence of geometrical properties, anisotropy, constitutive modeling, and optimization has been gained. The key conclusions from the work presented in this thesis are as follows:

9.1.1 Effects of Elastic-Plastic Behaviour on the Axial Crush Response of Square Tubes

- The ultimate tensile strength, hardening rate and the yield stress together have a strong positive effect on the energy absorption characteristics
- Peak crushing force is more sensitive to the yield stress than the steady state crushing force. This means that increasing the yield stress results in a decrease in the crush efficiency when the hardening capabilities of the material are low; a trade-off exists between energy absorption and crush efficiency in terms of yield stress.
- Imposing constraints on the peak crushing force results in lightweight alloys with a low yield stress that have significant work hardening capabilities outperform materials with a high yield stress and very little work hardening with respect to energy absorption.

9.1.2 Effects of Yield Surface Curvature and Anisotropy Constants on the Axial Crush Response of Circular Tubes

- Predictions of axial crush response strongly depend on the shape of the yield surface. Thus, the correct representation of the material anisotropy (yield stresses, R-values, etc.) alone is not sufficient for accurate predictions of axial crush.

- Energy absorption capabilities of a material can be linearly related to the area under the yield surface.
- For accurate first order predictions of energy absorption (ignoring local fracture), balanced biaxial tensile yield strength was a critical material anisotropy parameter. Accurate characterizations of the yield stress variation are important for predicting the initial and mean crush forces, while accurate characterizations of the R-values are important for predicting the resulting crush modes after initial impact.

9.1.3 Development of High Crush Efficient, Extrudable Aluminium Front Rails for Vehicle Lightweighting

- The new optimization framework can increase the mean crush force and energy absorption by 21.9% and 26.7% more energy absorption than baseline geometries.
- Specific energy absorption was shown to be an appropriate optimization objective function.
- The functionality of the specific energy absorption performance metric guided the optimization process to the maximum allowable mass.
- It was shown that the specific energy absorption linearly relates to the crush efficiency and that the optimization of the specific energy absorption function will tend to simultaneously increase the crush efficiency.
- Allowed a 6000-series aluminum alloy, in particular AA6063-T6 family alloy, to have competitive energy absorption characteristics compared to mass-produced 7000-series aluminum profiles.

9.1.4 Effects of Coupling Anisotropic Yield Functions with the Optimization Process of Extruded Aluminum Front Rail Geometries in Crashworthiness

- Applying sophisticated yield function during the optimization process resulted in better energy absorption characteristics than solutions using simplified yield functions.
- Incorporating the effect of the non-quadratic yield function exponent alone improved optimization process for constrained optimization of SEA.

- Using the Yld2004-18p yield function, an optimal extrusion configuration predicted an increase in energy absorption and mean crush force for a constrained mass when using specific energy absorption (SEA) as a single optimization objective function.
- Utilizing a von Mises yield function resulted in a decrease in energy absorption and mean crush force. This results highlights the interaction effect between geometry and material.
- A direct relationship exists between a material's ultimate tensile strength and mass constraints in the optimization of extrusions. Utilizing his information can help reduce the number of simulations to be performed.
- Each yield function converged to a local optimum for a constrained mass optimization formulation. Relaxing the mass constraint lead to a global optimum solution that was unique to each yield function for the sizing domain.

9.1.5 A New Multi-Scale Framework to Incorporate Microstructure Evolution into Phenomenological Plasticity

- A new constitutive model and calibration framework to incorporate microstructure evolution into phenomenological plasticity by bridging crystal plasticity.
- Simulations of simple uniaxial tension of extruded aluminum AA6063-T6 showed large microstructure evolution that generated significant differences in the strain field, stress state and ultimately, strain at fracture in the neck.
- Differences in prediction of fracture strains translated into differences in the prediction of energy absorption characteristics and volume fraction of fracture in extruded aluminum AA6063-T6 during axial crush.
- Capability of predicting macroscopic energy absorption characteristics of lab-scale components using a crystal plasticity-based phenomenological framework.

9.2 Future Work

The results in this thesis highlighted the influence of coupling anisotropic constitutive models with optimization of aluminum axial crush structures for automotive applications. However, automotive crush structures are subjected to various loading scenarios, such as off-axis and oblique loading (see Ref. [3, 165, 166, 167, 134]). Although this work focused on the optimization of axial crush, these converged solutions may be detrimental in off-axis or oblique

loading scenario. Thus, a multi-objective optimization study that utilizes this framework should be performed to simultaneously improve axial and oblique loading scenarios. In this thesis, a study was presented to understand and optimize the elastic-plastic response of the crashworthiness behaviour of square aluminum tubes. This work assumed homogeneous elastic-plastic properties along the length of the structure. However, new technologies exist that allow for tailored properties throughout the length of the structure (i.e. Ref [168, 169]). Utilizing this existing framework, an optimization study can be performed to determine the optimal gradient in material properties for a crush structure. Extensions of the optimization beyond extrusions framework beyond extrusions is recommended.

In the current work, an initial experiment was used to verify the construction of the finite element models before continuing to the optimization procedure. A critical assumption was made that the finite element model is valid throughout the entire domain of study during the optimization process. Once the optimization process is complete, the newly generated geometries and materials require experimental testing to verify these frameworks and assumption. To further verify the material optimization framework, a new alloy chemistry and manufacturing processing scheme should be designed to achieve the desired elastic-plastic properties for optimal energy absorption characteristics. Newly generated geometries through the optimization process would require manufacturing, fabrication and experimental testing to verify these frameworks. Furthermore, each geometric cross section generated by each yield function would also require fabrication and experimentally crushed. This would verify the influence of coupling anisotropic yield functions with the optimization scheme. As mentioned earlier, a simplified fracture model, where element deletion occurs when the effective strain reaches a single value, was used during this study. Enriching the constitutive model of aluminum with failure and fracture models [109, 110, 111, 112] is recommended to prevent converged solutions that would unexpectedly and catastrophically fail during experimental crush.

REFERENCES

[1] U. E. P. Agency, "Draft Technical Assessment Report: Midterm Evaluation of Light-Duty Vehicle Greenhouse Gas Emission Standards and Corporate Average Fuel Economy Standards for Model Years 2022-2025," U.S. Environmental Protection Agency, Washington, 2016.

[2] M. Ghanna, M. Niesluchowski and P. Culkeen, "Analysis of a Frontal Rail Structure in a Frontal Collision," in *SAE 2002 World Congress*, Detroit, Michigan, 2002.

[3] N.H.T.S.A., "Overview of NHTSA Priority Plan for Vehicle Safety and Fuel Economy, 2015 to 2017," N.H.T.S.A., Washington, 2015.

[4] K. Yamazaki and J. Han, "Maximization of the crushing energy absorption of tubes," *Structural Optimization,* vol. 16, pp. 37-46, 1998.

[5] K. Yamazaki and J. Han, "Maximization of the crushing energy absorption of cylindrical shells," *Advances in Engineering Software,* vol. 31, pp. 425-434, 2000.

[6] H. Zarei and M. Kroger, "Multiobjective crashworthiness optimization of circular aluminum tubes," *Thin-Walled Structures,* vol. 44, pp. 301-308, 2006.

[7] J. Marzbanrad and M. Ebrahimi, "Multi-Objective Optimization of aluminum hollow tubes for vehicle crash energy absorption using a genetic algorithm and neural networks," *Thin-Walled Structures,* vol. 49, pp. 1605-1615, 2011.

[8] J. Forsberg and L. Nilsson, "On Polynomial Response Surfaces and Kriging for Use in Structural Optimization of Crashworthiness," *Journal of Structural Multidisciplinary Optimization,* vol. 29, pp. 232-243, 2005.

[9] Y. Liu, "Optimum Design of Straight Thin-Walled Box Section Beams for Crashworthiness Analysis," *Finite Elements in Analysis and Design,* vol. 44, pp. 139-147, 2008.

[10] T. Jansson, L. Nilsson and M. Redhe, "Using surrogate models and response surfaces in structural optimization - with application to crashworthiness design and sheet metal forming," *Structural Mutlidisciplinary Optimization,* vol. 25, pp. 129-140, 2003.

[11] S. Esfahlani, H. Shirvani, A. Shirvani, S. Nwaubani, H. Mebrahtu and C. Chriwa, "Hexagonal honeycomb cell optimisation by way of meta-model techniques," *International Journal of Crashworthiness,* vol. 18, no. 3, pp. 264-275, 2013.

[12] W. Roux, N. Stander and R. Haftka, "Response surface approximations for structural optimization," *International Journal for Numerical Methods in Engineering,* vol. 42, pp. 517-534, 1998.

[13] K. Inal, "Numerical simulation of sheet metal forming processes and localized deformation phenomena for FCC Polycrystals," PhD Thesis, University of Sherbrooke, 2001.

[14] B. Williams, C. Simha, N. Aberdrabbo, R. Mayer and M. Worswick, "Effect of anisotropy, kinematic hardening, and strain-rate sensitivity on the predicted axial crush of hydroformed aluminum alloy tubes," *International Journal of Impact Engineering,* vol. 37, pp. 652-661, 2010.

[15] T. Giagmouris, S. Kyriakides, Y. Korkolis and L.-H. Lee, "On the localization and failure in aluminum shells due to crushing induced bending and tension," *International Journal of Solids and Structures,* vol. 47, pp. 2680-2692, 2010.

[16] C. Kohar, M. Mohammadi, R. Mishra and K. Inal, "The effects of Yield Surface Curvature and Anisotropy Constants on the Axial Crush Response of Circular Crush Tubes," *Thin-Walled Structures,* vol. 106, pp. 28-50, 2016.

[17] K. Inal, P. Wu and K. Neale, "Simulation of earing in textured aluminum sheets," *International Journal of Plasticity,* vol. 16, pp. 635-648, 2000.

[18] K. Inal, P. Wu and K. Neale, "Finite element analysis of localization in FCC polycrystalline sheets under plane stress tension," *International Journal of Solids and Structures,* vol. 39, pp. 3469-3486, 2002.

[19] R. Asaro and A. Needleman, "Texture Development and Strain Hardening in Rate Dependent Polycrystals," *Acta Mechanica,* pp. 923-953, 1985.

[20] J. Hutchinson and K. Neale, "Sheet Necking - II. Time-independent behaviour," in *Mechanics of Sheet Metal Forming*, New York, Plenum Press, 1978, pp. 127-153.

[21] J. Hutchinson and K. Neale, "Sheet Necking - III: Strain-Rate Effects," in *Mechanics of Sheet Metal Forming*, New York, Plenum Press, 1978, pp. 269-285.

[22] G. Taylor, "The Mechanism of Plastic Deformation of Crystals. Part I. Theoretical," *Proceedings of the Royal Soiety of London. Series A, Containing Papers of Matermatical and Physical Character,* pp. 362-387, 1934.

[23] P. Wu, K. Neale, E. van der Giessen, M. Jain, A. Makinde and S. MacEwen, "Simulation of the Behaviour of FCC Polycrystals During Reversed Torsion," *International Journal of Plasticity,* vol. 12, no. 9, pp. 1199-1219, 1996.

[24] J. Rossiter, A. Brahme, M. Simha, K. Inal and R. Mishra, "A new crystal plasticity scheme for explicit time integration codes to simulate deformation in 3D microstructures: Effects of strain path, strain rate and thermal softening on localized deformation in the aluminum alloy 5754 during simple shear," *International Journal of Plasticity,* vol. 26, pp. 1702-1725, 2010.

[25] A. Najafi, E. Marin and M. Rais-Rohani, "Concurrent multi-scale crush simulations with a crystal plasticity model," *Thin-Walled Structures,* vol. 53, pp. 176-187, 2012.

[26] J. Bassani and H. Pan, "A phenomenological model for microstructural evolution during plastic flow," *Comptes Rendus Macanique,* vol. 340, pp. 369-377, 2012.

[27] D. Pierce, R. J. Asaro and A. Needleman, "An Analysis of Nonuniform and Localized Deformation in Ductile Single Crystals," *Acta Metallurgia,* pp. 1087-1119, 1982.

[28] Y. Chang and R. Asaro, "An Experimental Study of Shear Localization in Aluminum-Copper Single Crystals," *Acta Metallurigica,* pp. 241-257, 1981.

[29] R. von Mises, "Mechanik der festen Korper im plastisch-deformablen Zustand," *Nachrichten von der Gesellschaft der Wissenschaften zu Göttingen, Mathematisch-Physikalische Klasse,* pp. 582-592, 1913.

[30] R. Hill, "A theory of the yielding and plastic flow of anisotropic metals," *Proceedings of the Royal Society London A,* vol. 193, pp. 281-297, 1948.

[31] W. Hosford, "A Generalized Isotropic Yield Criterion," *Journal of Applied Mechanics,* vol. 39, no. 2, pp. 607-609, 1972.

[32] R. Hill, "Theoretical plasticity of textured aggregates," *Mathematical Proceedings of the Cambridge Philosophical Society,* vol. 85, no. 1, pp. 197-191, 1979.

[33] F. Barlat and J. Lian, "Plastic behaviour and stretchability of sheet metals. Part I: A yield function for orthotropic sheets under plane stress conditions," *International Journal of Plasticity,* vol. 5, pp. 51-66, 1989.

[34] F. Barlat, J. Brem, J. Yoon, K. Chung, R. Dick, D. Lege, F. Pourboghrat, S.-H. Choi and E. Chu, "Plane stress yield function for aluminum alloy sheets - part 1: theory," *International Journal of Plasticity,* vol. 19, pp. 1297-1319, 2003.

[35] F. Barlat, H. Aretz, J. Yoon, M. Karabin, J. Brem and R. Dick, "Linear transformation-based anisotropic yield functions," *International Journal of Plasticity,* vol. 21, pp. 1009-1039, 2005.

[36] O. Cazacu, B. Plunkett and F. Barlat, "Orthotropic yield criterion for hexagonal closed packed metals," *International Journal of Plasticity,* vol. 22, pp. 11171-1194, 2006.

[37] J. Yoon, F. Barlat, R. Dick, K. Chung and T. Kang, "Plane stress function for aluminum alloy sheets-part II: FE formulation and its implementation," *Internation Journal of Plasticity,* vol. 22, pp. 495-522, 2004.

[38] J. Friis, B. Holmedal, Ø. Ryen, E. Nes, O. Myhr, Ø. Grong, T. Furu and K. Marthinsen, "Work hardening behaviour of heat-treatable Al-Mg-Si-alloys," *Materials Science Forum,* vol. 519, pp. 1901-1906, 2006.

[39] B. Plunkett, O. Cazacu and F. Barlat, "Orthotropic yield criteria for description of the anisotropy in tension and compression of sheet metals," *International Journal of Plasticity,* vol. 24, pp. 847-866, 2008.

[40] A. Brahme, K. Inal, R. Mishra and S. Saimoto, "A new strain hardening model for rate-dependent crystal plasticity," *Computational Materials Science,* vol. 50, pp. 2898-2908, 2011.

[41] W. Muhammad, A. Brahme, J. Kang, R. Mishra and K. Inal, "Large Strain Cyclic Simple Shear Behavior of Aluminum Extrusions: An Experimental and Numerical Study," *Light Metals 2016,* pp. 169-174, 2016.

[42] W. Muhammad, A. Brahme, J. Kang, R. Mishra and I. K., "Experimental and numerical investigation of texture evolution and the effects of intragranular backstresses in aluminum alloys subjected to large strain cyclic simple shear," *Submitted to International Journal of Plasticity,* 2016.

[43] C. Bronkhorst, S. Kalidindi and L. Anand, "Polycrystalline Plasticity and the Evolution of Crystallographic Texture in FCC Metals," *Proceedings of the Royal Society A: Mathematical, Physical and Engineering Sciences,* pp. 443-477, 1992.

[44] S. R. Kalidindi, C. A. Bronkhorst and L. Anand, "Crystallographic Texture Evolution in Bulk Deformation Processing of FCC Metals," *Journal of the Mechanics and Physics of Solids,* pp. 537-569, 1992.

[45] J. Bassani and T. Wu, "Latent Hardening in Single Crystals II. Analytical Characterization and Predictions," *Proceedings of the Royal Society A; Materical, Physical & Engineering Sciences,* pp. 21-41, 1991.

[46] D. Ghaffari Tari, M. Worswick, U. Ali and M. Gharghoui, "Mechanical response of AZ31B magnesium alloy: Experimental characterization and material modeling considering proportional loading at room temperature," *International Journal of Plasticity,* pp. 247-267, 2014.

[47] R. Hill, "A general theory of uniqueness and stability in elastic-plastic solids," *Journal of Mechanics and Physics of Solids,* vol. 6, pp. 236-249, 1958.

[48] R. Hill, "Some basic principles in the mechanics without a natural time," *Journal of Mechanics and Physics of Solids,* vol. 7, pp. 209-225, 1959.

[49] J. Hallquist, LS-DYNA Theory Manual, Livermore, California: Livermore Software Technology Corporation, 2006.

[50] E. Voce, "A practical strain-hardening function," *Metallurgia,* vol. 51, no. 307, pp. 219-226, 1955.

[51] G. Johnson and H. Cook, "A constitutive model and data for metals subjected to large strains, high strain rates and high temperatures," *Proceedings of the 7th International Symposium on Ballistics,* vol. 21, pp. 541-547, 1983.

[52] G. Cowper and P. Symonds, "Strain Hardening and Strain-Rate Effects in the Impact Loading of Centilevered Beams," Brown University Division of Applied Mathematics, Providence, Rhode Island, USA, 1957.

[53] W. Hosford, "On the crystallographic basis of yield criteria," *Textures and Microstructures,* Vols. 26-27, pp. 479-493, 1996.

[54] F. Barlat and O. Richmond, "Prediction of Tricomponent Plane Stress Yield Surfaces and Associated Flow and Failure Behavior of Strongly Textured F.C.C. Polycrystalline Sheets," *Material Science and Engineering,* vol. 95, pp. 15-29, 1987.

[55] R. Rockafellar, "Convex Analysis," in *Princeton Mathematical Series*, Princeton University Press 46, 1970.

[56] F. Barlat, D. Lege and J. Brem, "A six-component yield function for anisotropic materials," *International Journal of Plasticity,* vol. 7, pp. 693-712, 1991.

[57] K. Chung and O. Richmond, "A deformation theory of plasticity based on minimum work paths," *International Journal of Plasticity,* no. 16, pp. 1215-1241, 1993.

[58] N. Abedrabbo, F. Pourboghrat and J. Carsley, "Forming of aluminum alloys at elevated temperatures - Part 2: Numerical modeling and experimental verification," *International Journal of Plasticity,* vol. 22, pp. 342-373, 2006.

[59] J. Mandel, "Equations constitutive et directeurs dans les milieux plastiques et viscoplastiques," *International Journal of Solids and Structures,* vol. 9, pp. 725-740, 1973.

[60] E. Nesterova, B. Bacroix and C. Teodosiu, "Microstructural and Texture Evolution under Strain-Path Changes in Low-Carbon Interstitiial-Free Steel," *Metallurgical and Materials Transactions A,* vol. 32A, pp. 2527-2538, 2001.

[61] A. Alghamdi, "Collapsible impact energy absorbers: an overview.," *Thin-Walled Structures,* pp. 189-213, 2001.

[62] A. Olabi, E. Morris and M. Hashmi, "Metallic tube type energy absorbers: A synopsis," *Thin-Walled Structures,* vol. 45, pp. 706-726, 2007.

[63] S. Yuen and G. Nurick, "The energy-absorbing characteristics of tubular structure with geometric and material modifications: an overview," *Applied Mechanics Review,* vol. 61, pp. 020802-1-15, 2008.

[64] A. Hanssen, M. Langseth and O. Hopperstad, "Static and Dynamic Crushing of Circular Aluminum Extrusions with Aluminum Foam Filler," *International Journal of Impact Engineering,* vol. 24, pp. 475-507, 2000.

[65] A. Hanssen, M. Langseth and O. Hopperstad, "Static and Dynamic Crushing of Square Aluminum Extrusions with Aluminum Foam Filler," *International Journal of Impact Engineering,* vol. 24, pp. 347-383, 2000.

[66] H.-S. Kim, "New extruded multi-cell aluminum profile for maximum crash energy absorption and weight efficiency," *Thin-Walled Structures,* vol. 40, pp. 311-327, 2002.

[67] D. Marzougui, C. Kan and N. Bedewi, "Development and Validation of an NCAP Simulation Using LS-DYNA3D," FHWA/NHTSA National Crash Analysis Center, Ashburn, Virginia, USA, 1996.

[68] J. Alexander, "An Approximate Analysis of the Collapse of Thin Cylindrical Shells Under Axial Loading," *The Quarterly Journal of Mechanics and Applied Mathematics,* pp. 10-15, 1960.

[69] T. Wierzbicki, "Crushing Analysis of Metal Honeycombs," *International Journal of Impact Engineering,* vol. 1, no. 2, pp. 157-174, 1983.

[70] T. Wierzbicki and W. Abramowicz, "On the Crushing Mechanics of ThinWalled Structures," *Journal of Applied Mechanics,* vol. 50, no. December, pp. 727-734, 1983.

[71] W. Abramowicz, "The Effective Crushing Distance in Axially Compressed Thin-Walled Metal Columns," *International Journal of Impact Engineering,* vol. 1, no. 3, pp. 309-317, 1983.

[72] W. Abramowicz and N. Jones, "Dynamic Axial Crushing of Square Tubes," *International Journal of Impact Engineering,* vol. 2, no. 2, pp. 79-208, 1984.

[73] F. Bardi, H. Yun and S. Kyriakides, "On the axisymmetric progressive crushing of circular tubes under axial compression," *International Journal of Solids and Structures,* no. 40, p. 3137–3155, 2003.

[74] A. Najafi and R. Masoud, "Mechanics of Axial Plastic Collapse in Multi-Cell, Multi-Corner Crush Tubes," *Thin-Walled Structures,* pp. 1-12, 2011.

[75] B. Williams, M. Worswick, G. D'Amours, A. Rahem and R. Mayer, "Influence of Forming Effects on the Axial Crush Response of Hydroformed Aluminum Alloy Tubes," *International Journal of Impact Engineering,* vol. 37, pp. 1008-1020, 2010.

[76] M. Langseth and O. Hopperstad, "Static and Dynamic Axial Crushing of Square Thin-Walled Aluminum Extrusions," *International Journal of Impact Engineering,* vol. 18, no. 7-8, pp. 949-968, 1996.

[77] M. Langseth, O. Hopperstad and T. Berstad, "Crashworthiness of Aluminum Extrsions: Validation of Numerical Simulation, Effect of Mass Ratio and Impact Velocity," *International Journal of Impact Engineering,* vol. 22, pp. 829-854, 1999.

[78] N. Abedrabbo, M. Mayer, A. Thompson, C. Salisbury, M. Worswick and I. van Riemsdijk, "Crash response of advanced high-strength steel tubes: Experiment and model," *International Journal of Impact Engineering,* vol. 36, pp. 1044-1057, 2009.

[79] O. Fyllinger, O. Hopperstad, A. Hanssen and M. Langseth, "Brick versus shell elements in simulations of aluminum extrusions subjected to axial crushing," in *7th European LS-DYNA Conference*, Salzburg, Austria, 2009.

[80] T. Belytschko, W. Liu, B. Moran and K. Elkhodary, Nonlinear Finite Elements for Continua and Structures, John Wiley & Sons, 2013.

[81] N. Stander, W. Roux, M. Giger, M. Redhe, N. Fedorova and J. Haarhoff, "Crashworthiness Optimization in LS-OPT: Case Studies in Metamodeling and Random Search Techniques," *4th European LS-DYNA Users Conferece,* pp. J-I-11-26, 2003.

[82] M. Avalle, G. Chiandussi and G. Belingardi, "Design optimization by response surface methodology: application to crashworthiness design of vehicle structures," *Structural and Mutlidisciplinary Optimization,* vol. 24, pp. 325-332, 2002.

[83] N. Stander, W. Roux, T. Goel, T. Eggleston and K. Craig, LS-OPT User's Manual - A Design Optimization and Probabilistic Analysis Tool for the Engineering Analyst, Livermore, California, USA: Livermore Software Technology Corporation, 2012.

[84] MathWorks, Statistics Toolbox User's Guide - R2014b: For Use with MATLAB, MathWorks, 2014.

[85] S. Rao, Applied Numerical Methods for Engineers and Scientists, London: Pearson Education Ltd., 2002.

[86] M. Papadrakakis, N. Lagaros and Y. Tsompanakis, "Strucutral optimization using evolution strategies and neural networks," *Computer Methods in Applied Mechanics and Engineering,* vol. 156, pp. 309-333, 1998.

[87] D. Goldberg, Genetic algorithms in search, optimization and machine learning, Reading, MA, USA: Addison-Wesley, 1989.

[88] S. Kirkpatrick, C. Gelatt and M. Vecchi, "Optimization by Simulated Annealing," *Science,* vol. 220, no. 4598, pp. 671-680, 1983.

[89] N. Stander and K. Craig, "On the robustness of a simple domain reduction scheme for simulation-based optimization," *Engineering Computations,* vol. 19, no. 4, pp. 431-450, 2002.

[90] A. Bjorck, Numerical Methods for Least Squares Problems, Linkoping, Sweden: Society for Industrial and Applied Mathematics, 1996.

[91] K. Hornik, M. Stinchombe and W. Halbert, "Universal Appoximation of an Unknown Mapping and Its Derivatives Using Multilayer Feedforward Networks," *Neural Networks,* vol. 3, pp. 551-560, 1990.

[92] S. Haylin, Neural Networks: A Comprehensive Foundation - 2nd Edition, London: Prentice-Hall Inc., 1999.

[93] I. Aleksander and M. Helen, An introduction to neural computing: 2nd edition, London: International Thomson Computer Press, 1995.

[94] D. Rumelhart, G. Hinton and R. Williams, "Learning representations of back-propagation errors," *Nature,* vol. 323, pp. 533-536, 1986.

[95] J. Snyman, "A new and dynamic method for unconstrained minimization," *Applied Mathematical Modeling,* pp. 449-460, 1982.

[96] J. Holland, Adaptation in Natural and Artificial Systems, Ann Arbor, MI: University of Michigan, 1975.

[97] C. Reeves and J. Rowe, Genetic Algorithms - Principles and Perspectives: A Guide to GA Theory, Boston: Kluwer Academic Publishers, 2003.

[98] P. Schuur, "Classification of Acceptance Criteria for the the Simulated Annealing Algorithm," *Mathematics of Operations Research,* vol. 22, no. 2, pp. 266-275, 1997.

[99] L. Ingber, "Adaptive simulated annealing (ASA): Lessons learned.," *arXiv preprint cs/0001018,* 2000.

[100] H. Szu and R. Hartley, "Fast simulated annealing," *Physics Letters A,* vol. 122, no. 3-4, pp. 157-162, 1987.

[101] P. Van Laarhoven and E. Aarts, Simulated Annealing: Theory and Applications. Springer, Springer, 1987, pp. 7-15.

[102] C. Kohar, M. Mohammadi, R. Mishra and K. Inal, "Effects of elastic-plastic behaviour on the axial crush response of square tubes," *Thin-Walled Structures,* vol. 93, pp. 64-87, 2015.

[103] C. Kohar, A. Zhumagulov, A. Brahme, M. Worswick, R. Mishra and K. Inal, "Development of High Crush Efficient, Extrudable Aluminum Front Rails for Vehicle Lightweighting," *International Journal of Impact Engineering,* no. 95, pp. 17-34, 2016.

[104] C. Kohar, A. Brahme, R. Mishra and K. Inal, "Effects of Coupling Anisotropic Yield Functions with the Optimization Process of Extruded Aluminum Front Rail Geometries in Crashworthiness," *Submitted to International Journal of Solids and Structures,* 2017.

[105] C. Kohar, M. Cherkaoui, H. El Kadiri and K. Inal, "Numerical Modeling of TRIP Steel in Axial Crashworthiness," *International Journal of Plasticity,* pp. 1-31, 2016.

[106] A. Zhumagulov, J. Imbert, C. Kohar, K. Inal, M. Worswick and R. Mishra, "Energy absorption characterization of multicellular AA6063-T6 extrusions," in *1st International Conference on Impact Loading of Structures and Materials*, Turin, Italy, 2016.

[107] T. Sheppard and A. Jackson, "Constitutive equations for use in prediction of flow stress during extrusion of aluminium alloys," *Materials Science and Technology,* vol. 13, no. 3, pp. 203-209, 1997.

[108] A. Pandey, A. Khan, E. Kim, S. Choi and T. Gnäupel-Herold, "Experimental and numerical investigations of yield surface, texture, and deformation mechanisms in AA5754 over low to high temperatures and strain rates," *International Journal of Plasticity,* vol. 41, pp. 165-188, 2013.

[109] Y.-L. Bai and T. Wierzbicki, "A new model of metal plasticity and fracture with pressure and Lode dependence," *International Journal of Plasticity,* vol. 24, pp. 1071-1096, 2008.

[110] Y.-L. Bai and T. Wierzbicki, "Application of extended Mohr-Coulomb criterion to ductile fracture," *International Journal of Fracture,* no. 161, pp. 1-20, 2010.

[111] J. Papasidero, V. Doquet and D. Mohr, "Ductile fracture of aluminum 2024-T351 under proportional and non-proportional multi-axial loading: Bao–Wierzbicki results revisited," *International Journal of Solids and Structures,* Vols. 69-70, pp. 459-474, 2015.

[112] M. Scales, N. Tardif and S. Kyriakides, "Ductile failure of aluminum alloy tubes under combined torsion and tension," *International Journal of Solids and Structures,* Vols. 97-87, pp. 116-128, 2016.

[113] G. Nagel and D. Thambiratnam, "A numerical study on the impact response and energy absorption of tapered thin-walled tubes," *International Journal of Mechanical Science,* pp. 201-216, 2004.

[114] G. Nagel and D. Thambiratnam, "Computer simulation and energy absorption of tapered thin-walled rectangular tubes," *Thin-Walled Structures,* pp. 1225-1242, 2005.

[115] G. Nagel and D. Thambiratnam, "Dynamic simulation and energy absorption of tapered tubes under impact loading," *International Journal of Crashworthiness,* pp. 389-99, 2004.

[116] N. Jones, "Energy-absorbing effectiveness factor," *International Journal of Impact Engineering,* vol. 37, pp. 754-765, 2010.

[117] W. Abramowicz, "The Macro Element Approach in Crash Calculations, in: Ambrosio, J.C.C, Pereira, M.F.O.S, da Silva, F.P.;," in *Crashworthiness of Transportation Systems: Structural Impact and Occupant Protection*, vol. 332, Dordrecht, Kluwer Academic Publishers, 1997, pp. 291-320.

[118] R. Smerd, S. Winkler, C. Salisbury, M. Worswick, D. Lloyd and M. Finn, "High Strain Rate Tensile Testing of Automotive Alloy Sheet," *International Journal of Impact Engineering,* vol. 32, pp. 541-560, 2005.

[119] A. Niechajowicz and A. Tobota, "Dynamic tension testing of DP600, DP800 steel and Al 6061 T4 alloy sheets by means of rotary hammer," *Archives of Metallurgy and Materials,* vol. 54, no. 3, pp. 647-657, 2009.

[120] S. Hsu and N. Jones, "Quasi-static and Dynamic Axial Crushing of Thin-Walled Circular Stainless Steel, Mild Steel and Aluminum Alloy Tubes," *International Journal of Crashworthiness,* vol. 9, no. 2, pp. 195-217, 2004.

[121] W. Abramowicz and N. Jones, "Dynamic Progressive Buckling of Circular and Square Tubes," *International Journal of Impact Engineering,* vol. 4, no. 4, pp. 243-270, 1986.

[122] Y. Liu, "Crashworthiness Design of Multi-Corner Thin-Walled Columns," *Thin-Walled Structures,* vol. 46, pp. 1329-1337, 2008.

[123] D. Achani, O. Hopperstad and O.-G. Lademo, "Behaviour of extruded aluminum alloys under proportional and non-proportional strain paths," *Journal of Materials Processing Technology,* vol. 209, pp. 4750-4764, 2009.

[124] R. Myers, D. Montgomery and C. Anderson-Cook, Response Surface methodology; Process and Product Optimization Using Designed Experiments, Hoboken, New Jersey: John Wiley & Sons, 2009.

[125] D. Bates and D. Watts, Nonlinear Regression Analysis and Its Application, New York: John Wiley & Sons, 1988.

[126] J. Fox, Nonlinear Regression and Nonlinear Least Squares: Appendix to an R and S-PLUS Companion to Applied Regression., Thousand Oaks, California: Sage Publication Inc., 2002.

[127] B. Williams, A Study of the Axial Crush Response of Hydroformed Aluminum Alloy Tubes, Waterloo: Ph.D. Thesis , 2007.

[128] T. Iwamoto, T. Sawa and M. Cherkaoui, "A study on impact deformation and transformation behaviour of TRIP steel by finite element simulation and experiment," *International Journal of Modern Physics B,* vol. 22, pp. 5985-5990, 2008.

[129] M. Shiekhelsouk, V. Favier, K. Inal and M. Cherkaoui, "Modelling the behaviour of polycrystalline austenitic steel with twinning-induced plasticity effect," *International Journal of Plasticity,* pp. 105-133, 2009.

[130] J. Simo and T. Hughes, Computational Inelasticity, New York : Springer-Verlag, 1998.

[131] L. Aktay, A. Johnson and B.-H. Kroplin, "Numerical modelling of honeycomb core crush behaviour," *Engineering Fracture Mechanics,* vol. 75, pp. 2616-2630, 2008.

[132] V. Tarigopula, M. Langseth, O. Hopperstad and A. Clausen, "Axial Crushing of Thin-Walled High-Strength Steel Sections," *International Journal of Impact Engineering,* vol. 32, pp. 847-882, 2006.

[133] P. Dassappa, K. Inal and R. Mishra, "The effects of anisotropic yield functions and their material parameters on prediction of forming limit diagrams," *International Journal of Solids and Structures,* vol. 49, pp. 3528-3550, 2012.

[134] N. Abedrabbo, F. Pourboghrat and C. Carsley, "Forming of AA5182-O and AA5754-O at elevated temperatures using coupled thermo-mechanical finite element models," *International Journal of Plasticity,* vol. 23, pp. 841-875, 2007.

[135] M. Lee, D. Kim, C. Kim, M. Wenner, R. Wagoner and K. Chung, "Spring-back evaluation of automotive sheets based on isotropic-kinematic hardening laws and non-quadratic anisotropic yield functions Part II: characterization of material properties," *International Journal of Plasticity,* vol. 21, pp. 883-914, 2005.

[136] C. Salisbury, M. Worswick and R. Mayer, "High rate constitutive modeling of aluminium alloy tube," *Journal de Physique IV (Proceedings),* vol. 134, pp. 43-48, 2006.

[137] E. Avallone, T. Baumeister and A. Sadegh, Mark's Standard Handbook for Mechanical Engineers, New York: McGraw-Hill, 2007.

[138] N. Norton, Design of machinery: an introduction to the synthesis and analysis of mechanisms and machines, New York: McGraw-Hill, 2004.

[139] W. Abramowicz and N. Jones, "Dynamic Axial Crushing of Circular Tubes," *International Journal of Impact Engineering,* vol. 2, no. 3, pp. 263-281, 1984.

[140] S. Yang and C. Qi, "Multiobjective optimization for empty and foam-filled square columns under oblique impact loading," *International Journal of Impact Engineering,* vol. 54, pp. 177-191, 2013.

[141] A. Bardelcik, M. Worswick and M. Wells, "The influence of martensite, bainite and ferrite on the as-quenched constitutitve response of simultaneously quenched and deformed boron

steel - Experiments and model," *Materials and Design,* vol. 55, pp. 509-525, 2014.

[142] M. Jansson, L. Nilsson and K. Simonsson, "On strain localisation in tube hydroforming of aluminium extrusions," *Journal of Materials Processing Technology,* vol. 195, pp. 3-14, 2008.

[143] V. Cerny, "Thermodynamical Approach to the Traveling Salesman Problem: An Efficient Simulation Algorithm," *Journal of Optimization Theory and Applications,* vol. 45, no. 1, pp. 41-51, 1985.

[144] M. Pincus, "A Monte Carlo Method for the Approximate Solution of Certian Types of Constrained Optimization Problems," *Operations Research,* vol. 18, pp. 1225-1228, 1970.

[145] M. Gasperini, C. Pinna and W. Swiatnicki, "Microstructure evolution and strain localization during shear deformation of an aluminium alloy," vol. 44, no. 10, pp. 4195-4208, 1996.

[146] J. J. Gracio, F. Barlat, E. F. Rauch, P. T. Jones, V. F. Neto and A. B. Lopes, "Artificial aging and shear deformation behaviour of 6022 aluminium alloy," *International Journal of Plasticity,* vol. 20, no. 3, pp. 427-445, 2004.

[147] D. Achani, O. Lademo, O. Engler and O. Hopperstad, "Evaluation of constitutive models for textured aluminium alloys using plane-strain tension and shear tests," *International Journal of Material Forming,* no. 4, pp. 227-241, 2011.

[148] Y. Bao and T. Wierzbicki, "On fracture locus in the equivalent strain and stress triaxiality space," *International Journal of Mechanical Sciences,* vol. 46, pp. 81-91, 2004.

[149] J. Qiao, J. Chen and H. Che, "Crashworthiness assessment of square aluminum extrusions considering the damage evolution," *Thin-Walled Structures,* vol. 44, pp. 692-700, 2006.

[150] N. Tardif and S. Kyriakides, "Determination of anistropy and material hardening for aluminum sheet metal," *International Journal of Solids and Structures,* vol. 49, pp. 3496-3506, 2012.

[151] S. Haltom, S. Kyriakides and K. Ravi-Chandar, "Ductile failure under combined shear and tension," *International Journal of Solids and Structures,* vol. 50, pp. 1507-1522, 2013.

[152] K. Kim and J. Yin, "Evolution of anisotropy under plane stress," *Journal of Mechanics and Physics of Solids,* vol. 45, no. 5, pp. 841-851, 1997.

[153] K. Inal, R. Mishra and O. Cazacu, "Forming simulation of aluminum sheets using an anisotropic yield function coupled with crystal plasticity theory," *International Journal of Solids and Structures,* vol. 47, p. 2223–2233, 2010.

[154] H. Bunge and I. Nielsen, "Experimental determination of plastic spin in polycrystalline materials," *International Journal of Plasticity,* vol. 13, no. 5, pp. 435-446, 1997.

[155] A. Brahme, M. Alvi, D. Saylor, J. Fridy and A. Rollett, "3D reconstruction of microstructure in a commercial purity aluminum," *Scripta Materialia,* vol. 55, pp. 75-80, 2006.

[156] A. Eringen, Mechanics of Continua, vol. Appendix B, Robert E. Krieger Publishing Company, 1980, p. 530–536.

[157] G. Losilla, J. Boehler and Q. Zheng, "A generally anisotropic hardening model for big offset-strain yield stresses," *Acta Mechanica,* vol. 144, pp. 169-183, 2000.

[158] F. Bachmann and R. Hielscher, "Texture analysis with MTEX-free and open source software toolbox.," *Solid State Phenomena,* vol. 160, pp. 63-68, 2010.

[159] E. van der Giessen and K. Neale, "Analysis of the inverse Swift effect using a rate-sensitive polycrystal model," *Computer Methods in Applied Mechanics and Engineering,* vol. 103 , pp. 291-313, 1993.

[160] P. Tugcu, P. Wu and K. Neale, "Finite strain analysis of simple shear using recent anisotropic yield criteria," *International Journal of Plasticity,* vol. 15, pp. 939-962, 1999.

[161] P. Tugcu, P. Wu and K. Neale, "On the predictive capabilities of anisotropic yield criteria for metals undergoing shearing deformations," *International Journal of Plasticity,* vol. 18, p. 1219–1236, 2002.

[162] M. Iadicola, T. Foecke and S. Banovic, "Experimental observations of evolving yield loci in biaxially strained AA5754-O," *International Journal of Plasticity,* vol. 24, pp. 2084-2101, 2008.

[163] F. Neukamm, M. Feucht and A. Haufe, "Consistent Damage Modelling in the Process Chain of Forming to Crashworthiness Simulations," *LS-DYNA Anwenderforum 30,* pp. H-I-1-20, 2008.

[164] M. Basaran, S. Wolkerling, M. Feucht, F. Neukamm and D. Weichert, "An Extension of the GISSMO Damage Model Based on Lode Angle Dependence," *Dynamore, Bamberg,* 2010.

[165] D. E. Malen, Fundamentals of automobile body structure design, Warrendale, Pennsylvania: SAE International, 2011.

[166] A. Reyes, M. Langseth and O. Hopperstad, "Crashworthiness of aluminum extrusions subjected to oblique loading: experiments and numerical analyses," *International Journal of Mechanical Sciences,* vol. 44, p. 1965 – 1984, 2002.

[167] A. Reyes, M. Langseth and O. Hopperstad, "Square aluminum tubes subjected to oblique loading," *International Journal of Impact Engineering,* vol. 28, p. 1077–1106, 2003.

[168] P. Krajewski, A. Luo, S. Hartfield-Wünsch and P. McNamara, "Crush zone and method for introducing crush zone into vehicle structure". U.S. Patent 6,994,350, 7 Feb 2006.

[169] K. Omer, L. ten Kortenaar, C. Butcher, M. Worswick, S. Malcolm and D. Detwiler, "Testing of a hot stamped axial crush member with tailored properties – Experiments and models," *International Journal of Impact Engineering,* vol. 103, pp. 12-28, 2017.

[170] O. Hopperstad, M. Langseth and S. Remseth, "Cyclic Stress-Strain Behaviour of Alloy AA6060 T4, Part II: Biaxial Experiments and Modeling," *International Journal of Plasticity,* vol. 11, no. 6, pp. 741-762, 1995.

[171] F. Yoshida and T. Uemori, "A Model of Large-Strain Cyclic Plasticity and its Application to Springback Simulation," *International Journal of Mechanical Sciences,* vol. 45, pp. 1687-1702, 2003.

APPENDIX

A.1 - Numerical Simulation Parameter Test Matrix for Optimal Material Selection

Simulation Parameters					Measured Responses				
Test #	σ_0 [MPa]	U_0	D	ε_f	F_{max} [kN]	F_{ss} [kN]	η_{ss}	d [mm]	E_{abs} [kJ]
1	100.0	1.000	5.500	2.000	108.00	36.57	0.431	216.71	8.37
2	300.0	1.100	11.000	1.801	280.00	102.61	0.411	203.21	21.46
3	225.0	1.400	5.000	3.000	208.00	93.00	0.442	205.60	19.23
4	50.0	0.860	5.000	3.000	71.70	24.58	0.548	219.56	5.59
5	300.0	1.400	14.000	1.001	273.00	74.74	0.335	207.75	16.90
6	275.0	1.400	15.000	1.201	252.00	75.29	0.353	207.55	17.02
7	100.0	0.800	15.000	3.000	129.00	57.78	0.524	212.52	12.88
8	50.0	1.400	9.000	2.200	71.60	23.10	0.523	219.79	5.30
9	275.0	0.800	14.000	3.000	297.00	151.74	0.536	196.05	27.90
10	50.0	1.160	11.000	2.800	72.70	28.14	0.551	218.71	6.45
11	225.0	1.400	5.000	1.001	184.00	58.68	0.338	211.34	13.58
12	300.0	1.340	5.000	2.200	277.00	102.43	0.411	203.40	21.28
13	150.0	1.400	5.000	1.001	145.00	39.45	0.347	215.47	9.40
14	50.0	0.860	15.000	2.600	73.30	29.62	0.528	218.57	6.63
15	50.0	1.040	5.000	1.001	70.70	18.36	0.438	221.11	3.99
16	50.0	1.400	15.000	1.001	70.70	15.58	0.405	221.25	3.70
17	50.0	1.100	5.000	1.201	70.80	16.98	0.427	221.09	3.92
18	275.0	1.100	9.000	2.800	268.00	126.37	0.483	199.86	24.39
19	50.0	1.400	7.000	2.800	71.90	26.08	0.568	219.29	5.87
20	300.0	0.800	10.000	3.000	301.00	145.44	0.512	196.07	27.71
21	300.0	0.980	5.000	1.001	273.00	80.36	0.349	207.09	17.57
22	300.0	0.980	15.000	2.400	298.00	135.12	0.482	197.90	26.13
23	175.0	0.800	5.000	1.001	161.00	55.97	0.347	214.74	10.97
24	300.0	1.400	14.000	3.000	308.00	157.08	0.539	194.36	29.30
25	50.0	0.800	5.000	1.801	71.10	20.07	0.492	220.36	4.65
26	75.0	1.400	5.000	3.000	88.70	35.68	0.519	217.29	7.92
27	300.0	1.400	11.000	1.601	277.00	96.71	0.393	204.13	20.39
28	175.0	1.400	15.000	3.000	203.00	101.64	0.531	204.76	20.02
29	50.0	0.860	15.000	1.001	70.70	16.76	0.411	221.29	3.75
30	175.0	1.040	6.000	3.000	163.00	77.91	0.464	208.53	16.44
31	175.0	0.800	8.000	1.001	161.00	56.03	0.347	214.79	10.96
32	50.0	1.100	13.000	1.001	70.70	16.30	0.432	221.11	3.94
33	200.0	1.280	5.000	2.200	180.00	70.66	0.399	209.59	15.29
34	50.0	0.800	5.000	2.200	71.30	21.68	0.499	220.26	4.87
35	50.0	1.400	15.000	2.200	72.10	24.69	0.539	219.33	5.76
36	250.0	0.800	5.000	3.000	233.00	98.70	0.447	203.65	21.00
37	50.0	1.400	5.000	3.000	71.60	25.22	0.557	219.50	5.66
38	300.0	0.800	15.000	2.000	288.00	108.00	0.430	201.46	23.05

39	300.0	1.400	5.000	2.800	281.00	111.89	0.446	201.20	23.22
40	50.0	1.400	9.000	1.601	71.10	19.46	0.471	220.53	4.49
41	300.0	0.980	10.000	1.001	273.00	81.22	0.349	207.13	17.58
42	225.0	0.800	15.000	2.000	213.00	86.61	0.423	206.24	18.82
43	225.0	1.040	15.000	1.001	184.00	56.68	0.383	209.77	15.25
44	250.0	0.800	12.000	1.001	217.00	85.84	0.349	210.74	15.41
45	75.0	1.400	7.000	1.401	85.20	25.74	0.421	219.18	5.87
46	75.0	0.800	15.000	1.401	86.60	29.52	0.439	218.94	6.32
47	300.0	1.040	9.000	1.001	273.00	80.21	0.364	205.96	18.22
48	300.0	1.400	5.000	1.001	273.00	74.77	0.335	207.75	16.90
49	175.0	1.280	15.000	3.000	205.00	102.19	0.531	204.68	20.08
50	200.0	1.400	15.000	3.000	228.00	114.11	0.534	202.34	22.24
51	50.0	1.400	15.000	3.000	73.60	31.69	0.544	218.02	7.18
52	300.0	0.980	5.000	2.800	281.00	111.80	0.447	201.09	23.28
53	300.0	0.860	5.000	3.000	283.00	115.12	0.458	200.34	23.93
54	275.0	1.400	5.000	3.000	258.00	109.41	0.452	202.13	22.44
55	200.0	1.400	15.000	1.601	181.00	66.40	0.385	209.88	14.86
56	300.0	0.800	5.000	1.801	276.00	91.71	0.383	204.90	19.74
57	200.0	1.100	8.000	2.200	183.00	76.89	0.420	208.48	16.48
58	300.0	0.800	14.000	2.000	287.00	108.14	0.430	201.64	22.94
59	175.0	0.800	10.000	3.000	187.00	88.40	0.500	206.26	18.53
60	75.0	1.340	5.000	1.001	83.50	22.44	0.384	219.75	5.25
61	50.0	1.400	14.000	3.000	73.50	31.33	0.549	218.11	7.09
62	225.0	0.860	5.000	1.201	193.00	67.50	0.357	210.66	14.50
63	50.0	0.920	5.000	1.001	70.70	17.07	0.418	221.21	3.81
64	300.0	1.400	7.000	1.001	273.00	74.82	0.335	207.75	16.91
65	150.0	0.800	15.000	3.000	187.00	80.64	0.526	207.04	17.95
66	300.0	1.400	15.000	2.400	293.00	134.58	0.481	198.26	25.85
67	300.0	1.400	8.000	2.800	288.00	131.15	0.478	198.93	25.29
68	50.0	0.800	15.000	1.201	70.90	19.03	0.431	221.17	4.00
69	50.0	0.800	7.000	1.001	70.70	16.21	0.408	221.28	3.72
70	300.0	0.800	5.000	3.000	283.00	112.72	0.457	200.26	23.86
71	275.0	1.400	10.000	3.000	274.00	133.61	0.508	198.20	25.82
72	50.0	1.400	12.000	1.001	70.70	15.58	0.405	221.25	3.70
73	175.0	1.220	15.000	1.001	161.00	48.00	0.350	213.98	11.03
74	50.0	0.860	5.000	1.001	70.70	16.34	0.409	221.28	3.74
75	300.0	0.800	15.000	1.001	273.00	87.29	0.333	208.91	16.87
76	50.0	0.920	15.000	3.000	74.20	32.30	0.528	217.89	7.34
77	300.0	1.340	15.000	1.001	273.00	75.33	0.340	207.45	17.11
78	50.0	1.160	13.000	1.001	70.70	15.36	0.406	221.26	3.71
79	50.0	1.100	13.000	3.000	73.50	30.32	0.541	218.16	7.03
80	300.0	0.800	15.000	3.000	319.00	163.94	0.544	193.66	29.92
81	50.0	1.400	5.000	2.800	71.50	24.13	0.540	219.70	5.44
82	300.0	1.400	15.000	3.000	311.00	159.75	0.545	193.98	29.64
83	300.0	0.920	5.000	1.001	273.00	86.03	0.353	207.52	17.78

84	50.0	1.400	15.000	1.401	71.10	18.22	0.452	220.67	4.30
85	50.0	0.860	15.000	2.200	72.50	26.61	0.533	219.26	5.92
86	50.0	0.980	5.000	2.800	71.60	24.11	0.538	219.71	5.43
87	50.0	0.800	9.000	2.800	72.50	27.02	0.557	219.01	6.23
88	300.0	0.800	6.000	1.001	273.00	88.93	0.335	208.89	17.02
89	300.0	0.800	5.000	1.001	273.00	87.36	0.332	208.92	16.85
90	300.0	1.400	6.000	2.200	279.00	105.03	0.419	202.90	21.77
91	50.0	1.400	5.000	2.600	71.40	23.00	0.524	219.89	5.21
92	50.0	1.160	5.000	1.001	70.70	15.42	0.406	221.26	3.71
93	300.0	0.860	15.000	1.001	273.00	86.07	0.338	208.50	17.14
94	225.0	0.800	5.000	1.601	201.00	69.28	0.367	209.81	15.29
95	300.0	1.040	15.000	3.000	315.00	161.69	0.549	193.49	30.00
96	50.0	1.220	15.000	1.001	70.70	15.82	0.409	221.25	3.74
97	150.0	0.800	11.000	1.001	145.00	49.32	0.355	216.09	9.66
98	75.0	0.800	7.000	3.000	90.50	37.87	0.543	216.69	8.60
99	50.0	0.800	12.000	1.001	70.70	15.07	0.405	221.24	3.70
100	50.0	1.100	15.000	3.000	74.00	30.99	0.530	217.94	7.25
101	175.4	1.307	14.992	3.000	205.00	102.27	0.532	204.66	20.11
102	191.6	0.811	11.621	1.010	169.00	60.28	0.346	213.78	11.96
103	295.1	1.324	14.487	1.475	272.00	91.85	0.385	204.70	19.75
104	60.4	1.069	13.681	2.935	81.80	35.32	0.536	217.04	8.18
105	54.3	1.392	7.116	1.048	72.00	16.91	0.403	220.94	4.01
106	281.6	1.186	9.848	3.000	281.00	136.21	0.509	197.65	26.29
107	78.1	1.397	9.193	2.161	91.10	33.61	0.480	217.52	7.60
108	258.3	0.808	6.191	1.090	229.00	77.55	0.336	210.30	15.37
109	196.0	1.007	5.023	2.725	179.00	77.74	0.434	208.31	16.66
110	93.6	0.809	13.823	1.060	99.60	31.74	0.391	218.66	6.71
111	54.7	0.810	7.091	1.061	72.20	21.23	0.433	220.90	4.33
112	170.3	0.815	14.923	1.560	160.00	58.63	0.420	211.05	13.90
113	183.0	0.808	11.268	2.550	183.00	80.27	0.464	207.34	17.60
114	254.7	1.120	14.688	2.219	247.00	102.81	0.452	202.62	21.86
115	275.6	1.245	14.595	2.911	290.00	146.78	0.533	196.37	27.57
116	168.9	1.150	14.892	1.787	159.00	62.08	0.409	211.13	13.78
117	93.4	1.384	10.975	1.185	100.00	27.91	0.388	218.23	6.69
118	83.7	0.846	9.715	2.969	99.50	44.77	0.541	215.19	10.13
119	53.6	0.845	11.348	2.294	73.80	25.92	0.535	219.12	6.06
120	75.0	1.102	9.370	2.998	91.90	41.76	0.550	216.06	9.21
121	172.4	1.222	11.957	1.372	160.00	52.56	0.373	212.75	12.15
122	163.3	0.801	6.422	2.031	156.00	58.03	0.408	212.12	12.95
123	98.5	1.160	11.666	2.427	110.00	47.02	0.497	214.79	10.42
124	182.8	1.393	7.436	2.925	173.00	84.46	0.473	207.37	17.53
125	185.0	0.802	6.856	2.962	175.00	81.64	0.473	207.17	17.72
126	50.0	1.071	9.122	2.196	71.70	22.69	0.525	219.75	5.34
127	258.8	0.883	12.054	2.939	273.00	134.80	0.518	198.50	25.68
128	63.5	1.355	5.100	2.421	78.30	26.99	0.489	218.97	6.13

129	262.3	1.386	5.091	1.239	236.00	70.97	0.347	208.67	16.08
130	150.4	1.209	5.177	2.407	147.00	57.60	0.428	212.40	12.64
131	208.8	1.129	12.885	2.774	222.00	108.30	0.496	203.43	21.20
132	279.8	1.379	10.354	1.865	260.00	97.94	0.409	204.27	20.47
133	131.2	1.189	5.003	1.561	132.00	41.63	0.390	215.50	9.56
134	199.7	1.391	14.694	1.828	183.00	73.74	0.406	208.94	15.95
135	297.0	0.855	5.792	1.849	274.00	94.93	0.390	204.63	20.05
136	192.4	0.801	8.506	1.414	170.00	60.56	0.376	211.28	13.54
137	50.6	1.018	14.431	1.190	71.10	17.55	0.476	220.66	4.45
138	296.4	1.007	5.056	1.141	271.00	78.62	0.366	206.05	18.31
139	132.5	0.804	14.304	2.299	137.00	59.42	0.469	211.91	13.39
140	52.4	1.244	13.980	1.010	71.40	16.51	0.408	221.09	3.90
141	55.7	1.127	5.234	2.765	74.00	26.57	0.530	219.18	5.97
142	90.3	1.291	7.578	2.884	103.00	45.33	0.526	215.24	10.01
143	145.5	1.398	11.863	2.649	149.00	70.77	0.492	209.88	15.21
144	124.0	1.020	11.878	1.376	127.00	41.62	0.411	215.58	9.59
145	264.0	1.167	10.749	1.384	243.00	76.92	0.364	207.29	17.24
146	201.3	1.141	5.165	1.100	171.00	57.00	0.359	212.05	13.05
147	277.8	1.366	6.426	2.740	262.00	110.42	0.455	201.74	22.76
148	109.0	1.359	12.568	1.846	116.00	41.69	0.433	215.50	9.53
149	294.6	0.816	14.835	2.448	296.00	132.65	0.478	198.12	25.77
150	243.0	1.086	14.911	1.011	209.00	61.98	0.367	208.80	15.68
151	51.5	1.032	5.013	2.073	71.70	21.06	0.485	220.23	4.83
152	268.2	1.018	8.329	1.880	249.00	92.24	0.399	205.36	19.42
153	182.9	1.276	10.677	2.064	167.00	70.93	0.424	209.58	15.39
154	167.4	1.051	11.402	2.067	158.00	65.91	0.426	210.57	14.43
155	142.2	0.986	14.977	1.010	140.00	42.33	0.374	215.53	9.63
156	286.2	1.370	14.816	2.207	276.00	111.59	0.455	200.65	23.58
157	294.8	1.357	9.005	1.188	270.00	78.98	0.352	206.83	17.74
158	88.7	0.863	5.008	2.455	99.20	36.17	0.459	217.02	8.12
159	279.6	1.072	5.230	2.434	260.00	101.16	0.422	203.67	21.08
160	50.3	0.840	7.573	2.001	71.50	22.29	0.502	220.12	5.00
161	121.3	0.896	9.651	1.845	126.00	43.94	0.420	214.89	10.13
162	50.7	0.806	14.951	1.723	71.90	24.67	0.540	219.61	5.51
163	295.2	0.803	14.215	1.041	269.00	88.28	0.337	208.83	16.95
164	216.2	1.361	14.355	1.080	181.00	60.59	0.360	210.80	14.03
165	78.5	0.841	14.081	2.993	101.00	46.49	0.528	214.96	10.44
166	159.7	1.229	9.869	2.906	165.00	80.29	0.497	208.19	16.81
167	192.1	1.353	6.296	1.802	172.00	61.99	0.382	210.81	13.95
168	56.8	0.833	10.603	1.374	73.30	21.37	0.457	220.24	4.85
169	121.3	0.963	8.219	1.125	123.00	35.88	0.409	216.19	9.06
170	220.4	0.980	5.104	1.951	198.00	72.08	0.381	208.94	15.81
171	51.7	1.110	6.323	1.153	71.30	17.19	0.422	221.00	4.00
172	139.5	1.013	7.238	2.255	140.00	55.20	0.435	212.91	12.16
173	276.1	0.977	8.819	2.776	268.00	126.18	0.480	200.04	24.28

174	221.2	0.898	12.295	1.796	203.00	77.23	0.396	207.91	16.99
175	124.3	1.382	14.509	1.156	126.00	35.85	0.373	216.35	8.57
176	54.8	1.303	12.729	2.822	75.80	31.97	0.547	217.99	7.21
177	52.2	1.232	6.171	1.839	71.90	20.80	0.477	220.28	4.78
178	150.4	0.992	10.370	2.850	158.00	74.83	0.502	208.90	16.15
179	90.0	0.920	5.148	1.494	97.70	30.68	0.427	217.99	7.14
180	297.3	0.865	5.339	2.760	279.00	111.75	0.448	201.15	23.25
181	293.1	0.949	14.875	1.795	275.00	101.23	0.416	203.09	21.63
182	119.5	0.981	6.664	2.986	126.00	57.24	0.498	212.70	12.51
183	244.4	1.367	11.130	2.804	245.00	118.96	0.492	201.10	23.22
184	183.7	0.921	5.060	1.241	166.00	49.37	0.371	212.33	12.45
185	261.5	1.203	6.026	1.681	240.00	79.99	0.373	206.96	17.58
186	229.9	0.985	8.110	1.018	191.00	64.74	0.357	210.44	14.61
187	185.3	1.116	8.416	1.675	167.00	59.86	0.383	211.22	13.58
188	124.2	1.239	14.981	2.381	131.00	59.20	0.486	212.16	13.00
189	241.7	1.222	8.132	2.274	224.00	92.74	0.428	205.18	19.62
190	293.5	0.962	11.853	1.287	270.00	85.85	0.377	205.46	19.03
191	69.7	1.125	9.897	1.008	79.30	20.83	0.391	220.05	4.96
192	201.2	0.808	14.732	2.825	231.00	114.15	0.515	203.18	21.76
193	208.7	1.246	8.549	1.009	173.00	57.18	0.350	211.96	13.08
194	149.9	1.368	6.116	1.135	146.00	41.38	0.358	215.14	9.78
195	282.2	0.813	10.940	2.223	269.00	106.78	0.440	202.15	22.47
196	61.5	1.170	14.825	1.824	77.90	25.87	0.487	218.98	6.09
197	288.9	1.157	11.148	2.310	277.00	112.19	0.455	200.75	23.54
198	290.8	0.830	9.033	1.494	268.00	87.62	0.376	205.66	19.04
199	92.9	0.977	13.600	1.967	104.00	38.82	0.462	216.22	8.91
200	96.6	1.194	10.272	1.682	105.00	34.85	0.428	216.94	8.09

A.2 - Numerical Simulation Parameter Test Matrix for FROST of UWR4

	Input Parameters: Wall Thickness					**Output Response: Energy Absorption Characteristics**						
#	**t_1 [mm]**	**t_2 [mm]**	**t_3 [mm]**	**t_4 [mm]**	**t_5 [mm]**	**Mass [kg]**	**F_{mean} [kN]**	**F_{peak} [kN]**	**Eff. η**	**Meas. SEA [kJ/kg]**	**Pred. SEA [kJ/kg]**	**Residual Error [%]**
1	1.82	1.85	2.09	1.80	1.88	1.278	116.74	218.41	0.53	91.367	91.204	0.179
2	1.75	2.40	1.75	2.08	2.40	1.383	132.37	239.62	0.55	95.707	95.548	0.166
3	2.40	2.40	2.40	2.24	2.24	1.574	164.18	284.80	0.58	104.326	104.268	0.056
4	2.08	1.75	2.40	1.75	2.40	1.385	134.59	238.31	0.56	97.176	98.910	-1.784
5	2.40	2.32	2.32	2.40	1.75	1.523	156.56	278.40	0.56	102.825	102.838	-0.012
6	1.83	2.32	1.75	1.91	1.75	1.296	118.32	221.94	0.53	91.295	91.293	0.003
7	1.91	1.75	2.24	2.40	1.75	1.366	132.42	244.08	0.54	96.941	96.928	0.014
8	1.75	2.40	2.40	1.75	2.24	1.443	141.20	247.54	0.57	97.833	97.459	0.382
9	2.40	1.75	1.75	1.75	2.24	1.284	118.03	217.30	0.54	91.956	95.233	-3.563
10	1.75	1.75	2.08	2.40	2.32	1.373	134.56	242.06	0.56	98.019	98.509	-0.499
11	2.32	1.75	2.39	2.40	2.40	1.494	153.88	270.89	0.57	103.007	102.051	0.928
12	2.14	1.97	1.75	2.35	2.39	1.387	137.14	246.64	0.56	98.871	101.334	-2.491
13	2.00	2.19	2.14	2.39	2.10	1.459	147.88	262.12	0.56	101.353	101.672	-0.314
14	1.87	1.82	1.84	1.83	2.39	1.283	120.54	218.62	0.55	93.967	93.685	0.300
15	1.94	2.36	2.28	2.02	1.75	1.425	139.31	251.06	0.55	97.760	97.368	0.401
16	2.24	2.32	1.75	2.00	2.16	1.386	136.75	240.27	0.57	98.633	98.447	0.189
17	1.78	1.76	1.75	2.22	1.90	1.255	113.50	219.01	0.52	90.455	90.601	-0.162
18	2.27	2.32	2.24	1.75	2.12	1.442	141.78	248.43	0.57	98.316	98.840	-0.533
19	2.30	1.76	2.40	1.75	1.76	1.350	130.28	232.59	0.56	96.500	96.991	-0.509
20	2.39	1.91	2.13	2.09	2.07	1.408	140.21	249.08	0.56	99.591	99.204	0.388
21	2.16	1.96	2.37	2.40	2.24	1.494	152.16	270.86	0.56	101.862	102.933	-1.052
22	2.24	2.08	2.04	2.26	2.26	1.444	145.81	258.03	0.57	100.966	101.061	-0.094
23	2.25	1.85	2.00	2.06	2.31	1.378	136.01	241.76	0.56	98.683	98.651	0.032
24	2.23	2.12	2.14	2.26	1.89	1.434	144.81	257.43	0.56	100.974	100.160	0.806
25	2.01	2.10	2.25	2.01	2.40	1.442	147.09	253.30	0.58	101.988	101.979	0.008
26	2.01	1.83	2.07	2.26	2.29	1.389	137.56	246.87	0.56	99.059	99.698	-0.645
27	2.40	1.91	2.30	2.38	2.02	1.474	150.69	267.96	0.56	102.228	101.510	0.702
28	2.02	2.07	2.31	2.07	2.11	1.431	142.68	253.24	0.56	99.720	100.857	-1.140
29	2.10	1.76	2.17	2.31	2.00	1.385	136.12	248.13	0.55	98.302	99.076	-0.787
30	2.28	1.94	2.40	2.12	2.14	1.462	149.29	261.41	0.57	102.145	102.193	-0.047
31	2.21	2.10	2.24	2.26	2.40	1.494	156.04	268.38	0.58	104.457	103.849	0.581
32	2.20	2.28	2.19	2.07	2.12	1.462	146.75	258.74	0.57	100.371	100.243	0.128
33	2.30	2.20	2.17	2.38	2.11	1.496	151.48	270.92	0.56	101.272	101.885	-0.605
34	2.16	1.96	2.21	2.09	2.27	1.426	143.77	252.37	0.57	100.828	100.652	0.175
35	2.37	1.90	2.22	2.30	2.32	1.472	149.12	265.11	0.56	101.333	101.587	-0.250
36	2.28	1.93	2.07	2.34	2.07	1.423	141.28	255.85	0.55	99.316	99.753	-0.440
37	2.09	2.07	2.06	2.13	2.08	1.397	137.97	246.97	0.56	98.735	98.190	0.553
38	2.38	2.11	2.40	2.32	2.24	1.535	160.08	278.88	0.57	104.281	103.707	0.551
39	1.98	2.16	2.26	2.28	2.30	1.478	153.21	264.40	0.58	103.680	103.186	0.477
40	2.18	2.32	2.12	2.11	2.39	1.484	154.01	262.68	0.59	103.795	102.812	0.948
41	1.95	2.16	2.30	2.30	2.40	1.494	156.08	267.43	0.58	104.478	103.897	0.557
42	1.85	2.27	2.09	2.38	2.37	1.471	148.60	262.26	0.57	100.999	101.495	-0.491
43	2.07	2.01	2.12	2.40	2.25	1.448	146.81	260.43	0.56	101.376	102.094	-0.709
44	1.97	2.31	2.29	2.13	2.04	1.463	147.95	259.86	0.57	101.136	101.386	-0.247
45	2.12	2.30	2.36	2.36	2.12	1.527	159.55	276.77	0.58	104.478	103.849	0.603

46	1.98	2.24	2.40	2.08	2.26	1.486	153.54	263.66	0.58	103.322	103.479	-0.152
47	1.75	2.01	2.22	2.28	2.19	1.413	142.10	249.64	0.57	100.575	100.206	0.366
48	1.91	2.19	2.05	2.17	2.19	1.413	139.16	249.28	0.56	98.517	98.819	-0.307
49	2.02	1.92	2.34	2.27	2.39	1.464	152.27	262.26	0.58	103.996	103.582	0.398
50	1.92	2.01	2.39	2.37	2.19	1.473	151.94	264.40	0.57	103.148	102.964	0.179
51	1.94	2.07	2.40	2.28	2.40	1.494	155.62	267.49	0.58	104.178	104.253	-0.071
52	2.13	2.34	2.07	2.38	2.29	1.500	151.41	270.07	0.56	100.953	101.598	-0.638
53	1.77	1.89	2.40	2.37	2.36	1.456	150.78	258.82	0.58	103.568	102.549	0.983
54	1.98	2.12	2.39	2.27	1.98	1.464	148.96	262.95	0.57	101.717	102.071	-0.349
55	1.86	1.96	2.16	2.37	2.39	1.435	147.19	255.51	0.58	102.564	102.322	0.236
56	1.92	1.89	2.19	2.06	2.30	1.386	138.16	243.24	0.57	99.714	99.208	0.507
57	1.98	1.94	2.20	2.25	2.11	1.410	143.45	251.32	0.57	101.772	100.327	1.420
58	1.76	2.03	1.96	2.39	2.20	1.385	134.23	244.71	0.55	96.902	97.643	-0.765
59	1.88	1.84	2.40	2.18	2.23	1.421	144.48	252.25	0.57	101.641	100.642	0.983
60	1.75	2.20	2.33	2.15	2.20	1.448	147.69	255.16	0.58	102.023	101.052	0.952
61	1.93	2.04	2.40	2.32	2.40	1.493	156.03	267.66	0.58	104.488	104.224	0.253
62	2.04	2.06	2.27	2.18	2.39	1.464	150.46	260.86	0.58	102.763	103.204	-0.429
63	2.13	2.19	2.17	2.33	2.22	1.481	154.50	266.48	0.58	104.352	102.510	1.764
64	1.89	2.08	2.39	2.15	2.28	1.460	149.01	259.17	0.57	102.037	102.982	-0.926
65	1.77	1.97	2.39	2.21	2.33	1.443	147.01	255.12	0.58	101.885	102.169	-0.278
66	2.10	1.91	2.21	2.28	2.27	1.437	148.20	257.50	0.58	103.126	102.319	0.783
67	1.76	2.19	2.21	2.31	2.26	1.452	146.92	257.38	0.57	101.196	101.735	-0.533
68	2.05	1.97	2.32	2.17	2.22	1.443	147.58	257.35	0.57	102.287	102.620	-0.325
69	1.87	2.06	2.14	2.37	2.23	1.434	145.30	255.68	0.57	101.315	101.625	-0.306
70	1.87	2.25	2.23	2.05	2.35	1.450	144.53	254.46	0.57	99.684	100.057	-0.374

A.3 – CPB06ex5 Coefficients for Single Crystal FCC Cube Simulations

This table presents the coefficients used calibrating the single crystal FCC cube simulations with $a = 100$

C_{11}	C_{12}	C_{13}	C_{22}	C_{23}	C_{33}	C_{44}
1.8793	0.3528	1.8776	-0.0070	0.8738	0.3254	0.9974
C_{11}'	C_{12}'	C_{13}'	C_{22}'	C_{23}'	C_{33}'	C_{44}'
1.2711	1.1983	-0.0428	0.9222	1.5097	1.4986	0.9860
C_{11}''	C_{12}''	C_{13}''	C_{22}''	C_{23}''	C_{33}''	C_{44}''
2.6622	1.8815	0.7680	1.9895	0.4580	0.9174	-1.0021
C_{11}'''	C_{12}'''	C_{13}'''	C_{22}'''	C_{23}'''	C_{33}'''	C_{44}'''
2.0239	2.0499	3.0241	0.1227	1.1079	2.0806	0.6891
C_{11}''''	C_{12}''''	C_{13}''''	C_{22}''''	C_{23}''''	C_{33}''''	C_{44}''''
-2.5478	-1.2956	-0.8376	-0.3070	0.6708	0.6985	0.9764

A.4 – CPB06ex3 Coefficients for Extruded Aluminum AA6063-T6 Simulations

This table presents the coefficients used calibrating extruded aluminum AA5754-O polycrystalline FCC simulations with $a = 9.7577$

C_{11}	C_{12}	C_{13}	C_{22}	C_{23}	C_{33}	C_{44}
0.9048	0.5445	-0.6493	1.8424	0.4846	0.3465	-0.6734
C_{11}'	C_{12}'	C_{13}'	C_{22}'	C_{23}'	C_{33}'	C_{44}'
1.1705	0.5249	2.0902	1.5076	2.3193	1.8714	0.8650
C_{11}''	C_{12}''	C_{13}''	C_{22}''	C_{23}''	C_{33}''	C_{44}''
1.1630	0.2331	0.7209	2.0200	1.2297	-0.0297	1.2161

A.5 – CPB06ex3 Coefficients for Sheet Aluminum AA5754-O Simulations

This table presents the coefficients used calibrating sheet aluminum AA5754-O polycrystalline FCC simulations with $a = 10.4212$

C_{11}	C_{12}	C_{13}	C_{22}	C_{23}	C_{33}	C_{44}
0.4087	2.1051	1.4282	0.4634	1.3853	2.3470	1.6122
C_{11}'	C_{12}'	C_{13}'	C_{22}'	C_{23}'	C_{33}'	C_{44}'
1.6148	2.7180	0.9758	1.9443	1.2307	-0.3031	1.0839
C_{11}''	C_{12}''	C_{13}''	C_{22}''	C_{23}''	C_{33}''	C_{44}''
-0.7244	0.2549	1.1070	0.0694	0.9464	2.2032	0.9729

GLOSSARY

Adaptive simulated annealing (ASA) algorithm: a stochastic optimization procedure used in local optimization that mimics the annealing process in metallurgy

Anisotropy: directional dependent material properties caused by favourable orientations of grains within a material

Artificial neural network (ANN): a class of artificial intelligence that is used for determining input-to-output relationships; structured to replicate the architecture of a human brain, where nodes are connected in a massively parallel network, as an input-to-output relationship

Associative flow rule: an assumption that the plastic strain increment tensor is related to the normality of a yield function/surface

Back propagation algorithm: gradient descent method for calibrating the coefficients in an artificial neural network

Bosses: fixtures/clamps used to secure crush specimen during dynamic sled testing

Cauchy stress (true stress): stress tensor that associates the current load to the current geometrical configuration; referred to the stress components aligned in the reference/lab system of coordinates

Collapse elements: geometric representation of the bends and folds generated during progressive crush

Constitutive model: a relationship between two physical quantities. In plasticity, it is the relationship between kinetics (stress, force) to kinematics (strain, displacement)

Courant-Friedrichs-Lewy criterion: critical time-step criteria used in explicit dynamic formulations that must be satisfied for the numerical solution to be stable

Crashworthiness: the focus of occupant protection during an automotive collision

Crush efficiency: energy absorption performance metric defined as the ratio of the mean crush force to the peak crush force

Crystal plasticity: a physics-based model that relates the crystallographic slip that results from dislocation glide to mechanical response of a material

Crystallographic slip: deformation where a dislocation occurs on a slip plane

Deformation gradient: a particle's current material point location in space with respect to the particle's initial material point location

Design of Experiments (DoE): Combinations or sets of parameters within a specified domain of parameters

Deterministic process: a process that produces the same output for the same given input or starting condition; no randomness in the system

Dislocation: the shearing of atoms along a row of slip planes in a localized region when the shear stress along a slip plane reaches a critical stress

Dynamic loading: a loading process that evolves over a short period of time, such that time and inertial dependent effects are significant

Elasticity: the ability of a solid or body to return to its original shape after an applied deformation has been removed

Energy absorption: integrated of the force-displacement response

Explicit dynamic formulation: using the central difference method to perform time integration of governing equations

Failure: post-necking region of the stress-strain response where uniform deformation transitions into non-homogenous deformation, such as a diffused or localized neck

Finite element methods: a branch of numerical methods that is used to solve boundary value problems for applied engineering problems. Boundary value problems are a class of mathematical problems that must satisfy a differential equation within the domain of interest and specific constraints and initial conditions

Fracture: physical cracking or separation of material

Front rail: crush structure located at the front a vehicle that is designed to absorb energy in the event of a frontal collision

Gauss-Newton method: a deterministic optimization scheme used in parameter identification or objective function minimization/maximization

Genetic algorithms: a stochastic optimization scheme used in global optimization that replicates the process of natural selection

Intermediate stress tensor: Cauchy stress tensor projection onto the orthotropic axes of anisotropy

Kirchoff Stress: stress tensor that associates the nominal load to the initial geometrical configuration

Lankford coefficients (R-value): ratio of transverse strain to thickness strain during uniaxial tension

Localization (strain): non-homogeneous deformation within a material during constrained deformation

Material spin*:* the anti-symmetric components of the velocity gradient tensor that represents the vorticity of a particle in a continuum

Mean crush force: the average crush force value determined by integrated the entire force-displacement response and normalizing by the total displacement

Metamodel: a mathematical model that is constructed to represent the input-to-output relationship of a system

Microstructure (texture): geometric structuring of atoms that occur throughout the material

Microstructure evolution (spin): deformation induced rotation of the orthotropic axes of anisotropy

Multi-scale modeling: bridging information from lower (micro) length scales to higher (macro) length scales

Nonlinear metamodeling: a user-defined mathematical function to represent the input-to-output relationship of a system

Non-proportional strain paths: deformation where the components of the symmetric strain rate changes with respect to time

Objective function: quantity to be maximized or minimized

Optimization: a procedure for achieving the best result of an operation while satisfying constraints

Orientation distribution function: representation of crystallographic orientations in 3-dimensional Bunge Euler space $(\theta_1, \Phi, \theta_2)$

Orthotropic (anisotropic) axes: axes of three mutually orthogonal symmetry planes that represents the frame of reference for initial anisotropy

Peak crush force: maximum magnitude in the crush force response

Phenomenological plasticity: a model for plasticity that is generated from fitting a mathematical function to observations in experiments

Plane-stress: through-thickness stress components of the stress tensor are zero

Plasticity: permanent deformation in a solid or body that remains after an applied deformation has been removed; caused by the dislocation of atoms along a row of slip planes in a localized region along crystal lattice planes

Pole figure: a 2-dimensional representation in polar space (R_i, θ_j) of the 3-dimensional Euler angles with respect to the sample frame on crystallographic planes, where the frequency of

orientations is represented by intensity $W(R_i, \theta_j)$ in bins with respect to R_i and θ_j , such that $0 \leq R_i \leq 1$ and $0 \leq \theta_j \leq 2\pi$.

Polycrystalline materials: a material composed of several crystals or solids of various sizes, shapes, and orientations

Polynomial metamodeling: using a polynomial function to represent the input-to-output relationship of a system

Post-necking behaviour: stress-strain response of the material after the ultimate tensile strength has been reached

Principal stresses: components of the stress tensor after a basis transformation where the shear stresses are zero; eigenvalues of the stress tensor

Quasi-static loading: a loading process that evolves over a long period of time, such that time and inertial dependent effects are negligible

Response surface methodology: a framework that is used to construct a global approximation of a system's behaviour

Single crystal materials: a material composed of predominantly one orientation throughout the microstructure

Specific energy absorption: energy absorption performance metric defined as the total energy absorbed normalized by the mass of the structure

Steady state crush force: the crushing force value determined by integrated the force-displacement response after the initial impact when the steady progressive folding occurs and normalized by the displacement within the steady state regime

Stochastic process: a process that produces the different output for the same given input or starting condition; randomness in the system

Strain: a tensor that describes the deformation of a particle in a continuum

Strain (Flow Stress) hardening: an increase in the required yield stress to cause an increase in strain; the accumulation of dislocations within atoms that require a higher shear stress along the slip system for shearing to occur

Strain rate sensitivity: the change in the flow stress hardening behaviour due to changes in rate of deformation

Stress: a tensor that expresses the internal forces exerted by neighbouring particles in a continuum

Symmetric strain rates: the symmetric components of the velocity gradient tensor that represents the rate of stretch (deformation)

Training data: data points (inputs and outputs) that are used to calibrate a metamodel

Ultimate tensile strength: maximum stress a material can endure during uniaxial tension

Updated-Lagrangian formulation: the configuration of the system is updated at the end of each time step

User-defined material subroutine*:* a customizable module in a finite element code that allows a user to create and implement their own constitutive model

Velocity gradient*:* the gradient of a velocity field of particles in a continuum

Yield criterion/function/surface: a mathematical function that determines if a stress state is elastic or plastic

Yield stress: stress level where the behaviour of the material transitions from an elastic to plastic behaviour